



Modelling proto-neutron star evolution

Aurélien Pascal

► To cite this version:

Aurélien Pascal. Modelling proto-neutron star evolution. Astrophysics [astro-ph]. Université Paris sciences et lettres, 2021. English. NNT : 2021UPSLO010 . tel-03850824

HAL Id: tel-03850824

<https://theses.hal.science/tel-03850824>

Submitted on 14 Nov 2022

HAL is a multi-disciplinary open access archive for the deposit and dissemination of scientific research documents, whether they are published or not. The documents may come from teaching and research institutions in France or abroad, or from public or private research centers.

L'archive ouverte pluridisciplinaire **HAL**, est destinée au dépôt et à la diffusion de documents scientifiques de niveau recherche, publiés ou non, émanant des établissements d'enseignement et de recherche français ou étrangers, des laboratoires publics ou privés.



THÈSE DE DOCTORAT
DE L'UNIVERSITÉ PSL
Préparée à l'Observatoire de Paris

Modélisation de l'évolution des Proto-Étoiles à Neutrons

Modeling Proto-Neutron Star evolution

Soutenue par

Aurélien PASCAL

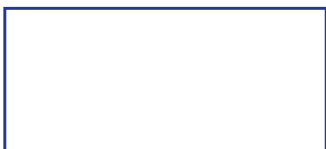
Le 06/07/2021

Ecole doctorale n° 127

**Astronomie et astrophysique
d'Ile-de-France (AAIF)**

Spécialité

Astronomie et astrophysique



Composition du jury :

Marie-Christine ANGONIN Professeure, Sorbonne Université	<i>Présidente</i>
Jose PONS Full professor, University of Alicante	<i>Rapporteur</i>
Jérôme MARGUERON Directeur de recherche, Institut de physique des deux infinis	<i>Rapporteur</i>
Nicolas CHAMEL Maître de recherche, Université libre de Bruxelles	<i>Examineur</i>
Armen SEDRAKIAN Professor, Frankfurt Institute for Advanced Studies	<i>Examineur</i>
Anthéa FANTINA Chargée de recherche, GANIL	<i>Examinatrice</i>
Jérôme GUILLET Ingénieur-Chercheur, CEA-Saclay	<i>Examineur</i>
Micaela OERTEL Directrice de recherche, Observatoire de Paris	<i>Directrice de thèse</i>

Acknowledgements

I would like to thank all the researchers I had the opportunity to work with. Simon Giraud, Anthea Fantina, Francesca Gulminelli and Adriana Raduta for our collaboration on the subject of electron capture rates, Edwan Preau for our collaboration on the first application of my proto-neutron star evolution code, and of course Micaela Oertel and Jérôme Novak, for the time they devoted to me and for helping me to bring this work to fruition in these difficult times for all students.

I wish to express my gratitude to both Yann Rasera and Jérôme Guilet for participating in my thesis monitoring committee during these three years, and to Bernard Müller for providing pieces of the Fast Multigroup Transport code, upon which I have based the neutrino transport scheme used in my thesis.

I am grateful to Jose Pons and Jérôme Margueron for accepting to give of their time to review my thesis, and I also thank Marie-Christine Angonin, Nicolas Chamel, Armen Sedrakian, Anthea Fantina and Jérôme Guilet for accepting to be among my jury members.

Contents

Introduction	5
I Context	6
1 Neutron stars in a nutshell	7
1.1 A short history of neutron star discovery	7
1.1.1 From a theoretical hypothesis...	7
1.1.2 ...to actual observations	7
1.2 Observation of neutron stars	8
1.2.1 Pulsar timing	8
1.2.2 Mass measurements	9
1.2.3 Surface temperature measurements	11
1.2.4 Radius measurements	11
1.3 Neutron star theory : structure and composition	12
1.3.1 Nuclear equation of state	12
1.3.2 Masses and radii	14
2 Formation of neutron stars : the core-collapse mechanism	17
2.1 Core-collapse dynamics	17
2.1.1 Onset of the collapse and infall	17
2.1.2 Bounce and shock propagation	18
2.1.3 Delayed neutrino heating and final explosion	19
2.1.4 Neutrino driven wind and nucleosynthesis	20
2.2 Trapping of neutrinos in dense matter	21
2.2.1 The weak interaction	21
2.2.2 Relevant processes	21
2.2.3 Cross-sections : some orders of magnitude	22
2.2.4 Mean free path and neutrinospheres	23
2.2.5 Chemical equilibrium and thermalization	24
3 Thermal evolution of proto-neutron stars	26
3.1 The proto-neutron star (PNS)	26
3.1.1 Initial structure of the PNS	26
3.1.2 PNS cooling	27
3.1.3 Equation of state of a PNS	28
3.1.4 Convection in proto-neutron stars	29
3.1.5 Emission of gravitational waves	30
3.2 Previous works on proto-neutron star evolution	31
3.2.1 Quasi-static studies	31
3.2.2 Full hydrodynamic studies	32
3.2.3 Open questions in PNS evolution	33

3.3	Neutrino detection capabilities	33
3.3.1	The SN1987A supernova event	33
3.3.2	Types of neutrino detectors	34
3.3.3	SuperNova Early Warning System (SNEWS)	37

II Transport of neutrinos in dense matter 38

4	Boltzmann equation and collision integral 39
4.1	General relativistic Boltzmann transport 39
4.1.1	One-particle distribution function 39
4.1.2	Boltzmann equation 40
4.2	Case of a TOV spacetime 41
4.2.1	Momentum coordinates 41
4.2.2	Boltzmann equation and angular moments 42
4.2.3	Macroscopic conservation laws 42
4.3	Collision integral 43
4.3.1	Charge exchange processes 43
4.3.2	Scattering processes 44
4.3.3	Thermal pair production 47
4.4	Limits of the Boltzmann equation 48
4.4.1	The diffusion limit 48
4.4.2	The free-streaming limit 49
4.5	The Fast Multigroup Transport (FMT) 49
4.5.1	Steady-state neutrino transport 49
4.5.2	High optical depths : the two-ray approximation 50
4.5.3	Low optical depths : two-moment closure 51
4.6	Other neutrino transport methods used in PNS simulations 52
4.6.1	Equilibrium Flux Limited Diffusion (EFLD) 52
4.6.2	Variable Eddington factor method 53
4.6.3	Comparison of various methods 53
5	Weak processes occuring in core-collapse and (proto-)neutron stars 55
5.1	Neutrino interactions with free nucleons 55
5.1.1	Charged current interactions with nucleons 55
5.1.2	Scattering off nucleons 57
5.1.3	Pair production by nucleon-nucleon bremsstrahlung 58
5.2	Neutrino interactions with nuclei 59
5.2.1	Composition of the medium : nuclear distributions 59
5.2.2	Electron captures on nuclei 60
5.2.3	Scattering off nuclei 61
5.3	Neutrino interactions with charged leptons 62
5.3.1	Scattering off charged leptons 62
5.3.2	Pair production by electron-positron annihilation 63
5.4	Other relevant processes 64
5.4.1	Plasma and Photo emission processes 64
5.4.2	Neutrino-neutrino interactions 64
5.4.3	Neutrino flavor evolution 65

III	Proto-neutron star evolution	66
6	Quasi-static modeling of proto-neutron stars	67
6.1	The quasi-static approximation	67
6.1.1	Motivation : PNS evolution timescales	67
6.1.2	Hydrostatic stellar structure : the TOV equations	68
6.1.3	Quasi-static evolution equations	69
6.1.4	Summary of the algorithm	70
6.2	Example of simulation	70
6.2.1	Evolution of global properties of the PNS	71
6.2.2	Structure of the PNS	72
6.2.3	Neutrino emission from the PNS	75
7	Masses and radii of proto-neutron stars	78
7.1	Gravitational waves and PNS properties	78
7.1.1	Eigenmodes for oscillations of a PNS	78
7.1.2	Relation with the PNS properties	79
7.1.3	Possible difficulties	79
7.2	Getting information from a PNS mass and radius	81
7.2.1	Parametrized initial profiles	81
7.2.2	Evolution of proto-neutron stars in the (M,R) plane	83
7.2.3	Conclusion and limitations	84
8	Modeling convection with the Mixing Length Theory	87
8.1	Instability to convective motion	87
8.1.1	Ledoux criterion for the stability of a stratified media	87
8.1.2	Causes of convection : entropy and composition gradients	88
8.1.3	Case of proto-neutron stars	89
8.2	Mixing length theory	89
8.2.1	Particle and thermal diffusion with the MLT	89
8.2.2	Estimation of the diffusion coefficients	90
8.2.3	Numerical implementation	90
8.2.4	Advantages and weaknesses of the MLT	91
8.3	PNS evolution with the MLT	91
8.3.1	Evolution timescale	91
8.3.2	Structure and convective mixing	91
8.3.3	Effect of convection on the neutrino emission	94
IV	Influence of charged current processes	96
9	Electron captures on nuclei during the infall of the iron core	97
9.1	Electron capture rates on neutron rich nuclei	97
9.1.1	Approximation of independent particles	98
9.1.2	Fit on the Q -value dependancy (LMP)	98
9.1.3	Nuclear masses and Q -values	100
9.2	Core-collapse simulations	100
9.2.1	The CoCoNuT code	100
9.2.2	Equation of state	101
9.2.3	Neutrino transport	102
9.2.4	Initial data : the progenitor	102

9.3	Results	102
9.3.1	Evolution of the electron fraction	102
9.3.2	Propagation of the shock and deleptonization burst	104
9.3.3	Influence of other parameters on the infall	106
9.3.4	Determination of the most relevant nuclei	107
10	Improved charged-current reaction rates on nucleons	109
10.1	Approximations and models for charged current rates	109
10.1.1	The Elastic approximation with non-interacting particles	109
10.1.2	The Elastic approximation with Mean Field corrections	110
10.1.3	Full kinematics within the Mean Field theory (MF)	111
10.1.4	Full kinematics with the Random Phase Approximation (RPA)	111
10.2	Resulting neutrino opacities	112
10.2.1	Tabulated rates and interpolation procedure	112
10.2.2	Some example of opacities	112
10.3	Influence on a core-collapse	115
10.3.1	Pre-bounce deleptonization	116
10.3.2	Post-bounce evolution	116
11	PNS evolution with improved reaction rates on nucleons	119
11.1	Charged current rates and PNS cooling	119
11.1.1	Failure of the elastic approximation	119
11.1.2	Modified URCA processes	120
11.1.3	Example of charged-current rates relevant in PNS cooling conditions . . .	121
11.2	Results of simulations	122
11.2.1	Effect on the PNS evolution	122
11.2.2	Influence on the emitted neutrino spectrum	123
11.2.3	Influence of the equation of state	124
11.2.4	Conclusion and limitations	125
	Conclusion and perspectives	127
	Appendix A Analytic fit for nucleon-nucleon bremsstrahlung	130
	Appendix B Analytic fit for the ion screening effect	132
	Appendix C Kernel for neutrino-charged lepton scattering	134
	Appendix D Kernel for electron-positron pair process	136
	Appendix E Precomputation of functions for charged leptons processes	137
	Appendix F Nuclear shell model and neutron blocking	138
	Appendix G Numerical implementation of the PNS evolution code	140
	G.0.1 Grid and discrete set of equations	140
	G.0.2 Treatment of neutrino transport	143
	Appendix H Gauss-Legendre quadrature method	145
	Appendix I Implicit solver for the MLT scheme	146
	References	147

Introduction

When massive stars reach the end of their life, they collapse because their core exceeds the Chandrasekhar limit. This collapse is followed by a bounce once the center reaches approximately nuclear density, and this can cause a core-collapse supernova [1] [2]. After the bounce, the central object, called a proto-neutron star, will evolve to become either a neutron star or a black hole [3]. If the main features of the core-collapse supernova mechanism are now understood, some important details about the microphysics are still subject to a lot of uncertainties. In particular, neutrinos are playing a key role in the core-collapse mechanism but interaction rates between neutrinos and dense matter are difficult to determine precisely due to the strongly interacting dense matter [4]. The evolution of the proto-neutron star is also subject to these uncertainties, and undergoes convective motions that play a significant role in the cooling process [5].

This thesis focuses on modelisations of core-collapse supernova and proto-neutron star evolution, and more particularly on the role of neutrinos. It is organised as follows.

Part I is dedicated to the presentation of the physical context of studied phenomena. A brief review of neutron star physics and history is given in chapter 1, then chapter 2 presents the core-collapse mechanism and chapter 3 presents the cooling mechanism of a proto-neutron star.

Then, in part II we focus on the role of neutrinos. Chapter 4 presents the framework needed to model neutrino transport and the model used in this thesis, whereas in chapter 5 we review the weak processes involving neutrinos occurring in core-collapse and proto-neutron stars and present the formulas and approximations used to compute the corresponding reaction rates.

In part III we present a new code modeling proto-neutron star evolution along with some applications to specific problems. Chapter 6 presents the algorithm, with the generic framework and its implementation. Then in chapter 7 we give an application of this code to the early evolution of proto-neutron stars in connection with some recent work on proto-neutron star asteroseismology and the corresponding gravitational wave emission. Chapter 8 is then dedicated to the study of convection effects in proto-neutron stars, with the mixing length theory.

Finally, in part IV, we study the role of charged current interactions in the core-collapse supernova and proto-neutron star cooling mechanisms. In chapter 9 we present the various approximations used for the computation of electron capture rates on nuclei and study their influence on core-collapse simulations, then in chapter 10 we focus on the various prescriptions used for charged-current processes of neutrinos with nucleons and their influence on core-collapse, before expanding this study to the case PNS cooling in chapter 11.

In all this thesis we will use Penrose's abstract index notation for tensors : latins letters a, b, c, \dots are abstract indices such that X^a represent the vector itself and not its components. Components of a tensor are given by greek indices μ, ν, \dots (spanning from 0 to 3) and the latins letters i, j, k, \dots (spanning from 1 to 3). We also use units in which $k_B = 1$.

Part I

Context

Chapter 1

Neutron stars in a nutshell

1.1 A short history of neutron star discovery

1.1.1 From a theoretical hypothesis...

The existence of neutron stars was suggested by Baade & Zwicky in 1934 [6], less than two years after the discovery of the neutron by Chadwick [7]. They were originally looking for an explanation of the supernova phenomenon, and hypothesised that they could be powered by the collapse of a massive star into a compact star consisting mainly of neutrons.

In 1939 Tolman, Oppenheimer & Volkoff made the first computation of the structure of such a star [8] [9], assuming that they were constituted of a degenerate ideal gas constituted of free neutrons. They predicted a maximum mass of neutron stars of about $0.75 M_{\odot}$.

Studies on neutron stars did not go beyond these few theoretical considerations during a few decades, as they were believed to be too faint to produce an observable signal. At the end of the 50s - beginning of the 60s, there was a renewed interest in neutron stars from the nuclear physics point of view, in the search of an equation of state of dense nuclear matter and for the role neutron stars might play in nucleosynthesis [10] (in particular Migdal predicted the possible superfluidity of neutron star matter [11]). Those studies showed that the pressure due to nuclear interactions between nucleons is dominant compared with the neutron's degeneracy pressure, such that the maximum mass of neutron stars should be much higher than the $0.75 M_{\odot}$ limit of Oppenheimer & Volkoff.

1.1.2 ...to actual observations

The search for observational evidences of neutron stars began with x-ray astronomy, some x-ray sources were believed to be thermal emissions from neutron stars. But it was impossible to conclude due to lack of consistency with the models [10].

It was also hypothesised that the quasi stellar objects (quasars) were neutron stars, but this was incompatible with the high redshift at which some of them were observed.

The turning point was the discovery of pulsating radio sources (pulsars) by Jocelyn Bell and Antony Hewish [12]. The link with neutron stars was then quickly established because only an extremely compact object such as a neutron star could explain the high rotation frequency of millisecond pulsars [10].

Since then an increasing number of pulsars have been discovered, with the famous Hulse-Taylor

binary PSR B1913+16 [13] among them. This pulsar was first observed in 1974 and lead Hulse and Taylor to earn to Nobel Prize in 1993. The observation of the supernova SN1987A was also a major discovery, because the detection of the neutrino emission [14] allowed to confirm the scenario of core-collapse as main source of neutron star formation. Indeed, even if no neutron star has been detected up to now as a remnant of SN1987A, the observed neutrino emission was consistent with the loss of the gravitational binding energy that has to be emitted during the formation of a neutron star and with the scenario of core-collapse involving the neutronization of the core.

Today even optical observations of closest neutron stars have been made possible by the increasing sensitivity of instruments (see e.g. [15]). And of course the observation of gravitational waves emitted during the neutron star merger GW170817 by the LIGO and Virgo collaborations [16] completely changed the picture, as we also detected the electromagnetic counterpart during this event (see e.g. [17] and [18]). This combined observation allowed to obtain the proof of heavy-element nucleosynthesis in binary neutron stars mergers, and the measure of the deformabilities

Thus, the use of those various ways of observations allows to gain new insights on neutron star and is the beginning of multimessenger astronomy.

1.2 Observation of neutron stars

In the last few decades, observations of neutron stars yielded important results, allowing for more constraints on their physics. What made (at first) the study of neutron star possible is the pulsar emission mechanism, which allow for an extremely accurate timing to measure their rotation and orbital motion.

1.2.1 Pulsar timing

A pulsar is a strongly magnetized rotating neutron star which emits a tight beam of electromagnetic radiation, which is detected at the star's rotation frequency, with a period ranging from around 1 ms to several tens of seconds.

The simple model for pulsar emission is the *rotation powered pulsar*, which rely on two rotational effects. The first is the misalignment between the pulsar rotation axis and its magnetic dipole axis with an angle $\alpha \geq 0$. Because of it the pulsar can be considered as a spinning magnetic dipole which generates an electromagnetic radiation. The second is the complex interaction between the rotating neutron star and its magnetosphere, which leads to the establishment of electric currents and thus to an electromagnetic radiation. In [19], the author obtained a fit formula for the electromagnetic power radiated by the pulsar :

$$P_{rad} = \frac{\mu^2 \Omega^4}{c^3} (1 + \sin^2 \alpha) \quad (1.1)$$

Where μ is the magnetic moment and Ω the rotation frequency.

The first pulsar observed [12] was a *rotation powered pulsar*.

Some other emission mechanisms are possible, such as the case of *accretion powered pulsars* (also called x-ray pulsars), which consists of a pulsar accreting matter from its stellar companion in a binary system. x-ray hotspots [20] are created on the pulsar at the accretion points, and these hotspots are visible at the rotation frequency.

There exists also several strongly magnetized neutron stars, which have been classified as *magnetars*. They are isolated x-rays pulsars for which the x-rays emission is powered by the decay of their extremely high magnetic field, see e.g. [21].

The pulse period is extremely stable, and because of this particularity pulsars can be used as extremely accurate astronomical clocks. They have been extensively studied for this reason, indeed their timing can provide tests of general relativity (see e.g. [22]) and/or accurate measurement of orbital parameters if the pulsar is part of a binary system.

Another interesting application of pulsar timing is the construction of a Pulsar Timing Array (PTA), which consists of a set of pulsars observed regularly (about once a week) in order to search for correlations in the pulse arrival times (see e.g. [23]). Such correlations could contain the signature of low-frequency (between 10^{-9} and 10^{-6} Hz) gravitational waves.

1.2.2 Mass measurements

Mass measurements of neutron stars provide constraints on their maximum mass. This point will be discussed in the section 1.3.2. The figure 1.1 reports some mass measurements of neutron stars (up to 2016).

Various methods are used for mass measurements of neutron stars, but the most accurate one is to use the orbital period of binary systems. If one of the two companions is a pulsar, an accurate measurement of the orbital period P_{orb} of the binary can be performed, as well as the peak radial velocity of the pulsar v_{psr}^{peak} . From this we can deduce the *binary mass function*

$$f = \frac{(M_c \sin i)^3}{(M_c + M_{psr})^2} = \frac{P_{orb}(v_{psr}^{peak})^3}{2\pi G} \quad (1.2)$$

where $\sin i$ is the inclination of the orbital plane and M_{psr} and M_c are respectively the masses of the pulsar and its companion.

Since we have three unknowns in this equation, we need some additional information to obtain the masses, which can be obtained using the observation of the orbit of the companion or the measurement of post-keplerian parameters such as the advance of the periastron or the Shapiro delay (see [24] for a review).

The other methods available such as the observation of x-ray binaries can also provide estimations of the masses, but those estimates are subject to several sources of systematic uncertainties due to their dependance on a given model. For exemple the mass of Vela X-1 has been estimated using measurements of the radial velocity of its companion, which are subject to a lot of uncertainties and rely on a model for the oscillation modes of the companion and its interaction with the neutron star [26].

Among the highest measured masses there is the millisecond pulsar J1748-2021B [27], with a mass of $(2.74 \pm 0.21) M_\odot$, measured via the advance of the periastron. But this value comes with a lot of uncertainties due to the inclination of the system and the fact the the periastron advance may not be caused only by general relativistic effects. Some black widow pulsars also have a very high measured mass, but they come with a lot of uncertainties.

To constrain the maximum mass of neutron stars, we usually retain the less massive but much more accurate measurements of J0740+6620 [25] and J1614-2230 [28][29], both obtained at a very high precision via Shapiro delay. They have respectively masses of $(2.08 \pm 0.07) M_\odot$ and $(1.908 \pm 0.016) M_\odot$. The pulsar J0348+0432 [30], also has a very high measured mass of $(2.01 \pm 0.04) M_\odot$, but is less reliable as it is based on a spectroscopic modeling of its white dwarf companion.

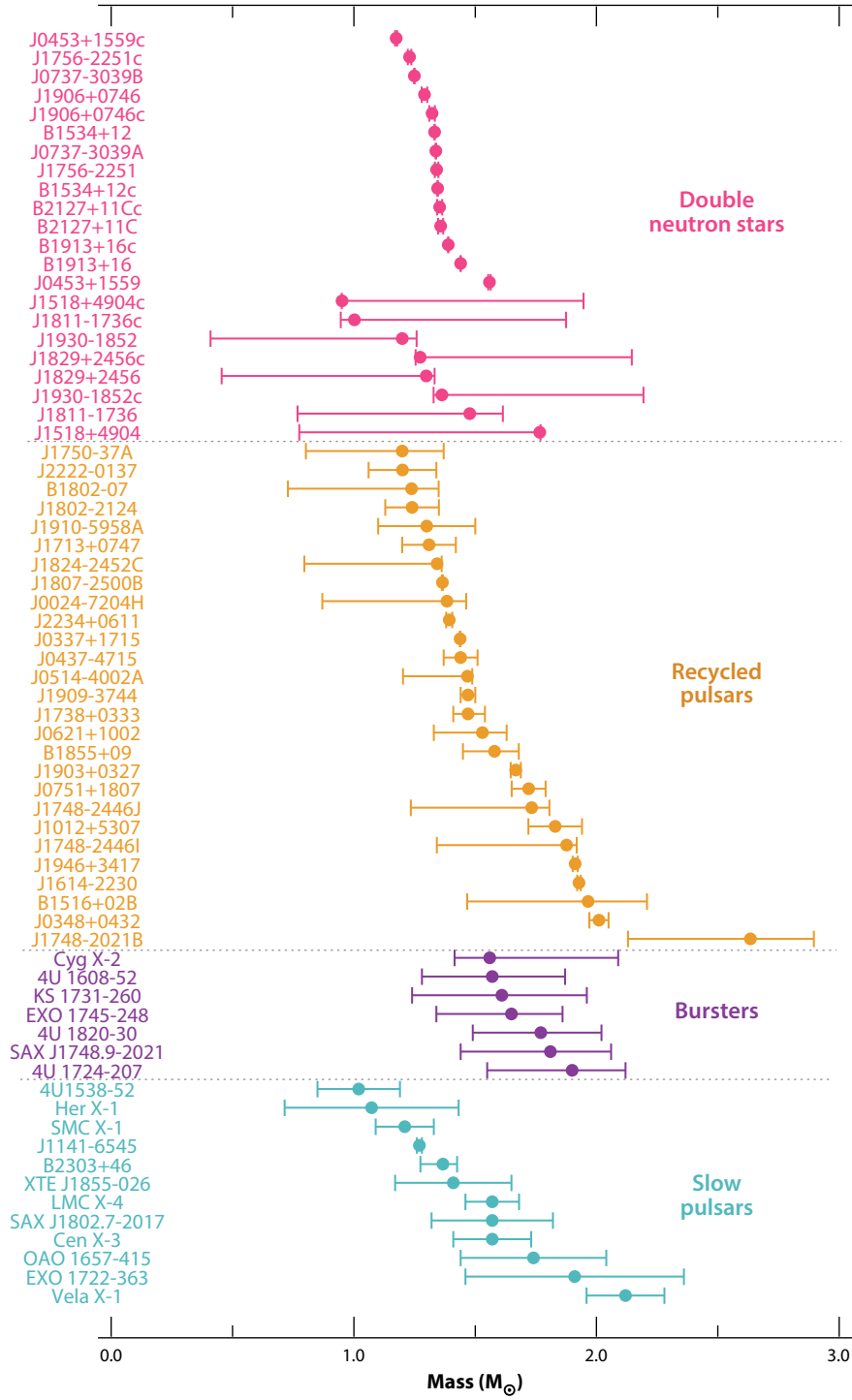


Figure 1.1: Some mass measurements of neutron stars (up to 2016). This figure is extracted from [24]. A different method of measurement is used for each color set. Among the masses measured after 2016, one should mention the millisecond pulsar MSP J0740+6620 which has a mass $(2.08 \pm 0.07) M_{\odot}$ [25]

Regarding the lowest neutron star mass measurement, the most accurate measurement comes from the asymmetric double neutron star system PSR J0453+1559 [31]. In this binary the two objects have respectively a mass of $(1.559 \pm 0.005) M_{\odot}$ and $(1.174 \pm 0.004) M_{\odot}$.

1.2.3 Surface temperature measurements

Relatively young neutron stars have a surface temperature of about $T \approx 10 - 100$ keV ($10^6 - 10^7$ K), therefore they emit thermal radiation in x-rays which can in principle be measured and fitted to a black body spectrum to determine the surface temperature of the star.

In order to be a good observational candidate the thermally emitting neutron star must be isolated because binaries are subject to accretion and other transient phenomena which pollutes the thermal spectrum. The small size of neutron stars makes the x-ray radiation hard to detect and only the closest neutron stars present a measurable x-ray spectrum. Because of these constraints, we can only measure the surface temperatures of a few neutron stars [32].

Among the observed neutron stars, Cassiopeia A is worth mentioning, as a detailed measurement of its cooling rate has been performed [33] : its surface temperature was of $(2.12 \pm 0.01) \times 10^6$ K in 2000 and of $(2.04 \pm 0.01) \times 10^6$ K in 2009. However this result is very controversial and have been claimed to be not significant, see e.g. [34].

The determination of the temperature also comes with additional uncertainties : the observed flux has to be corrected for the gravitational redshift and the magnetic field effect on the emission [24], as well as for interstellar absorption. The distance of the star have to be known precisely to obtain the absolute magnitude, and additionally, neutron stars are not ideal black bodies, the composition of their atmosphere is extremely uncertain and strongly influences the emission. Various models of atmospheres exist and the result usually depends on which atmosphere model is used in the analysis [32].

Magnetar candidates are subject to even higher uncertainties due to the complex modelisation of radiation transfer in strongly magnetised atmospheres.

1.2.4 Radius measurements

Radius measurements are also complicated and not so accurate. Among the available methods are the measurements by x-ray observations (see e.g. the mission ATHENA [35] and the mission NICER [36][20]), and the measurements by observation of gravitational waves of binary mergers [37].

The radius determination from thermal spectrum observations relies on the thermal emission of a neutron star surface : in principle one should be able to determine the radius from the neutron star's surface temperature, total luminosity and distance to Earth. But as mentioned above temperature measurements are subject to a lot of uncertainties, which make radius measurements from thermal spectra strongly model-dependent [38].

Because of these difficulties, radius measurements from x-ray observations now rely more on x-ray timing methods (see e.g. [39]), which are based on the fact that in some cases the neutron star presents hotspots on its surface (because of accretion points or hot polar regions heated by the magnetic fields). The x-ray signal presents modulations because of the presence of these hotspots, and we can extract the radius from the shape of the signal.

These observations have constrained most of measured radii between 9 km and 14 km. The NICER collaboration recently announced the determination of the radius of the millisecond pulsar J0740+6620 (discussed in section 1.2.2, as being the pulsar with the highest mass known at a high precision). Two independent teams provided a measurement : in [40] they estimate the radius to be $12.39^{+1.30}_{-0.98}$ km, and in [41] they estimate it to be $13.7^{+2.6}_{-1.5}$ km.

It should be noted that a general problem of x-ray observations is that they are usually impossible in systems for which accurate mass measurements are possible, therefore it is hard to provide a

good constraint both on the mass and the radius, which could allow to discriminate between equations of state (see section 1.3.1). The recent results of the NICER collaboration are thus extremely promising in this sense.

The birth of gravitational wave astronomy opened new possibilities and methods for the measurement of radii, indeed waves emitted during neutron star mergers carry a lot of informations and are extremely promising to provide strong and reliable constraints for the radius. The method is indirect : the tidal deformabilities can be recovered by a parameter estimation on the detected waveform [37], which can then be translated into a radius, either by using a given equation of state or by using inferred universal relations¹ between the tidal deformability and the compactness (see e.g. [42]). Up to now, two gravitational wave observations correspond to a binary neutron star merger with a high level of confidence : GW170817 [16] and GW190425 [43].

Examples of joint analysis combining GW observations with results from x-ray astronomy to constraint the radius of a neutron star are given in [44] and in [45].

1.3 Neutron star theory : structure and composition

A lot of progress has been made since the first model of Oppenheimer & Volkoff [8], thanks to observational data, nuclear physics experiments and general progress in numerical computations. If a lot of uncertainties remain on the exact structure and composition of neutron stars, we definitely have a lot more insight in those exotic objects.

1.3.1 Nuclear equation of state

In order to understand the structure of neutron stars, a first step is to understand how to compute the pressure by using the density, temperature and composition of the neutron star (i.e., we need an equation of state).

Principle and degrees of freedom

A typical order of magnitude for the central density of baryons in a neutron star is $n_B \approx 0.3 - 0.7 \text{ fm}^{-3}$ (this corresponds to a rest mass density $\rho \approx 5 - 12 \times 10^{17} \text{ kg m}^{-3}$), which is above the nuclear saturation density $n_{sat} \approx 0.16 \text{ fm}^{-3}$, meaning that nuclei dissolve under these conditions and that neutron stars are mainly constituted of nuclear matter.

Regarding the temperature, after an initial cooling phase which can last several minutes an isolated neutron star has a temperature below $T = 1 \text{ MeV}$ (10^9 K).

In dense media it is instructive to compare the average interparticle spacing $n_B^{-1/3}$ to the de Broglie thermal wavelength λ_{th} in order to estimate the degeneracy of the gas and thus the need for a quantum description.

In the case of non relativistic nucleons the thermal de Broglie wavelength λ_{th} is given by :

$$\frac{1}{\lambda_{th}^3} = \frac{1}{h^3} (2\pi m T)^{3/2} = \left(\frac{T}{1 \text{ MeV}} \right)^{3/2} \times 2.4 \times 10^{-4} \text{ fm}^{-3} \quad (1.3)$$

¹in the context of neutron star, a universal relation is an observed relation that does not depend upon the used equation of state

and in the case of relativistic particles (such as electrons in a neutron star) it is given by :

$$\frac{1}{\lambda_{\text{th}}^3} = \frac{1}{(hc)^3} 8\pi T^3 = \left(\frac{T}{1 \text{ MeV}} \right)^3 \times 1.3 \times 10^{-8} \text{ fm}^{-3} \quad (1.4)$$

The average particle density inside a neutron star is several orders of magnitude above these density scales, therefore neutron stars are mainly constituted of degenerate matter and the pressure should not depend upon their temperature.

Now about the composition of neutron stars, we usually consider that they are constituted of cold catalyzed nuclear matter, which means that complete thermodynamical equilibrium is achieved in the $T = 0$ limit with respect to all interaction channels that do not include neutrinos.

The case of neutrino is different, they are not in thermodynamic equilibrium and leave the star after their creation because of their large mean free path. There is a state of dynamic equilibrium between two weak interaction processes : neutron decay and electron captures (1.5) :

$$\begin{cases} n \rightarrow p + e^- + \bar{\nu}_e & (\Gamma_{n \rightarrow p}) \\ p + e^- \rightarrow n + \nu_e & (\Gamma_{p \rightarrow n}) \end{cases} \quad (1.5)$$

These two processes should occur at an equal rate :

$$\Gamma_{n \rightarrow p} = \Gamma_{p \rightarrow n} \quad (1.6)$$

This situation is called β -equilibrium, and because of it there exists a relation between the baryon density n_B and the (charged) lepton density n_L .

To conclude, the equation of state of a neutron star only has one degree of freedom : the pressure is a function of the baryon density only $P(n_B)$: it is a *barotropic equation of state*.

Note that this hypothesis of cold catalyzed matter is not valid if the temperature is too high or if chemical equilibrium is not achieved (either because of weak processes out of β -equilibrium [46] or because there are ongoing nuclear processes in the crust [47]). This is the case for young neutron stars that did not have enough time to cool down and achieve equilibrium, or for accreting neutron stars that are very dynamic systems.

Difficulties and uncertainties

There are still a lot of uncertainties on the nuclear equation of state describing the matter at such high densities, for several reasons :

- the complex nature of the problem, involving many particles interacting via the strong interaction, makes all investigations *ab initio* extremely difficult
- the very high density of the medium makes the particles strongly correlated and complexifies a many-body modelisation
- the particle spectrum to consider is by itself subject to a lot of uncertainties, as an example the possibility of stable hyperons or even of a quark transition in the inner core is considered by several authors
- the strong asymmetry (neutron over proton ratio) encountered in neutron stars makes it difficult to obtain constraints from nuclear physics experiments

The review [48] covers the various methods to investigate the problem and the review [49] covers existing constraints for nuclear matter equations of state.

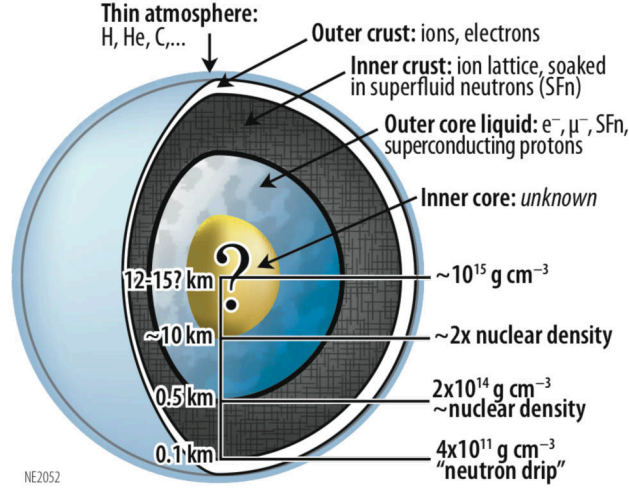


Figure 1.2: Schematic representation of neutron stars interior. This figure is extracted from the NICER mission overview [50].

Composition of neutron stars

The structure of neutron stars can be viewed schematically as follows :

1. the envelope is an extremely thin (less than about 100 m) layer consisting of the oceans and the atmosphere surrounding the neutron star
2. the outer crust is a relatively thin layer made of an ion lattice and electrons
3. beyond the neutron drip density² the inner crust is mainly constituted of an ion lattice in a neutron superfluid
4. beyond roughly nuclear density, the outer core is constituted of a neutron-proton fermi-liquid with few charged leptons
5. at extreme densities, the inner core is of uncertain composition

The figure 1.2 represents the range of densities and the composition of neutron star interiors.

The equations of state used in this work come from the CompOSE³ database [51], which aims to provide the most common equations of state in open access.

1.3.2 Masses and radii

By using the nuclear equation of state and what we know about general relativity, we can deduce information about the masses and radii.

The structure of a spherically symmetric neutron star of a given mass can be computed by using

²*i.e.* the density above which the nuclei emit neutrons, and therefore form a situation of equilibrium with a neutron gas

³compose.obspm.fr

the Tolman–Oppenheimer–Volkoff equations (1.7) and (1.8), see [9] and [8].

$$\frac{dm}{dr} = 4\pi r^2 \frac{\mathcal{E}}{c^2} \quad (1.7)$$

$$\frac{dP}{dr} = -(\mathcal{E} + P) \frac{Gm}{r^2 c^2} \left(1 + \frac{4\pi r^3 P}{mc^2}\right) \left(1 - \frac{2Gm}{rc^2}\right)^{-1} \quad (1.8)$$

where \mathcal{E} is the energy density in the star, P the pressure, r the radial coordinate and $m(r)$ a metric potential equivalent to the enclosed mass in the Newtonian limit. The boundary conditions are $m(r=0) = 0$ and $P(R) = 0$, where R is the radius of the star. The radius of the star is then related to its total baryon number N_B as

$$N_B = 4\pi \int_0^R n_B \left(1 - \frac{2Gm}{rc^2}\right)^{-1/2} r^2 dr \quad (1.9)$$

where n_B is the baryon density in the star. It is also common to define the baryonic mass M_B of the star as $M_B = m_N N_B$ where m_N is the mass of a nucleon. This baryonic-mass is different from the gravitational mass $M = m(R)$ of the star, the difference between the two is related to the gravitational binding energy ($\mathcal{B} = (M_B - M)c^2$) of the neutron star.

This procedure yields a relation between the mass of a neutron star and its radius, some of which are represented in the figure 1.3.

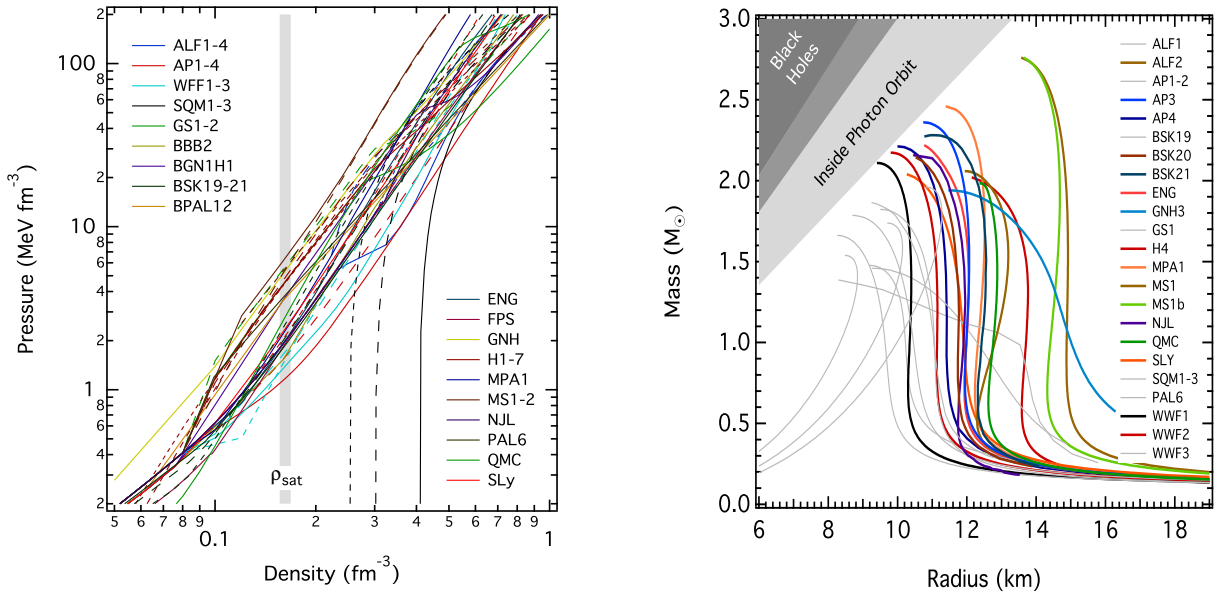


Figure 1.3: On the left panel the pressure-density relation is given for a large sample of equations of state calculated under different physical assumptions and using a range of computational approaches. On the right panel the corresponding mass-radius relations are represented. This figure is extracted from [24], to which the reader should refer for the description of the various equations of state.

Each mass-radius relation presents a maximum mass, above which the neutron star is unstable and collapses into a black hole. The distinction is generally made between *stiff equations of state*, which presents a high slope in the pressure-density relation associated to a high maximum mass and large radii, and the so-called *soft equations of state*, which present a less important slope associated to a lower maximum mass and smaller radii.

Because the scenario of neutron star formation involves the collapse of a massive star, there should also exist a lower boundary of the masses of neutron stars. In [52], the authors investigate

this issue and found a minimum mass of $1.17 M_{\odot}$, which is consistent with the lowest neutron star mass measured [31]. This scenario corresponds to the collapse of a low mass carbon-oxygen stellar core.

Chapter 2

Formation of neutron stars : the core-collapse mechanism

2.1 Core-collapse dynamics

Neutron stars are formed during the collapse of massive stars at the end of their life, which can trigger a cataclysmic explosion named *core-collapse supernova*.

This section summarizes what we understand about this mechanism, it is based on the reviews [1], [2] and [53], to which the reader can refer for more details.

2.1.1 Onset of the collapse and infall

A massive star at the end of its evolution has an iron core which is growing due to silicon burning. The collapse of the core starts when it reaches its *Chandrasekhar mass*, which is approximately $1.2 M_{\odot}$ (the exact value depends upon the electron density in the star), which correspond to the moment when the electron degeneracy pressure is no longer enough to counter the self-gravity of the core (see fig. 2.1, left pannel). When that happens, the core has a radius of about 1500 km.

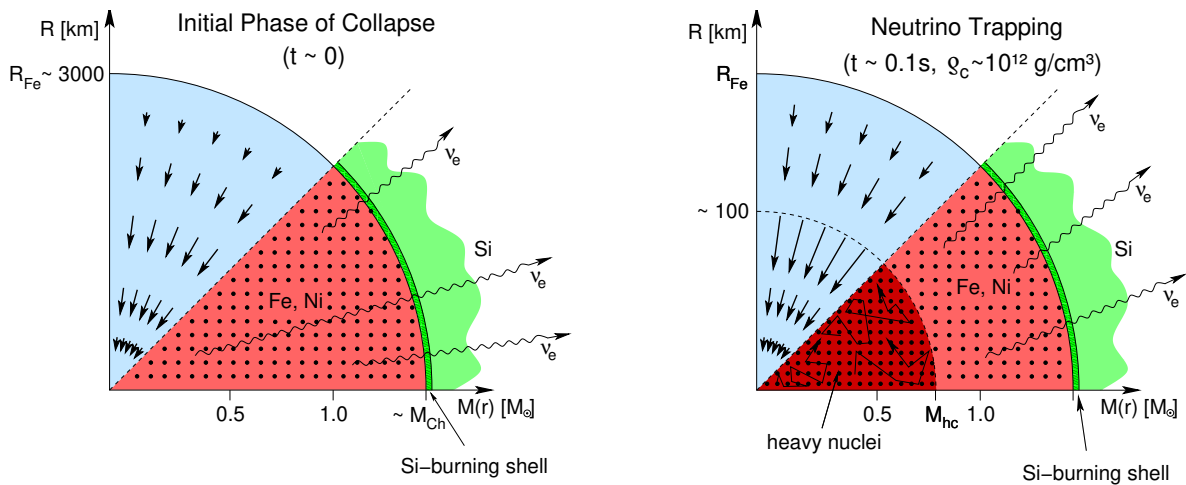


Figure 2.1: Schematic representation of the core-collapse mechanism (1st part). The upper slice of diagrams gives information about the dynamics and the lower slice gives information about matter composition and microphysical processes. M_{Ch} is the Chandrasekhar mass and M_{hc} is the mass of the internal core in homologous collapse. This figure is extracted from [1]

The inner core quickly undergoes a subsonic homologous collapse, while beyond the sonic point the outer core collapses more slowly (see fig. 2.1, right pannel).

During the collapse the neutronization of matter begins with electron capture processes on nuclei

$${}^A_ZX + e^- \rightarrow {}^A_{Z-1}X + \nu_e \quad (2.1)$$

This results in an increasing emission of electron neutrinos. As the density of electrons in the medium diminishes, the electron degeneracy pressure acting against the collapse diminishes as well, resulting in an acceleration of the process.

About 40% of the electrons of the iron-core are removed because of electron capture processes during the infall.

As the density increases the neutrino mean free path is getting lower and lower, such that when the density becomes high enough ($n_B \approx 10^{-3} \text{ fm}^{-3}$) neutrinos become trapped, stopping momentarily the neutronization.

The limit where neutrinos start to free-stream is called the *neutrinosphere*, by analogy to a stellar *photosphere* (more details on this notion are given in the section 2.2.4).

2.1.2 Bounce and shock propagation

When the central area reaches about half the nuclear saturation density $n_{\text{sat}} \approx 0.16 \text{ fm}^{-3}$, the nuclei dissolve into free nucleons and the nuclear interaction between them becomes strongly repulsive, giving rise to a nuclear pressure that stops the collapse and makes the core bounce. When that happens the inner core has a radius of about 10-20 km.

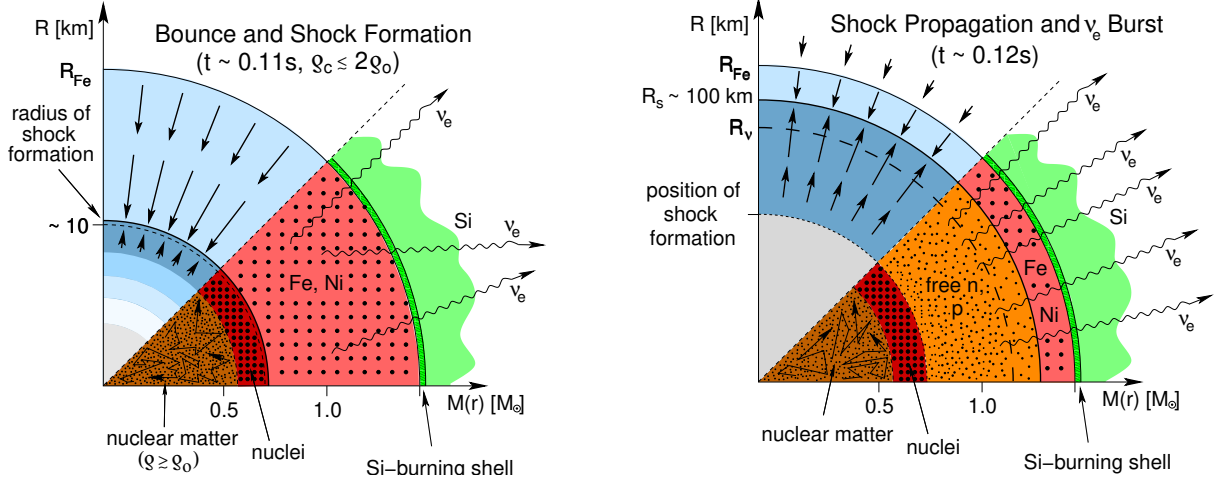


Figure 2.2: Schematic representation of the core-collapse mechanism (2nd part). $\rho_0 = m_N n_{\text{sat}}$ is the nuclear saturation density, R_s is the shock radius and R_ν is the neutrinosphere radius. This figure is extracted from [1]

It is commonly accepted that the collapse of an iron Chandrasekhar-mass core cannot lead directly to the formation of a black hole : the inner homologous collapsing core is never massive enough and therefore bounces back to the outer core [53]. The bounce of the core therefore seems to be an unavoidable step.

The bounce generates an hydrodynamic shock which propagates outwards (see fig. 2.2). But the shock quickly exhausts all its kinetic energy by heating the matter and dissolving nuclei in the still infalling material from the outer parts of the star, therefore it stops while still inside the iron core, at a radius of about 100-200 km.

When the shock reaches the *neutrinosphere* (located at a radius of about 60-80 km), the nuclei are photodissociated, accelerating the electron captures in this electron-rich area where neutrinos are not trapped. This triggers a sudden deleptonization burst in the electron neutrino emission.

2.1.3 Delayed neutrino heating and final explosion

The shock then stalls while accretion of infalling matter continues. The supernova explosion can be triggered by the *delayed neutrino heating mechanism* : the newly formed central object (which is called a *Proto Neutron Star*, or PNS) emits all flavors of neutrinos, which deposit energy behind the shock, in the *gain layer* (see fig. 2.3). This can revive the shock and trigger the explosion.

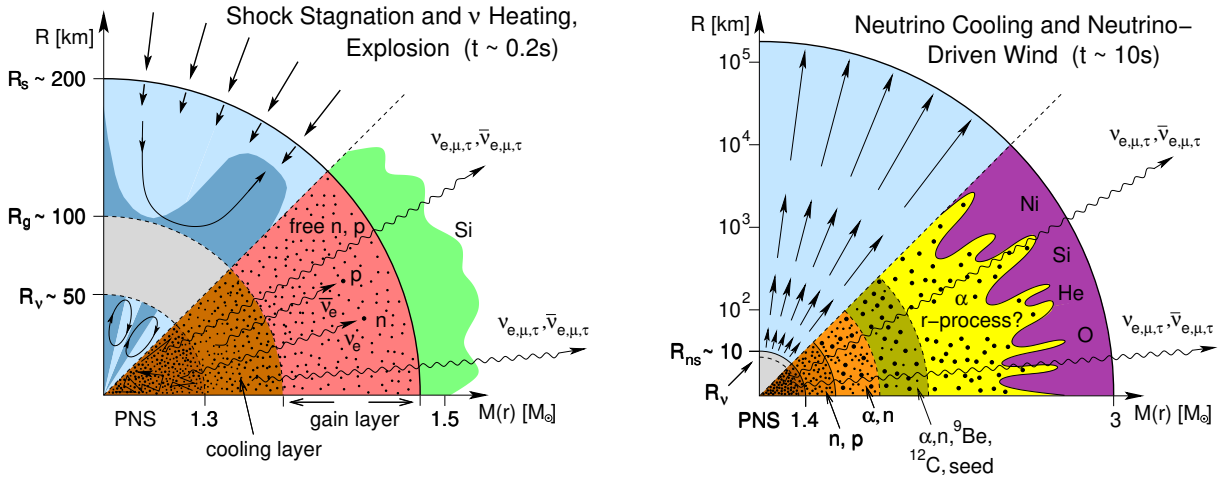


Figure 2.3: Schematic representation of the core-collapse mechanism (3rd part). R_s is the shock radius, R_g is the limit between the gain and cooling layers and R_v is the neutrinosphere radius. This figure is extracted from [1]

When the shock is stalling, the structure of the core is as showed in fig. 2.3 : the inner part constitutes the proto-neutron star, and is surrounded by a cooling layer and a gain layer before the position of the shock.

Inside the proto-neutron star, neutrinos are trapped because of the high densities and temperatures (see sec 2.2), and therefore the proto-neutron star slowly cools down over diffusion timescales, that are long compared with the short timescales involved in the core-collapse mechanism.

Just outside the proto-neutron star, where the mean free path of neutrinos becomes high enough to allow them to escape (i.e. outside the *neutrinosphere*), is the so called *cooling layer*. This cooling is dominated by e^\pm captures on nucleons. The cooling rate by emission of neutrinos q_ν^- scales as $q_\nu^- \propto T^6$ (see e.g. [2]).

The outgoing neutrino flux from the core is also partially absorbed by the surrounding layers and contributes to a neutrino heating rate which scales as $q_\nu^+ \propto L_\nu \langle \epsilon_\nu^2 \rangle / r^2$. L_ν is the neutrino luminosity, $\langle \epsilon_\nu^2 \rangle$ the average squared neutrino energy and r the radial coordinate. There is a radius in the core where $q_\nu^- = q_\nu^+$, which is called the *gain radius*. Between this radius and the shock the net neutrino heating rate is positive, hence the name *gain layer*.

But the delayed neutrino heating mechanism is not sufficient in itself to trigger the explosion : the most detailed simulations in spherical symmetry concluded that 1D models cannot explode

and that asymmetries are playing a crucial role (see e.g. [54]). Convection effects are a key ingredient, and the standing accretion shock instability (SASI) does also play a crucial role by allowing more matter to be heated (see e.g. [55]). Today many 3D simulations are able to trigger an explosion via the delayed neutrino heating mechanism, see e.g. [56], [57], [58], [59], [60], [61] and [62].

During this phase the collapse of the central object into a black hole can occur, either because too much matter has been accreted through the shock before its revival or because the neutrino delayed mechanism failed to revive the shock. This is the *fallback* mechanism (see e.g. [63]).

2.1.4 Neutrino driven wind and nucleosynthesis

After a successful explosion, the neutrinos emitted by the proto-neutron star core continue to deposit some energy in the outer layers of the PNS, where the matter presents steep gradients of temperature and densities. This results in a fraction of the matter being blown off outside the star in a *neutrino driven wind*. The presentation of this phenomena is based on the review [64].

The wind can last from one second up to several tens of seconds after the explosion. This is an important feature of core-collapse supernova as nucleosynthesis can occur in the wind. Indeed when the entropy becomes low enough to avoid photodissociation, seed nuclei start to form. Then various nucleosynthesis processes can occur depending on the neutron-to-seed ratio.

If the medium is extremely neutron rich, the fast neutron capture process (or r-process) can occur. This process consists of fast enough neutron capture to avoid β -decay up to the neutron dripline.

However most recent supernova simulations are in favor of a proton-rich neutrino driven wind, therefore the most probable processes occurring in the wind are the weak r-process and the νp -process. The νp -process consists in rapid proton captures followed by (n, p) reactions (the capture of a neutron followed by the emission of a proton) which stabilise the nuclei [65]. The supply of neutrons needed for the (n, p) processes is provided via inverse β -decay because of the abundance of antineutrinos $\bar{\nu}_e$ in the medium.

Since supernova simulations with full hydrodynamics and neutrino treatments are computationally expensive, the neutrino driven wind is usually studied by using the approximation of a spherically symmetric steady state outflow. The corresponding equations are

$$\dot{M} = 4\pi r^2 \rho u \quad (2.2)$$

$$\rho u \frac{du}{dr} = -\frac{dP}{dr} - \frac{GM\rho}{r^2} \quad (2.3)$$

$$\dot{q} = u \left(\frac{d\mathcal{E}}{dr} + P \frac{d(1/\rho)}{dr} \right) \quad (2.4)$$

where u is the velocity of the wind, ρ its density, \mathcal{E} its energy density and P its pressure.

The parameters \dot{M} and \dot{q} represent respectively the mass outflow and the neutrino heating rate.

Within this framework, the electron fraction in the wind can be estimated by using the hypothesis of a weak equilibrium $dY_e/dt = 0$. In [66] the authors obtain the following formula :

$$Y_e^{\text{NDW}} = \left[1 + \frac{L_{\bar{\nu}_e}(\epsilon_{\bar{\nu}_e} - 2\Delta + 1.2\Delta^2/\epsilon_{\bar{\nu}_e})}{L_{\nu_e}(\epsilon_{\nu_e} + 2\Delta + 1.2\Delta^2/\epsilon_{\nu_e})} \right]^{-1} \quad (2.5)$$

where L_{ν_e} and $L_{\bar{\nu}_e}$ are the electron neutrino and antineutrino luminosities, $\Delta = m_n c^2 - m_p c^2 = 1.293 \text{ MeV}$ is the neutron-proton mass difference, and ϵ_ν is defined as $\epsilon_\nu = \langle \varepsilon^2 \rangle / \langle \varepsilon \rangle$ where ε is the energy of the neutrino ν .

The above formula is obtained by considering only the processes $n + \nu_e \rightleftharpoons p + e^-$ and $p + \bar{\nu}_e \rightleftharpoons n + e^+$. The rates are computed in the elastic approximation (see sec. 5.1.1 and 10.1.1), by neglecting the mass of the electron m_e and the Pauli blocking effect of leptons on the final state.

The luminosities and mean energies as a function of time come from core-collapse or proto-neutron star simulations, and are taken as input parameters of wind simulations, which makes the electron fraction evolution predetermined in such models.

Note that the formula (2.5) is obtained by considering that the neutrino driven wind is composed of free neutrons and protons only. By doing so we neglect the so-called *alpha effect*, which result from the formation of alpha particles and can introduce significant changes in the electron fraction [67]. Indeed the charged currents reaction rates on alpha particles is usually negligible in these conditions, therefore the alpha effect will tend to bring the electron fraction in the neutrino driven wind closer to $Y_e = 0.5$ by allowing neutrino capture processes only on the most abundant nucleon [68].

2.2 Trapping of neutrinos in dense matter

At very high densities and temperatures the matter becomes opaque to neutrinos. It is important to understand this process as well as the relevant densities and temperatures to get some insight in the core-collapse mechanism.

2.2.1 The weak interaction

Neutrinos interact only via the weak interaction. This section provides a brief overview of the standard model of weak interactions.

These interactions can be classified in two types, depending upon the force mediating boson involved :

- in *charged current interactions*, the mediating boson is W^\pm . This interaction systematically couples neutrinos ν_l to their corresponding charged lepton l^- , whereas neutrons n are coupled to protons p . We say that they form weak doublets : (ν_l, l^-) , (p, n) . The β -decay of nuclei is an example of such interaction
- in *neutral current interactions*, the mediating boson is Z^0 . The processes are similar to electromagnetism, but occur with extremely short range because of the high mass of the Z boson

It should be stressed however that some processes occur via both charged and neutral currents (as the example of neutrino-electron scattering).

2.2.2 Relevant processes

With electron captures on nuclei (see eq. (2.1)), the charged current interactions with the nucleons are among the most important weak processes occurring during core-collapse supernova, as they are changing the lepton composition of the medium :

$$p + e^- \rightleftharpoons n + \nu_e \quad (2.6)$$

$$p \rightleftharpoons n + e^+ + \nu_e \quad (2.7)$$

$$n + e^+ \rightleftharpoons p + \bar{\nu}_e \quad (2.8)$$

$$n \rightleftharpoons p + e^- + \bar{\nu}_e \quad (2.9)$$

It should be pointed out that if proton decay (2.7) is a forbidden process in vacuum, there exists some thermodynamic conditions in dense matter that would allow this process to happen.

Neutrinos can also scatter off nucleons and nuclei via flavor independent neutral current interactions :

$$\nu + N \rightleftharpoons \nu + N \quad (2.10)$$

$${}^A_Z\text{X} + \nu \rightleftharpoons {}^A_Z\text{X} + \nu \quad (2.11)$$

and can scatter off electrons and positrons via both charged and neutral currents :

$$\nu + e^\pm \rightleftharpoons \nu + e^\pm \quad (2.12)$$

These scattering processes play a role in neutrino trapping and spectrum equilibration (see e.g. [69] and the section 2.2.5 of this thesis).

Finally, neutrino-antineutrino pairs can be created by various processes because of thermal excitations, contributing to the cooling of the medium.

The predominant one is nucleon-nucleon bremsstrahlung occuring via the neutral current (see e.g. [70]) :

$$N + N \rightleftharpoons N + N + \nu + \bar{\nu} \quad (2.13)$$

And we also have electroweak processes from electrons and photons (see e.g. [71]) :

$$e^- + e^+ \rightleftharpoons \nu + \bar{\nu} \quad (2.14)$$

$$\tilde{\gamma} \rightleftharpoons \nu + \bar{\nu} \quad (2.15)$$

$$\gamma + e^\pm \rightleftharpoons e^\pm + \nu + \bar{\nu} \quad (2.16)$$

the above processes are called respectively the *pair*, *plasma* and *photo* processes. $\tilde{\gamma}$ represent a plasma excitation of the medium.

2.2.3 Cross-sections : some orders of magnitude

The relevant energy scale of the weak interaction is given by the Fermi coupling constant¹

$$\frac{G_F}{\hbar c} = \frac{\sqrt{2}}{8} \frac{g^2}{m_W^2 c^4} = (1.166\,378\,7 \pm 0.000\,000\,6) \times 10^{-5} \text{ GeV}^{-2} \quad (2.17)$$

where g is the coupling constant of the weak interaction and m_W the mass of the W boson.

The associated cross-section for the interaction of neutrinos with fixed targets (such as nucleons) is given by

$$\sigma_0 = \frac{G_F^2}{\pi} \varepsilon_\nu^2 \approx 1.6 \times 10^{-16} \left(\frac{\varepsilon_\nu}{10 \text{ MeV}} \right)^2 \text{ fm}^2 \quad (2.18)$$

with ε_ν the energy of the neutrino. In areas where nucleons are non-degenerate this formula gives a good estimation of the actual cross-section, indeed the thermal velocities of nucleons are negligible compared with the speed of neutrinos (*i.e.* the speed of light c), and they can be considered as fixed.

¹the value is taken from the CODATA 2018 recommended values

The cross-sections of the two charged current processes $\nu_e + n \rightleftharpoons p + e^-$ and $\bar{\nu}_e + p \rightleftharpoons n + e^+$ can be roughly estimated at first order within the elastic approximation² and by considering non degenerate nucleons by (see e.g. [72])

$$\sigma_{cc} = \sigma_0(1 + 3g_A^2) \approx 5.8 \sigma_0 \quad (2.19)$$

where $g_A = 1.2695$ is the nucleon coupling factor to weak axial currents.

Regarding the neutral current interactions $\nu + n \rightleftharpoons \nu + n$ and $\nu + p \rightleftharpoons \nu + p$, similar expressions can be obtained for both cross-sections by using the same approximations :

$$\sigma_{\nu n} = \frac{\sigma_0}{6} (1 + 5g_A^2) \approx 1.5 \sigma_0 \quad (2.20)$$

$$\sigma_{\nu p} = \frac{\sigma_0}{6} ((1 - 4 \sin^2 \theta_W)^2 + 5g_A^2) \approx 1.3 \sigma_0 \quad (2.21)$$

where $\sin^2 \theta_W = 0.22290$ is the sine of Weinberg's weak mixing angle.

The coupling to charged currents is stronger than the coupling to neutral currents. This is important because the various neutrino flavors have different sensitivities to the weak currents

- the neutral current couples to all neutrino flavors identically
- the charged current couples a neutrino to its corresponding charged lepton, therefore the charged current cross sections depend on the abundance and the flavor of charged leptons in the medium

As the mass of the muon is $m_\mu = 105.65 \text{ MeV c}^{-2}$, muons (and the even heavier τ lepton) are far less abundant than electrons, which makes electron neutrinos and antineutrinos much more sensitive to charged currents.

But it should be stressed that despite the fact that muons have a low abundance and have little influence on the neutrino interactions, their presence in the medium has a significant softening effect on the equation of state that can lead to important differences in the dynamics of the collapse, as pointed out in [73].

2.2.4 Mean free path and neutrinospheres

The opacity or inverse mean free path of neutrinos $\kappa = \frac{1}{\lambda}$ can be estimated by considering only the processes on free nucleons, we obtain

$$\kappa_{\nu_e} = n_n(\sigma_{cc} + \sigma_{\nu n}) + n_p\sigma_{\nu p} \quad (2.22)$$

$$\kappa_{\bar{\nu}_e} = n_p(\sigma_{cc} + \sigma_{\nu p}) + n_n\sigma_{\nu n} \quad (2.23)$$

$$\kappa_{\nu_x} = n_p\sigma_{\nu p} + n_n\sigma_{\nu n} \quad (2.24)$$

where n_n is the density of neutrons, n_p the density of protons and $\nu_x \in \{\nu_\mu, \bar{\nu}_\mu, \nu_\tau, \bar{\nu}_\tau\}$.

Because the matter in the falling core and the nascent neutron star is more and more neutron rich, we have the following ordering : $\kappa_{\nu_x} < \kappa_{\bar{\nu}_e} < \kappa_{\nu_e}$, which means that electron neutrinos ν_e are more easily trapped than electron antineutrinos $\bar{\nu}_e$, which are themselves easier to trap than heavy flavor neutrinos $\nu_\mu, \bar{\nu}_\mu, \nu_\tau$ and $\bar{\nu}_\tau$.

²i.e. considering that there is no momentum transfer to the nucleon

We can estimate the baryon density n_B needed to trap neutrinos :

$$\lambda = \frac{1}{\sigma_0 n_B} = 10 \left(\frac{n_B}{6 \times 10^{-4} \text{ fm}^{-3}} \right)^{-1} \text{ km} \quad (2.25)$$

for a baryon density $n_B = 6 \times 10^{-4} \text{ fm}^{-3}$, the mean free path starts to be comparable to the size of the neutron star, and will only decrease at higher densities.

A useful notion to understand neutrino trapping is the *neutrinosphere*, defined as the sphere inside which neutrino are trapped, and are free-streaming outside. It is named by analogy to a stellar *photosphere*. Usually the neutrinosphere radius R_ν is defined as

$$\int_{R_\nu}^{+\infty} \kappa_\nu dr = \frac{2}{3} \quad (2.26)$$

where r is the radial coordinate.

The radius of the various neutrinospheres obeys the same ordering : $R_{\nu_x} < R_{\bar{\nu}_e} < R_{\nu_e}$.

In reality there is a more or less thick layer in which the medium is semi-transparent to neutrinos, and the neutrinosphere is more a theoretical tool used to obtain some insight and explain the trapping mechanism.

It should be stressed that as the cross-section σ_0 depends on the energy of the neutrino (c.f. eq. (2.18)), this definition of neutrinosphere depends on the neutrino energy ϵ_ν . And in order to make sense the integral (2.26) has to be computed with the redshifted energy along a ray.

When "the" neutrinosphere of neutrinos is mentioned, it usually refers to the neutrinosphere radius $\langle R_\nu \rangle_3$ computed with the averaged opacities $\langle \kappa_\nu \rangle_3$:

$$\langle \kappa_\nu \rangle_3 = \left(\int \kappa_\nu(\epsilon) f_\nu^{(eq)}(\epsilon) \epsilon^3 d\epsilon \right) / \left(\int f_\nu^{(eq)}(\epsilon) \epsilon^3 d\epsilon \right) \quad (2.27)$$

where $f_\nu^{(eq)}$ is the equilibrium neutrino distribution function, defined as in eq. (4.31).

The *gray* neutrinosphere is then defined as

$$\int_{\langle R_\nu \rangle_3}^{+\infty} \langle \kappa_\nu \rangle_3 dr = \frac{2}{3} \quad (2.28)$$

It represents the sphere of emission that could be used in Stefan-Boltzmann formula to estimate the total energy flux of neutrinos emitted by the star.

2.2.5 Chemical equilibrium and thermalization

When neutrinos are trapped in the matter, they will progress toward chemical equilibrium and thermalize with the medium.

Since neutrinos stay in the medium, inverse processes corresponding to the absorption of neutrinos can occur :

$(p + e^- \rightleftharpoons n + \nu_e)$, and the particles fractions will evolve such that the rate of the forward process becomes equal to the rate of the backward process. The timescale needed to reach this equilibrium depends on the rate at which occur the process.

It should be stressed that inverse processes involving neutrinos are also relevant outside the neutrinosphere, because of the outgoing neutrino flux interacting with the medium. But in this case these interactions do not lead to thermal and chemical equilibration.

When chemical equilibrium occurs, we have the following equalities between equilibrium chemical potentials :

$$\mu_{\nu_e} = \mu_p + \mu_e - \mu_n \quad (2.29)$$

$$\mu_{\nu_x} = 0 \quad (2.30)$$

where μ_{ν_e} , μ_{ν_x} , μ_p , μ_e and μ_n are respectively the chemical potentials of electron neutrinos, heavy neutrinos, protons, electrons and neutrons. The chemical potential of antineutrinos is simply given by $\mu_{\bar{\nu}} = -\mu_{\nu}$.

This state of neutrinos in chemical equilibrium is referred to as *β -equilibrium*, as the neutron and proton number do not evolve anymore. But the situation is different from the case of the *β -equilibrium* occurring in cold neutron stars (see the section 1.3.1 of this thesis), indeed here we have a full chemical equilibrium with neutrinos participating in backward reactions. In the cold case this was not the case, as the neutrinos leave the star without further interactions with the medium.

In addition to the chemical equilibrium, neutrinos will also achieve thermal equilibrium thanks to processes allowing a redistribution of energy. When thermal equilibrium occurs, the neutrino distribution functions are given by Fermi-Dirac distributions.

For electron neutrinos ν_e and electrons anti-neutrinos $\bar{\nu}_e$, the most important processes for spectrum equilibration are the charged current processes on nucleons (2.6), (2.7), (2.8) and (2.9). Those processes are far more efficient for spectrum equilibration than scattering processes and the neutrinos ν_e and $\bar{\nu}_e$ quickly reach thermal equilibration when they are trapped.

For heavy flavor neutrinos ν_μ , $\bar{\nu}_\mu$, ν_τ and $\bar{\nu}_\tau$, the situation is different. Only inelastic scattering processes (2.10) and (2.12) can redistribute the energy with enough efficiency to achieve thermal equilibrium.

Supernova theoreticians worked for a long time with the idea that scattering off nucleons (2.10) is done coherently because of the high mass of nucleons (see e.g. [74]), meaning that only the scattering off charged leptons (2.12) contributes to spectrum equilibration. But more recent works showed that at high densities and temperatures nucleons have thermal velocities, such that the process (2.10) becomes highly inelastic (see e.g. [69]). It can even be more important than scattering off charged leptons for the spectrum equilibration in the denser areas of the star.

A consequence of these complicated equilibration mechanisms is that neutrinos can decouple thermally from the matter before being able to escape. Some authors such as [69], [70] and [75] introduce the notion of *energysphere*, which delimits the zone of space where neutrinos are in thermal equilibrium with the matter. It has usually a smaller radius than the *neutrinosphere*, which delimits the zone where neutrinos are trapped. This is especially the case for heavy flavor neutrinos, because their thermal equilibration relies on less efficient processes.

Chapter 3

Thermal evolution of proto-neutron stars

3.1 The proto-neutron star (PNS)

The newly formed compact object constituted by the bounced core and the shocked matter is called a *Proto Neutron Star* (PNS). This object will accrete matter through the shock and cool down to become either a neutron star or a black hole.

3.1.1 Initial structure of the PNS

Schematically the newly formed proto neutron star is constituted of two very different layers :

- a core constituted by the matter that has undergone the homologous collapse and the bounce, which has relatively low entropy per baryon and high electron fraction
- a mantle constituted by the matter crossed by the shock, which has a high entropy per baryon and low electron fraction

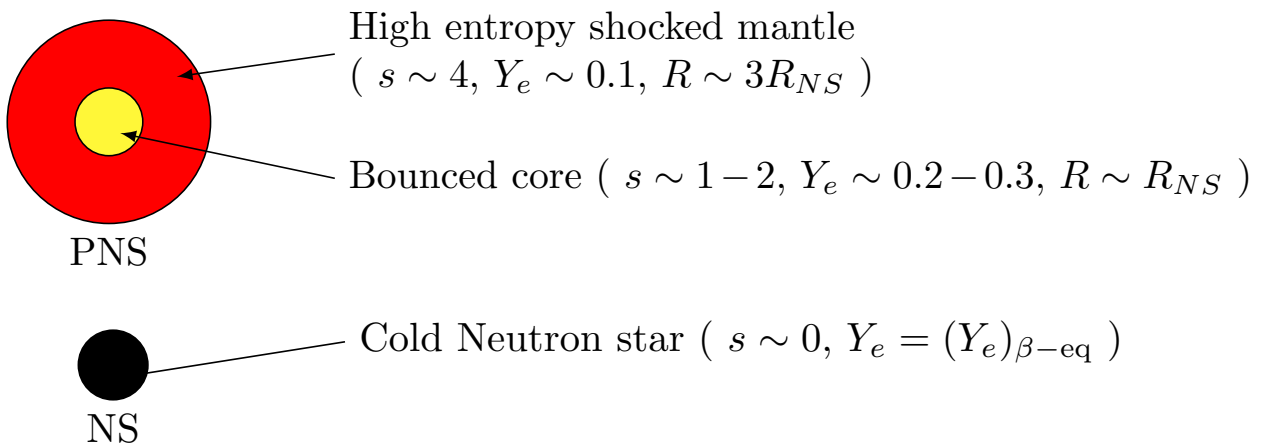


Figure 3.1: Schematic representation of a proto neutron star structure (PNS), compared with the corresponding cold catalysed neutron star (NS). R is the radius of the PNS, s is the entropy per baryon and Y_e is the electron fraction (net number of electrons per baryons $Y_e = (n_{e^-} - n_{e^+})/n_B$)

The core radius is approximately the same as the corresponding cold neutron star, such that the cooling of the PNS mainly corresponds to the contraction of the hot mantle onto the core. The figure 3.1 shows a sketch of the PNS structure.

An example of profiles for the PNS structure at about 500 ms after bounce are given by the figure 3.2.

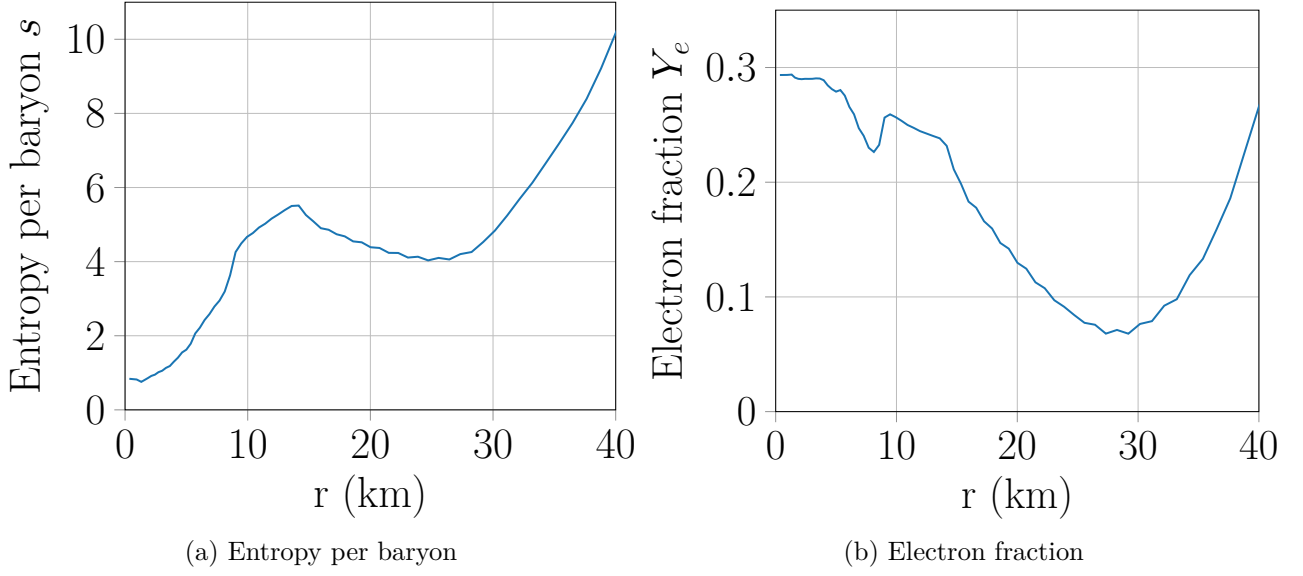


Figure 3.2: Typical structure of a proto neutron star. The panel (a) represents the radial profile of entropy per baryon and the panel (b) represents the radial profile of electron fraction. Those profiles have been produced with the `CoCoNuT` code, with the same setup as used in the chapter 10 of this thesis, with elastic charged current reaction rates

The size of the core depends on the mass of the inner homologous core, its limit corresponds to the radius of the shock formation. The size of the mantle depends on the distance travelled by the shock before it exhausts its kinetic energy.

This distance is a function of the inner core mass, because the kinetic energy of the shock comes from the binding energy of the nascent proto-neutron star [76], thus one can expect that the relative size of these two layers will remain approximately the same between various situations. This argument seems to hold in multi-dimensional simulations : as shown in the figure 3.3 from the work of [5], where the various models present few differences in the electron fraction and entropy profiles.

But multi-dimensional simulations are qualitatively different and the profiles present isentropic regions where convective effects have been highly efficient (such as in the mantle of the PNS), see *e.g.* [5].

3.1.2 PNS cooling

The proto-neutron star continues to cool down and deleptonizes by emission of neutrinos after the departure of the shock. At this moment it has an average temperature of about 20 – 40 MeV. During this process its temperature diminishes until reaching a few MeV to finally reach neutrino transparency, after which it will cool much more slowly. The reader can refer to [3] or [77] for more details on the various thermal evolution stages of neutron stars.

A first phase corresponds to a quasi-thermal emission of neutrinos (or *shallow decay phase*) during which the average mean free path of neutrinos is smaller than the PNS radius. Neutrinos are trapped and thermalized with the dense matter. During this phase, the mantle heat diffuses in the core such that the maximum of temperature is progressively displaced towards the center of the star, and after several seconds the maximum of temperature is located in the center. This process has been referred to as *Joule heating* in previous works. More details about this phase

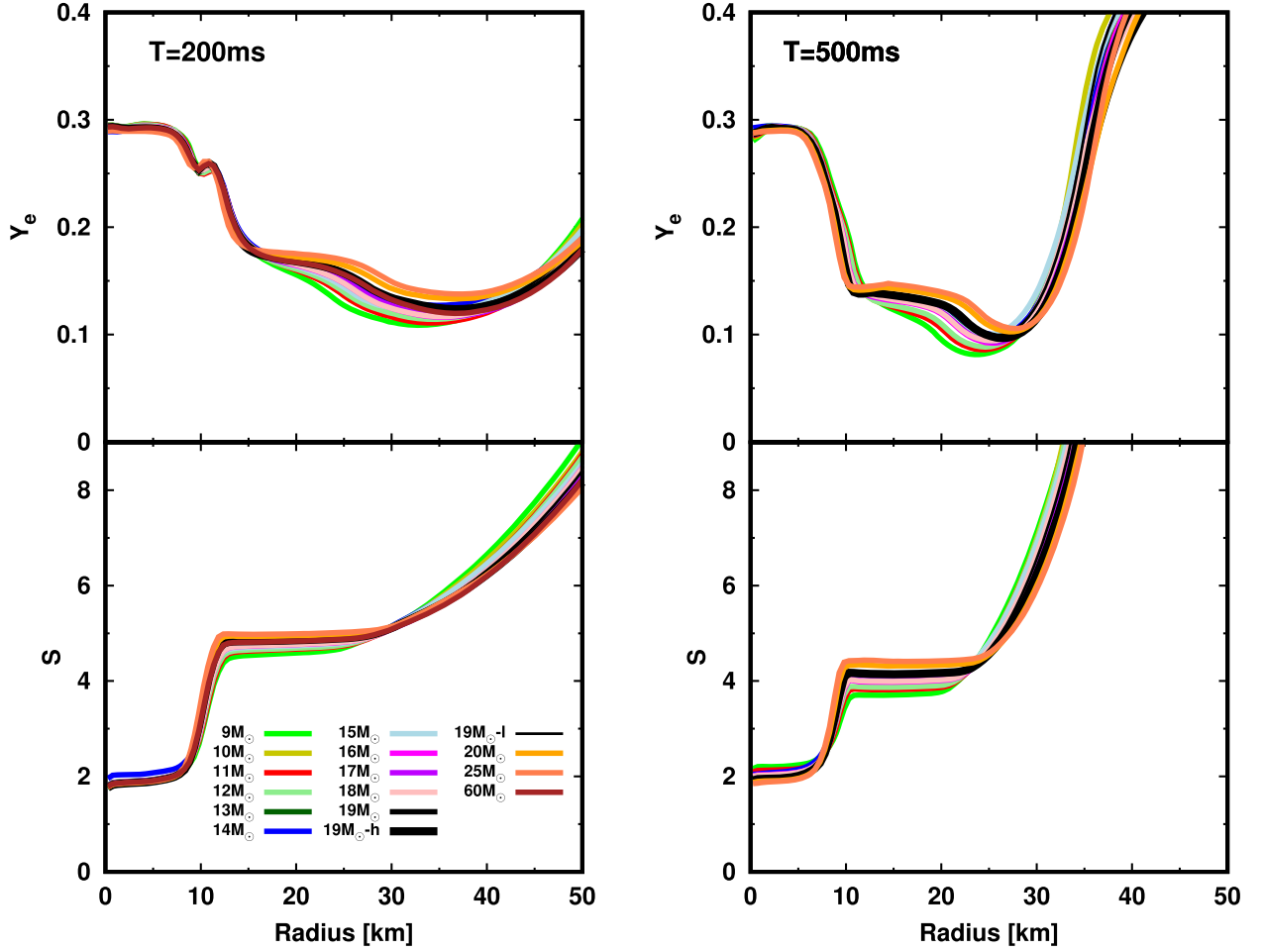


Figure 3.3: Radial profiles of angle-averaged electron fraction Y_e on top and entropy per baryon s on bottom panels at 200 (left panels) and 500 ms (right panels) after bounce, respectively, for various progenitor models. This figure is extracted from [5], and comes from 3D CCSN simulations.

are given in section 6.2.2.

The mean free path of neutrinos in dense and hot matter has an extreme dependency on the temperature of the medium (because of Pauli blocking effects in degenerate baryon matter), such that when the temperature is about a few MeV neutrinos decouple from the PNS matter and the emission becomes non-thermal. This first phase lasts several about tens of seconds [3].

After the onset of neutrino-transparency, a second and poorly understood phase is given by the crust crystallisation. Finally, after the formation of the crust, the cooling of the neutron star continues to be dominated by neutrino emission for millions of years. Photon emission only becomes relevant once the star is cold enough and has a temperature of about 10 keV (see e.g. [77]).

3.1.3 Equation of state of a PNS

Contrary to the cold neutron star case (see sec. 1.3.1), in a proto-neutron star thermal effects are not negligible and the matter is not necessarily β -equilibrated. As a consequence the equation of state has two additional degrees of freedom : the temperature T and the electron fraction Y_e . It also depends on the neutrino pressure and energy density in the trapped region.

If electrons alone have a marginal influence on the nuclear matter because their contribution to

the pressure is negligible compared with the contribution of the nuclear forces, they do have an indirect influence by setting the neutron-to-proton ratio required for local charge neutrality, as we have (for the case of a nucleon-only equation of state) $n_p = n_e$ thus $n_p/n_B = Y_p = Y_e$.

If we define the isospin asymmetry $\delta = 1 - 2n_p/n_B$, the energy per nucleon is given at second order by

$$E(n_B, T, \delta) = E_0(n_B, T) + E_{\text{sym}}(n_B, T) \delta^2 + \dots \quad (3.1)$$

where $E_{\text{sym}} \geq 0$ is the symmetry energy. Its contribution vanishes when neutron and proton densities are equal (this situation is called *symmetric nuclear matter*).

Therefore the energy per nucleon and the pressure are higher in asymmetric matter than in symmetric matter and we usually have $\left(\frac{\partial P}{\partial Y_e}\right)_{n_B, T} \leq 0$ in nuclear matter.

Equations of state with temperature and electron fraction dependence are also available on the **CompOSE** database [51], under the name *general purpose equations of state*.

3.1.4 Convection in proto-neutron stars

The shocked mantle of proto-neutron stars is known to be highly unstable to convection (see e.g. [78], [79] and [80]), and the associated convective engine can speed up the cooling and the deleptonization processes.

The instability of a stratification to convective motion appears if after an upward vertical adiabatic motion a fluid element is lighter than its surrounding, in which case it will not fall back to its original position. In a star the instability to convection is given by the Ledoux criterion (a demonstration of this formula is given in the chapter 8 of this thesis) :

$$C_L(r) = \frac{1}{\gamma} \frac{\partial \ln P}{\partial r} - \frac{\partial \ln \rho}{\partial r} \leq 0 \quad (3.2)$$

where ρ is the density in the star, P the pressure, $\gamma = (\partial \ln P / \partial \ln \rho)_s$ is the adiabatic index and r is the radial coordinate. Convection will occur in regions where $C_L(r) \leq 0$. Typically a strong negative temperature gradient (such as the one caused by the passing of the shock) can give rise to convection.

In the case of proto-neutron stars we can express this criterion in terms of more intuitive thermodynamic parameters :

$$C_L(r) = \frac{1}{\Gamma_{n_B}} \left(\Gamma_s \frac{\partial \ln s}{\partial r} + \Gamma_{Y_e} \frac{\partial \ln Y_e}{\partial r} \right) \leq 0 \quad (3.3)$$

where $\Gamma_{n_B} = \left(\frac{\partial \ln P}{\partial \ln n_B} \right)_{s, Y_e}$, $\Gamma_s = \left(\frac{\partial \ln P}{\partial \ln s} \right)_{n_B, Y_e}$, $\Gamma_{Y_e} = \left(\frac{\partial \ln P}{\partial \ln Y_e} \right)_{n_B, s}$. This criterion is identical to the one used in [81].

The convective motion starts in the mantle because of its strong negative entropy gradient, but progressively generalizes itself to the entire PNS as the heat from the mantle diffuses inside the core.

More recently, systematic studies of proto-neutron star convection with 3D simulations have been made possible [5]. They show in particular that the presence of convection in proto-neutron stars is a common feature present in all models which has a huge impact on the PNS neutrino emission :

- the deleptonization and the cooling are faster because the convective motions are carrying electrons and heat from the inside to the outer boundary of the convective zone, which enhance all neutrino luminosities during the early post-bounce phase
- later, when the convection stops, a sharp drop of the neutrinos luminosities is observed, which makes the luminosities going below the detectable threshold at a much earlier time [81]

3.1.5 Emission of gravitational waves

As core-collapse supernova are highly energetic events involving the formation of a compact object and some asymmetries, we expect them to emit gravitational waves.

The gravitational waveform emitted during the core-collapse mechanism is composed of a peak associated to the core-bounce, and a more complicated signal emitted by the post-bounce evolution of the nascent proto-neutron star.

The bounce signal is mostly sensitive to the rotational properties of the infalling core and is largely independent of the equation of state that is used [82].

The post-bounce signal is much more difficult to study as several mechanisms are at play. Torres-Forné *et al.* studies the asteroseismology of the proto-neutron star and proposed a systematic method to classify the oscillations modes [83]. They make the distinction between :

- *g*-modes (for *gravity modes*), which can appear only in region where the buoyancy is a restoring force, which corresponds to Ledoux stable regions $C_L \geq 0$ (defined by eq. 3.2)
- *p*-modes (for *pressure modes*), which use the pressure as a restoring force (i.e. they are supported by sound waves)
- hybrid modes, a combination of the previous two
- discontinuity modes, resulting from the density jump occuring with some equations of state presenting a phase transition

Most of the groups which possess a 3D core-collapse simulation code have studied the emission of gravitational waves (see e.g. [84], [85], [86], [87] and [88]). We can retain from these works that there are three main mechanisms of gravitational wave emission during the core-collapse event :

- the SASI instability gives rise to significant movements of the shock and can generate *p*-mode oscillations, which can emit gravitational waves. The convection in the gain layer also contributes to this emission
- the convection inside the proto-neutron star may also generate a considerable amount of *p*-mode oscillations, which can also generate GWs
- the outer layers of the proto-neutron are subject to gravity waves (*g*-mode oscillations), excited either from below because of the proto-neutron star convection or from above because of the infalling matter, this results in an emission of gravitational waves

The situation is represented schematically on the figure 3.4.

It is yet unclear what the dominant mechanism of gravitational wave emission in a core-collapse supernova is, the various simulation groups arrive to different conclusions about what the dominant mode of emission and the exact waveform (see e.g. [88]) is. But as this field of study is very new there is a lot of room for improvements in the predictions.

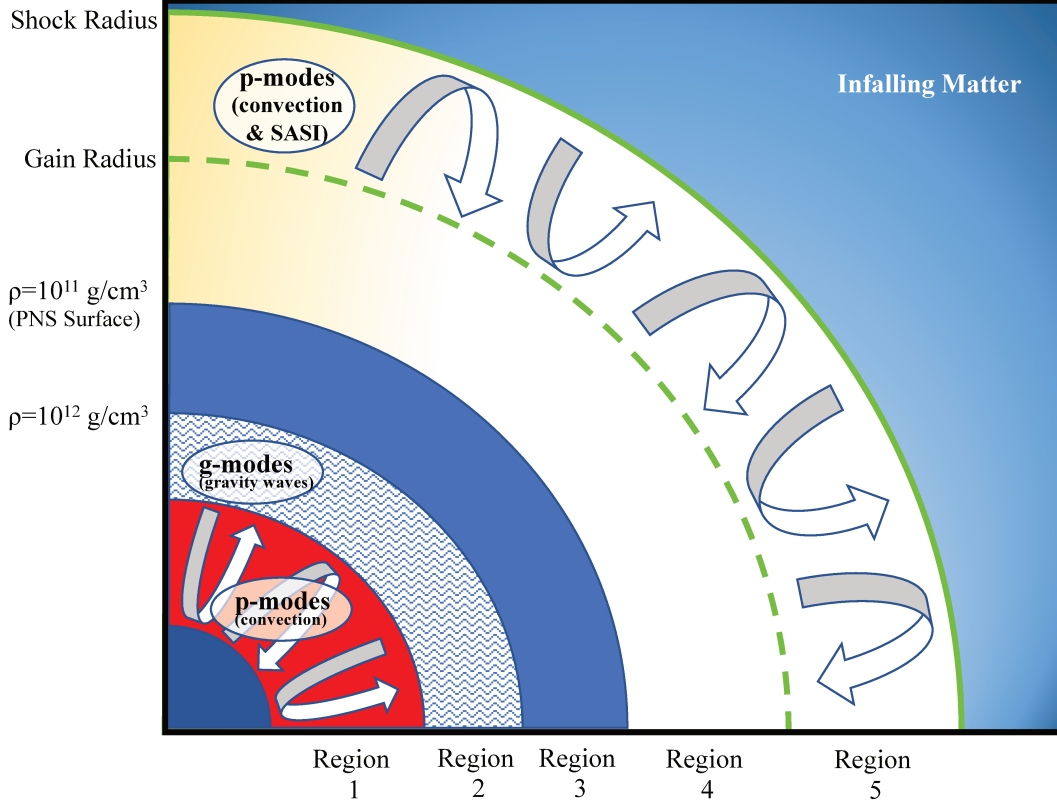


Figure 3.4: Schematic representation of the various regions emitting gravitational waves during the post-bounce evolution. Figure extracted from [88]

Regarding the gravitational wave strain, detectors with sensitivities down to $h \approx 10^{-23}$ at frequencies between 20 Hz and 1 kHz should be able to detect the signal of a supernova occurring at 10 kpc¹. This is the case of Advanced-LIGO, Advanced-VIRGO and KAGRA.

3.2 Previous works on proto-neutron star evolution

Two approaches are possible to model proto-neutron star evolution :

- using a full-hydrodynamics simulation, since such frameworks already exist to study core-collapse supernovae they can be used to study PNS
- using a quasi-static approach, by considering that the PNS evolves in hydrostatic equilibrium

The first method produces more reliable results but has strong limitations because the evolution timescale of a PNS is much longer than the acoustic timescale, which limits the timestep of full-hydrodynamics simulations. This point is discussed in more detail in the section 6.1.1.

3.2.1 Quasi-static studies

The first simulations of proto-neutron star evolution were relying on a quasi-static approximation for the PNS structure, which means that the star is considered in hydrostatic equilibrium

¹the stellar disk of the milky way is about 30 kpc in diameter

throughout the evolution, and that we consider only the evolution of intensive thermodynamic quantities such as the electron fraction and the entropy per baryon (more details are given on this approximation in the chapter 6 of this thesis). They were also using a diffusion approximation for the neutrino transport. Among other we can cite [89], [90], [91] and [92] (more details are given in the sec. 4.6).

The initial profiles of electron fraction and entropy per baryon are obtained with CCSN simulations or rescaled from available profiles using the same arguments of invariance as presented in the sec. 3.1.1. The usual method is to remove all the matter beyond the stalled shock to account for an explosion. The remaining matter will constitute the proto-neutron star.

They find in particular that the PNS neutrino emission does not depend much upon the details of the initial profiles and that the used equation of state has not a significant influence on them at early times [92].

The neutrino emission decays exponentially during the evolution, this is the *shallow decay phase* (see sec. 3.1.2). Then, at the end of the evolution, the neutrino emission sharply drop as neutrino transparency sets in the PNS.

Recent studies tend to use more detailed neutrino transport methods, as is the case of [93], which implements a variable Eddington factor method (more details about this method are given in the sec. 4.6).

Most of these studies neglect the convection in the PNS, but there are some recent studies of PNS convection within the *mixing length theory approach*, as in [81]. Indeed this method is quite adapted to such a quasi-static modeling (see the chapter 8 for more details on this approximation). There also exists toy models of stationary flows due to convection in this context [94], and some detailed MHD simulations using the anelastic approximation [95].

3.2.2 Full hydrodynamic studies

The progressive improvements of core-collapse simulation codes during the past 30 years made possible the modelisation of proto-neutron stars with full-hydrodynamic codes, either in spherical symmetry [96] or with three-dimensional simulations [5].

Such codes allow to evaluate the importance of the convection inside the proto-neutron star and it is instructive to compare the quasi-static models with theses fiducial full-hydrodynamic simulations. But such a comparison can be difficult, especially at early times, because of the significant accretion observed in some simulations, see e.g. [97] and [98]. Indeed, the quasi-static models completely neglect the accretion process (by considering that it has already ended at the beginning of the simulation). This is of importance in the prediction of neutrino luminosity curves and emitted spectrum, which contains the signature of the accretion process, and also modify the structure of the outer layers of the PNS.

Full-hydrodynamic studies are therefore more reliable, but as they have a significant computational cost and cannot model the evolution on very long timescales : 1D models take days of computation to reach several seconds of evolution, and 3D models are even more expensive and most of them are stopped before reaching one second. There exists however some hydrodynamic simulations performed over long timescales, such as [99], which start the simulation in 2D and switch to a 1D simulation after shock revival to study the PNS until 70s of evolution. Their results agree qualitatively with other other quasi-static 1D simulations.

Because of this limitation, the quasi-static simulations are thus still of great help in proto-neutron star studies.

3.2.3 Open questions in PNS evolution

Despite the significant progress made on proto-neutron star modeling, a lot of open questions remain and/or would gain from some deeper investigation :

- As in core-collapse modeling, there are a lot of uncertainties in the microphysics (on the choice of equation of state and on the appropriate approximations for the computation of weak cross sections). Therefore investigating the effect of the microphysic on the cooling is always interesting to determine what could be learned from future observations.
- At some point of the PNS cooling process, the neutron star crust will form [100]. This process is not fully understood yet and could influence the cooling as the crust can act as an insulating blanket (see e.g. [101]). Some studies of this exists [99] but relies on a crude estimate of the cristallisation point.
- The transition to the ν -transparency and the subsequent evolution have not been studied extensively in the litterature, because such a transition cannot be modeled with a neutrino diffusion approximation. Even the full hydrodynamic simulations which has been carried out up to very long timescales usually relies on a very simplified neutrino transport [99]. Therefore the study of this phase, especially with the influence of weak cross sections, would be instructive.
- Models with high rotation rates might be very different from the spherically symmetric case, for example because of differential rotation and rotation-induced meridional currents. The rotation frequency of proto-neutron stars can go up to about 300 Hz during its initial contraction if no spin-up mechanism, such as accretion, is involved [102].

3.3 Neutrino detection capabilities

As neutrinos only interact via the weak interaction, their detection is a complicated task : they can only be detected indirectly by observing the charged particles produced during charged current interaction or by measuring the recoil of neutral current scattering targets.

Because of this, neutrino astronomy is a very recent field of study, which was born with the observation of solar neutrinos by R. Davis [103]. This important detection allowed to confirm the model for nuclear burning in the Sun. Another extremely important event was the detection of neutrinos produced by the supernova SN1987A.

3.3.1 The SN1987A supernova event

During the night of the 23rd February 1987, a neutrino burst was simultaneously observed in three detectors : Kamioka-II [104], IMB [105] and Baksan [106]. This burst occured several hours before the first optical observation of the supernova. The main reason for this delay is that the neutrino burst signal is emitted shortly after bounce, when the shock reaches the neutrinosphere (see sec. 2.1.2), whereas the photon signal is emitted once the shock wave bursted out the mantle of the dying star, which can take up to several hours.

Kamioka-II detected 11 events spread over 12.5s whereas IMB detected 8 events spread over 5.6s. Regarding the Baksan detector, a burst is strongly suspected but a detailed analysis was not possible.

Those detectors are mostly sensitive to the inverse β -decay (IBD) :

$$\bar{\nu}_e + p \rightarrow e^+ + n \quad (3.4)$$

therefore the 21 detected neutrinos are electron antineutrinos $\bar{\nu}_e$.

This process also has the disadvantage of being nearly isotropic, making it difficult to obtain the direction of incoming neutrinos. Nevertheless, the Kamioka-II observations were able to point back the first two events to the Large Magellanic Cloud (host of the SN1987A event) [104].

The corresponding signal has been thoroughly analysed during the following years (see e.g. [107]) and today it seems certain that this burst is originated from neutrinos emitted during the cooling of the proto-neutron star in the SN1987A event.

Since this event the detector's sensitivity has considerably increased, and we expect several thousands of events in Super-Kamiokande from a galactic supernova.

3.3.2 Types of neutrino detectors

There is no neutrino detector perfectly adapted to the supernova case. Various technologies exist and are complementary to each other.

Water Cherenkov detectors

Water Cherenkov detectors are looking for the Cherenkov light emitted by faster-than-light charged particles in water. They consist of a large volume of ultra pure water associated with an array of photomultipliers to detect the Cherenkov radiation.

Since there are protons in the medium, interaction channels are highly dominated by the inverse β -decay, as shown in fig. 3.5. Therefore they are mostly sensitive to electron antineutrinos. Scattering processes off electrons are also useful to point back to the source.

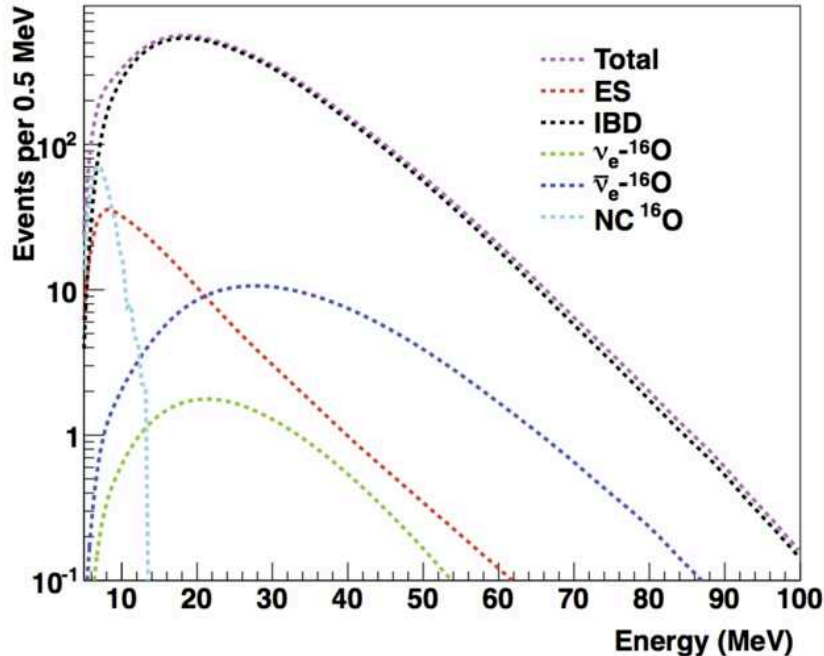


Figure 3.5: Event rates in a water Cherenkov detector for various interaction modes. This figure is extracted from [108]. IBD is inverse β -decay, ES is scattering off electrons and other rates are charged and neutral current interactions with ^{16}O nuclei.

Charged current processes involving muon neutrinos ν_μ and $\bar{\nu}_\mu$ are not considered here because the threshold needed to create a muon would need a neutrino with an energy much higher than

the supernova neutrino spectrum.

An example of such a detector is Super-Kamiokande [109], which consists of a cylindrical tank filled with 50 000 m³ of water. Its successor Hyper-Kamiokande will be 20 times larger and should be operational in 2027.

Another example is the IceCube neutrino observatory, but its design makes it mostly sensitive to high energy neutrinos much higher than the supernova spectrum. However the detector can observe the high neutrino flux generated by a supernova as a large coincident event on all photomultipliers.

Scintillation counters

A scintillation counter relies on a scintillating material, which produces photons in response to the passage of a charged particle. This material is associated to photomultipliers to detect the resulting photon.

A common method is to use a liquid organic compound as a scintillator medium. One advantage is that despite the fact that the interaction channels are still dominated by IBD, the resonant de-excitation peak from neutral current interaction on ¹²C is clearly visible and exists for all neutrino flavors, see fig. 3.6.

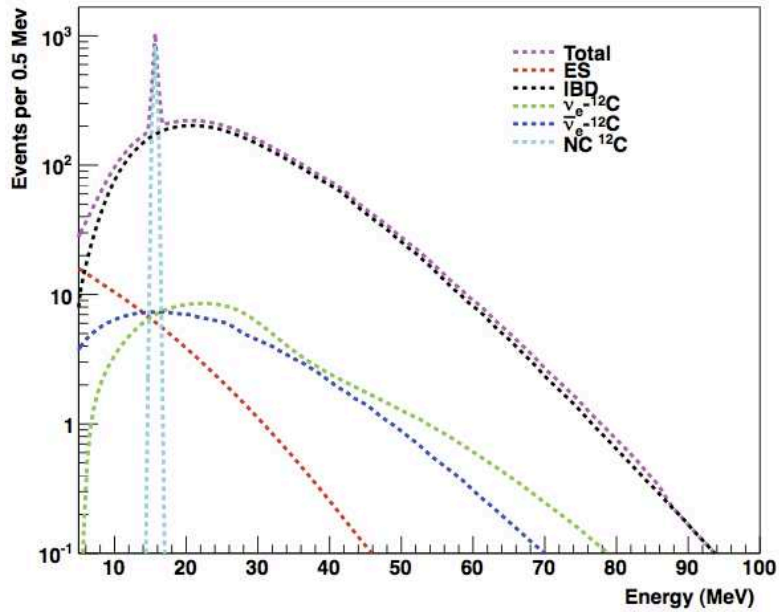


Figure 3.6: Event rates in an organic liquid scintillator for various interaction modes. This figure is extracted from [108]. IBD is inverse β -decay, ES is scattering off electrons and other rates are charged and neutral currents interactions with ¹²C nuclei.

The Baksan detector mentioned in the SN1987A case is an example of such a detector. Another example is the Large Volume Detector (LVD) at the INFN Gran Sasso National Laboratory [110], with an active mass of 1000 t of liquid scintillator.

Liquid Argon time projection chambers

In a time projection chamber a combination of electric and magnetic field is associated with a position-sensitive electron collector in order to reconstruct the trajectory of incoming electrons

on the collector.

In this case the medium is constituted by liquid atomic argon, and particles produced by interactions of neutrinos will ionise the medium and generate a unique signature.

This kind of detector stands out from the other two because there are no protons in the interacting medium, therefore the detector is not sensitive to IBD. The predominant interaction channel is the charged current interaction of the electron neutrino ν_e , see fig. 3.7.

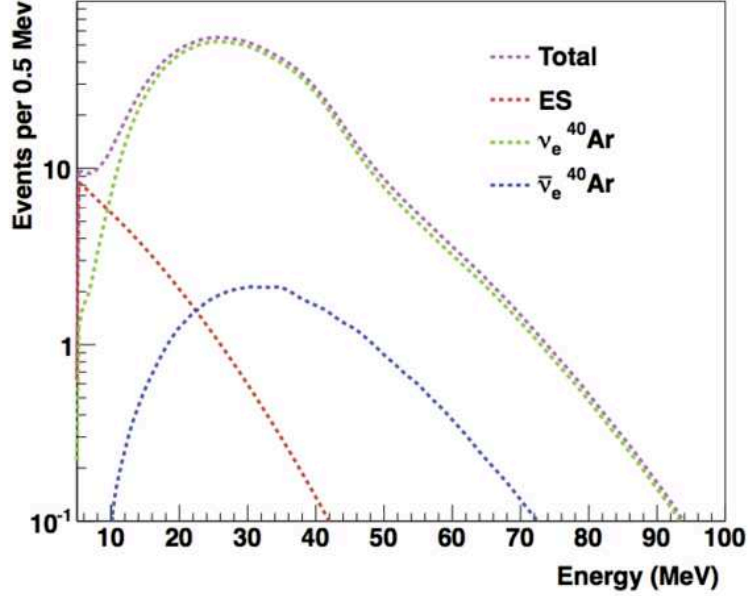


Figure 3.7: Event rates in a liquid argon TPC for various interaction modes. This figure is extracted from [108]. ES is scattering off electrons and other rates are charged currents interactions with ^{40}Ar nuclei.

The sensitivity of this kind of detector to electron neutrinos ν_e makes it complementary to the other two, which are mostly sensitive to $\bar{\nu}_e$ via the IBD channel.

Among the available experiments the MicroBooNE experiment began to collect data in October 2015 and has an active mass of 170 t of liquid argon. The Deep Underground Neutrino Experiment (DUNE) is also a promising project for the future [111].

Other detectors

The previous categories represent the majority of large neutrino detectors, but some smaller experiments do not fall under any of these categories.

Among those other supernova detectors a promising one is the Helium and Lead Observatory (HALO) [112], which rely on charged current interactions with the doubly magic nucleus ^{208}Pb . It is designed as a low cost neutrino detector mostly sensitive to electron neutrinos ν_e and able to detect a supernova neutrino burst. A neutron is produced in the CC interaction of ν_e with a lead nucleus ($\nu_e + ^{208}_{82}\text{Pb} \rightarrow e^- + n + ^{207}_{83}\text{Bi}$). As this neutron cannot be captured by another doubly magic lead nucleus it goes through the medium until reaching the ^3He detector.

3.3.3 SuperNova Early Warning System (SNEWS)

SNEWS [113] is an international collaboration of neutrino detectors able to detect a supernova neutrino burst. The goal is to detect the neutrino emission, which is the first signal (with the GW emission) to arrive on Earth (as explained in the sec. 3.3.1), in order to have the time to prepare all other experiments before other signals becomes available. The involved detectors should have a prompt response and be able to point back the source.

The detectors currently involved in SNEWS are :

- Super-Kamiokande, a big water Cherenkov detector in Japan
- The Large Volume Detector (LVD), a scintillation counter in Italy
- IceCube, on the South Pole
- Borexino neutrino observatory, a liquid scintillator in Italy, joined SNEWS in July 2009
- Kamioka Liquid Scintillator Antineutrino Detector (KamLAND), from Kamioka observatory, joined SNEWS in December 2013
- The Daya Bay Reactor Neutrino Experiment, another liquid scintillator in China, joined SNEWS in November 2014
- The Helium And Lead Observatory (HALO), in Canada, was the last to join SNEWS in October 2015

The SNEWS system checks those detectors for coincident detections and send an alert to the astronomical community in case of a positive neutrino burst. The system has been built with the requirement of a very low false alert rate (less than one per century).

Part II

Transport of neutrinos in dense matter

Chapter 4

Boltzmann equation and collision integral

The modelisation of neutrino transport in the context of core-collapse supernova and proto-neutron star evolution relies on the relativistic kinetic theory. Indeed the mean free path of neutrinos varies from several orders of magnitude, and neutrinos can be trapped in some areas while free-streaming in others, as already discussed in 2.2. This is why the description of the neutrino gas has to be made within various approximations of the Boltzmann equation.

This chapter is focused on the Boltzmann equation and the usage of one-particle distribution functions in general relativity, and more particularly in spherically symmetric spacetimes. It aims to present a generic framework used to model neutrino transport throughout all this thesis. And since the aim of this work is to focus on neutrino transport, we will restrict ourselves to ultrarelativistic particles.

4.1 General relativistic Boltzmann transport

The Boltzmann transport equation describes the behaviour of a diluted (or weakly interacting) gas out of thermodynamical equilibrium. It is an evolution equation for the one-particle distribution function of the gas.

4.1.1 One-particle distribution function

The one-particle distribution function of neutrinos $f_\nu(t, x^i, p^i)$ is a marginal distribution of the full many-body particle distribution of the neutrino gas which describes the average behaviour of a particle in the system. It is a relativistic scalar (see, e.g. [114]), and p^a is used as an *on-shell momentum*. As we can neglect the masses of neutrinos because of their low value compared with the system's energy scales ¹, the on-shell condition is given by

$$g_{ab}p^ap^b = 0 \quad (4.1)$$

where g_{ab} is the space-time metric, with the signature $(-, +, +, +)$.

This means that the time component p^0 is a function of the other degrees of freedom p^i :

$$p^0(t, x^i, p^i) = \frac{1}{g_{00}} \left(-g_{i0}p^i + \sqrt{(g_{i0}p^i)^2 - g_{ij}g_{00}p^ip^j} \right) \quad (4.2)$$

¹for the electron neutrino ν_e the upper bound is $m_{\nu_e} < 1.1 \text{ MeV c}^{-2}$ [115] at 90 % confidence level

Therefore f_ν only depends upon p^i and not upon p^0 (this point is important in the formulation of Boltzmann equation 4.5).

The particle distribution function contains information about the microscopic distribution of momenta. A macroscopic hydrodynamic-like description can be obtained by computing some relevant moment integrals of the one-particle distribution function (see, e.g. [116]) : we may define the particle current density N_ν^a of neutrinos and the stress-energy tensor T_ν^{ab} of neutrinos as

$$N_\nu^a = \frac{c}{h^3} \int p^a f_\nu \sqrt{-g} \frac{d^3 p^i}{-p_0} \quad (4.3)$$

$$T_\nu^{ab} = \frac{c^2}{h^3} \int p^a p^b f_\nu \sqrt{-g} \frac{d^3 p^i}{-p_0} \quad (4.4)$$

where $g = \det(g_{ab})$ is the metric determinant.

In the above expressions the integration element $\sqrt{-g} \frac{d^3 p^i}{-p_0}$ is a relativistic scalar [114].

Note that the minus sign in the integration element comes from our choice of metric signature $(-, +, +, +)$.

4.1.2 Boltzmann equation

The general relativistic Boltzmann equation reads

$$\frac{p^0}{c} \frac{\partial f_\nu}{\partial t} + p^i \frac{\partial f_\nu}{\partial x^i} - \Gamma_{ab}^i p^a p^b \frac{\partial f_\nu}{\partial p^i} = (-u_a p^a) \mathcal{B}_u[f_\nu] \quad (4.5)$$

Where Γ_{ab}^i are the Christoffel symbols and u_μ is the four velocity of the local inertial frame in which the collision integral $\mathcal{B}_u[f_\nu]$ is computed.

This is a scalar equation, but it is not manifestly covariant because we used *on-shell* momentum, distribution function and collision integral. A manifestly covariant formulation of Boltzmann equation is given in [117], and relies on the construction of an *off-shell* distribution function and collision integral. The authors then recover equation (4.5) by integrating their equation on the mass shell.

Equation (4.5) can be derived from Liouville's theorem, see e.g. [118] for the special relativistic case.

The left hand side is the *streaming term* (it is *Liouville's operator* applied to f_ν) while the right hand side is the *collision integral*, which takes all microphysics inputs.

By taking moments of this equation we get the macroscopic conservation laws for particle number and stress-energy :

$$\nabla_a N_\nu^a = \frac{c}{h^3} \int (-u_a p^a) \mathcal{B}_u[f_\nu] \sqrt{-g} \frac{d^3 p^i}{-p_0} \quad (4.6)$$

$$\nabla_a T_\nu^{ab} = \frac{c^2}{h^3} \int (-u_a p^a) p^b \mathcal{B}_u[f_\nu] \sqrt{-g} \frac{d^3 p^i}{-p_0} \quad (4.7)$$

In the case of neutrino transport in dense matter the right hand side terms will describe the exchange of energy and lepton number with the neutron star matter. If the neutrino gas is at

local thermal and chemical equilibrium with the neutron star matter then the right hand side of these equations vanishes.

Note that since energy and lepton number are globally conserved quantities, one should have

$$\nabla_a N_L^a = 0 \quad (4.8)$$

$$\nabla_a T_{\text{tot}}^{ab} = 0 \quad (4.9)$$

where N_L^a and T^{ab} are respectively the total lepton current density and the total stress-energy tensor.

4.2 Case of a TOV spacetime

In this section we consider the case of a stationary, spherically symmetric spacetime using the Schwarzschild gauge :

$$ds^2 = -\alpha^2(r)c^2 dt^2 + \psi^2(r)dr^2 + r^2(d\theta^2 + \sin^2(\theta)d\varphi^2) \quad (4.10)$$

where (r, θ, φ) are the usual spherical coordinates. We also introduce the four natural basis vectors $\{(\partial_t)^a, (\partial_r)^a, (\partial_\theta)^a, (\partial_\varphi)^a\}$.

$\alpha(r)$ and $\psi(r)$ are two metric potentials. α is usually called the *lapse function*.

Finally, we introduce the four velocity of the Eulerian observer $l^a = \frac{1}{\alpha}(\partial_t)^a$

4.2.1 Momentum coordinates

The momentum coordinates $(\hat{\epsilon}, \Theta, \Phi)$ are defined such that Θ represents the angle between the momentum and the radial coordinate, and Φ is an azimuthal coordinate with respect to $(\partial_r)^a$:

$$p^a = \frac{\hat{\epsilon}}{c\alpha^2}(\partial_t)^a + \frac{\hat{\epsilon} \cos \Theta}{\alpha\psi}(\partial_r)^a + \frac{\hat{\epsilon} \sin \Theta \cos \Phi}{\alpha r}(\partial_\theta)^a + \frac{\hat{\epsilon} \sin \Theta \sin \Phi}{\alpha r \sin \theta}(\partial_\varphi)^a \quad (4.11)$$

Here $\hat{\epsilon}$ represents the energy of the neutrino measured by an asymptotic observer : $(\partial_t)^a p_a = -\hat{\epsilon}$. The energy measured in the Eulerian frame is $l^a p_a = -\epsilon = -\hat{\epsilon}/\alpha$. This is this value which should be used in the computation of the collision integral $\mathcal{B}_l[f_\nu]$. This choice of variables allows for a considerable simplification of the formulation of Boltzmann equation by putting redshift effects into the definition of the coordinates.

Using those coordinates the scalar integration element used in equations 4.3 and 4.4 is given by

$$\sqrt{-g} \frac{d^3 p^i}{-p_0} = \frac{\hat{\epsilon} d\hat{\epsilon}}{\alpha^2} \sin \Theta d\Theta d\Phi = \epsilon d\epsilon \sin \Theta d\Theta d\Phi \quad (4.12)$$

In the following we will also assume that the neutrino distribution is isotropic in the horizontal direction² : $\frac{\partial f_\nu}{\partial \Phi} = 0$ and is spherically symmetric in the star : $\frac{\partial f_\nu}{\partial \theta} = \frac{\partial f_\nu}{\partial \varphi} = 0$.

²this property also stems from the spherical symmetry

4.2.2 Boltzmann equation and angular moments

With the definition (4.11) the Boltzmann equation reads

$$\frac{1}{c\alpha} \frac{\partial f_\nu}{\partial t} + \frac{\cos \Theta}{\psi} \frac{\partial f_\nu}{\partial r} - \left(\frac{1}{r} - (\partial_r \ln \alpha) \right) \frac{\sin \Theta}{\psi} \frac{\partial f_\nu}{\partial \Theta} = \mathcal{B}_l[f_\nu] \quad (4.13)$$

The advantage of $\hat{\epsilon}$ as a choice of variable is that the different energies are only correlated via the collision integral (with e.g. inelastic scattering), indeed the redshift is taken into account in the coordinate.

Since the problem is computationally very expensive despite the geometrical simplifications, it is common to study only the few first angular moments. The n^{th} angular moment is defined (in spherical symmetry) as

$$\frac{1}{2} \int f_\nu(t, r, \hat{\epsilon}, \Theta) \cos(\Theta)^n \sin(\Theta) d\Theta \quad (4.14)$$

In this work we will need only the three first angular moments :

$$J_\nu(t, r, \hat{\epsilon}) = \frac{1}{2} \int f_\nu(t, r, \hat{\epsilon}, \Theta) \sin(\Theta) d\Theta \quad (4.15)$$

$$H_\nu(t, r, \hat{\epsilon}) = \frac{1}{2} \int f_\nu(t, r, \hat{\epsilon}, \Theta) \cos(\Theta) \sin(\Theta) d\Theta \quad (4.16)$$

$$K_\nu(t, r, \hat{\epsilon}) = \frac{1}{2} \int f_\nu(t, r, \hat{\epsilon}, \Theta) \cos(\Theta)^2 \sin(\Theta) d\Theta \quad (4.17)$$

The zeroth angular integral of Θ of the Boltzmann equation (4.13) yields

$$\frac{1}{c\alpha} \frac{\partial J_\nu}{\partial t} + \frac{\alpha^2}{r^2 \psi} \frac{\partial}{\partial r} \left(\frac{r^2}{\alpha^2} H_\nu \right) = \frac{1}{2} \int \mathcal{B}_l[f_\nu] \sin(\Theta) d\Theta \quad (4.18)$$

whereas the first angular integral of the Boltzmann equation (4.13) yields

$$\frac{1}{c\alpha} \frac{\partial H_\nu}{\partial t} + \frac{1}{\psi} \frac{\partial K_\nu}{\partial r} + \left(\frac{1}{r} - (\partial_r \ln \alpha) \right) \frac{1}{\psi} (3K_\nu - J_\nu) = \frac{1}{2} \int \mathcal{B}_l[f_\nu] \cos \Theta \sin(\Theta) d\Theta \quad (4.19)$$

4.2.3 Macroscopic conservation laws

Moments of the equation (4.18) yield the macroscopic conservation laws.

The neutrino number conservation law is

$$\frac{1}{\alpha} \frac{\partial n_\nu}{\partial t} + \frac{1}{r^2 \alpha \psi} \frac{\partial}{\partial r} \left(r^2 \alpha F_\nu^{(n)} \right) = \Gamma_\nu \quad (4.20)$$

where n_ν is the number density of neutrinos, $F_\nu^{(n)}$ is the outgoing number flux of neutrinos and Γ_ν is the production rate of neutrinos, which are defined as

$$n_\nu = \frac{\alpha}{c} N_\nu^0 = \frac{4\pi}{(hc)^3} \int J_\nu \frac{\hat{\epsilon}^2 d\hat{\epsilon}}{\alpha^3} \quad (4.21)$$

$$F_\nu^{(n)} = \psi N_\nu^r = \frac{4\pi c}{(hc)^3} \int H_\nu \frac{\hat{\epsilon}^2 d\hat{\epsilon}}{\alpha^3} \quad (4.22)$$

$$\Gamma_\nu = \nabla_a (N_\nu^a) = \frac{c}{(hc^3)} \int \mathcal{B}_l[f_\nu] \frac{\hat{\epsilon}^2 d\hat{\epsilon}}{\alpha^3} \sin(\Theta) d\Theta d\Phi \quad (4.23)$$

Another useful law is the neutrino energy conservation law :

$$\frac{1}{\alpha} \frac{\partial \mathcal{E}_\nu}{\partial t} + \frac{1}{r^2 \alpha^2 \psi} \frac{\partial}{\partial r} \left(r^2 \alpha^2 F_\nu^{(\mathcal{E})} \right) = Q_\nu \quad (4.24)$$

where \mathcal{E}_ν is the energy density of neutrinos, $F_\nu^{(\mathcal{E})}$ is the outgoing energy flux carried by neutrinos and Q_ν is the neutrino heating rate, defined as

$$\mathcal{E}_\nu = \alpha^2 T_\nu^{00} = \frac{4\pi}{(hc)^3} \int J_\nu \frac{\hat{\epsilon}^3 d\hat{\epsilon}}{\alpha^4} \quad (4.25)$$

$$F_\nu^{(\mathcal{E})} = \alpha \psi c T_\nu^{0r} = \frac{4\pi c}{(hc)^3} \int J_\nu \frac{\hat{\epsilon}^3 d\hat{\epsilon}}{\alpha^4} \quad (4.26)$$

$$Q_\nu = -l_b \nabla_a (T_\nu^{ab}) = \frac{c}{(hc)^3} \int \mathcal{B}_l[f_\nu] \frac{\hat{\epsilon}^3 d\hat{\epsilon}}{\alpha^4} \sin(\Theta) d\Theta d\Phi \quad (4.27)$$

The neutrino total number luminosity $L_\nu^{(n)}$ and energy luminosity $L_\nu^{(\mathcal{E})}$ are defined as

$$L_\nu^{(n)} = \lim_{r \rightarrow \infty} 4\pi r^2 \alpha F_\nu^{(n)} \quad (4.28)$$

$$L_\nu^{(\mathcal{E})} = \lim_{r \rightarrow \infty} 4\pi r^2 \alpha^2 F_\nu^{(\mathcal{E})} \quad (4.29)$$

4.3 Collision integral

The collision integral $\mathcal{B}_u[f_\nu]$ is the right hand side of the Boltzmann equation (4.5), it contains the effect of all interactions between particles on the distribution function.

A generic property which should hold for a collision kernel to be physically meaningful is the *detailed balance condition* : each interaction term should vanish if the involved particles are at equilibrium :

$$\mathcal{B}_u^{(eq)}[f_\nu^{(eq)}] = 0 \quad (4.30)$$

$f_\nu^{(eq)}$ is the neutrino equilibrium distribution, which is a Fermi-Dirac distribution :

$$f_\nu^{(eq)}(\epsilon_\nu) = f_{FD}(\epsilon_\nu - \mu_\nu) = \frac{1}{1 + e^{(\epsilon_\nu - \mu_\nu)/T}} \quad (4.31)$$

where μ_ν is the chemical potential of neutrinos.

We will now discuss the various processes entering the collision integral.

4.3.1 Charge exchange processes

Interactions which fall under this category are of the type

$$X + l^- \rightleftharpoons Y + \nu_l \quad \text{or} \quad X \rightleftharpoons Y + l^+ + \nu_l$$

The particularity of these interactions is that the neutrino is created or absorbed in the process. This results in a very simple form for the collision integral, which is linear in f_ν :

$$\mathcal{B}_{CE}[f_\nu] = j(\epsilon)(1 - f_\nu(\epsilon, \Theta)) - \frac{1}{\lambda(\epsilon)} f_\nu(\epsilon, \Theta) \quad (4.32)$$

Where j is the emissivity and $1/\lambda$ is the inverse mean free path. These quantities are related by the *detailed balance condition* :

$$j(\epsilon) e^{(\epsilon - \mu_\nu)/T} = \frac{1}{\lambda(\epsilon)} \quad (4.33)$$

where T is the temperature and μ_ν is the chemical potential of the neutrino ν .

The *detailed balance condition* can also be made explicit in the collision integral by recasting the expression as

$$\mathcal{B}_{CE}[f_\nu] = \kappa^*(\epsilon) \left(f_\nu^{(eq)}(\epsilon) - f_\nu(\epsilon, \Theta) \right) \quad (4.34)$$

Where $\kappa^* = j + \frac{1}{\lambda} = \frac{j}{f_\nu^{(eq)}} = \frac{1}{\lambda} \frac{1}{1 - f_\nu^{(eq)}}$ is the opacity corrected for stimulated absorption.

The two first Legendre moments of $\mathcal{B}_{CE}[f_\nu]$ are given by

$$\frac{1}{2} \int \mathcal{B}_{CE}[f_\nu] \sin(\Theta) d\Theta = \kappa^*(\epsilon) \left(J_\nu^{(eq)}(\epsilon) - J_\nu(\epsilon) \right) \quad (4.35)$$

$$\frac{1}{2} \int \mathcal{B}_{CE}[f_\nu] \cos(\Theta) \sin(\Theta) d\Theta = -\kappa^*(\epsilon) H_\nu(\epsilon) \quad (4.36)$$

4.3.2 Scattering processes

Neutrinos can scatter off any weakly interacting particle present in the medium :

$$X + \nu \rightleftharpoons X + \nu$$

The scattering integral can be written as

$$\begin{aligned} \mathcal{B}_S[f_\nu] = \frac{1}{4\pi} \int (\epsilon')^2 d\epsilon' d\Omega' \left\{ R^{in}(\epsilon, \epsilon', \Omega \cdot \Omega') f_\nu(\epsilon', \Omega') (1 - f_\nu(\epsilon, \Omega)) \right. \\ \left. - R^{out}(\epsilon, \epsilon', \Omega \cdot \Omega') f_\nu(\epsilon, \Omega) (1 - f_\nu(\epsilon', \Omega')) \right\} \end{aligned} \quad (4.37)$$

where $\Omega = (\cos \Theta, \sin \Theta \cos \Phi, \sin \Theta \sin \Phi)$

The interaction is described by R^{in} and R^{out} , which are respectively the ingoing and outgoing scattering kernels. They must fullfill the *in/out symmetry* :

$$R^{in}(\epsilon, \epsilon', \Omega \cdot \Omega') = R^{out}(\epsilon', \epsilon, \Omega \cdot \Omega') \quad (4.38)$$

This symmetry simply stems from the conservation of neutrino number during the scattering (the number of outgoing neutrinos must be equal to the number of ingoing neutrinos). And indeed using this symmetry we can easily show that the scattering integral (4.37) has a vanishing second energy moment :

$$\int \mathcal{B}_S[f_\nu] \epsilon^2 d\epsilon = 0 \quad (4.39)$$

But the third moment is usually non vanishing as the neutrino energy changes during the process.

In more practical terms, this means that the contribution of scattering processes to the neutrino production rate Γ_ν given by equation (4.23) is zero whereas its contribution to the heat function Q_ν given by equation (4.27) is usually non-zero.

The kernel must also fullfill the *detailed balance condition*, which gives an additional relation between outgoing and ingoing kernels :

$$e^{\epsilon/T} R^{in}(\epsilon, \epsilon', \Omega \cdot \Omega') = e^{\epsilon'/T} R^{out}(\epsilon, \epsilon', \Omega \cdot \Omega') \quad (4.40)$$

therefore, as pointed out in [119], the kernel has an internal symmetry :

$$R^{in}(\epsilon', \epsilon, \mathbf{\Omega} \cdot \mathbf{\Omega}') = e^{(\epsilon - \epsilon')/T} R^{in}(\epsilon, \epsilon', \mathbf{\Omega} \cdot \mathbf{\Omega}') \quad (4.41)$$

$$R^{out}(\epsilon', \epsilon, \mathbf{\Omega} \cdot \mathbf{\Omega}') = e^{(\epsilon' - \epsilon)/T} R^{out}(\epsilon, \epsilon', \mathbf{\Omega} \cdot \mathbf{\Omega}') \quad (4.42)$$

Systems with azimuthal symmetry

When the neutrino distribution has an azimuthal symmetry $\frac{\partial f}{\partial \Phi} = 0$, we can perform the integration over Φ' in the scattering integral (4.37).

To make it explicit we expand the scattering kernel into a Legendre series :

$$R^{in/out}(\epsilon, \epsilon', \mathbf{\Omega} \cdot \mathbf{\Omega}') = \sum_{l=0}^{\infty} \frac{2l+1}{2} R_l^{in/out}(\epsilon, \epsilon') P_l(\mathbf{\Omega} \cdot \mathbf{\Omega}') \quad (4.43)$$

where P_l are the Legendre polynomials.

Then we use the *spherical harmonic addition theorem* :

$$P_l(\mathbf{\Omega} \cdot \mathbf{\Omega}') = P_l(\cos \Theta) P_l(\cos \Theta') + 2 \sum_{m=1}^l \frac{(l-m)!}{(l+m)!} P_l^m(\cos \Theta) P_l^m(\cos \Theta') \cos[m(\Phi - \Phi')] \quad (4.44)$$

where P_l^m are the associated Legendre polynomials.

Finally, we define the azimuthal average of the kernel :

$$R_{az}^{in/out}(\epsilon, \epsilon', \Theta, \Theta') = \frac{1}{2\pi} \int R^{in/out}(\epsilon, \epsilon', \mathbf{\Omega} \cdot \mathbf{\Omega}') d\Phi' = \sum_{l=0}^{\infty} \frac{2l+1}{2} R_l^{in/out}(\epsilon, \epsilon') P_l(\cos \Theta) P_l(\cos \Theta') \quad (4.45)$$

we obtain

$$\begin{aligned} \mathcal{B}_S[f_\nu] = \frac{1}{2} \int (\epsilon')^2 d\epsilon' \sin(\Theta') d\Theta' \left\{ R_{az}^{in}(\epsilon, \epsilon', \Theta, \Theta') f_\nu(\epsilon', \Theta') (1 - f_\nu(\epsilon, \Theta)) \right. \\ \left. - R_{az}^{out}(\epsilon, \epsilon', \Theta, \Theta') f_\nu(\epsilon, \Theta) (1 - f_\nu(\epsilon', \Theta')) \right\} \end{aligned} \quad (4.46)$$

Legendre moments of the scattering integral

In numerical applications we usually truncate the Legendre expansion (4.43) after the dipole :

$$R^{in/out}(\epsilon, \epsilon', \mathbf{\Omega} \cdot \mathbf{\Omega}') = \frac{1}{2} R_0^{in/out}(\epsilon, \epsilon') + \frac{3}{2} R_1^{in/out}(\epsilon, \epsilon') \mathbf{\Omega} \cdot \mathbf{\Omega}' \quad (4.47)$$

therefore, for the azimuthal average we obtain

$$R_{az}^{in/out}(\epsilon, \epsilon', \Theta, \Theta') = \frac{1}{2} R_0^{in/out}(\epsilon, \epsilon') + \frac{3}{2} R_1^{in/out}(\epsilon, \epsilon') \cos(\Theta) \cos(\Theta') \quad (4.48)$$

With this expression we can rewrite the scattering integral in terms of effective emissivities and opacities (see e.g. [119]) :

$$\mathcal{B}_S[f_\nu] = j_0^{(S)}(\epsilon) - \kappa_0^{(S)}(\epsilon) f_\nu(\epsilon, \mathbf{\Omega}) + 3 \cos(\Theta) \left[j_1^{(S)}(\epsilon) - \kappa_1^{(S)}(\epsilon) f_\nu(\epsilon, \mathbf{\Omega}) \right] \quad (4.49)$$

with the following definitions :

$$j_0^{(S)}(\epsilon) = \frac{1}{2} \int (\epsilon')^2 d\epsilon' R_0^{in}(\epsilon, \epsilon') J_\nu(\epsilon') \quad (4.50)$$

$$\kappa_0^{(S)}(\epsilon) = j_0^{(S)}(\epsilon) + \frac{1}{2} \int (\epsilon')^2 d\epsilon' R_0^{out}(\epsilon, \epsilon') (1 - J_\nu(\epsilon')) \quad (4.51)$$

$$j_1^{(S)}(\epsilon) = -\frac{1}{2} \int (\epsilon')^2 d\epsilon' R_1^{in}(\epsilon, \epsilon') H_\nu(\epsilon') \quad (4.52)$$

$$\kappa_1^{(S)}(\epsilon) = j_1^{(S)}(\epsilon) + \frac{1}{2} \int (\epsilon')^2 d\epsilon' R_1^{out}(\epsilon, \epsilon') H_\nu(\epsilon') \quad (4.53)$$

The two first Legendre moments of the scattering integral $\mathcal{B}_S[f_\nu]$ are then given by

$$\frac{1}{2} \int \mathcal{B}_S[f_\nu] \sin(\Theta) d\Theta = j_0^{(S)}(\epsilon) - \kappa_0^{(S)}(\epsilon) J_\nu(\epsilon) - 3\kappa_1^{(S)}(\epsilon) H_\nu(\epsilon) \quad (4.54)$$

$$\frac{1}{2} \int \mathcal{B}_S[f_\nu] \cos(\Theta) \sin(\Theta) d\Theta = -\kappa_0^{(S)}(\epsilon) H_\nu(\epsilon) + j_1^{(S)}(\epsilon) - \kappa_1^{(S)}(\epsilon) K_\nu(\epsilon) \quad (4.55)$$

Case of isoenergetic scattering

When the scattering process is isoenergetic, we can write

$$R^{in/out}(\epsilon, \epsilon', \mathbf{\Omega} \cdot \mathbf{\Omega}') = \frac{2}{(\epsilon)^2} \delta(\epsilon - \epsilon') \kappa^{IS}(\epsilon, \mathbf{\Omega} \cdot \mathbf{\Omega}') \quad (4.56)$$

therefore the scattering integral (4.37) is simply

$$\mathcal{B}_S[f_\nu] = \frac{1}{2\pi} \int d\mathbf{\Omega}' \kappa^{IS}(\epsilon, \mathbf{\Omega} \cdot \mathbf{\Omega}') (f_\nu(\epsilon, \mathbf{\Omega}') - f_\nu(\epsilon, \mathbf{\Omega})) \quad (4.57)$$

We can expand the isoenergetic opacity in its two first Legendre moments :

$$\kappa^{IS}(\epsilon, \mathbf{\Omega} \cdot \mathbf{\Omega}') = \frac{1}{2} \kappa_0^{IS}(\epsilon) + \frac{3}{2} \kappa_1^{IS}(\epsilon) \mathbf{\Omega} \cdot \mathbf{\Omega}' \quad (4.58)$$

in the case of azimuthal symmetry this yields the following Legendre moments of the scattering integral

$$\frac{1}{2} \int \mathcal{B}_S[f_\nu] \sin(\Theta) d\Theta = 0 \quad (4.59)$$

$$\frac{1}{2} \int \mathcal{B}_S[f_\nu] \cos(\Theta) \sin(\Theta) d\Theta = (\kappa_1^{IS}(\epsilon) - \kappa_0^{IS}(\epsilon)) H_\nu(\epsilon) \quad (4.60)$$

this is why we often define the *transport opacity* κ_{tr}^{IS} as

$$\kappa_{tr}^{IS}(\epsilon) = \kappa_0^{IS}(\epsilon) - \kappa_1^{IS}(\epsilon) = \int (1 - \cos \Theta) \kappa^{IS}(\epsilon, \cos(\Theta)) \sin(\Theta) d\Theta \quad (4.61)$$

κ_{tr}^{IS} is the effective opacity contributing to the transport properties of the medium.

4.3.3 Thermal pair production

The pair production of neutrinos

$$X \rightleftharpoons Y + \nu + \bar{\nu}$$

is also an important feature in neutrino transport, as it can produce heavy flavors neutrinos ν_μ and ν_τ . They can also be created by charged current interactions with muons and τ leptons, but as discussed in the section 2.2.3, they will be neglected in this work.

The thermal pair creation integral can be written as

$$\mathcal{B}_{TP}[f_\nu] = \frac{1}{4\pi} \int (\epsilon')^2 d\epsilon' d\Omega' \{ R^p(\epsilon, \epsilon', \Omega \cdot \Omega') (1 - f_\nu(\epsilon, \Omega)) (1 - f_{\bar{\nu}}(\epsilon', \Omega')) - R^a(\epsilon, \epsilon', \Omega \cdot \Omega') f_\nu(\epsilon, \Omega) f_{\bar{\nu}}(\epsilon', \Omega') \} \quad (4.62)$$

Where R^p and R^a are respectively the production and absorption kernels for thermal pairs. They must fullfill the *particle exchange symmetry*, which means that we obtain the corresponding kernels for the antineutrino by exchanging $\epsilon \leftrightarrow \epsilon'$ in the kernel expression.

Using this symmetry we can demonstrate the following equality between energy moments, which means that those processes create as many neutrinos as antineutrinos and do not change lepton numbers :

$$\int \epsilon^2 \mathcal{B}_{TP}[f_\nu] d\epsilon d\Omega = \int \epsilon^2 \mathcal{B}_{TP}[f_{\bar{\nu}}] d\epsilon d\Omega \quad (4.63)$$

In terms of production rate, this means that the contribution of the pair production kernel to the neutrino and antineutrino production rates is the same : $\Gamma_\nu^{TP} = \Gamma_{\bar{\nu}}^{TP}$.

We have also the following relation between kernels, which stems from the *detailed balance condition* :

$$R^a(\epsilon, \epsilon', \Omega \cdot \Omega') = e^{(\epsilon + \epsilon')/T} R^p(\epsilon, \epsilon', \Omega \cdot \Omega') \quad (4.64)$$

Systems with azimuthal symmetry

The procedure is the same as in the scattering case : we expand the kernel in a Legendre series :

$$R^{p/a}(\epsilon, \epsilon', \Omega \cdot \Omega') = \sum_{l=0}^{\infty} \frac{2l+1}{2} R_l^{p/a}(\epsilon, \epsilon') P_l(\Omega \cdot \Omega') \quad (4.65)$$

and we introduce the azimuthal average

$$R_{az}^{p/a}(\epsilon, \epsilon', \Theta, \Theta') = \frac{1}{2\pi} \int R^{p/a}(\epsilon, \epsilon', \Omega \cdot \Omega') d\Phi' = \sum_{l=0}^{\infty} \frac{2l+1}{2} R_l^{p/a}(\epsilon, \epsilon') P_l(\cos \Theta) P_l(\cos \Theta') \quad (4.66)$$

we obtain

$$\mathcal{B}_{TP}[f_\nu] = \frac{1}{2} \int (\epsilon')^2 d\epsilon' \sin(\Theta') d\Theta' \{ R_{az}^p(\epsilon, \epsilon', \Theta, \Theta') (1 - f_\nu(\epsilon', \Theta')) (1 - f_\nu(\epsilon, \Theta)) - R_{az}^a(\epsilon, \epsilon', \Theta, \Theta') f_\nu(\epsilon, \Theta) f_\nu(\epsilon', \Theta') \} \quad (4.67)$$

Legendre moments of the thermal pair production integral

If we truncate the kernel after the dipole term we can obtain the same expression as eq. (4.49) with effective opacities and emissivities :

$$\mathcal{B}_{TP}[f_\nu] = j_0^{(TP)}(\epsilon) - \kappa_0^{(TP)}(\epsilon) f_\nu(\epsilon, \Omega) + 3 \cos(\Theta) [j_1^{(TP)}(\epsilon) - \kappa_1^{(TP)}(\epsilon) f_\nu(\epsilon, \Omega)] \quad (4.68)$$

and the Legendre moments are obtained by analogy with eq. (4.54) and (4.55).

The only difference comes from the expression of effective interaction terms :

$$j_0^{(TP)}(\epsilon) = \frac{1}{2} \int (\epsilon')^2 d\epsilon' R_0^p(\epsilon, \epsilon') (1 - J_\nu(\epsilon')) \quad (4.69)$$

$$\kappa_0^{(TP)}(\epsilon) = j_0^{(TP)}(\epsilon) + \frac{1}{2} \int (\epsilon')^2 d\epsilon' R_0^a(\epsilon, \epsilon') J_\nu(\epsilon') \quad (4.70)$$

$$j_1^{(TP)}(\epsilon) = -\frac{1}{2} \int (\epsilon')^2 d\epsilon' R_1^p(\epsilon, \epsilon') H_\nu(\epsilon') \quad (4.71)$$

$$\kappa_1^{(TP)}(\epsilon) = j_1^{(TP)}(\epsilon) + \frac{1}{2} \int (\epsilon')^2 d\epsilon' R_1^a(\epsilon, \epsilon') H_\nu(\epsilon') \quad (4.72)$$

4.4 Limits of the Boltzmann equation

In this section we briefly present the two limits of the Boltzmann equation obtained in the diffusive case and in the free-streaming case.

4.4.1 The diffusion limit

A useful limit of the Boltzmann equation is the diffusion limit, as it allows to recover Fick's and Fourier's laws for the transport of heat and particles.

In this limit we consider that the neutrino distribution function f_ν is close to the equilibrium distribution $f_\nu^{(eq)}$, such that it is almost isotropic :

$$f_\nu(t, r, \hat{\epsilon}, \Theta) \approx J_\nu(t, r, \hat{\epsilon}) + 3 \cos(\Theta) H_\nu(t, r, \hat{\epsilon}) \quad (4.73)$$

with $H_\nu \ll J_\nu$. The second angular moment of the neutrino distribution function is then simply $K_\nu = \frac{1}{3} J_\nu$.

with $f_\nu \approx f_\nu^{(eq)}$ we can also approximate the first moment of the diffusion equation as

$$\frac{1}{2} \int \mathcal{B}_S[f_\nu] \cos(\Theta) \sin(\Theta) d\Theta = -\kappa_D H_\nu(\epsilon) \quad (4.74)$$

The first moment of Boltzmann equation (4.19) is then simply

$$\frac{\tau_D}{\alpha} \frac{\partial H_\nu}{\partial t} + H_\nu = -\frac{1}{\psi(3\kappa_D)} \frac{\partial J_\nu}{\partial r} \quad (4.75)$$

where $\tau_D = 1/(c\kappa_D)$ is a relaxation time and ψ is a metric coefficient introduced in eq. (4.10). The equation above is known as *causal diffusion law*. By taking the $\tau_D = 0$ limit we recover the classic diffusion law, Fick's (/Fourrier's) law, where the flux of particles (/heat) is proportional to the gradient of the transported quantity, but we also loose causality (Fick's and Fourier's laws are not compatible with relativity).

Fick's law (for particle transport) is obtained by taking the second energy moments of the above equation, as the particle density and flux are given by eq. (4.21) and (4.22), whereas Fourier's law (for heat transport) is obtained by taking the third energy moments, as in eq. (4.25) and (4.26).

The (energy dependant) diffusion coefficient is given by $D = 1/(3\kappa_D)$.

4.4.2 The free-streaming limit

Neutrinos are said to be free-streaming when the collision integral $\mathcal{B}_u[f_\nu]$ is vanishing for all possible values of f_ν . In this case we have a strict conservation of individual neutrino number currents and stress-energy tensors :

$$\nabla_a N_\nu^a = 0 \quad (4.76)$$

$$\nabla_a T_\nu^{ab} = 0 \quad (4.77)$$

The spherical geometry also has the effect of forward-peaking the neutrino angular distribution in the radially outgoing direction far away from the star. At long distance this results in all angular moments being equal : $J_\nu = H_\nu = K_\nu$.

4.5 The Fast Multigroup Transport (FMT)

The formalism presented in the previous sections was still fairly general and applicable to any spherically symmetric system. But the Boltzmann equation (4.13) is still very expensive to solve.

In this work we used a transport scheme to obtain an approximate solution of eq. (4.13) while needing much less computational time. This scheme relies on a steady-state transport of neutrinos, it is based on the fast multigroup transport developed in [120].

The equation of steady-state transport is solved at high optical depth by using a two-stream approximation, which replaces the detailed angular distribution by a description in terms of a balance between an ingoing and an outgoing ray.

As this approximation is valid only at high optical depth, the solution at low optical depth is solved by using an Eddington factor closure, in which we solve the two first angular moments of the Boltzmann equation closed by an analytic relation between the three first angular moments J_ν , H_ν and K_ν .

4.5.1 Steady-state neutrino transport

In a steady-state neutrino transport, we assume that the neutrino distribution function f_ν is independent of time : $\frac{\partial f_\nu}{\partial t} = 0$. This is a situation of dynamical equilibrium : all neutrinos leaving the star by diffusing out are considered as instantly replaced by pair production and/or charged current processes. This approximation is justified if the timescale corresponding to the establishment of radiative equilibrium is small compared with other timescales of interest. An order of magnitude of this timescale is given by the inverse mean free path of neutrinos, with eq. (2.25) we obtain

$$\tau = \frac{\lambda}{c} = 1.3 \times 10^{-7} \left(\frac{n_B}{0.16 \text{ fm}^{-3}} \right) \text{ s} \quad (4.78)$$

Therefore this approximation is well justified in a PNS. When the PNS is cooling the neutrino mean free path will eventually become much larger than the PNS radius, which may cause this approximation to fail. But only the transition to transparency may present some issues, indeed once the medium is transparent the only relevant quantities are the neutrino emissivities and the scheme will necessarily make the correct predictions.

The corresponding transport equation is eq. (4.13) without the time dependence :

$$\frac{\cos \Theta}{\psi} \frac{\partial f_\nu}{\partial r} - \left(\frac{1}{r} - (\partial_r \ln \alpha) \right) \frac{\sin \Theta}{\psi} \frac{\partial f_\nu}{\partial \Theta} = \mathcal{B}_l[f_\nu] \quad (4.79)$$

This assumption of steady-state transport is reasonable as long as the background medium (the thermodynamic conditions and the metric) has a long evolution timescale compared with neutrino diffusion timescale in the star.

The effect of neutrinos on the transport of heat and lepton number in the matter is then deduced after the resolution of this equation by using the macroscopic conservation laws (4.20) and (4.24): The source terms are given by the divergence of outgoing neutrino fluxes

$$\frac{1}{r^2 \alpha \psi} \frac{\partial}{\partial r} \left(r^2 \alpha F_\nu^{(n)} \right) = \Gamma_\nu \quad (4.80)$$

$$\frac{1}{r^2 \alpha^2 \psi} \frac{\partial}{\partial r} \left(r^2 \alpha^2 F_\nu^{(\mathcal{E})} \right) = Q_\nu \quad (4.81)$$

One disadvantage of steady-state transport is that lepton number and energy conservation cannot be enforced globally : diagnostic equations³ are solved for neutrino transport to deduce source terms which are used a posteriori in the electron number and energy conservation laws of dense matter. Therefore one cannot verify the consistency of the method by checking global conservation laws.

Regarding the evaluation of the collision integral $\mathcal{B}_l[f_\nu]$ in eq. (4.79), the effective emissivities and opacities involved in equations (4.49) and (4.68) are computed by using the neutrino distribution function of the previous timestep instead of being solved consistently with the current timestep. This greatly simplifies the evaluation of the collision integral and has a negligible influence on the evolution if the steady-state approximation is valid.

We will also make the approximation of considering that all interactions are isotropic : we truncate scattering and pair production kernels after their zeroth Legendre momenta.

Therefore we can use a collision integral of the form

$$\mathcal{B}_l[f_\nu] = j[f] - \chi[f] f_\nu(\epsilon, \Theta) \quad (4.82)$$

4.5.2 High optical depths : the two-ray approximation

The solution of the steady-state transport equation (4.79) at high optical depths (*i.e.* in zones where neutrinos are trapped and in quasi-equilibrium) is obtained by using a two stream approximation. This approach is valid if the distribution function is close to the isotropic, diffusive case, $H_\nu \ll J_\nu$.

Note that we do not use this approximation to compute the full solution, but only as a closure method to obtain the ratio $h_\nu = H_\nu/J_\nu$ (called the *flux factor*) and we then solve the neutrino flux equation (4.18) :

$$\frac{\alpha^2}{r^2 \psi} \frac{\partial}{\partial r} \left(\frac{r^2}{\alpha^2} H_\nu \right) = j - \chi \frac{H_\nu}{h_\nu} \quad (4.83)$$

Now to obtain this flux factor, we consider an outgoing ray $f_\nu^{(out)} = f_\nu(r, \hat{\epsilon}, \Theta = 0)$ and an ingoing ray $f_\nu^{(in)} = f_\nu(r, \hat{\epsilon}, \Theta = \pi)$. The details of the angular distribution and the fact that neutrinos are trapped (*i.e.* close to isotropy) or free-streaming (*i.e.* forward peaked toward $\Theta = 0$) is encoded in the balance between the two streams.

³a diagnostic equation relates quantities at a given time without influence from previous events, by opposition to a prognostic equation. As an exemple, an equation of state is a diagnostic equation

The two stream solution is computed by solving the corresponding transport equation (4.79) for both of them :

$$\frac{1}{\psi} \frac{\partial f_{\nu}^{(out)}}{\partial r} = j - \chi f_{\nu}^{(out)} \quad (4.84)$$

$$-\frac{1}{\psi} \frac{\partial f_{\nu}^{(in)}}{\partial r} = j - \chi f_{\nu}^{(in)} \quad (4.85)$$

The boundary conditions are given by : $f_{\nu}^{(in)}(r = R) = 0$ (no ingoing radiation from outside the star) and $f_{\nu}^{(in)}(r = 0) = f_{\nu}^{(out)}(r = 0)$ (central isotropy).

Note that these two equations are coupled because j and χ are computed by using f_{ν} .

We then need to compute the flux factor h_{ν} by using the obtained solutions for $f_{\nu}^{(out)}$ and $f_{\nu}^{(in)}$. Usually the two-stream approximation is used in planar geometry, and with the assumption that $f_{\nu} = f_{\nu}^{(out)}\delta(\Theta) + f_{\nu}^{(in)}\delta(\Theta - \pi)$, which gives a flux factor

$$h_{\nu} = \frac{f_{\nu}^{(out)} - f_{\nu}^{(in)}}{f_{\nu}^{(out)} + f_{\nu}^{(in)}} \quad (4.86)$$

But here, in order to perform a smoother transition and have a better description in the diffusive region, we will compute the flux factor as in [120], by assuming a continuous distribution $f_{\nu} \propto e^{a \cos(\Theta)}$, we obtain

$$f_{\nu}(\epsilon, \Theta) = \sqrt{f_{\nu}^{(in)} f_{\nu}^{(out)}} \left(\sqrt{\frac{f_{\nu}^{(out)}}{f_{\nu}^{(in)}}} \right)^{\cos \Theta} \quad (4.87)$$

Which yields the following flux factor

$$h_{\nu} = 1 + \frac{2f_{\nu}^{(in)}/f_{\nu}^{(out)}}{1 - f_{\nu}^{(in)}/f_{\nu}^{(out)}} + \frac{2}{\ln(f_{\nu}^{(in)}/f_{\nu}^{(out)})} \quad (4.88)$$

4.5.3 Low optical depths : two-moment closure

At low optical depth (*i.e.* in the free-streaming zone) the two-ray approach is flawed because of its planar geometry, and does not take correctly into account the forward peaking toward $\Theta = 0$ caused by the spherical geometry.

Therefore we use a variable Eddington factor with an M1 closure to solve the two first moment equations consisting of eq. (4.83) and (4.89)

$$\frac{1}{\psi} \frac{\partial K_{\nu}}{\partial r} + \left(\frac{1}{r} - (\partial_r \ln \alpha) \right) \frac{1}{\psi} (3K_{\nu} - J_{\nu}) = -\chi H_{\nu} \quad (4.89)$$

The Eddington factor is defined as the ratio $p_{\nu} = K_{\nu}/J_{\nu}$, and we will use the following M1 closure :

$$p_{\nu}(h_{\nu}) = \frac{1 - 2h_{\nu} + 4h_{\nu}^2}{3} \quad (4.90)$$

Note that the choice of this analytic closure is arbitrary, and a lot of possible choices are available in the literature (see e.g. [121] for a review on M1 closures). As explained below, this choice of closure in the FMT is motivated by the position of its critical point (the radial derivative of h_{ν} generally presents a point of divergence, this is the critical point of the two-moments scheme). The closure should however have the correct limits for the diffusive limit ($p(0) = \frac{1}{3}$) and for the free-stream limit ($p_{\nu}(1) = 1$).

Using eq. (4.89) we get an ODE for the flux factor :

$$\frac{\partial h_\nu}{\partial r} = \frac{1}{p_\nu(h_\nu) - h_\nu p'_\nu(h_\nu)} \left\{ \left(\frac{1}{r} - \partial_r \log \alpha \right) (p_\nu - 1) h_\nu - \psi \left(\chi h_\nu^2 - p_\nu \frac{j}{J_\nu} + p_\nu \chi \right) \right\} \quad (4.91)$$

We see that this equation presents a critical point for $p_\nu(h_\nu) - h_\nu p'_\nu(h_\nu) = 0$, which in our case corresponds to $h_\nu^{\text{crit}} = 0.5$. As this equation is easy to solve by an outward integration after the critical point (for $h_\nu \geq h_\nu^{\text{crit}}$) but much stiffer before this point, we match the solution obtained by solving the system constituted by equations (4.83) and (4.91) with the interior two-stream solution at the critical point $h_\nu = h_\nu^{\text{crit}} = 0.5$.

Regarding the choice of closure (4.90), it is not a standard choice, but this one has the advantage of presenting a critical point much closer to the high optical depth region, which limits the error due to the use of the two-stream approximation at low optical depth. Indeed most closures proposed in the literature [121] present a critical point much higher, around $h_\nu^{\text{crit}} \sim 0.7$.

4.6 Other neutrino transport methods used in PNS simulations

In this section we briefly outline two methods which have been used for neutrino transport in the context of proto-neutron star evolution : the Equilibrium Flux Limited Diffusion (EFLD) and the variable Eddington factor method. We also discuss their advantages and disadvantages compared with our method.

4.6.1 Equilibrium Flux Limited Diffusion (EFLD)

In ELFD, the outgoing neutrino fluxes $F_\nu^{(n)}$ and $F_\nu^{(\mathcal{E})}$ (defined respectively by eq. (4.22) and (4.26)) are computed by using an adapted Fick's (/Fourrier's) law (see e.g. [92]) :

$$F_{\text{lep}}^{(n)} = F_{\nu_e}^{(n)} - F_{\bar{\nu}_e}^{(n)} = -\frac{T^2}{6\pi^2\alpha\psi} \left[D_3 \frac{\partial(\alpha T)}{\partial r} + (\alpha T) D_2 \frac{\partial(\mu_{\nu_e}/T)}{\partial r} \right] \quad (4.92)$$

$$F_{\text{tot}}^{(\mathcal{E})} = F_{\nu_e}^{(\mathcal{E})} + F_{\bar{\nu}_e}^{(\mathcal{E})} + 4F_{\nu_x}^{(\mathcal{E})} = -\frac{T^3}{6\pi^2\alpha\psi} \left[D_4 \frac{\partial(\alpha T)}{\partial r} + (\alpha T) D_3 \frac{\partial(\mu_{\nu_e}/T)}{\partial r} \right] \quad (4.93)$$

where D_n is a diffusion coefficient reflecting all microscopic processes involving neutrinos, we have

$$D_2 = D_2^{\nu_e} + D_2^{\bar{\nu}_e} \quad , \quad D_3 = D_3^{\nu_e} - D_3^{\bar{\nu}_e} \quad , \quad D_4 = D_4^{\nu_e} + D_4^{\bar{\nu}_e} + 4D_4^{\nu_x} \quad (4.94)$$

where D_n^ν is defined as

$$D_n^\nu = \frac{1}{T^{n+1}} \int \epsilon^n d\epsilon \left(\kappa^*(\epsilon) + \kappa_{tr}^{IS}(\epsilon) \right)^{-1} f_\nu^{(eq)}(\epsilon) \left[1 - f_\nu^{(eq)}(\epsilon) \right] \quad (4.95)$$

κ^* is the opacity corrected for stimulated absorption (see eq. (4.34)), and $\kappa_{tr}^{IS}(\epsilon)$ is the transport opacity due to scattering (see eq. 4.61).

These fluxes can then be used in the macroscopic conservation laws of neutrinos (4.20) and (4.24).

This approximation has the advantage of having a low computational cost, and predict correct results in the high optical depth region.

But eq. (4.92) and (4.93) have the disadvantage of predicting unphysical fluxes in low optical depth regions, which exceed the black body limit⁴. Because of this some flux limiters have been proposed in the literature, such as in [122] and [123]. This choice of flux limiter can have a significant influence if the transport in semi-transparent region is relevant (as in the case of core-collapse or in the case of the transition to transparency in proto-neutron stars). But EFLD is not really adapted for this kind of situation anyway.

It should be stressed that EFLD methods can also be formulated as multigroup methods, meaning that several energy bins are considered instead of integrating over the total fluxes $F_\nu^{(n)}$ and $F_\nu^{(\mathcal{E})}$. Doing so allows to make predictions of the emitted neutrino spectrum.

There are numerous works using EFLD in the context of proto-neutron stars evolution, see e.g. [89], [90], [91] and [92].

4.6.2 Variable Eddington factor method

Variable Eddington factors are a class of methods which rely upon solving the two first angular moments of the Boltzmann equation.

In the general case, these angular moments equations relate the four first angular moments of the neutrino distribution J_ν , H_ν , K_ν and L_ν . The transport used in this thesis uses an Eddington factor method at low optical depths (see section 4.5.3), but in our case the fourth moment L_ν is not involved (c.f. eq. (4.18) and 4.19), the reason is that we considered that the fluid is not moving (i.e. we neglected the Doppler shift induced in the neutrino radiation).

The variable Eddington factors are defined as

$$p_\nu^{(0)} = \frac{K_\nu}{J_\nu} \quad \text{and} \quad p_\nu^{(1)} = \frac{L_\nu}{H_\nu} \quad (4.96)$$

and the variable Eddington factor method then relies upon providing a method of closure to obtain these two factors.

Two classes of methods can be employed :

- we can use an analytic closure, as presented in section 4.5.3 or in [124]. As stated earlier a list of available closures can be found in [121]. This class of methods is called the *M1 closure method*.
- we can solve a simplified version of Boltzmann equation to compute the two Eddington factors numerically at each timestep. This is the *model Boltzmann equation method*, used e.g. in the context of core-collapse by [125] and in the context of proto-neutron stars evolution by [93]

This second class of methods provides more accurate results in low optical depth areas (i.e. closer to full radiation transfer), but has a heavier computational cost.

4.6.3 Comparison of various methods

In the diffusion zone (i.e. at high optical depth, where neutrinos are trapped), all methods yield similar results. This is not surprising as all approximations behave the same way near thermodynamic equilibrium.

⁴The black body radiation is an upper limit for the emission of an opaque solid surface. This limit is also valid for fermionic emission and only differ from the bosonic case by a numerical factor

The differences appear in the semi-transparent region. Here the EFLD method appears to be the worst, because it predicts unphysical fluxes that have to be artificially reduced, but EFLD has the advantage of a very low computational cost. Regarding variable Eddington factor methods with model Boltzmann equations, they are perhaps the most accurate approximations in regards to full radiation transfer. Indeed they are using a set of equations very close to the original Boltzmann equation, such that they accurately model the low optical depth area. But they come with an heavy computational cost.

The FMT method described in the previous section stands somewhere in the middle : it is not so accurate in semi-transparent areas but still yields better results than EFLD, while having a computational cost similar to multigroup EFLD.

Chapter 5

Weak processes occuring in core-collapse and (proto-)neutron stars

In this part we present the various weak processes involved in the core-collapse mechanism and the evolution of proto-neutron stars. For convenience in this chapter we will use units in which $\hbar = c = 1$.

5.1 Neutrino interactions with free nucleons

Neutrinos can interact with free neutrons and protons via charged and neutral current interactions. These are the most important processes to describe proto-neutron star evolution.

5.1.1 Charged current interactions with nucleons

Charge exchange reactions play a major role in core-collapse and proto-neutron star cooling because they are responsible for the deleptonization of matter and the onset of *beta equilibrium*.

Direct processes

In this section we will consider the following processes :

$$\begin{aligned} p + e^- &\rightleftharpoons n + \nu_e & p &\rightleftharpoons n + e^+ + \nu_e \\ n + e^+ &\rightleftharpoons p + \bar{\nu}_e & n &\rightleftharpoons p + e^- + \bar{\nu}_e \end{aligned}$$

In a fairly general way, emissivity j and inverse mean free path $1/\lambda$ of neutrinos for the process $p + e^- \rightleftharpoons n + \nu_e$ can be written as an integral over the electron momentum [126]

$$j(\epsilon_\nu) = -G_F^2 |V_{ud}|^2 \int \frac{d^3 p_e}{(2\pi)^3} \left(\text{Im}(\Pi_V(q^-)) + 3g_A^2 \text{Im}(\Pi_A(q^-)) \right) \times \quad (5.1)$$
$$\left[1 + f_{BE}(q_0^-) \right] \left[f_{FD}(\epsilon_e - \mu_e) \right]$$

$$\frac{1}{\lambda(\epsilon_\nu)} = -G_F^2 |V_{ud}|^2 \int \frac{d^3 p_e}{(2\pi)^3} \left(\text{Im}(\Pi_V(q^-)) + 3g_A^2 \text{Im}(\Pi_A(q^-)) \right) \times \quad (5.2)$$
$$\left[f_{BE}(q_0^-) \right] \left[1 - f_{FD}(\epsilon_e - \mu_e) \right]$$

The weak interaction coupling constants G_F and g_A involved in this formula have been introduced in the section 2.2.3, and $|V_{ud}| = 0.97427$ is the modulus of the up/down element of

CKM matrix.

ϵ_e and p_e are respectively the energy and the momentum of the electron (note that $\epsilon_e = \sqrt{p_e^2 + m_e^2}$ is the *on-shell* energy), $\Pi_V(q)$ and $\Pi_A(q)$ are the vector and axial contributions to the polarisation tensor (for more details see [126]), whereas f_{BE} and f_{FD} are the usual Bose-Einstein and Fermi-Dirac distributions.

Finally the 4-vector q^- is given by $q^- = (\epsilon_e - \epsilon_\nu - \mu_e + \mu_{\nu_e}, \vec{p}_e - \vec{p}_{\nu_e})$, meaning that the argument of the Bose-Einstein distribution is $q_0^- = \epsilon_e - \epsilon_\nu - \mu_e + \mu_{\nu_e}$.

We see that these formulas fulfill explicitly the detailed balance condition (4.33), indeed

$$\left[1 + f_{BE}(q_0^-) \right] \left[f_{FD}(\epsilon_e - \mu_e) \right] e^{(\epsilon_\nu - \mu_{\nu_e})/T} = \left[f_{BE}(q_0^-) \right] \left[1 - f_{FD}(\epsilon_e - \mu_e) \right] \quad (5.3)$$

The rates for the corresponding positronic process $p \rightleftharpoons n + e^+ + \nu_e$ can be obtained by integration over the positron momentum :

$$j(\epsilon_\nu) = -G_F^2 |V_{ud}|^2 \int \frac{d^3 p_e}{(2\pi)^3} \left(\text{Im}(\Pi_V(q^+)) + 3g_A^2 \text{Im}(\Pi_A(q^+)) \right) \times \quad (5.4)$$

$$\left[1 + f_{BE}(q_0^+) \right] \left[1 - f_{FD}(\epsilon_e + \mu_e) \right]$$

$$\frac{1}{\lambda(\epsilon_\nu)} = -G_F^2 |V_{ud}|^2 \int \frac{d^3 p_e}{(2\pi)^3} \left(\text{Im}(\Pi_V(q^+)) + 3g_A^2 \text{Im}(\Pi_A(q^+)) \right) \times \quad (5.5)$$

$$\left[f_{BE}(q_0^+) \right] \left[f_{FD}(\epsilon_e + \mu_e) \right]$$

with $q^+ = (-\epsilon_e - \epsilon_\nu - \mu_e + \mu_{\nu_e}, -\vec{p}_e - \vec{p}_{\nu_e})$.

For completeness we also provide the expression of the rates for the antineutrino processes. For the neutron decay $n \rightleftharpoons p + e^- + \bar{\nu}_e$ we have

$$j(\epsilon_\nu) = -G_F^2 |V_{ud}|^2 \int \frac{d^3 p_e}{(2\pi)^3} \left(\text{Im}(\Pi_V(\bar{q}^-)) + 3g_A^2 \text{Im}(\Pi_A(\bar{q}^-)) \right) \times \quad (5.6)$$

$$\left[f_{BE}(\bar{q}_0^-) \right] \left[1 - f_{FD}(\epsilon_e - \mu_e) \right]$$

$$\frac{1}{\lambda(\epsilon_\nu)} = -G_F^2 |V_{ud}|^2 \int \frac{d^3 p_e}{(2\pi)^3} \left(\text{Im}(\Pi_V(\bar{q}^-)) + 3g_A^2 \text{Im}(\Pi_A(\bar{q}^-)) \right) \times \quad (5.7)$$

$$\left[1 + f_{BE}(\bar{q}_0^-) \right] \left[f_{FD}(\epsilon_e - \mu_e) \right]$$

with $\bar{q}^- = (\epsilon_e + \epsilon_\nu - \mu_e + \mu_{\nu_e}, \vec{p}_e + \vec{p}_{\nu_e})$.

and for the positron capture $n + e^+ \rightleftharpoons p + \bar{\nu}_e$ we have

$$j(\epsilon_\nu) = -G_F^2 |V_{ud}|^2 \int \frac{d^3 p_e}{(2\pi)^3} \left(\text{Im}(\Pi_V(\bar{q}^+)) + 3g_A^2 \text{Im}(\Pi_A(\bar{q}^+)) \right) \times \quad (5.8)$$

$$\left[f_{BE}(\bar{q}_0^+) \right] \left[f_{FD}(\epsilon_e + \mu_e) \right]$$

$$\frac{1}{\lambda(\epsilon_\nu)} = -G_F^2 |V_{ud}|^2 \int \frac{d^3 p_e}{(2\pi)^3} \left(\text{Im}(\Pi_V(\bar{q}^+)) + 3g_A^2 \text{Im}(\Pi_A(\bar{q}^+)) \right) \times \quad (5.9)$$

$$\left[1 + f_{BE}(\bar{q}_0^+) \right] \left[1 - f_{FD}(\epsilon_e + \mu_e) \right]$$

with $\bar{q}^+ = (-\epsilon_e + \epsilon_\nu - \mu_e + \mu_{\nu_e}, -\vec{p}_e + \vec{p}_{\nu_e})$.

The expressions above are fairly general, and therefore we need the expressions of the polarisation functions $\Pi_V(q)$ and $\Pi_A(q)$ in order to compute them. The various models and approximations used in core-collapse or proto-neutron star cooling simulations to compute these rates will be detailed in the chapter 10 of this thesis.

Processes involving a spectator nucleon

In cold neutron stars, it is well known that the so-called dURCA (for direct URCA) process

$$\begin{cases} n \rightarrow p + e^- + \bar{\nu}_e \\ p + e^- \rightarrow n + \nu_e \end{cases}$$

is kinematically forbidden unless the proton fraction Y_p exceeds a certain value [127].

The reasoning is the following : in cold neutron stars the momenta of the involved neutron, proton and electron are close to their Fermi value p_{Fn} , p_{Fp} and p_{Fe} , and as a consequence the above processes are possible only if

$$p_{Fp} + p_{Fe} > p_{Fn} \quad (5.10)$$

We can then rewrite this condition by using the relation $p_{Fi} \propto n_i^{1/3}$ (where n_i for $i = n, p, e$ are the particle densities) and the charge neutrality relation $n_p = n_e$ to obtain

$$Y_p = \frac{n_p}{n_n + n_p} > \frac{1}{9} \approx 11\% \quad (5.11)$$

For a given equation of state, the density above which this condition is met (if it is met) is called the *dURCA threshold*.

The above reasoning is given for a neutron star composed uniquely of neutrons, protons and electrons. It can be generalised to all compositions (but yields different threshold values).

This effect is also expected to play a role in late time proto-neutron star cooling : as the temperature drops the direct charged current processes with nucleons become strongly suppressed.

In this case, the so-called modified URCA (mURCA) processes are relevant. They involve a spectator nucleon N :

$$\begin{array}{ll} p + e^- + N \rightleftharpoons n + \nu_e + N & p + N \rightleftharpoons n + e^+ + \nu_e + N \\ n + e^+ + N \rightleftharpoons p + \bar{\nu}_e + N & n + N \rightleftharpoons p + e^- + \bar{\nu}_e + N \end{array}$$

By including this additional particle we can lift the kinematic restriction discussed above as additional momenta can be exchanged.

If these processes have been extensively studied in the case of cold neutron stars [128], there exists only a few attempts to extend this work to this case of hot matter and produce rates usable in core-collapse and proto-neutron stars simulations. In [4], the authors modeled this effect with a phenomenological approach, by including a collisional broadening factor. This approach will be discussed in section 11.1.2.

5.1.2 Scattering off nucleons

Neutrinos of all flavors can scatter off nucleons via a flavor-independent neutral current interaction

$$\nu + N \rightleftharpoons \nu + N$$

If the first supernova simulations were using mostly rates computed with the elastic approximation [129], it has been pointed out later that this scattering can actually be highly inelastic because at high densities and temperatures the nucleons have non-negligible thermal velocities. This

process might thus play a key role in spectrum equilibration for heavy flavor neutrinos (ν_μ and ν_τ) [69].

Therefore in our studies we used an inelastic scattering kernel [69] :

$$R^{out}(\epsilon, \epsilon', \cos \Theta) = \frac{2G_F^2}{(2\pi)^2} S_x(q, \omega) \left\{ (h_V^x)^2 (1 + \cos \Theta) + (h_A^x)^2 (3 - \cos \Theta) \right\} \quad (5.12)$$

R^{out} is the outgoing scattering kernel, defined as in eq. (4.37).

In this expression $S(q, \omega)$ is the dynamic structure function, $\omega = \epsilon - \epsilon'$ is the energy transferred to the nucleon and $q = \sqrt{(\epsilon)^2 + (\epsilon')^2 - 2\epsilon\epsilon' \cos \Theta}$ is the momentum transferred to the nucleon.

The vector and axial coupling constants (h_V^x) and (h_A^x) (with $x = n$ or p) are given by

$$\begin{aligned} h_V^n &= -\frac{1}{2} & h_A^n &= -\frac{1}{2}g_A \\ h_V^p &= \frac{1}{2} - 2\sin^2 \theta_W & h_A^p &= \frac{1}{2}g_A \end{aligned} \quad (5.13)$$

Finally, the dynamic structure function is given by

$$\begin{aligned} S_x(q, \omega) &= \frac{2}{1 - e^{-\omega/T}} \frac{m_x^2 T}{2\pi q} \ln \left(\frac{1 + e^{-Q^2 + \eta_x}}{1 + e^{-Q^2 + \eta_x - \omega/T}} \right) \\ \text{with } Q &= \sqrt{\frac{m_x}{2T}} \left(-\frac{\omega}{q} + \frac{q}{2m_x} \right) \end{aligned} \quad (5.14)$$

where $\eta_x = \mu_x/T$ is the nucleon degeneracy factor and m_x is the nucleon mass (we use the values without mean field corrections).

This expression respects detailed balance (4.42) as we have $S_x(q, -\omega) = e^{-\omega/T} S_x(q, \omega)$.

For $\omega = 0$ (isoenergetic scattering) this expression becomes

$$S_x(q, \omega = 0) = 2 \frac{m_x^2 T}{2\pi q} \frac{e^{-Q^2 + \eta_x}}{1 + e^{-Q^2 + \eta_x}} \quad (5.15)$$

5.1.3 Pair production by nucleon-nucleon bremsstrahlung

Nucleon-nucleon bremsstrahlung is an important process as it is a major contribution to the production of heavy flavor neutrinos. Neutrino-antineutrino pairs of all flavors are produced by this flavor-independent process :

$$N + N \rightleftharpoons N + N + \nu + \bar{\nu}$$

In our studies we have used an analytic approximation for the absorption kernel developed in [70]. This computation relies on the *one pion exchange model* for the interaction with the spectator nucleon :

$$R^a(\epsilon, \epsilon', \cos \Theta) = \pi G_F^2 g_A^2 n_B S_\sigma(\epsilon + \epsilon') (3 - \cos \Theta) \quad (5.16)$$

R^a is the pair absorbtion kernel, defined as in eq. (4.62), n_B is the baryon density and S_σ is the *spin autocorrelation function*, given by the ansatz

$$S_\sigma(\omega) = \frac{\Gamma_\sigma}{\omega^2 + \Gamma^2/4} s\left(\frac{\omega}{T}\right) \quad (5.17)$$

which allows to include multiple scattering effects. In this formula Γ_σ is called the *spin fluctuation rate*, $s(\omega/T)$ is an analytic fit formula [70], while Γ is simply a normalization factor, which is computed such that S_σ obeys the normalization requirement shown in [130] :

$$\int_{-\infty}^{+\infty} \frac{d\omega}{2\pi} S_\sigma(\omega) = \frac{1}{n_n} \int \frac{2d^3p}{(2\pi)^3} f_p(1 - f_p) \quad (5.18)$$

where f_p is the occupation number of a neutron level with momentum p .

The factorisation between Γ_σ and s is choosen such that Γ_σ corresponds to the result of [131], where the pion mass m_π is neglected in the propagator and the nucleons are considered as non-degenerate. We have

$$\Gamma_\sigma = \frac{8\sqrt{2\pi}\alpha_\pi^2}{3\pi^2} \eta_*^{3/2} \frac{T^2}{m_N} \quad (5.19)$$

where $\alpha_\pi \approx (2m_N/m_\pi)^2/(4\pi) \approx 15.423\,65$ and η_* is an effective degeneracy parameter given by

$$\eta_* = \frac{1}{2m_N T} \left(3\pi^2 n_B \right)^{2/3} \quad (5.20)$$

Finally, the production part of the kernel R^p is computed by using the detailed balance condition (4.64).

This analytic fit reproduces numerical computations to within 10 % in the physically interesting parameter space [70], and the one-pion exchange model seems sufficient to describe the interaction in the context of proto-neutron stars, as recent simulations with improved rates tend to show [132].

For completeness, the analytic fit function $s(\omega/T)$ is given in the appendix A.

5.2 Neutrino interactions with nuclei

Interaction of neutrinos with nuclei are very similar to interactions with free nucleons : they can scatter via neutral current or be involved in charge exchange processes via charged currents.

5.2.1 Composition of the medium : nuclear distributions

During the core-collapse, as the density and temperature increase, the medium becomes a mixture of all possible nuclei in statistical equilibrium (or NSE, for *Nuclear Statistical Equilibrium*). The figure 5.1 shows an example of such a distribution.

It should be stressed that initially in the NSE approximation there are no interactions between the nuclei : the distribution is computed with a Saha-like equation. Therefore it is only valid if the interparticle separation between nuclei is large enough to neglect interactions (i.e. it is only valid at low densities, at the beginning of the collapse). Recent equations of state are using *extended* NSE models including interactions, see e.g. [133] and [134].

In the *Single Nucleus Approximation* (SNA) the distribution of nuclei is replaced by a single representative nucleus. The figure 5.1 shows that such an approximation is a considerable simplification of the complexity of the medium.

In the first supernova simulations, it was common to use an equation of state computed within the SNA approximation but to add the NSE distribution of nuclei to compute the weak processes during the collapse, see e.g. [136].

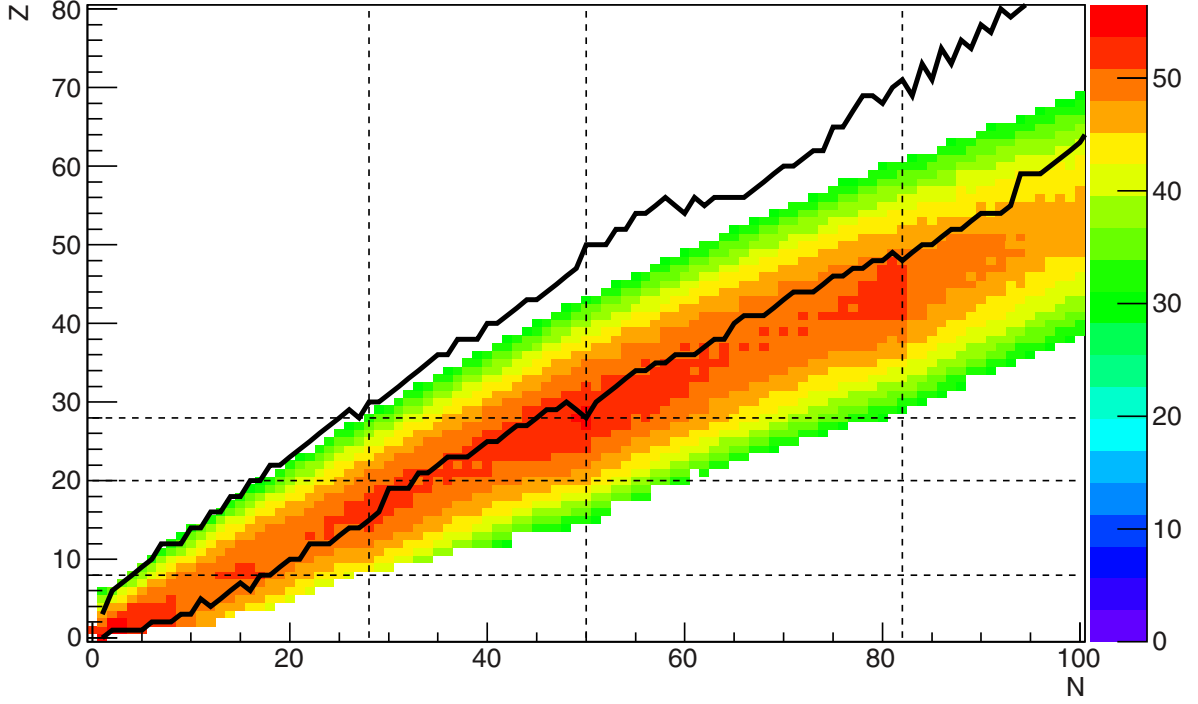


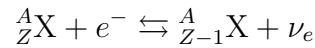
Figure 5.1: Typical nuclear abundance near the end of the collapse [135] (i.e. for a baryon density $n_B = 1.18 \times 10^{-3} \text{ fm}^{-3}$, a temperature $T = 2 \text{ MeV}$ and an electron fraction $Y_e = 0.275$), in arbitrary units. Solid lines mark boundaries of experimental mass measurements, dashed lines mark magic numbers

In particular, for some thermodynamic condition encountered during the collapse, the distribution of nuclei can be bimodal, centered around the two doubly magic¹ nuclei $^{78}_{28}\text{Ni}$ and $^{132}_{50}\text{Sn}$.

The core also becomes more and more neutron rich because of electron captures, such that near the end of the collapse the most abundant nuclei are far from the valley of stability, outside the boundaries of experimental mass measurements.

5.2.2 Electron captures on nuclei

Electron captures on nuclei play an important role during the infall phase of the supernova (see sec. 2.1.1), indeed about 40% of electrons of the iron-core are removed during this phase.



As explained in the previous section, two methods can be used to model the composition of the medium and obtain the neutrino emissivity j and inverse mean-free path $1/\lambda$ related to electron captures on nuclei :

- in the *Single Nucleus Approximation* (SNA), we consider that the medium is constituted of a single representative nucleus of mass number A_{SNA} and charge number Z_{SNA} and we

¹a magic nucleus has a closed nuclear shell of either protons or neutrons, and is thus particularly stable. The first magic numbers are 2,8,20,28,50,82. A doubly magic nucleus has a magic number of both protons and neutrons

have

$$j_{EC,\text{tot}}(\epsilon) = j_{EC}(\epsilon, A_{SNA}, Z_{SNA}) \quad (5.21)$$

- in a *Nuclear Statistical Equilibrium* model, we consider the full nuclei distribution as represented figure 5.1, and we have

$$j(\epsilon) = \sum_{\text{all nuclei}} j_{EC,\text{tot}}(\epsilon, A, Z) \quad (5.22)$$

Another important point is that as the most abundant nuclei can be outside the boundary of experimental mass measurements (see fig 5.1), the electron capture rates j_{EC} have to rely on theoretical models and physically motivated extrapolations.

The chapter 9 of this thesis is dedicated to the influence of the various approximations used to compute electron capture rates. The influence of the SNA approximation will also discussed in this chapter.

5.2.3 Scattering off nuclei

Neutrinos can scatter off nuclei via a flavor independent neutral current interaction :

$${}^A_Z\text{X} + \nu \rightleftharpoons {}^A_Z\text{X} + \nu$$

As in the case of electron capture, we have to either sum the opacities over all the distribution (NSE) or consider a representative nucleus (SNA).

We always consider that the scattering off nuclei is coherent and we describe the interaction with an isoenergetic opacity, defined as in eq. (4.56). The corresponding formula is given in [129]

$$\kappa^{IS}(\epsilon, \cos \Theta) = \frac{G_F^2}{2\pi} n(A, Z) (Zh_V^p + Nh_V^n)^2 \epsilon^2 (1 + \cos \Theta) e^{-y(1 - \cos \Theta)} \quad (5.23)$$

where $n(A, Z)$ is the density of the nucleus ${}^A_Z\text{X}$ and the vector coupling constants of nucleons to the neutral current h_V^p and h_V^n are given by eq. (5.13).

The exponential $e^{-y(1 - \cos \Theta)}$ arises from nuclear structure, y is given by :

$$y = \frac{2}{5} \epsilon^2 (1.07A)^{2/3} (\text{fm}^2) \quad (5.24)$$

The corresponding transport opacity (defined as in eq. (4.61)) is given by

$$\kappa_{tr}^{IS} = \int (1 - \cos \Theta) \kappa^{IS} \sin(\Theta) d\Theta = \frac{G_F^2}{2\pi} n(A, Z) (Zh_V^p + Nh_V^n)^2 \epsilon^2 \frac{y - 1 + (1 + y) e^{-2y}}{y^3} \quad (5.25)$$

At low neutrino energies, this interaction is screened by the fact that ions form a lattice, and therefore the corresponding opacity is reduced. The opacity formula becomes (see [137])

$$\kappa^{IS}(\epsilon, \cos \Theta) = \frac{G_F^2}{2\pi} n(A, Z) (Zh_V^p + Nh_V^n)^2 \epsilon^2 (1 + \cos \Theta) e^{-y(1 - \cos \Theta)} S_{\text{ion}}(\epsilon, \cos \Theta) \quad (5.26)$$

where $S_{\text{ion}}(\epsilon, \cos \Theta)$ is the *dynamic structure function*, sometimes also called the *dynamic form factor*.

In [138] the author provides an analytic fit of an angular average $\langle S(\epsilon) \rangle_{\text{ion}}$ to model this phenomenon :

$$\langle S(\epsilon) \rangle_{\text{ion}} = \frac{3}{4} \int (1 + \cos \Theta)(1 - \cos \Theta) S_{\text{ion}}(\epsilon, \cos \Theta) \sin \Theta d\Theta \quad (5.27)$$

The fit formula for $\langle S(\epsilon) \rangle_{\text{ion}}$ provided in [138] is based on Monte-Carlo simulations of the ion lattice in order to obtain the pair correlation function. For completeness, it is provided in the appendix B.

This angular average is appropriate for the computation of the transport opacity while neglecting the nuclear form factor. In our simulations we will make the same assumption as in [139] and we simply multiply the transport opacity of eq. (5.25) by the angular averaged factor $\langle S(\epsilon) \rangle_{\text{ion}}$.

5.3 Neutrino interactions with charged leptons

Heavy flavors neutrinos ν_μ , $\bar{\nu}_\mu$, ν_τ and $\bar{\nu}_\tau$ interact with electrons and positrons via the neutral current, whereas ν_e and $\bar{\nu}_e$ interact with them via both charged and neutral currents.

Two interactions are possible : the scattering off charged leptons and the electron-positron annihilation into a neutrino pair.

5.3.1 Scattering off charged leptons

Neutrino scattering off electrons and positrons is a relevant process as it can become more important than scattering on free nucleons for the thermalization at lower densities (the scattering on nucleons tends to become elastic at lower densities).

$$\nu + e^\pm \rightleftharpoons \nu + e^\pm$$

We have used the Legendre expansion of the outgoing kernel (4.43) obtained in [140] using the ultra relativistic limit. They write the kernel as a sum of three terms and neglect the third, which is proportional to m_e^2 .

$$R_l^{\text{out}}(\epsilon, \epsilon') = \alpha_I A_l^I(\epsilon, \epsilon') + \alpha_{II} A_l^{II}(\epsilon, \epsilon') \quad (5.28)$$

α_I and α_{II} are some coupling coefficients, which depend upon the nature of the particles involved. They are summarized in table 5.1. A^I and A^{II} are functions independent of the nature of the particles involved, they are given by an integral over the electron (or positron) energies :

$$A_l^k(\epsilon, \epsilon') = \frac{4G_F^2}{(hc)^3} \frac{1}{(\epsilon)^2(\epsilon')^2} \int_{\max(0, \epsilon' - \epsilon)}^{\infty} dE f_{FD}(E \pm \mu_e)(1 - f_{FD}(E + \epsilon - \epsilon' \pm \mu_e)) H_l^k(\epsilon, \epsilon', E) \quad (5.29)$$

The functions H_l^k are given in [140] and, for completeness, in the appendix C of this thesis.

Note that in order to reduce *on-the-fly* computations, the functions A_l^I and A_l^{II} can be precomputed in three-dimensional tables. The procedure is detailed in the appendix E.

Interaction	α_I	α_{II}
ν_e/e^-	$(1 + 2 \sin^2 \theta_W)^2$	$(2 \sin^2 \theta_W)^2$
ν_x/e^-	$(1 - 2 \sin^2 \theta_W)^2$	$(2 \sin^2 \theta_W)^2$
$\bar{\nu}_e/e^-$	$(2 \sin^2 \theta_W)^2$	$(1 + 2 \sin^2 \theta_W)^2$
$\bar{\nu}_x/e^-$	$(2 \sin^2 \theta_W)^2$	$(1 - 2 \sin^2 \theta_W)^2$
ν_e/e^+	$(2 \sin^2 \theta_W)^2$	$(1 + 2 \sin^2 \theta_W)^2$
ν_x/e^+	$(2 \sin^2 \theta_W)^2$	$(1 - 2 \sin^2 \theta_W)^2$
$\bar{\nu}_e/e^+$	$(1 + 2 \sin^2 \theta_W)^2$	$(2 \sin^2 \theta_W)^2$
$\bar{\nu}_x/e^+$	$(1 - 2 \sin^2 \theta_W)^2$	$(2 \sin^2 \theta_W)^2$

Table 5.1: Coupling coefficients for neutrino scattering off electrons and positrons [119]

5.3.2 Pair production by electron-positron annihilation

This is (along with nucleon-nucleon bremsstrahlung) another process responsible for the creation of heavy flavor neutrino pairs

$$e^- + e^+ \rightleftharpoons \nu + \bar{\nu}$$

We used the Legendre expansion of the production kernel (4.65) obtained in [129] using the ultra relativistic limit :

$$R_l^p(\epsilon, \epsilon') = \beta_I B_l^I(\epsilon, \epsilon') + \beta_{II} B_l^{II}(\epsilon, \epsilon') \quad (5.30)$$

The coupling constants β_I and β_{II} are given in the table 5.2. Note that they are given with the neutrinos (ν_e, ν_x) point of view. In order to obtain the kernel of antineutrinos ($\bar{\nu}_e, \bar{\nu}_x$), one should exchange the coefficients $\beta_I \leftrightarrow \beta_{II}$.

Interaction	β_I	β_{II}
$e^- + e^+ \rightleftharpoons \nu_e + \bar{\nu}_e$	$(1 + 2 \sin^2 \theta_W)^2$	$(2 \sin^2 \theta_W)^2$
$e^- + e^+ \rightleftharpoons \nu_x + \bar{\nu}_x$	$(1 - 2 \sin^2 \theta_W)^2$	$(2 \sin^2 \theta_W)^2$

Table 5.2: Coupling coefficients for electron-positron pair process

B^I and B^{II} are functions independent of the neutrino type, they are given by the integrals

$$B_l^k(\epsilon, \epsilon') = \frac{4G_F^2}{(hc)^3} \int_0^{\epsilon+\epsilon'} dE f_{FD}(E - \mu_e) f_{FD}(\epsilon + \epsilon' - E + \mu_e) J_l^k(\epsilon, \epsilon', E) \quad (5.31)$$

where the functions J_l^k are given in [129]. We also have the relation $B_l^I(\epsilon', \epsilon) = B_l^{II}(\epsilon, \epsilon')$, which results from particle exchange symmetry.

For completeness, the functions J_l^k are also provided in the appendix D.

As in the case of scattering processes, the functions B_l^I and B_l^{II} can be precomputed in three-dimensional tables, see the appendix E for the details.

5.4 Other relevant processes

In this section we discuss some other relevant microphysical processes involving neutrinos in dense environments, but which we did not take into account in our models, either because detailed interaction rates are unavailable or because of the considerable difficulty of their implementation.

5.4.1 Plasma and Photo emission processes

Among the weak processes occurring in a plasma, we took only into account the interactions of neutrinos with charged leptons (see sec. 5.3), but several other mechanisms of emission of neutrino pairs exist.

Because of interactions with e^-/e^+ pairs in a plasma, the photon γ acquires an effective mass, and can therefore decay into neutrino-antineutrino pairs via both charged and neutral current interactions [141]. This process is called the *plasma neutrino emissivity* :

$$\tilde{\gamma} \rightleftharpoons \nu + \bar{\nu}$$

The distinction can be made between the *transverse plasma emissivity*, caused by the decay of massive photons, and the *longitudinal plasma emissivity*, caused by the decay of collective plasma oscillations (i.e. plasmons). In [142], the authors proposed a generic framework to compute the Boltzmann collision integral for this process at all temperatures and densities.

Another process related to the interactions of charged leptons with the photon background can lead to the production of neutrino pairs via both charged and neutral currents [71] :

$$\gamma + e^\pm \rightleftharpoons e^\pm + \nu + \bar{\nu}$$

this process is called the *neutrino photo emissivity*. The computation of its emissivity is much more complicated than in the case of the pair and plasma processes (see [71] for the details).

In [71], the authors compute the neutrino emissivities due to the pair, plasma and photo processes at various temperature and densities. According to their results, the photo emissivity seems to never be the dominant process in the conditions encountered in CCSN and proto-neutron star evolution. But the plasma emissivity could be more important than the pair process at high densities.

5.4.2 Neutrino-neutrino interactions

With the dense and hot early universe, core-collapse supernova and proto-neutron stars are perhaps the only environments where neutrino-neutrino interactions can be probed because of their significant role.

But as they heavily couple the various neutrino flavors, it is difficult to take these processes into account in a stationary transport scheme.

Among neutrino-neutrino interactions, the pair annihilation of electron neutrinos into heavy neutrino pairs

$$\nu_e + \bar{\nu}_e \rightleftharpoons \nu_x + \bar{\nu}_x$$

plays a significant role in the creation of heavy neutrinos [143]. It is more important than electron-positron annihilation and can even compete with nucleon-nucleon bremsstrahlung in some thermodynamic conditions.

Neutrino-neutrino scattering

$$\nu_e + \nu_x \rightleftharpoons \nu_e + \nu_x$$

has also been considered in some studies [143], but has been found to have a less significant effect on the neutrino spectra than neutrino-electron scattering.

5.4.3 Neutrino flavor evolution

The observation of the fluxes of solar neutrinos in the mid-60s lead to a considerable discrepancy between observations and the predictions of the standard solar model. This problem is known as the *solar neutrino problem*.

A part of the solution is provided by the fact that neutrino flavors *oscillate* in vacuum. This idea was proposed before the discovery of the solar neutrino problem by Pontecorvo in 1958 [144] : if the flavor eigenstates of neutrinos $\{|\nu_e\rangle, |\nu_\mu\rangle, |\nu_\tau\rangle\}$ are not mass eigenstates $\{|\nu_1\rangle, |\nu_2\rangle, |\nu_3\rangle\}$, then the flavor of a neutrino can change during its propagation. The corresponding change of basis matrix is called the PMNS matrix².

This hypothesis was confirmed by the observation of atmospheric neutrinos by Super-Kamiokande in 1999 [145], but is not sufficient to explain the solar neutrino problem. Indeed because of the interaction of neutrinos with electrons in the sun, the oscillation phenomenon is strongly modified. This phenomenon is called the MSW effect³ [146] [147], and is the final piece needed to solve the solar neutrino problem. It can cause fast resonant flavor conversion of neutrinos.

Because of the MSW effect and the complex way it affects neutrino flavor conversions, in dense matter we prefer to use the term *neutrino flavor evolution* instead of neutrino oscillations.

Because core-collapse supernova and proto-neutron stars are subject to many neutrino interactions, the MSW effect is expected to play an important role in the neutrino transport, with the occurrence of fast neutrino flavor conversions, see e.g. [148]. This can have a significant effect on the neutrino spectra, and consequently on the neutrino driven wind nucleosynthesis and the shock revival.

Neutrino flavor evolution can be taken into account in the Boltzmann equation, with the formalism detailed in [149], but at the expense of a considerable complexification of the algorithm. Which is why, to our knowledge, there exists as of today no CCSN simulation using a self-consistent neutrino transport with flavor evolution.

Nevertheless, neutrino flavor evolution is not expected to have an effect in areas where neutrinos are trapped, because if neutrinos are heavily interacting, then the eigenstates of the Hamiltonian will approximately be given by the flavor eigenstates.

²for Pontecorvo–Maki–Nakagawa–Sakata

³for Mikheyev–Smirnov–Wolfenstein

Part III

Proto-neutron star evolution

Chapter 6

Quasi-static modeling of proto-neutron stars

In this chapter we motivate the quasi-static approximation for proto-neutron star evolution in spherical symmetry and describe its implementation in an evolution algorithm [150].

6.1 The quasi-static approximation

6.1.1 Motivation : PNS evolution timescales

What makes stellar evolution a difficult problem is the tremendous difference between the relevant timescales : nuclear burning takes place over secular times while structural adjustments and convection have a timescale ranging from one minute to several hours.

Therefore one of the most important issues in stellar modeling is to find a consistent way of averaging the short timescale effects over secular times.

The formation and initial cooling of a neutron star lasts less than 10 minutes, but despite this very short timescale we are facing very similar issues as in main sequence stellar modeling.

Indeed, due to the densities encountered in neutron stars, the speed of sound is close to the speed of light in the denser areas (see, e.g. [151]), which makes the acoustic timescale extremely small :

$$t_{\text{ac}} = \frac{l}{c_{\text{sound}}} = \left(\frac{l}{0.1 \text{ km}} \right) \left(\frac{c_{\text{sound}}}{10^8 \text{ m s}^{-1}} \right)^{-1} \times 1 \mu\text{s} \quad (6.1)$$

where l is a typical length of the neutron star stellar structure¹.

For the problem of neutron star formation, the other relevant timescales are the convection timescale, the rotation frequency, the deleptonization timescale and the Kelvin-Helmholtz timescale.

An estimate for the deleptonization timescale is

$$t_{\text{delep}} = \frac{Y_e N_B}{L_\nu^{(n)}} \approx \left(\frac{Y_e}{0.2} \right) \left(\frac{M_B}{1.6 M_\odot} \right) \left(\frac{L_\nu^{(n)}}{10^{55} \text{ s}^{-1}} \right)^{-1} \times 40 \text{ s} \quad (6.2)$$

Where N_B is the total baryon number, Y_e is the average electron fraction, $M_B = m_n N_B$ is the total baryon mass and $L_\nu^{(n)}$ the total neutrino number-luminosity.

¹i.e. the order of magnitude of spatial discretization needed in a numerical description

And an estimate for the Kelvin-Helmholtz timescale is

$$t_{\text{KH}} = \frac{GM^2}{RL_\nu^{(e)}} \approx \left(\frac{M}{1.6 \text{ M}_\odot} \right)^2 \left(\frac{R}{10 \text{ km}} \right)^{-1} \left(\frac{L_\nu^{(\mathcal{E})}}{10^{52} \text{ erg s}^{-1}} \right)^{-1} \times 70 \text{ s} \quad (6.3)$$

Where $L_\nu^{(e)}$ is the total neutrino energy-luminosity, M the (gravitational) mass of the neutron star and R its radius.

Thus we see that we are also facing long term evolution timescales which differ by several orders of magnitude from the acoustic timescale and that related to structural adjustments.

6.1.2 Hydrostatic stellar structure : the TOV equations

In order to perform without being limited by the timescales discussed above, we use the quasi-static approximation, in which we consider that the star is in hydrostatic equilibrium. Therefore we neglect the time derivatives of the density, the pressure and the metric, which allows to average hydrodynamic effects occurring on the acoustic effect and to focus on the evolution over the Kelvin-Helmholtz timescale.

As we consider a stationary and spherically symmetric spacetime, with the Schwarzschild gauge, the metric used is the same as in eq. (4.10).

Our last approximation, widely used in core-collapse simulations, is that the stress-energy tensor of the matter is given by the perfect fluid formula $T_{ab} = (\mathcal{E} + P)u_a u_b + P g_{ab}$, where \mathcal{E} is the energy density, P the pressure, u^a the four-velocity and g_{ab} is the metric tensor. The only exception is the neutrino part of the tensor (c.f. eq. (6.12)), which is computed via a neutrino transport scheme.

Within these approximations, Einstein Field equations (9.11) are equivalent to the following system :

$$\psi(r) = \left(1 - \frac{2Gm(r)}{rc^2} \right)^{-1/2} \quad (6.4)$$

$$\frac{dm}{dr} = 4\pi r^2 \frac{\mathcal{E}}{c^2} \quad (6.5)$$

$$g(r) = c^2 \frac{d \ln \alpha}{dr} = \psi^2 G \left(\frac{m}{r^2} + 4\pi r \frac{p}{c^2} \right) \quad (6.6)$$

Where $g(r)$ is the local gravitational acceleration and $m(r)$ is a metric potential corresponding to the enclosed mass in the Newtonian limit, which is obtained by taking $\psi = 1$, $\mathcal{E} \approx \rho c^2$ and $p \ll \mathcal{E}$ (where ρ is the mass density).

Outside the star (i.e. for $r \geq R$ where R is the radius of the star) the metric is simply given by the Schwarzschild solution :

$$\alpha(r) = \frac{1}{\psi(r)} = \left(1 - \frac{2GM}{rc^2} \right) \quad (6.7)$$

where $M = m(R)$ is the *total gravitational mass* of the proto-neutron star.

This system is completed by the *hydrostatic equation*, which stems from the radial projection of the stress-energy conservation equation (9.14) :

$$\frac{dP}{dr} = -(\mathcal{E} + P) \frac{g(r)}{c^2} \quad (6.8)$$

the boundary condition used here is $P(R) = P_{\text{surf}}$ where P_{surf} is the *surface pressure*. To model cold catalyzed neutron stars we usually set $P_{\text{surf}} = 0$, but in the case of proto-neutron stars this

can cause some difficulties at the beginning of the simulation. Indeed due to the high entropy in the mantle, the associated gradient of density is very low, and the surface of the PNS can prove difficult to properly define. The choice of P_{surf} is arbitrary and has a significant effect on the mantle during the first few milliseconds of the simulation, but a sufficiently low value proves to have no influence on the evolution of the internal structure on long timescales.

Note that this description is equivalent to the TOV equations (1.7) and (1.8) presented in the chapter 1.

Finally, this system of equations is closed by a hot equation of state from the **CompOSE** database [51], and by the fact that the total Baryon number N_B should be conserved during the evolution

$$N_B = 4\pi \int_0^R r^2 \psi n_B dr = \text{cte} \quad (6.9)$$

Note that it is common to use the Baryon mass M_B instead of the total baryon number, defined as $M_B = m_N N_B$.

One final remark should be done about our approximation : we have neglected the effect of the neutrino energy density in the computation of the metric, and the dynamical effect that neutrinos can have on the pressure. Indeed the energy density of neutrinos is relevant only in the central area of the PNS in the case of electron neutrinos, and their contribution is of roughly 1 %, but neglecting their contribution allows for a considerable simplification of the algorithm.

6.1.3 Quasi-static evolution equations

Despite the fact that the structure is computed with a static approximation, we do not neglect the time variation of the electron fraction Y_e and of the entropy per baryon s , which result from weak processes with a longer timescale. The method and the formalism is the same as in Pons et al. [92].

The lepton number conservation law (9.13) yields

$$\nabla_a(u^a n_B Y_e) + \nabla_a(N_{\nu_e}^a) - \nabla_a(N_{\bar{\nu}_e}^a) = 0 \quad (6.10)$$

where $u^a = \frac{1}{\alpha}(\partial_t)^a$ is the fluid four-velocity and $N_{\nu_e}^a$, $N_{\bar{\nu}_e}^a$ are respectively the electron neutrino and antineutrino particle current densities.

By using the conservation of baryon number $\nabla_a(u^a n_B) = 0$ we obtain

$$\frac{1}{\alpha} \frac{DY_e}{Dt} = \frac{\Gamma_{\bar{\nu}_e} - \Gamma_{\nu_e}}{n_B} \quad (6.11)$$

where $\frac{D}{Dt} = c\alpha u^a \nabla_a$ is the Lagrangian derivative and Γ_{ν_e} , $\Gamma_{\bar{\nu}_e}$ are respectively the electron neutrino and antineutrino local production rates, introduced in the equation (4.23).

Now regarding the energy conservation, we have

$$u_b \nabla_a (T^{ab} + T_{\nu_e}^{ab} + T_{\bar{\nu}_e}^{ab} + 4T_{\nu_x}^{ab}) = 0 \quad (6.12)$$

By considering that the stress-energy tensor of the neutron star matter is given by the perfect fluid formula $T_{ab} = (\mathcal{E} + P)u_a u_b + P g_{ab}$, we can rewrite this equation as

$$\frac{1}{\alpha} \frac{D}{Dt} \left(\frac{\mathcal{E}}{n_B} \right) + \frac{P}{\alpha} \frac{D}{Dt} \left(\frac{1}{n_B} \right) = - \frac{(Q_{\nu_e} + Q_{\bar{\nu}_e} + 4Q_{\nu_x})}{n_B} \quad (6.13)$$

where the Q_ν are the neutrino heating functions introduced in the equation (4.27).

Finally, by using the first law of therodynamics $d(\mathcal{E}/n_B) = -Pd(1/n_B) + Tds + \mu_e d(Y_e)$ we obtain the local conservation law of entropy

$$\frac{1}{\alpha} \frac{Ds}{Dt} = -\frac{(Q_{\nu_e} + Q_{\bar{\nu}_e} + 4Q_{\nu_x})}{Tn_B} + \frac{\mu_e (\Gamma_{\nu_e} - \Gamma_{\bar{\nu}_e})}{Tn_B} \quad (6.14)$$

where μ_e is the chemical potential of electrons, s is the entropy per baryon and T is the temperature.

In particular, we recover our hypothesis that neutrinos are the only particles responsible of transport phenomena : in the absence of neutrinos all processes are adiabatic ($Ds/Dt = 0$).

6.1.4 Summary of the algorithm

The full numerical implementation of the algorithm is detailed in appendix G.

The different steps followed during a single timestep are summarised as follows :

1. solve the structure equations (G.8), (G.13), (G.14), (G.15) and (G.16) to obtain the structure of the star
2. compute the lapse function using equation (G.17)
3. compute the neutrino source terms Γ_ν and Q_ν using the neutrino transport scheme
4. compute the new Y_e and s profiles by using evolution equations (G.10) and (G.12)
5. restart at step 1.

The figure 6.1 gives a schematic representation of this algorithm.

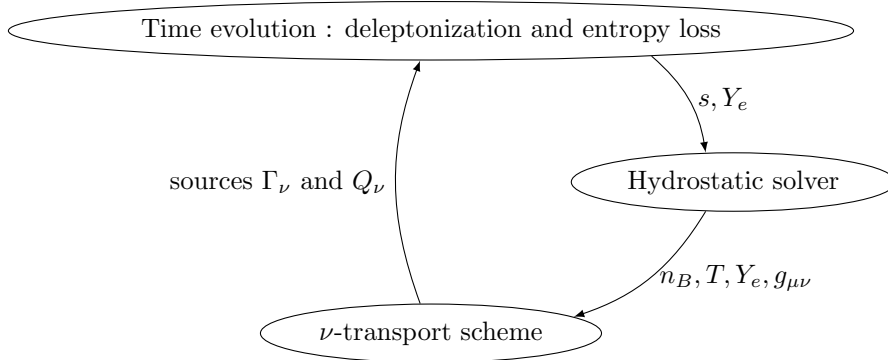


Figure 6.1: Schematic representation of the algorithm

6.2 Example of simulation

In this section we present, as an example, the result of a PNS simulation realised with the algorithm presented earlier in this chapter.

The initial data have been computed with the CoCoNuT code, with a similar setup as the one used in chapters 9 and 10 : we use the s15 progenitor from [152] (15 M_\odot with solar metallicity) and the RG(SLy4) equation of state [134]. The neutrino interactions are computed as in the chapter 10, with the MF prescription for charged currents on nucleons (see sec. 10.1.3). The simulation is stopped about 500 ms after bounce, when the shock is stalled.

The method is then similar to the one used in previous works [92], [93] : all matter beyond the shock is removed to simulate an explosion and we keep the electron fraction and entropy profiles. We obtain a baryon mass $M_B = 1.61 M_\odot$. Our initial profiles are given in the figure 6.5, they correspond to the $t = 0$ plots.

The simulations run up to $t = 67$ s at which point the outer layers start to become semi-transparent. Time t is counted from the start of the simulation, which uses initial data from about ~ 500 ms after bounce.

6.2.1 Evolution of global properties of the PNS

First let's have a look at the evolution of some global properties of the proto-neutron star, such as it's radius, mass, electron number and entropy.

The figure 6.2 shows the evolution of the gravitational mass $M = m(R)$ and of the radius R of the proto-neutron star.

The gravitational mass represents the total energy present in the PNS (internal energy minus gravitational binding), and diminishes as the PNS emits neutrinos.

We can distinguish two phases in the evolution

- during the first few seconds of evolution, the mantle of the PNS contracts rapidly and the radius diminishes to less than 20 km
- this initial contraction phase is followed by the *shallow phase*, during which the mass decay is approximately exponential by emission of neutrinos, while the star contracts more slowly. This phase can be modeled by the *Kelvin-Helmholtz mechanism*

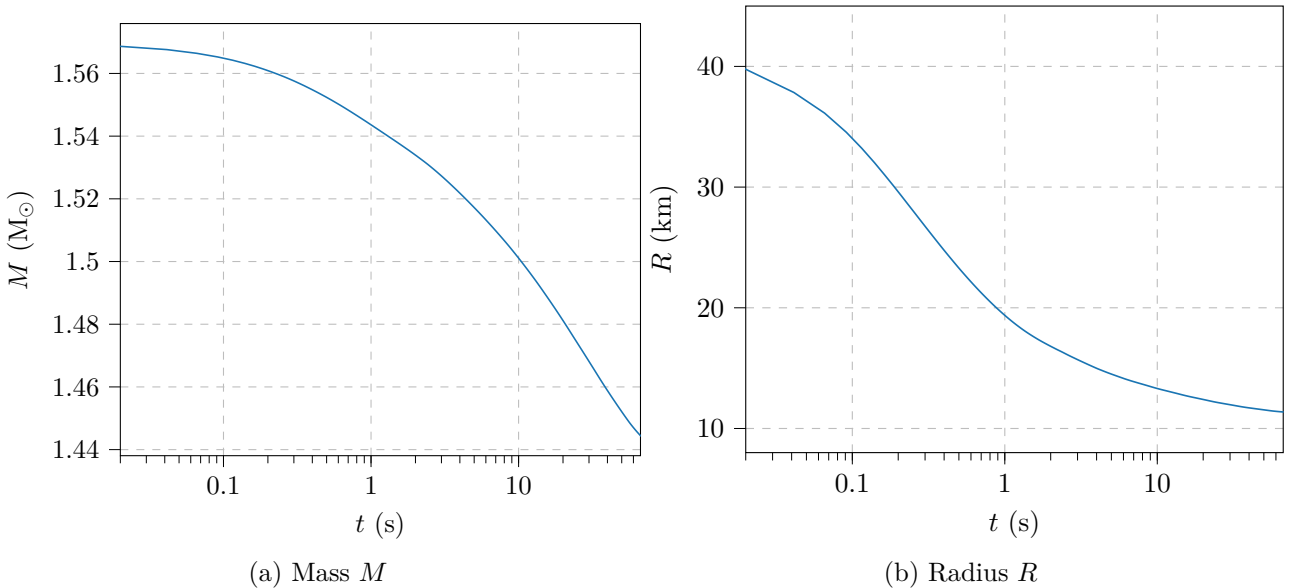


Figure 6.2: Evolution of the mass M and the radius R of the proto-neutron star, as a function of time, in our fiducial simulation.

It should be stressed that the definition of the radius depends on the value of the pressure P_{surf} used to integrate eq. (6.8). We found that during the first phase (the fast contraction of the mantle), the value of the radius strongly depends on this choice if the chosen value of P_{surf} is too high (because we do not take into account the outer layers of the PNS). The table 6.1 gives the values of the radius for different choices of P_{surf} , in our fiducial simulation, for the initial

model (as it is the most sensitive to this choice). But after this initial contraction, this choice

Surface pressure P_{surf} (MeV fm $^{-3}$)	10^{-9}	10^{-8}	10^{-7}	10^{-6}	10^{-5}	10^{-4}
Radius R (km)	73	73	73	70	60	48

Table 6.1: Values of the radius for different choices of P_{surf} , in our fiducial simulation, for the initial model

does not have a significant influence as long as the value of P_{surf} is low enough (i.e. less than about 10^{-5} MeV fm $^{-3}$).

The evolution of the mean entropy and electron fraction of the PNS is shown on the figure 6.3.

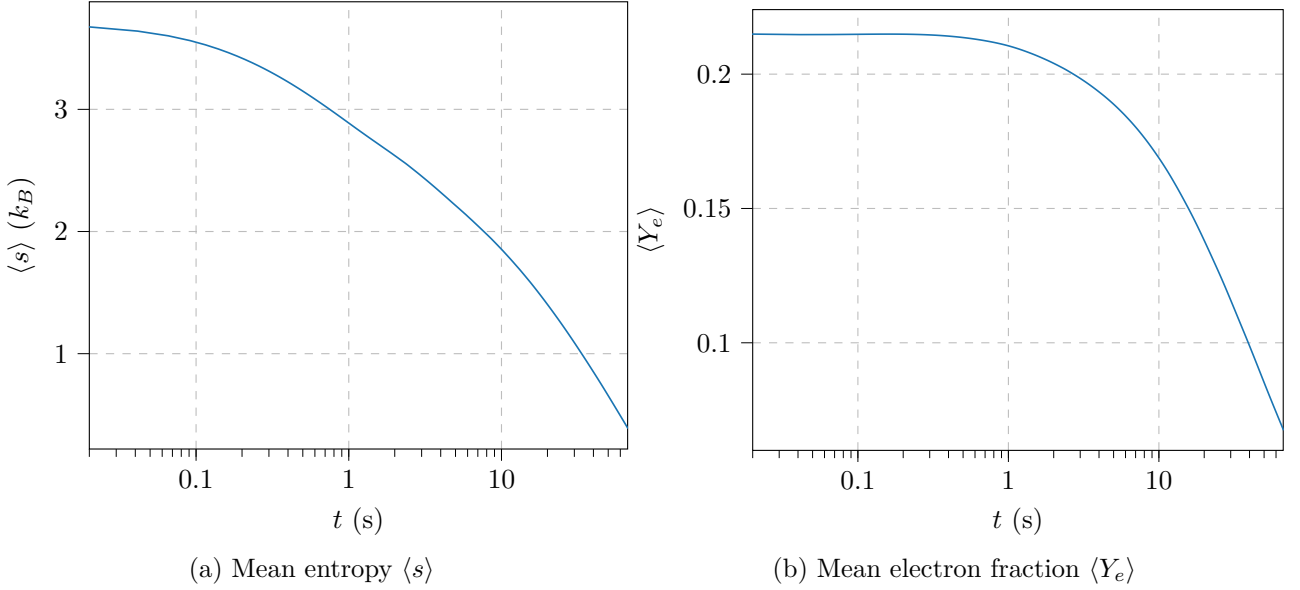


Figure 6.3: Evolution of the mean entropy per baryon $\langle s \rangle$ and the mean electron fraction $\langle Y_e \rangle$ of the proto-neutron star, as a function of time, in our fiducial simulation.

For better readability we show the mean values of the entropy par baryon $\langle s \rangle$ and the electron fraction $\langle Y_e \rangle$, defined as

$$\langle s \rangle = \frac{1}{N_B} 4\pi \int_0^R r^2 \psi n_B s dr \quad , \quad \langle Y_e \rangle = \frac{1}{N_B} 4\pi \int_0^R r^2 \psi n_B Y_e dr \quad (6.15)$$

but this figure can be understood as the evolution of total values, since $S = N_B \langle s \rangle$ is the total entropy and $N_e = N_B \langle Y_e \rangle$ is the total electron number.

We observe that half the loss of entropy happens during the first 10 s, while the deleptonization happens mostly during the shallow decay phase. Indeed, as we shall see below, in our model the PNS mantle is already extremely poor in electrons at the beginning of the simulation.

6.2.2 Structure of the PNS

Now let us have a look at the evolution of the internal structure of the proto-neutron star. The figure 6.5 shows the radial profile of several relevant thermodynamic quantities, as a function of the enclosed baryon mass $m_B = m_N a(r)$, at different times.

The initial profiles obtained with the CoCoNuT code as explained earlier in this section correspond to the $t = 0$ s case. We clearly see a structure similar to what was discussed in section 3.1.1, with a low entropy, lepton rich core and a high entropy, lepton poor mantle.

Regarding the evolution of temperature, we see that during the first phase of evolution it is mostly rising in the star, hence the name proto-neutron star *cooling* might not be the most adapted for the first phase of proto-neutron star evolution. This heating of the PNS is caused by two phenomena :

- the fast initial contraction of the mantle of the proto-neutron star generates a lot of heat because of the sudden compression of the matter
- the positive temperature gradient induces a net flux of $\bar{\nu}_e$ and ν_x into the core (but not of ν_e , as we shall explain below), which contributes to the core heating. This phenomena has been referred to as *Joule Heating* in previous works [92], [93]

The evolution of entropy is similar, the mantle constantly loses entropy because of neutrino emission and the core is (at first) gaining entropy because of *Joule Heating*. An interesting point to discuss is the evolution of the entropy gradient : at the beginning of the simulation it is negative in the mantle, making it unstable to convection (see sec. 3.1.4 and chapter 8), and as the *Joule Heating* of the core proceeds this negative entropy gradient progressively generalizes to the whole star, making it fully unstable to convection.

Now concerning lepton transport, during the first part of the evolution the mantle does not evolve much, actually the most important is the transport of electron neutrinos leaving the core because of the strong gradient of neutrino chemical potential μ_{ν_e} at the core boundary, as shown in fig. (6.4) for the initial model conditions. Therefore the electron fraction in the core is diminishing while it is increasing outside the core. It should also be stressed that because of the gradient of chemical potential, electron neutrinos do not behave like other flavors, which have a net flux going into the core, as explained above.

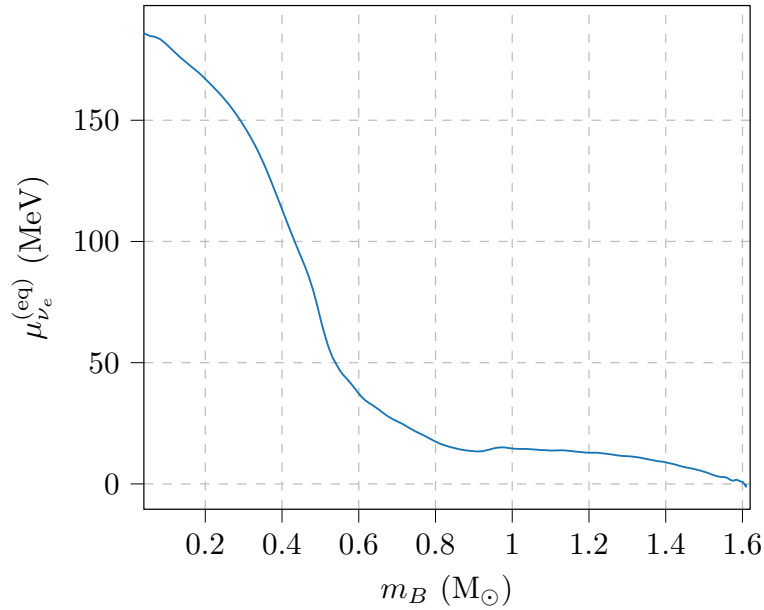


Figure 6.4: Profile of the electron neutrino equilibrium chemical potential, in our initial model.

Finally, regarding the evolution of the pressure P and of the baryon density n_B , both are progressively increasing during the evolution, as the star becomes more and more compact. As explained earlier, the gradient of baryon density in the mantle is very small at the beginning of the simulation, and the radius of the PNS is hard to define. But as the evolution proceeds, the density gradient at the surface becomes very high and the ambiguity in the definition of the radius become less and less relevant.

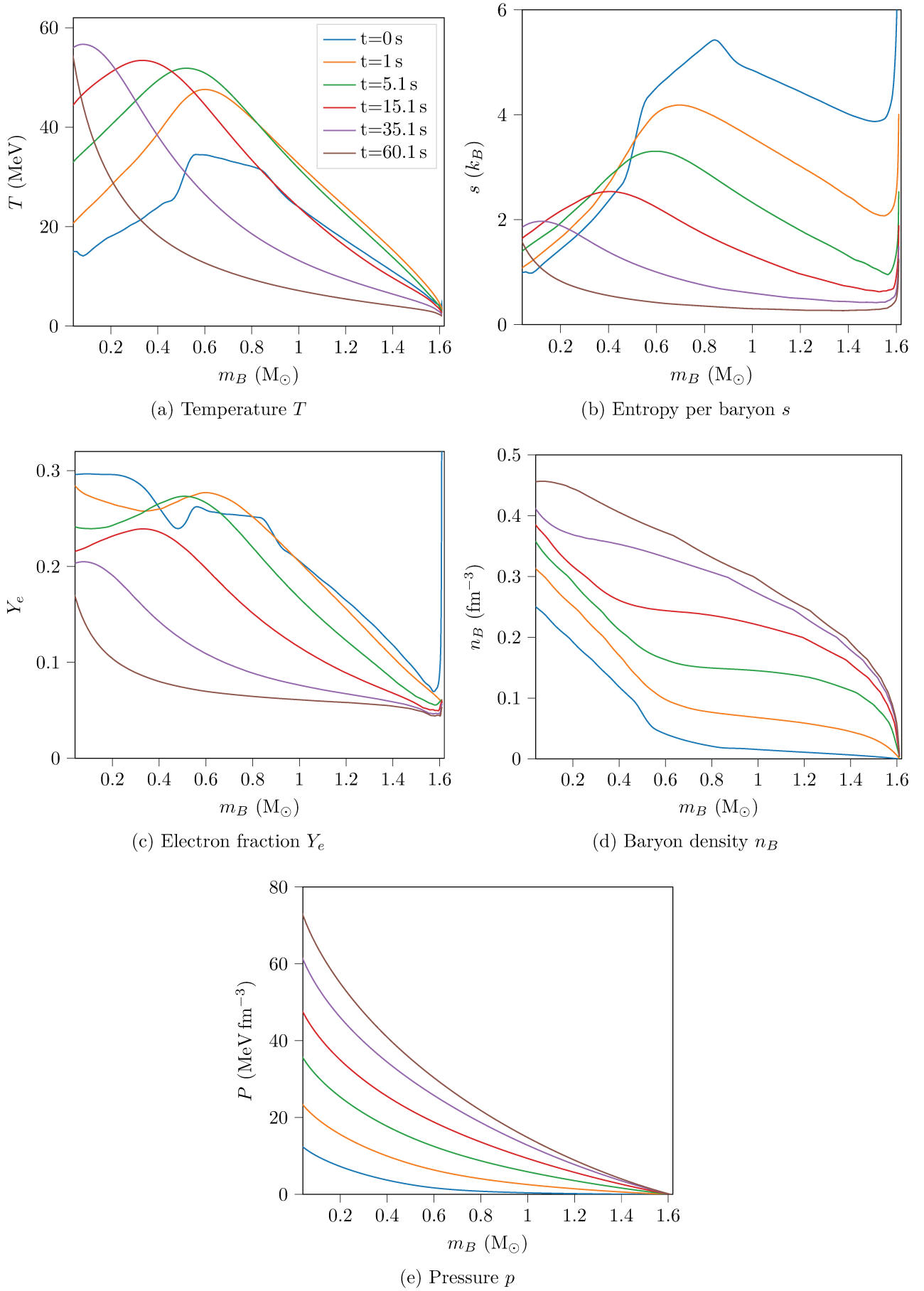


Figure 6.5: Internal structure of the PNS at selected times in our fiducial simulation. Various relevant thermodynamic quantities are plotted at different evolution times, as functions of the enclosed baryonic mass $m_B(r) = m_N a(r)$ (where $a(r)$ is defined as in eq. (G.1)).

6.2.3 Neutrino emission from the PNS

The fast multigroup transport employed in the evolution allows us to make predictions for the neutrino emission from the proto-neutron star.

An interesting quantity to compute is the neutrino energy luminosity $L_\nu^{(\mathcal{E})}$, defined in eq. (4.29), which represents the total energy loss rate of the proto-neutron star. The total neutrino energy luminosity $L_{\text{tot}}^{(\mathcal{E})}$ is the sum over all six flavors :

$$L_{\text{tot}}^{(\mathcal{E})} = L_{\nu_e}^{(\mathcal{E})} + L_{\bar{\nu}_e}^{(\mathcal{E})} + 4L_{\nu_x}^{(\mathcal{E})} \quad (6.16)$$

It is worth mentioning that eq. 4.29 corresponds to the redshifted luminosities (i.e. the luminosities as measured far away from the PNS gravitational influence).

The figure 6.6 represents the energy luminosity of all neutrino flavors, as well as the total luminosity, as a function of time.

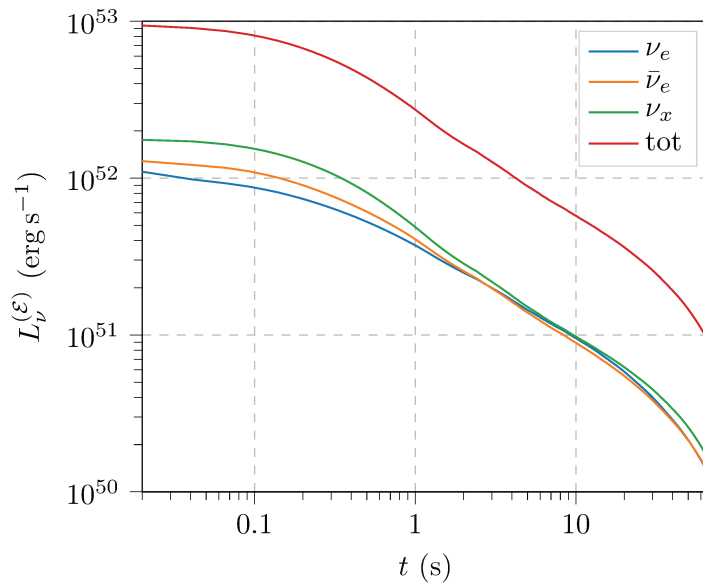


Figure 6.6: Neutrino energy luminosities (as defined in eq. (4.29)) as a function of time, in our fiducial simulation. The luminosities of three neutrino types are represented, as well as the total luminosity (sum of six flavors).

We clearly see that after an initial phase the luminosity decays exponentially. Regarding the relative value of the luminosities, at the beginning of the simulation we have $L_{\nu_e}^{(\mathcal{E})} < L_{\bar{\nu}_e}^{(\mathcal{E})} < L_{\nu_x}^{(\mathcal{E})}$. This ordering is related to the discussion done in section 2.2.4 about the neutrinosphere radii : as we usually have $R_{\nu_x} < R_{\bar{\nu}_e} < R_{\nu_e}$, neutrinos ν_x comes from deeper and hotter regions of the PNS, therefore they are emitted at higher energies and are more numerous, as we shall see in the two next figures.

The number luminosity of neutrinos $L_\nu^{(n)}$, defined in eq. (4.28), is the number of neutrinos leaving the star per unit of time (as $L_\nu^{(\mathcal{E})}$, it is a redshifted quantity). The figure 6.7 represents the number luminosities of all neutrinos flavors, as well as the deleptonization rate, defined as $L_{\nu_e}^{(n)} - L_{\bar{\nu}_e}^{(n)}$.

Heavy neutrinos ν_x are the most numerous, and as expected we see that for most of the evolution we have $L_{\nu_e}^{(n)} > L_{\bar{\nu}_e}^{(n)}$ (the star deleptonizes).

At the beginning of the simulation there are a few milliseconds during which this is not the case. But we recall here that as two different codes are used for the core-collapse simulation

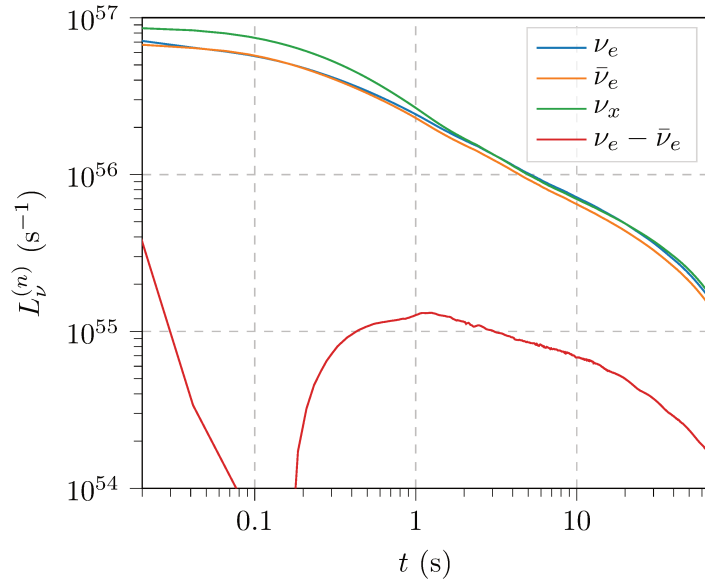


Figure 6.7: Neutrino number luminosities (as defined in eq. (4.28)) as a function of time, in our fiducial simulation. The luminosities of three neutrino types are represented, as well as the deleptonization rate ($L_{\nu_e}^{(n)} - L_{\bar{\nu}_e}^{(n)}$).

and the proto-neutron star modelisation, our initial model is not in radiative equilibrium at the beginning of the simulation, and this phase thus can be interpreted as a slight "re-leptonization" of the mantle due to our different models.

Now regarding the mean energy of emitted neutrinos (measured at infinity), it can be defined as

$$\langle \epsilon_\nu \rangle = L_\nu^{(\mathcal{E})} / L_\nu^{(n)} \quad (6.17)$$

Mean energies of emitted neutrinos are represented in fig. 6.8 as a function of time, for all flavors.

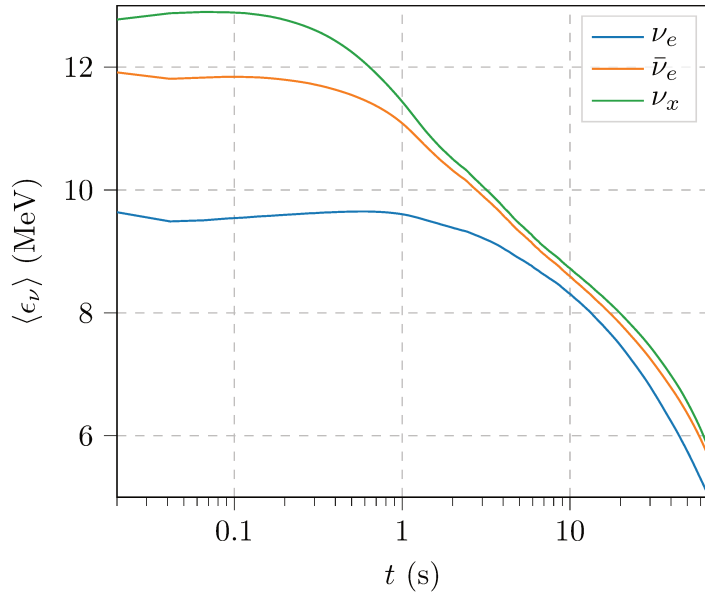


Figure 6.8: Mean energy of emitted neutrinos as a function of time, for each neutrino type, in our fiducial simulation.

The argument to explain this ordering is the same as above : the mean energy of emitted neutrinos should be approximately given by $\langle \epsilon_\nu \rangle \approx 3T_\nu$ (energy of a non-degenerate relativistic

gas in thermal equilibrium), where T_ν is the temperature of the neutrinosphere. And because we have $R_{\nu_x} < R_{\bar{\nu}_e} < R_{\nu_e}$, heavy neutrinos ν_x are created at higher temperatures.

Finally, let us discuss the evolution of the electron fraction in the neutrino driven wind Y_e^{NDW} . We compute it in our simulations by using eq. (2.5), with the hypotheses given sec. 2.1.4. The evolution of Y_e^{NDW} as a function of time is given by the figure 6.9.

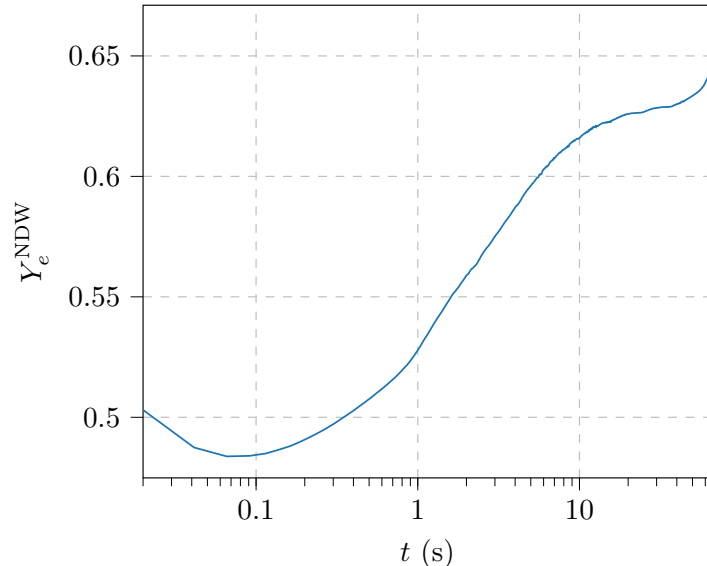


Figure 6.9: Electron fraction in the neutrino driven wind, computed with eq. (2.5), in our fiducial simulation.

This figure can be compared with the figure 8 of [93] (a quasi-static simulation similar to ours) and the figure 7 of [96] (a full-hydrodynamic simulation) who have obtained similar results. We observe that the neutrino driven wind is neutron rich ($Y_e^{\text{NDW}} < 0.5$) for a short period of time at the beginning of the simulation, and then becomes proton-rich ($Y_e^{\text{NDW}} > 0.5$) for the rest of the simulation. This fact might be of importance for the nucleosynthesis in the neutrino driven wind, as already discussed in section 2.1.4. The observation of a proton-rich neutrino driven wind is in agreement with most recent simulations [153].

Chapter 7

Masses and radii of proto-neutron stars

As introduced in the section 3.1.5, recent studies of asteroseismology of proto-neutron stars suggest that the gravitational wave signal emitted during the core-collapse mechanism could be used to extract information on the properties of the proto-neutron star.

This chapter is focused on these two questions : what can be learned on the proto-neutron star from gravitational wave analysis ? And how can we use these informations to put general constraints on (proto-)neutron star physics ?

7.1 Gravitational waves and PNS properties

7.1.1 Eigenmodes for oscillations of a PNS

In [83], the authors study linear perturbations of the general relativistic hydrodynamic equations governing hydrostatic equilibrium in a compact star. They use the Cowling approximation, *i.e.* they do not consider perturbations of metric-related quantities and only introduce perturbation of hydrodynamic quantities (density, pressure, velocity, ...).

They find that, as in the case of non-relativistic stars, two physical origins for linear plane-wave solutions, which are the so-called p -modes and g -modes, introduced in the section 3.1.5.

These modes correspond to very different physical phenomena. p -mode gravitational waves are associated to acoustic oscillations of the proto-neutron star, and their frequency depends on the speed of sound c_s . The characteristic frequency of acoustic modes in a sphere is the Lamb frequency ω_L :

$$\omega_L^2 = c_s^2 \frac{l(l+1)}{r^2} \quad (7.1)$$

where l designates the spherical harmonic index associated to the mode. The general relativistic formula differs only by a numerical factor (see e.g. [83]).

Regarding g -mode gravitational waves, they are related to gravity waves, for which the characteristic frequency is the Brunt-Väisälä frequency ω_{BV}

$$\omega_{BV}^2 = g(r)C_L(r) \quad (7.2)$$

where $g(r)$ is the local gravitational acceleration and $C_L(r) > 0$ is the Ledoux criterion (positive in stable stratifications subject to gravity waves), defined as in eq. (3.2). As for the Lamb frequency, the general relativistic case is given in [83]. The role played by this frequency in the stability analysis of stratified media will be discussed further in the chapter 8 of this thesis.

In [83], the authors proposed a generic method to classify the modes as p -mode or g -mode, depending upon their frequencies and their number of radial nodes n . The mode with zero radial nodes is called the fundamental mode f . Then modes at higher frequencies than the f -mode are classified as p -modes and modes at lower frequencies than the f -mode are classified as g -modes. The less radial nodes a specific mode has, the closer its frequency will be to the fundamental mode. This method of analysis has been used in simulations by various groups, but as explained in the section 3.1.5, the full picture of the GW emission is far from being perfectly drawn.

7.1.2 Relation with the PNS properties

In [154], the authors derive universal relations that relate the oscillation frequencies of the PNS to some of its fundamental properties, such as its surface gravity or its mean density.

For this they performed multiple 1D simulations with the codes AENUS-ALCAR [155] and CoCoNuT [156]. They used the procedure described in [83] to classify the modes and find that the p -mode frequencies can be fitted as functions of basic PNS properties depending upon their nature.

Case of p -modes

The p -modes, as well as the fundamental mode, can be fitted as functions of the square root of the PNS mean density inside the shock area

$$\sqrt{\langle \rho_{\text{shock}} \rangle} = \sqrt{\frac{3M_{\text{shock}}}{4\pi R_{\text{shock}}^3}} \propto \sqrt{\frac{M_{\text{shock}}}{R_{\text{shock}}^3}} \quad (7.3)$$

where M_{shock} and R_{shock} designate respectively the mass inside the shock and the shock radius.

The fit is represented on the figure 7.1. The points in this figure come from a wide variety of simulations with different progenitors and equations of states (see [154] for more details).

This dependency can be understood because the frequency of these acoustic modes depends mostly upon the local speed of sound c_s (see eq. 7.1), which depends mostly upon the local density.

Case of g -modes

Regarding the case of g -modes, they can be fitted as functions of the PNS surface gravity g_{surf}

$$g_{\text{surf}} = \frac{GM_{\text{pns}}}{R_{\text{pns}}^2} \propto \frac{M_{\text{pns}}}{R_{\text{pns}}^2} \quad (7.4)$$

where M_{pns} and R_{pns} designate respectively the mass and the radius of the proto-neutron star.

The fit is represented on the figure 7.2.

As g -modes depend mostly on the local gravitational acceleration (see eq. 7.2) and occur on the surface layer of the proto-neutron star, this result can also be understood.

7.1.3 Possible difficulties

In principle, if we were able to identify the various modes and frequencies composing the gravitational wave emission of the proto-neutron star, we should be able to give estimates for

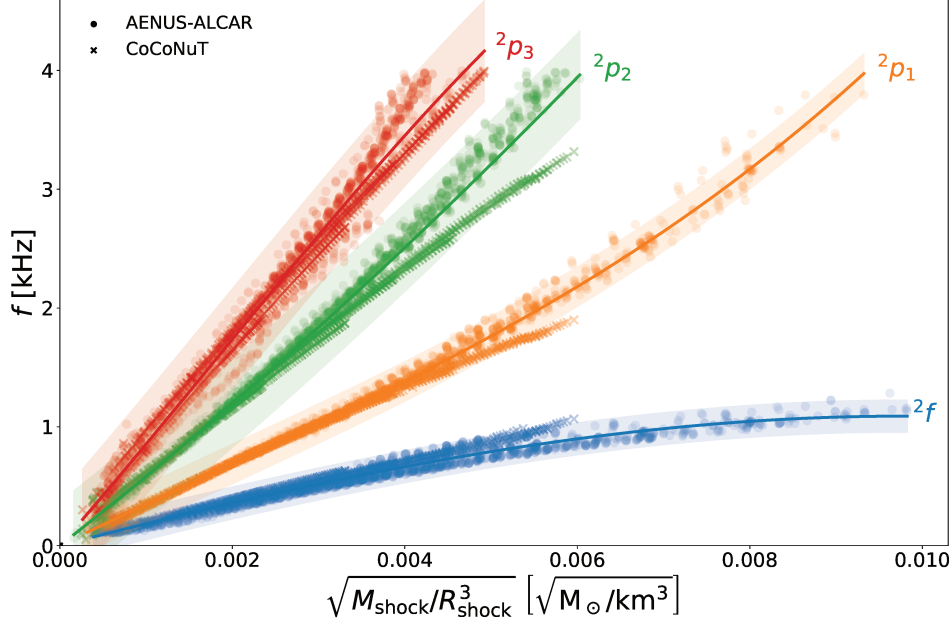


Figure 7.1: Results of the mode analysis and fit for the case of the p -modes. The notation ${}^l p_n$ designates the p -mode corresponding to the spherical harmonic l with n radial nodes. ${}^2 f$ is the $l = 2$ fundamental mode. Shaded areas represent the 2σ error intervals. This figure is extracted from [154].

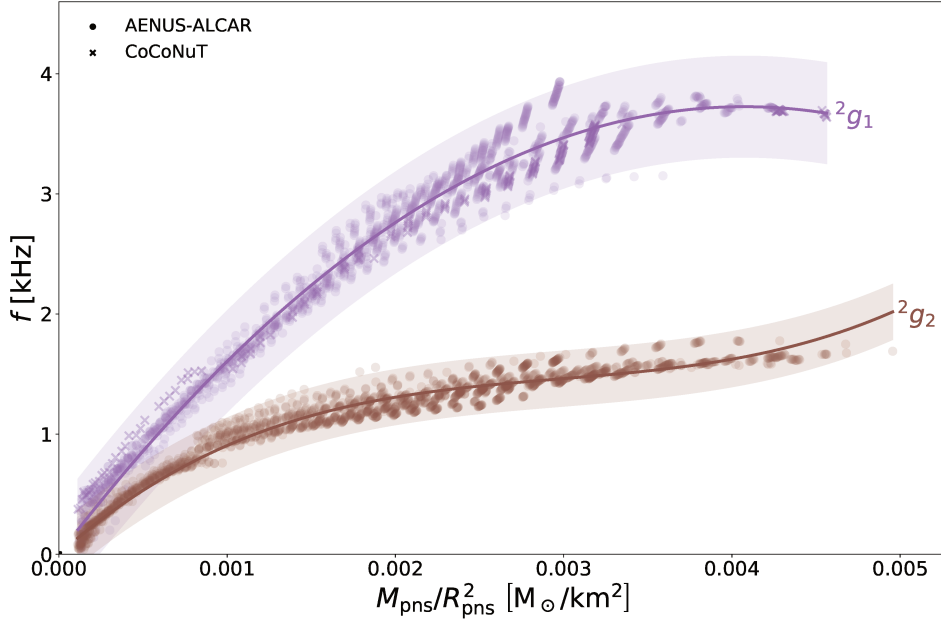


Figure 7.2: Results of the mode analysis and fit for the case of the g -modes. The notation ${}^l g_n$ designate the g -mode corresponding to the spherical harmonic l with n radial nodes. Shaded areas represent the 2σ error intervals. This figure is extracted from [154].

the values of the mass and radius of the proto-neutron star by using the fits reprinted on fig. 7.1 and 7.2.

However, there are at least two difficulties in this procedure :

- as discussed in section 3.1.5, p -mode gravitational waves are also emitted by the SASI oscillations of the shock. These modes are not related to neutron star properties and

might be difficult to separate from the rest of the signal

- g -modes should depend only on neutron star properties, however in some simulations, the emission of GWs is dominated by p -modes, which makes the identification of g -modes difficult. g -modes can also be excited by the convective motion in the proto-neutron star, which makes a clear separation between both types of modes more difficult.

Therefore it is yet unclear if the identification of the PNS properties from its gravitational wave emission is possible. Nevertheless, since PNS asteroseismology is a very recent field of study, the full picture is not perfectly drawn and the situation deserves some attention.

In the following section we will focus on what could be learned from the determination of a PNS mass and radius.

7.2 Getting information from a PNS mass and radius

In this work ([157]) we investigated two problems :

- **(P1)** how much would the determination of the mass and radius of a PNS born in core-collapse supernovae be able to constrain the M-R diagram of cold neutron stars and therefore also their cold equation of state $P(n_B)$?
- **(P2)** is it possible, with such observations, to constrain at least the (3-dimensional) EoS in hot newly born PNS ?

To tackle these questions, we use the PNS simulation code presented in section 6 to simulate the first second of evolution for several models of proto-neutron stars.

7.2.1 Parametrized initial profiles

In order to take into account the variability in the initial profiles for the electron fraction Y_e and the entropy per baryon s , we choose to use analytic parametrizations of these profiles.

These analytic profiles should reproduce the observed features of profiles extracted from simulations, which were discussed in section 3.1.1 :

1. an inner core with low entropy per baryon and high electron fraction
2. a hot mantle with high entropy and low electron fraction, which has a negative entropy and electron fraction gradient
3. the matter contained in the mantle should be proportional to the kinetic energy of the shock, which is itself proportional to the mass of the inner core (the ratio of mass between the two regions should not depend a lot on the simulation)
4. the outer zone is the position of the shock with very high electron fraction and entropy

Because of the feature 3, it is more convenient to use a parametrization as a function of the enclosed baryon mass $m_B = m_{Na}(r)$. The following parametrizations $s(m_B)$ and $Y_e(m_B)$ reproduces these main features.

The entropy per baryon is modeled by a plateau followed by a Gaussian and a power-law

divergence near the surface, with five parameters in total :

$$\begin{aligned}
s(m_B) = s_c \times & \left[1 + \exp \left(\frac{2s_{\max}}{s_c \sigma_s} \left(m_B - m_s + \frac{2\sigma_s}{3} \right) \right) \right]^{-1} \\
& + s_{\max} \exp \left(-\frac{(m_B - m_s)^2}{2(\sigma_s/2)^2} \right) \\
& + \frac{s_{\max}(M_B - m_B)^{-0.3}}{1 + \exp \left(-\frac{2}{\sigma_s} \left(m_B - \left(m_s + \frac{2\sigma_s}{3} \right) \right) \right)}
\end{aligned} \tag{7.5}$$

where s_c is the central entropy, s_{\max} is the maximal entropy between the inner core and the shocked mantle, σ_s is the width of the gaussian, m_s the mass at which s_{\max} is reached and M_B is the total baryon mass.

The figure 7.3 represents this parametrization for the set of parameters given in table 7.1.

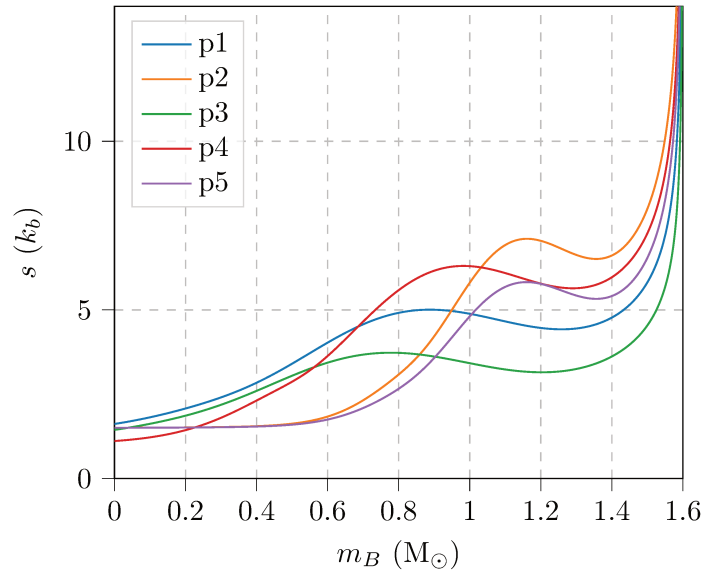


Figure 7.3: Entropy per baryon s as a function of the enclosed baryon mass m_B , for our chosen sets of parameterized profiles (see eq. (7.5) and table 7.1). The total baryon mass considered is $M_B = 1.6 M_\odot$ [157]

The electron fraction is modeled by a plateau followed by an inverse asymmetric Gaussian, with four parameters in total :

$$\begin{aligned}
Y_e(m_B) = Y_0 & + \frac{Y_c - Y_0}{1 + \exp \left(\frac{5}{2\sigma_Y} \frac{Y_{\min} - 0.5}{Y_c - 0.5} \left(m_B - M_B + \frac{2\sigma_Y}{3} \right) \right)} \\
& + (Y_{\min} - 0.5) \exp \left(-\frac{(m_B - M_B)^2}{2(\sigma_Y/2)^2} \right) \\
& \times \frac{1}{2} \left[1 + \operatorname{erf} \left(-15 \frac{m_B - M_B}{\sigma_Y / \sqrt{2}} \right) \right]
\end{aligned} \tag{7.6}$$

where erf is the error function, Y_c is the central electron fraction, Y_{\min} its minimal value and σ_Y the width of the gaussian.

Since the two profiles should be related by the relative size of the shocked region, we choose σ_Y such that $\sigma_Y = M_B - m_s$.

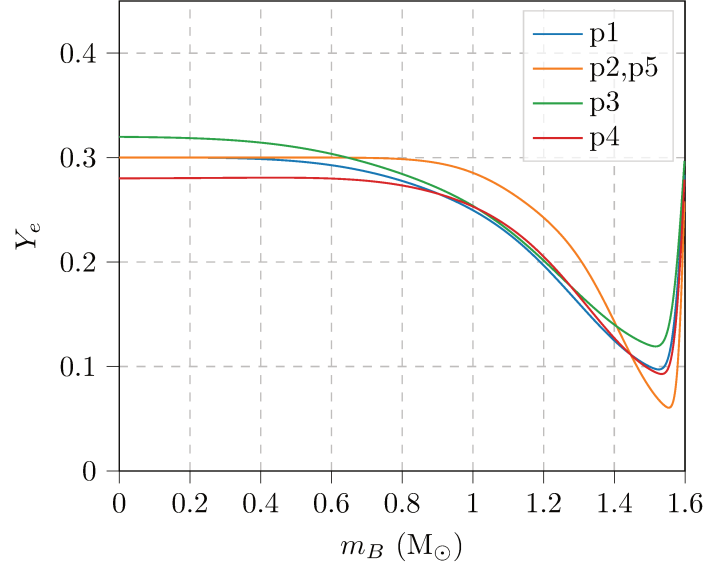


Figure 7.4: Electron fraction Y_e as a function of the enclosed baryon mass m_B , for our chosen sets of parameterized profiles (see eq. (7.5) and table 7.1). The total baryon mass considered is $M_B = 1.6 M_\odot$ [157]

The figure 7.4 represents this parametrization for the set of parameters given in table 7.1.

The set of parameters p1-p5 used in our simulations given in table 7.1 has been chosen such that p1 resembles the profiles shown in fig. 3.2 and p2 the profiles shown in [93]. In the following we will use these sets of parameters with different total baryon mass M_B to build our initial data sets in order to reproduce the variability and uncertainty inherent to these initial data.

Label	s_c	s_{\max}	σ_s	m_s/M_B	Y_c	Y_{\min}
p1	1.3	4	0.7	0.5	0.3	0.1
p2	1.5	5.5	0.4	0.6875	0.3	0.06
p3	1.1	3	0.7	0.4375	0.32	0.12
p4	1	5	0.6	0.5625	0.28	0.1
p5	1.5	4.5	0.4	0.6875	0.3	0.06

Table 7.1: Parameters defining for a given M_B the five parameterizations labeled p1 to p5 of the initial $s(m_B)$ and $Y_e(m_B)$ profiles [157]

7.2.2 Evolution of proto-neutron stars in the (M,R) plane

We present here a comparison of the evolution of various PNS models during the first second of simulation, in order to tackle the two problems (P1) and (P2) presented at the beginning of section 7.2.

Each PNS model is characterised by :

- its total baryon mass M_B
- the set of parameters used for the initial model (c.f. table 7.1)
- the equation of state used in the simulation

Four equations of state have been used in these simulations :

- HS(DD2), using the extended NSE model of [133] and the DD2 parametrization of the nuclear interaction [158]
- HS(SFHo), based on the same NSE model and using the SFHo parametrization [159]
- RG(SLy4), using the extended NSE model from [134] and the SLy4 Skyrme effective interaction [160]
- SRO(APR), computed in [161], is based on the SRO model [162], and uses the APR Skyrme-like effective interaction [163]

All these equations of state can be found in the **CompOSE** database [51].

Regarding the total baryon mass M_B , we used three different values : $1.6 M_\odot$, $1.8 M_\odot$ or $2.0 M_\odot$. With the four EoS and the five parameters sets for initial data this gives us 60 models of proto-neutron stars to study.

Each model is evolved for 1 s and we output detailed profiles every 0.1 s. For each result we recompute the PNS structure and we define the radius as in [154], with a fixed baryon density $n_B = 0.5970 \times 10^{-5} \text{ fm}^{-3}$. The masses and radii obtained are compiled in the figure 7.5, which represents the (M,R) plane, normalized for each model by the $T = 0$ values corresponding to a fully-evolved β -equilibrated neutron star.

We see that after 1 s of evolution, the mass of the PNS is still larger by about 6-10 % compared with the cold configuration. The mass evolves on a slow timescale, as it related to the total energy taken away by neutrinos. Therefore an accurate measurement of the mass should be possible in principle as it is not really influenced during the time over which the signal is integrated. Indeed the frequency of the g -modes should be of roughly 100-1000 Hz, and should therefore require an integration time of only several tens of milliseconds. This could in principle provide an upper bound on the mass of the cold configuration.

For the radius the situation is different : after 1 s of evolution it is larger by about 40-200 % compared with the cold configuration. And the radius is undergoing a fast evolution due to the contraction of the mantle. Therefore a constraint on the radius of the cold configuration will be difficult to provide by a measurement of the proto-neutron star's properties.

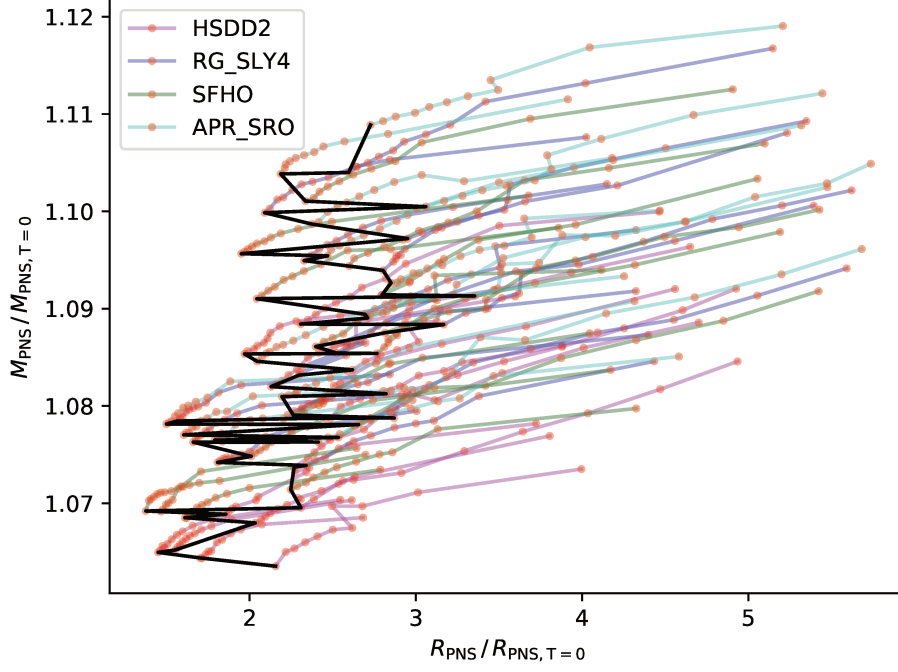
Now regarding the EoS dependence, the figure 7.6 represents the position of our 60 PNS models in the (M,R) plane after $t = 0.5 \text{ s}$ and $t = 1.0 \text{ s}$ of evolution.

We see that the clouds are largely mixed : the position of the proto-neutron star on the mass-radius plane largely depend on the set of parameters chosen to build the initial profiles. This is especially the case for the radius, which has an extreme variability. As a consequence we see that a clear identification of the equation of state is impossible without precise information about the entropy per baryon and electron fraction profiles in the proto-neutron star.

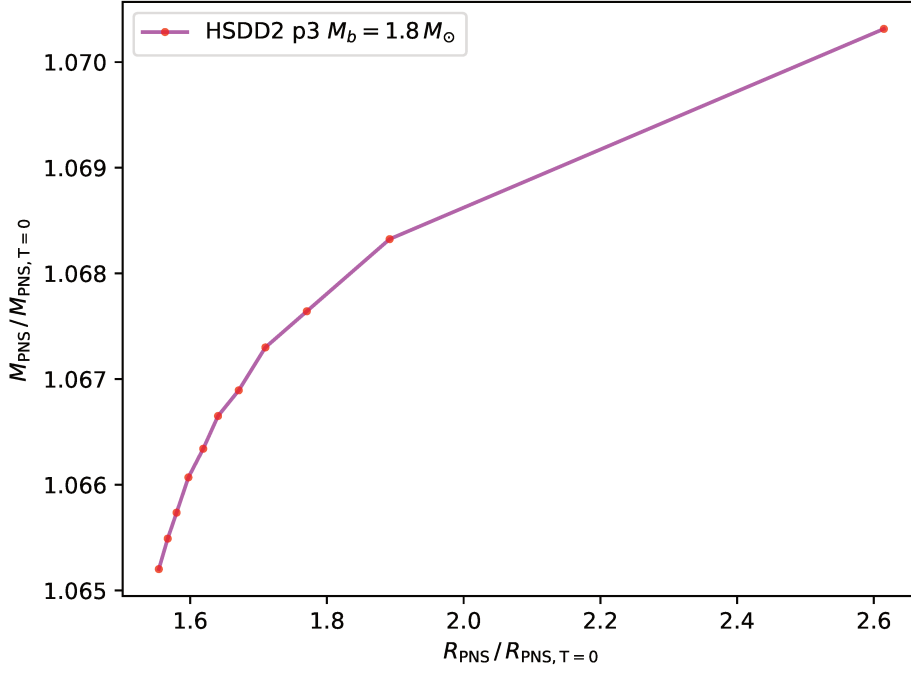
An interesting question is whether it is the uncertainty on the entropy profile or on the electron fraction profile which causes the extreme variability of the radius. To answer that question we studied profiles by varying only the s -profile or only the Y_e -profile, and we found that the contribution of the entropy is much more important on the determination of the radius than the Y_e -profile. Indeed by varying the Y_e -profile we found less than 10 % of variations in the radius, and by varying the s -profile the radius spread between roughly 15 km and 60 km.

7.2.3 Conclusion and limitations

To conclude on the two problems (P1) and (P2) that we wanted to adress in this section :



(a) Representation of all 60 models



(b) Case of the HS(DD2) EoS, parametrization p3 and $M_B = 1.8 M_\odot$

Figure 7.5: PNS evolution in the gravitational mass M_{PNS} - radius R_{PNS} plane, normalized to the zero temperature values (i.e. the value corresponding to the cold neutron star). Different colors correspond to the various EoS models (the labels are defined in the text). The red dots indicates points computed every 0.1 s and the black line indicate the points computed after 1 s of evolution. [157]

- **(P1)** The structure of the nascent proto-neutron star is still very far from the cold configuration. The radius is in particular still much larger and evolves very quickly. As a consequence the determination of the ratio M/R^2 proposed in [154], if possible with sufficient accuracy, would not provide strong constraints on the properties of the cold

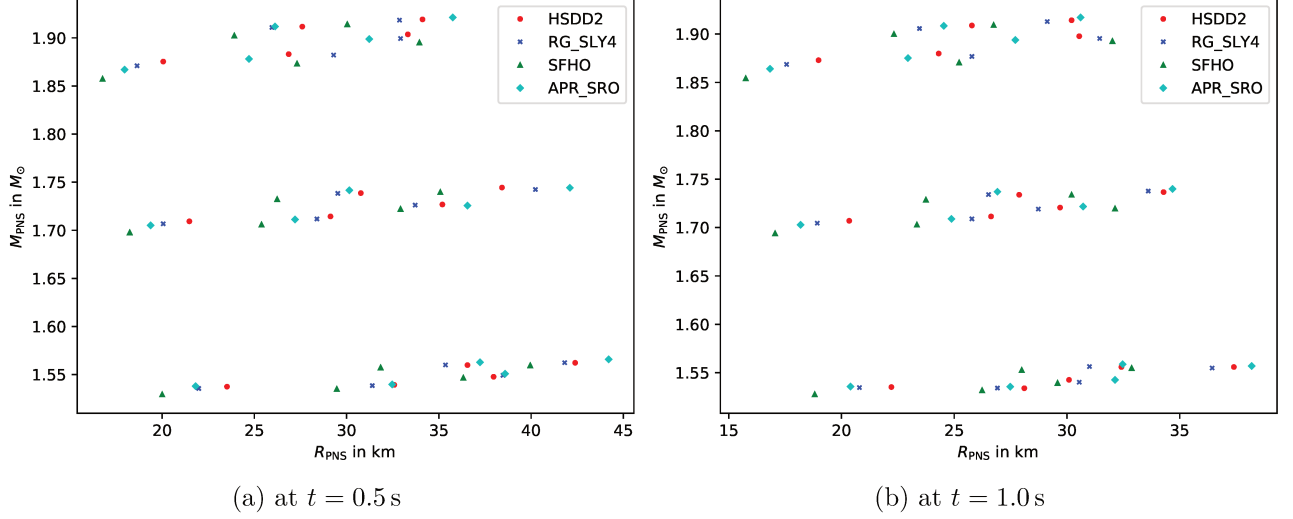


Figure 7.6: Points in the (M, R) plane obtained from the evolution of the 60 PNS models. The three clouds correspond to the three values of the total baryon mass $M_B = 1.6 M_\odot$ (bottom), $M_B = 1.8 M_\odot$ (middle) and $M_B = 2.0 M_\odot$ (top). Different colors correspond to the various EoS models (the labels are defined in the text) [157]

configuration of the neutron star

- **(P2)** The internal structure of the PNS (the s and Y_e profiles) are not constrained with a high precision. This leads to significant variations of the radius of the proto-neutron star at similar times, which are more important than the variation due to the various equations of state. Therefore the measure of global properties of the proto-neutron star would not provide reliable constraints on its hot equation of state

Therefore it seems that all the uncertainties inherent to the study of core-collapse (uncertainties on the progenitor, on weak processes, on the equation of state, ...) are causing a lot of variability in the behavior of the proto-neutron star during the studied time span of 1 s. Because of this, any information about its general structure would be difficult to interpret as all effects are extremely entangled.

We conclude by evoking several limitations to our study :

- The quasi-static approach may not be correct during the first second after bounce because of the significant accretion observed in some simulations, see e.g. [97] and [98]. Nevertheless this approximation is conservative with respect to our negative answers to the problems **(P1)** and **(P2)**. Indeed, if the PNS is accreting, its mass and radius after 1 s of evolution will be even further from the cold configuration, and its non-hydrostatic structure is not entirely determined by its equation of state and $s(/Y_e)$ profiles, will complexify even more the analysis required in **(P1)** and **(P2)**.
- We built our initial profiles by trying to reproduce some results of CCSN simulations and voluntarily broadened the choice of parameters to take into account uncertainties in CCSN simulations. Nevertheless our choices may be considered as too broad, as some choices could lead to unrealistic profiles
- We restrained our study to 1 s of simulation, because it is yet unclear if the emission of gravitational waves could be strong enough to be detected at later times. But if so, the situation could be very different as the mass and radius evolve much more slowly, allowing for more accurate measurement and constraints.

Chapter 8

Modeling convection with the Mixing Length Theory

This chapter focuses on the role of convection in proto-neutron stars, and presents the results of a simple modelisation with the mixing length theory (MLT) [150].

8.1 Instability to convective motion

8.1.1 Ledoux criterion for the stability of a stratified media

In this work we use the word "convection" to refer specifically to the natural fluid motion occuring in stratified media by temperature and composition induced variations of the buoyancy, and to the advection of heat and particles by this motion.

To explain the notion of convective instability, we consider the simple case of an ideal fluid in a vertical stratification submitted to a vertical gravitationnal acceleration $\mathbf{g} = -g\mathbf{e}_z$.

We consider a small vertical displacement of an eddy of mass density ρ , and we note respectively ρ_0 and P_0 the mass density and the pressure of the surrounding medium. The situation is represented in the figure 8.1.

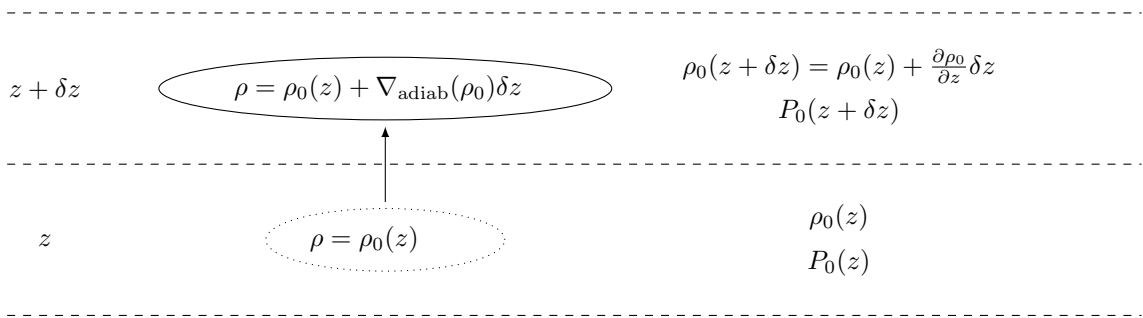


Figure 8.1: Small adiabatic displacement of a mass element in a stratified medium

The surrounding medium is in hydrostatic equilibrium, therefore we have $\frac{dP_0}{dz} = -\rho_0 g$. The small fluid element of mass density $\rho = \rho_0(z)$ is displaced adiabatically in the vertical direction with a height δz . The variation of density induced by this adiabatic motion is noted $\nabla_{\text{adiab}}(\rho_0)\delta z$.

The mass element is submitted only to buoyancy, and its equation of motion is given by

$$\begin{aligned}\rho_0 \frac{d^2(\delta z)}{dt^2} &= g(\rho_0(z + \delta z) - \rho) \\ \frac{d^2(\delta z)}{dt^2} &= g \left(\frac{\partial \ln \rho_0}{\partial z} - \frac{1}{\rho_0} \nabla_{\text{adiab}}(\rho_0) \right) \delta z\end{aligned}\tag{8.1}$$

Regarding the variation of density induced by the adiabatic motion, we can write

$$\frac{1}{\rho_0} \nabla_{\text{adiab}}(\rho_0) = \frac{1}{\gamma} \frac{\partial \ln P_0}{\partial z}\tag{8.2}$$

where $\gamma = (\partial \ln P / \partial \ln \rho)_S$ is the adiabatic index of the fluid.

We define the Brunt–Väisälä frequency ω_{BV} as

$$\omega_{BV}^2 = -g \left(\frac{\partial \ln \rho_0}{\partial z} - \frac{1}{\gamma} \frac{\partial \ln P_0}{\partial z} \right)\tag{8.3}$$

If $\omega_{BV}^2 \geq 0$ the equation (8.1) has an oscillatory solution : the stratification is stable, and the fluid element oscillates around its equilibrium position at the frequency ω_{BV} , resulting in the so-called *gravity waves*, already discussed in the section 3.1.5 and the chapter 7.

In the opposite case, the mass element will move away exponentially from its original position and the system can be subject to convective motion.

We usually give the Ledoux criterion for the stability of the stratification as

$$C_L(z) = \frac{\omega_{BV}^2}{g} = \frac{1}{\gamma} \frac{\partial \ln P_0}{\partial r} - \frac{\partial \ln \rho_0}{\partial r} \geq 0\tag{8.4}$$

This definition is identical to eq. (3.2). The quantity $C_L \delta z$ can be interpreted as the relative density contrast between the displaced mass element and its surrounding medium :

$$C_L(z) = \frac{1}{\rho_0} \left(\nabla_{\text{adiab}}(\rho_0) - \frac{\partial \rho_0}{\partial z} \right)\tag{8.5}$$

To resume this analysis :

- if $C_L(z) \geq 0$ the stratification is stable and can be subject to gravity waves
- if $C_L(z) \leq 0$ the stratification is unstable and convective motion will occur

8.1.2 Causes of convection : entropy and composition gradients

We will now connect the Brunt–Väisälä frequency and the instability criterion to more physically meaningful quantities, such as the specific entropy, the composition of the fluid and the equation of state of the fluid.

We consider that the fluid is constituted of N species of mass densities $\{\rho_i\}_{1 \leq i \leq N}$ and we note $Y_i = \rho_i / \rho_0$ their particle fractions. We also note s the specific entropy of the fluid.

The equation of state of the fluid may be written under the form

$$\frac{dP}{P} = \gamma \frac{d\rho}{\rho} + \Gamma_s \frac{ds}{s} + \sum_{i=1}^N \Gamma_{Y_i} \frac{dY_i}{Y_i}\tag{8.6}$$

where $\Gamma_s = \left(\frac{d \ln P}{d \ln s} \right)_{\rho, Y_i}$ and $\Gamma_{Y_i} = \left(\frac{d \ln P}{d \ln Y_i} \right)_{\rho, s, Y_j \neq Y_i}$ and the Ledoux criterion becomes

$$C_L = \frac{1}{\gamma} \left(\Gamma_s \frac{\partial \ln s}{\partial z} + \sum_{i=1}^N \Gamma_{Y_i} \frac{\partial \ln Y_i}{\partial z} \right) \geq 0 \quad (8.7)$$

We see that the stability of the fluid against convective motion relies not only on its thermodynamic profiles but also on coefficients depending on its equation of state.

8.1.3 Case of proto-neutron stars

In the case of a small adiabatic displacement of a mass element at non relativistic speeds, the above reasoning can be extended to the general relativistic case. Instead of mass density one needs to consider the baryon density n_B , and the Ledoux stability criterion becomes

$$C_L(r) = \frac{1}{\Gamma_{n_B}} \left(\Gamma_s \frac{\partial \ln s}{\partial r} + \Gamma_{Y_e} \frac{\partial \ln Y_e}{\partial r} \right) \geq 0 \quad (8.8)$$

where r is the radial coordinate and $\Gamma_{n_B} = \left(\frac{d \ln P}{d \ln n_B} \right)_{s, Y_e}$, $\Gamma_s = \left(\frac{d \ln P}{d \ln s} \right)_{n_B, Y_e}$, $\Gamma_{Y_e} = \left(\frac{d \ln P}{d \ln Y_e} \right)_{n_B, s}$.

This criterion is the same as the one used in [81], and as the one already presented in eq. (8.7)

For a fluid which respects thermodynamic stability criterions we always have Γ_{n_B} and $\Gamma_s \geq 0$, therefore a negative gradient of entropy per baryon $\partial_r s \leq 0$ is always a factor of instability in a stratification.

Regarding the role of the composition, in low density areas we have $\Gamma_{Y_e} \geq 0$ (pressure is dominated by degenerate electrons), therefore negative gradients of Y_e are a factor of instability to convection. But in denser areas we have usually $\Gamma_{Y_e} \leq 0$ because the pressure is dominated by nuclear symmetry effects, and in those areas positive gradients of Y_e are a factor of instability.

The full stability criterion (8.8) is of course a combination of these two contributions, which can compensate each other.

8.2 Mixing length theory

As a complete simulation of convection is computationally expensive, there exists various methods to model convective effects at a lower cost. While not capturing all the complex details of the physics of convection, those methods can model the influence of convective effects in a rather reliable way.

The simplest model of convection is the mixing length theory (MLT). It is a 1D model which considers that convection acts as a simple transport phenomenon and models its effect with diffusion equations.

8.2.1 Particle and thermal diffusion with the MLT

The main effect of convection is to tend to uniformize the entropy per baryon and electron fraction profiles in convectively unstable areas, in order to tend to $C_L = 0$. Therefore in the MLT we start by determining which are the areas unstable to convection by using the Ledoux stability criterion (8.8). Then, an additional flux of lepton number and entropy is computed by using a flux-gradient law :

$$F_N^{\text{MLT}} = -D^{\text{MLT}} n_B \frac{\partial Y_e}{\partial r} \quad (8.9)$$

$$F_S^{\text{MLT}} = -D^{\text{MLT}} n_B \frac{\partial s}{\partial r} \quad (8.10)$$

where D^{MLT} is a diffusion coefficient equal to 0 in areas stable to convection and is non 0 in convectively unstable layers.

The PNS evolution equations (6.11) and (6.14) become

$$\frac{1}{\alpha} \frac{DY_e}{Dt} + \frac{1}{r^2 \alpha \psi} \frac{\partial}{\partial r} \left(\alpha r^2 F_N^{\text{MLT}} \right) = \frac{\Gamma_{\bar{\nu}_e} - \Gamma_{\nu_e}}{n_B} \quad (8.11)$$

$$\frac{1}{\alpha} \frac{Ds}{Dt} + \frac{1}{r^2 \alpha \psi} \frac{\partial}{\partial r} \left(\alpha r^2 F_S^{\text{MLT}} \right) = -\frac{(Q_{\nu_e} + Q_{\bar{\nu}_e} + 4Q_{\nu_x})}{T n_B} + \frac{\mu_e (\Gamma_{\nu_e} - \Gamma_{\bar{\nu}_e})}{T n_B} \quad (8.12)$$

8.2.2 Estimation of the diffusion coefficients

The MLT diffusion coefficient D^{MLT} is estimated by using the same procedure as in [164]. We set

$$D^{\text{MLT}} = v_c \lambda_P \quad (8.13)$$

where λ_P is the length scale over which the convective turnover occurs and v_c is the convection velocity.

The length λ_P is called the *mixing length*, it is estimated as being of the same order of magnitude as the pressure length scale :

$$\lambda_P = \xi \left(\frac{\partial \ln P}{\partial r} \right)^{-1} \quad (8.14)$$

where ξ is a coefficient of order unity. This choice does not have a strong influence on the results, and taking $\xi = 1$ is the standard choice.

Regarding the convection velocity v_c , it is estimated by using energy conservation during a vertical displacement of λ_P :

$$\frac{1}{2} n_B v_c^2 = g |\Delta n_B| \lambda_P \quad (8.15)$$

where Δn_B is the density contrast between the displaced mass element and its surrounding medium after a displacement of height λ_P . According to eq. (8.5) we have $|\Delta n_B| = n_B |C_L| \lambda_P$, which yields

$$v_c = \begin{cases} \lambda_P \sqrt{2g|C_L|} & \text{if } C_L(r) \leq 0 \text{ (unstable stratification)} \\ 0 & \text{if } C_L(r) \geq 0 \text{ (stable stratification)} \end{cases} \quad (8.16)$$

8.2.3 Numerical implementation

The MLT diffusion fluxes F_N^{MLT} and F_S^{MLT} can be significant, especially at the beginning of the simulation. Therefore implementing the MLT with an explicit time scheme would force us to reduce considerably the timestep.

This is why we choose to solve eq. (8.11) and (8.12) in two steps with a semi-implicit scheme :

1. we use the discrete equations (G.10) and (G.12) to solve the neutrino part of the evolution
2. we use an implicit scheme to solve the MLT part, using the same timestep δt as used in the previous step. The procedure is detailed in appendix I

By doing so, the timestep is essentially limited by the neutrino source terms, as explained in section G.0.1.

8.2.4 Advantages and weaknesses of the MLT

This method has the advantage of being extremely simple to implement and adds almost no additional computational cost. It is also very adapted to our quasi-static modelisation as it relies on an estimation of convective fluxes with diagnostic equations, and doing so does not introduce any limitation in relation to any hydrodynamic timescale.

But the mixing length theory is a considerable simplification of the underlying physics and has several weaknesses :

- the convection velocity and the associated diffusion timescale are usually wrong. Therefore the mixing length theory does not produce reliable results on short timescales by comparison to hydrodynamic simulations. But in general when using MLT we are interested in timescales much longer than what is needed for the convective mixing of the layers to be complete, and in this case the MLT yields good results because it averages the convective effects occurring on short timescales
- when using MLT we consider that the layer in which the convective motion occurs stops at the radius where $C_L(r) = 0$. This is a considerable simplification : because of their inertia the moving fluid elements will continue after this "boundary" and mix with some Ledoux-stable layers. This phenomenon is called the *convective overshoot*, and is extremely difficult to estimate without a self-consistent hydrodynamic simulation

We have considered several possible improvements to study the weaknesses of the MLT. In particular the two-columns convection scheme of [165] seemed promising if combined with an anelastic approximation.

8.3 PNS evolution with the MLT

In this section we present the results of proto-neutron star cooling simulations with the mixing length theory. The setup of the simulation is the same as in our fiducial simulation, presented in section 6.2, with the addition of the MLT.

8.3.1 Evolution timescale

Simulations including convective effects are very different from those which do not. Indeed the convection considerably accelerates the cooling and the deleptonization by efficiently transporting heat and electrons from the inner core to the outer layers. The figure 8.2 represents the evolution of the mean entropy per baryon $\langle s \rangle$ and the mean electron fraction $\langle Y_e \rangle$, as defined by eq. (6.15).

Our fiducial simulation took about 65 s to completely deleptonize the star, while it took about 15 s with the simulation including convective effects within the mixing length theory. This faster cooling is confirmed by full hydrodynamic simulations [5].

Another interesting feature of simulations including convection is that they present a sudden change of behaviour after several seconds of evolution, which corresponds to the instant when the convection stops (see e.g. [166]). In our case we observe after about 4 s a sudden change in the deleptonization rate, which become much slower.

8.3.2 Structure and convective mixing

Regarding the evolution of the internal structure of the proto-neutron star, the figure 8.3 shows the radial profile of several relevant thermodynamic quantities, as a function of the enclosed

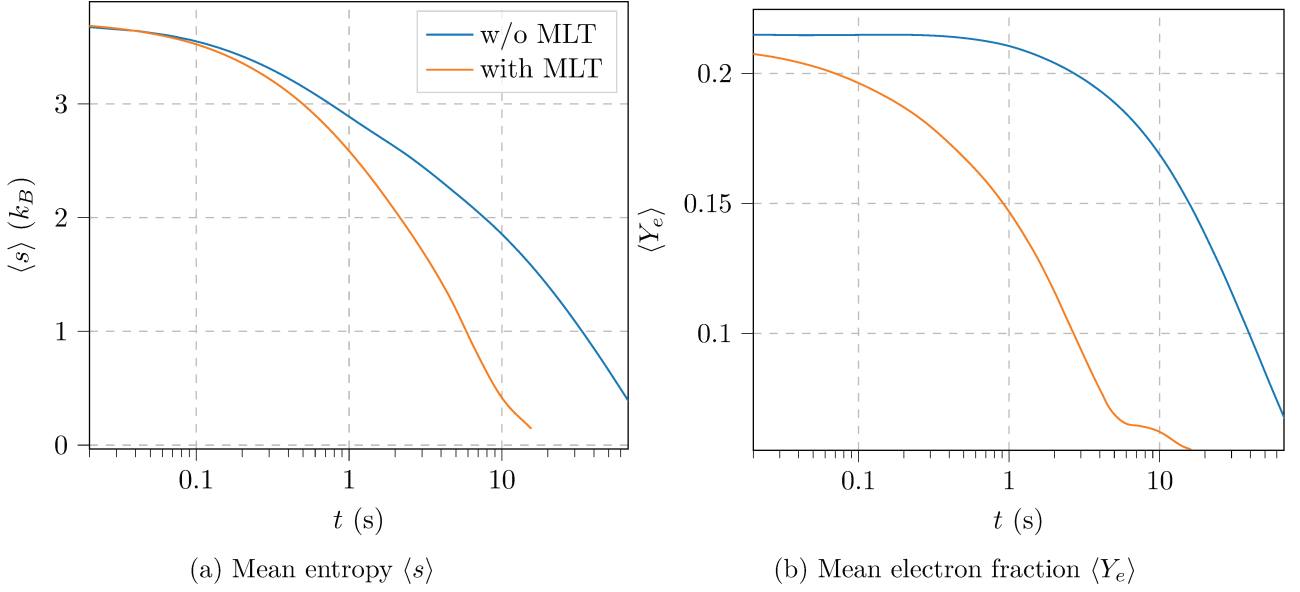


Figure 8.2: Evolution of the mean entropy per baryon $\langle s \rangle$ and the mean electron fraction $\langle Y_e \rangle$ of the proto-neutron star, as a function of time, in our fiducial simulation, with and without enabling MLT.

baryon mass $m_B = m_N a(r)$, at different times.

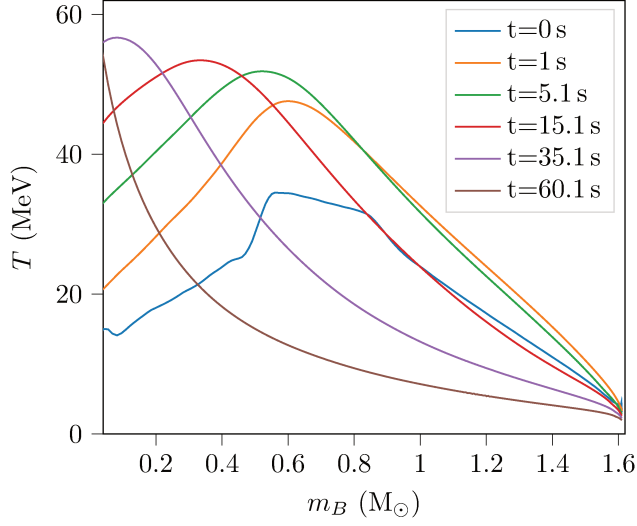
This figure makes clear the fact that the convection in the mantle of the proto-neutron star is extremely effective. Even by taking the same initial model as in our fiducial simulation (obtained with a spherically symmetric hydrodynamic simulation, thus without any convective effects) it takes less than about 100 ms to obtain a uniform entropy per baryon profile s and electron fraction Y_e in the convective zone, which is maintained in a state close to neutral buoyancy (i.e. $C_L \approx 0$). These observations are similar to what is observed in full hydrodynamic studies, such as [5]. Our s and Y_e profiles can be compared with their fig. 7 : they also observe the establishment of quasi-uniform profiles in the convective layer.

We also notice some differences between our simulations with and without MLT in the temperature profiles : the temperature is in general much higher in the outer layers and has an almost adiabatic profile in the convective layer.

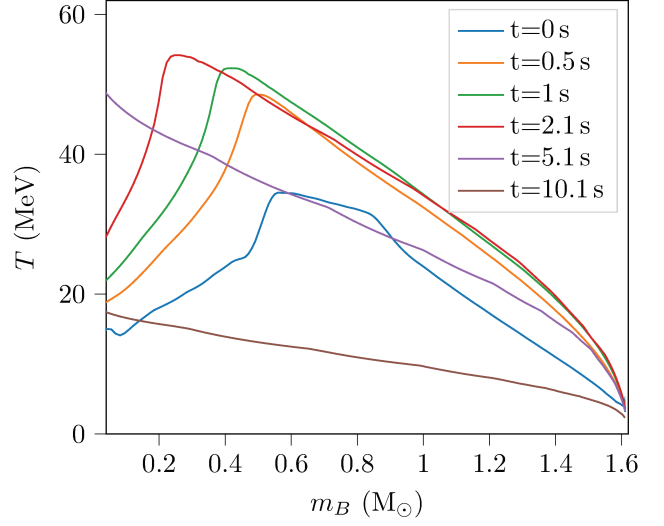
Regarding the evolution of the convective zone, we see that at the beginning of the simulation it consists only of the shocked mantle of the proto-neutron star. But as the *Joule heating* of the core proceeds (see section 6.2.2), the core progressively becomes also Ledoux-unstable, and the convective motion generalize to all regions of the proto-neutron star.

As discussed earlier in this section, a change of behaviour occurs after about 4 s, when the star reaches an adiabatic structure with a uniform composition (see the profiles at $t = 5.1$ s). At this moment we roughly have a state of neutral buoyancy ($C_L(r) \approx 0$) in all the star and the convective motion stops.

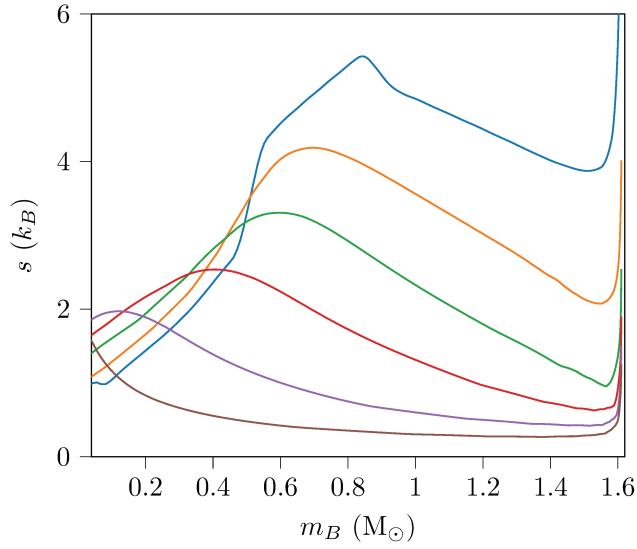
Finally, we notice a strong gradient of electron fraction between the inner core and the convective region, whereas in our fiducial simulation the Y_e profiles were much smoother. This strong gradient results in a change of slope in the baryon density profile at the core boundary (because of the effect of the symmetry energy, see section 3.1.3).



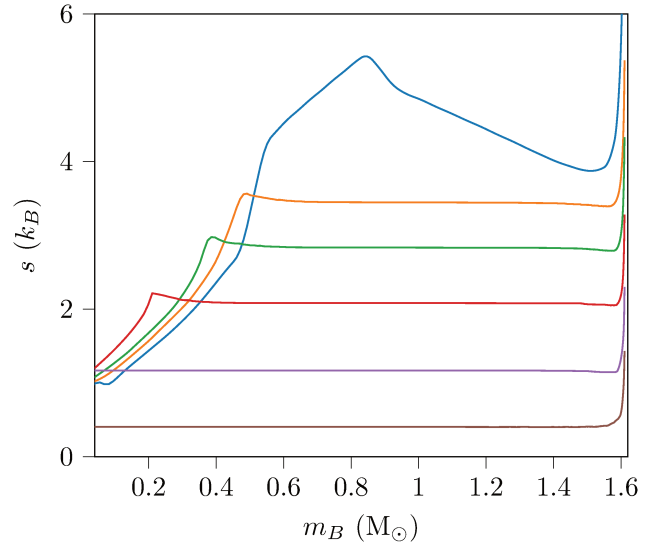
(a) Temperature T , w/o MLT



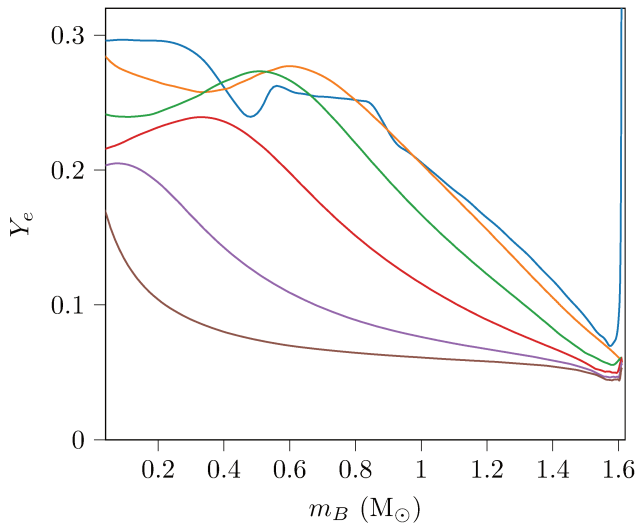
(b) Temperature T , with MLT



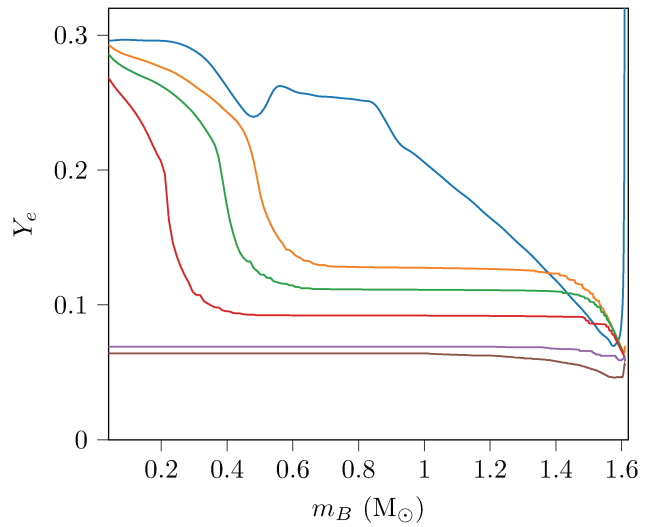
(c) Entropy per baryon s , w/o MLT



(d) Entropy per baryon s , with MLT



(e) Electron fraction Y_e , w/o MLT



(f) Electron fraction Y_e , with MLT

Figure 8.3: Same figure as 6.5, but with MLT enabled (right panels) and without MLT enabled (left panels)

8.3.3 Effect of convection on the neutrino emission

The deleptonization and the cooling proceed much faster in simulations taking into account convective effects than in those which do not. As a result the luminosity is higher in convective simulations at the beginning of the evolution, as shown in the figure 8.4, which represent the total energy luminosity of neutrinos.

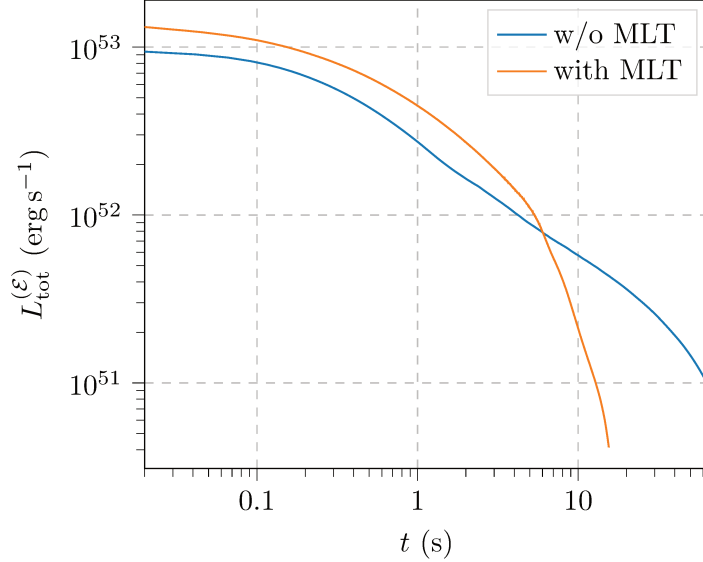


Figure 8.4: Total (sum of 6 flavors) neutrino energy luminosity as a function of time, in our fiducial simulation, with and without enabling MLT.

The luminosity with MLT is about 1.5 times higher than without during the convective phase. Then there is a change of slope when the convection ends, and the luminosity quickly drops. A similar observation was made in fig. 5 of [166], which performed similar simulations with a quasi-static approximation and the MLT. But in their case the decay of the luminosity after the end of convection is much slower than in our case.

Regarding the emitted energy spectrum, the figure 8.5 represents the evolution of the mean energy of emitted neutrinos (c.f. eq. (6.17)) as a function of time.

The energy of emitted neutrinos is always higher with convection. It also stays at a high level for longer and drops more quickly when convection ends.

Finally, any changes in the neutrino spectrum will have some consequences on the composition of the neutrino driven wind. The figure 8.6 represents the evolution of the electron fraction of the neutrino driven wind.

We see that in our simulation with MLT, the neutrino driven wind is always proton-rich, and presents a much higher electron fraction. As discussed in section 2.1.4, this fact is in favor of a nucleosynthesis by the νp -process in the neutrino driven wind.

We also observe a small decrease in Y_e^{NDW} at about 4-5s of simulation, which correspond to the instant when convection ends in the proto-neutron star, as discussed above.

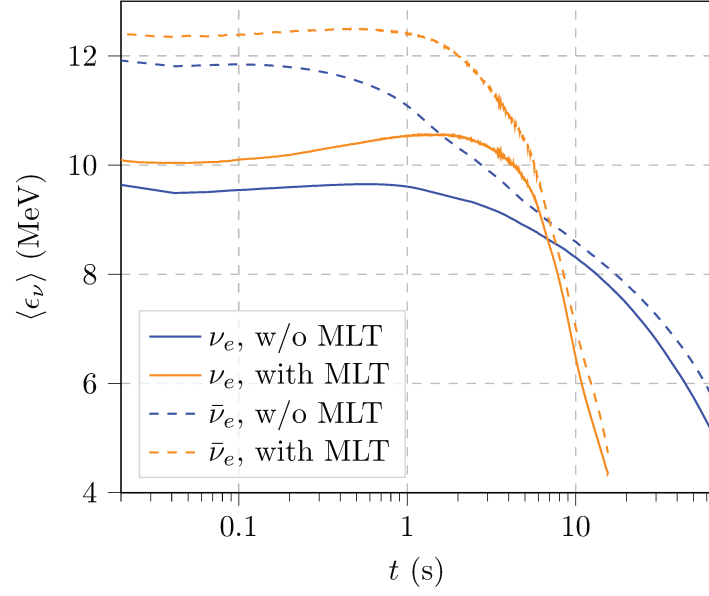


Figure 8.5: Mean energy of emitted neutrinos as a function of time, for each electron (anti-)neutrinos, in our fiducial simulation, with and without enabling MLT.

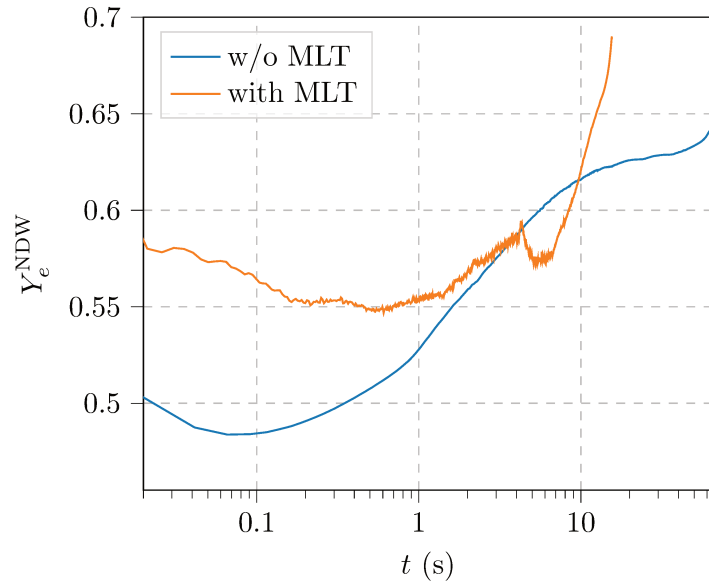


Figure 8.6: Electron fraction in the neutrino driven wind, computed with eq. (2.5), in our fiducial simulation, with and without enabling MLT.

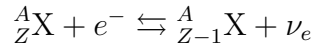
Part IV

Influence of charged current processes

Chapter 9

Electron captures on nuclei during the infall of the iron core

This chapter is focused on the influence of electron capture processes on nuclei, introduced in the section 5.2.2, which play a key role during the infall of the iron core.



9.1 Electron capture rates on neutron rich nuclei

During most of the infall the neutrinos are not trapped and can escape freely after their creation. In this context, it can be convenient to define the electron capture rate per volume unit Γ_{EC} as

$$\Gamma_{EC} = \frac{4\pi c}{(hc)^3} \int j_{EC,\text{tot}}(\epsilon) \epsilon^2 d\epsilon \quad (9.1)$$

where $j_{EC,\text{tot}}$ is the total neutrino emissivity related to electron captures on nuclei.

Note that this formula is valid only in the context of free-streaming neutrinos, when neutrinos are trapped this rate is modified because of their Pauli-blocking effect and because of the backward neutrino-capture process.

As explained in section 5.2.2, the composition in nuclei is relevant here and the rate of electron capture on nuclei depends not only on individual rates on a given nucleus but also on the nucleus relative abundance in the medium :

$$\Gamma_{EC} = \sum_{\text{all nuclei}} \lambda_{EC}(A, Z) n(A, Z) \quad (9.2)$$

$\lambda_{EC}(A, Z)$ the individual EC rate of the nucleus ${}^A_Z\text{X}$ and $n_{(A,Z)}$ is its density.

Therefore one needs to compute the nuclear abundances and the rates consistently with a given equation of state.

Within the SNA approximation (see sec. 5.2.1), this formula becomes

$$\Gamma_{EC} = \lambda_{EC}(A_{SNA}, Z_{SNA}) n(A_{SNA}, Z_{SNA}) \quad (9.3)$$

The lack of experimental data and microscopic calculations for the relevant nuclei makes it mandatory to use models and extrapolations when it comes to electron capture rates during core-collapse, in the following we will present the various models and approximations used in the computation of electron capture rates in the context of core-collapse simulations.

9.1.1 Approximation of independent particles

The first core-collapse simulations were using electron capture rates obtained by using the approximation of independent particles and within the lowest order nuclear shell model [129] (see appendix F).

Within those approximations, the reaction rate depends on the population in protons and neutrons of the nuclear energy levels involved in the process.

The dominant interaction channel is considered to be the electron capture of an electron on a proton from the $1f_{7/2}$ level, yielding a neutron on the $1f_{5/2}$ level (we say that is a $1f_{7/2} \rightarrow 1f_{5/2}$ transition). The corresponding emissivity is given by

$$j(\epsilon) = \frac{2}{7} \frac{G_F^2}{\pi} |V_{ud}|^2 (g_A)^2 n(A, Z) N_p(Z) N_h(N) (\epsilon + Q + \Delta)^2 \sqrt{1 - \frac{m_e^2 c^4}{|\epsilon + Q + \Delta|}} f_{FD}(\epsilon + Q + \Delta) \quad (9.4)$$

where $n(A, Z)$ is the density of nucleus ${}^A_Z\text{X}$, Q is the Q -value of the β -decay, given by the mass difference of the two nuclei

$$Q(A, Z) = M(A, Z - 1)c^2 - M(A, Z)c^2 \quad (9.5)$$

and $\Delta = 3 \text{ MeV}$ represents an average of the excitation energy of the daughter nucleus. This quantity is interesting as it is added to the reaction Q -value and influences the spectrum of the emitted neutrinos.

The quantities $N_p(Z)$ and $N_h(N)$ are respectively the number of protons in the level $1f_{7/2}$ and the number of holes available for neutrons in the level $1f_{5/2}$. They are given by

$$N_p(Z) = \begin{cases} 0, & \text{if } Z \leq 20 \\ Z - 20, & \text{if } 20 \leq Z \leq 28 \\ 8, & \text{if } Z \geq 28 \end{cases} \quad (9.6)$$

$$N_h(N) = \begin{cases} 6, & \text{if } N \leq 34 \\ 40 - N, & \text{if } 34 \leq N \leq 40 \\ 0, & \text{if } N \geq 40 \end{cases} \quad (9.7)$$

We see that no electron capture is possible with the transition $1f_{7/2} \rightarrow 1f_{5/2}$ for a nucleus which has a number of neutrons $N \geq 40$. This is known as the neutron shell blocking effect of electron captures [167]. This shell blocking effect is expected to have a significant influence on core-collapse, indeed neutron rich nuclei become more and more dominant in the medium during the collapse of the iron core, as mentioned in sec. 5.2.1.

A reminder of the nuclear shell model as well as additional explanations on the shell blocking effect are given in the appendix F.

9.1.2 Fit on the Q -value dependancy (LMP)

One of the most important predictions of the model presented in the previous section is that there are no electron captures on nuclei which have more than 40 neutrons because of neutron shell blocking. However, more recent work (see e.g. [168], [169]) pointed out that in such a dense and hot medium the thermal excitations and nuclear correlations play a major role : the shell closure is smeared out and electron captures become allowed on neutron rich nuclei.

In [170], Langanke *et al.* have proposed a formula (see eq. 9.8) fitted on results from improved nuclear shell models calculations, inspired by the dependance on the Q -value showed in [171].

$$\lambda_{EC}(A, Z) = \frac{\mathcal{B} \ln 2}{K} \left(\frac{T}{m_e c^2} \right)^5 \left[F_4(\eta) + 2\chi F_3(\eta) + \chi^2 F_2(\eta) \right] \quad (9.8)$$

where $\chi = \frac{Q + \Delta}{T}$ and $\eta = \frac{\mu_e - Q - \Delta}{T}$

Here T is the temperature of the medium, μ_e is the chemical potential of electrons, Q is the Q -value of the electron capture (given by eq. (9.5)) and $F_k(\eta) = \int_0^\infty x^k / (1 + e^{x-\eta}) dx$ is the Fermi integral of order k . The fit parameters proposed in [170] are $\mathcal{B} = 4.6$, $K = 6146$ s and $\Delta = 2.5$ MeV. The figure 9.1 shows, for some relevant thermodynamic conditions, this fit formula compared with detailed microscopic calculations of λ_{EC} .

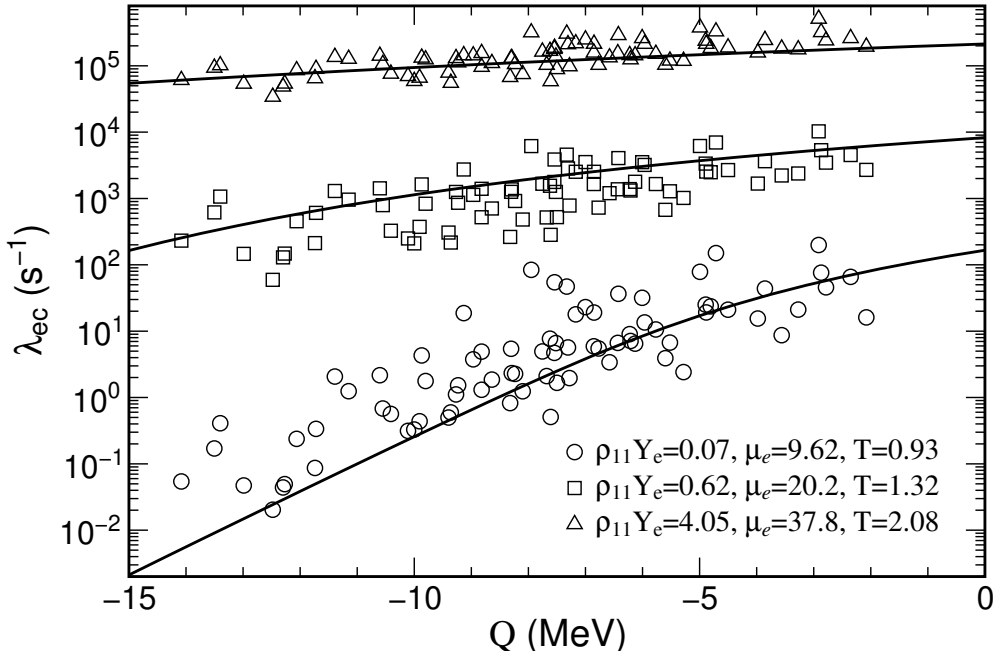


Figure 9.1: Electron capture rates on nuclei as function of Q -value for 3 different stellar conditions. Temperature T and electron chemical potential (denoted α_e on this figure) are measured in MeV. ρ_{11} measure the density in units of $10^{11} \text{ g cm}^{-3}$. The solid lines show the approximate Q -value dependance from eq. (9.8). Figure extracted from [170].

The parametrization of eq. (9.8) will be denoted LMP (for Langanke & Martinez-Pinedo) in the following.

An improvement of this model has been proposed in [172], by allowing a dependency of Δ upon various parameters such as the temperature T , the electron density n_e and nuclear parameters (isospin asymmetry and pairing). This improved parametrization will be noted ISO (for *isospin*-dependent) in the following.

As the parametrization presented in eq. (9.8) is integrated over neutrino energies, it cannot be implemented as it is in multigroup neutrino treatments. Instead we use the following expression for the neutrino emissivity (introduced in section 4.3) :

$$j(\epsilon, A, Z) = \Theta(\epsilon + Q + \Delta) \frac{\mathcal{B} \ln 2}{K} \left(\frac{1}{m_e c^2} \right)^5 \frac{(hc)^3}{4\pi c} n(A, Z) (\epsilon + Q + \Delta)^2 f_{FD}(\epsilon + Q + \Delta - \mu_e) \quad (9.9)$$

where Θ is the usual Heaviside step function.

It is straightforward to check that once integrated we recover eq. (9.8) :

$$n(A, Z)\lambda_{EC}(A, Z) = \frac{4\pi c}{(hc)^3} \int j(\epsilon, A, Z)\epsilon^2 d\epsilon \quad (9.10)$$

9.1.3 Nuclear masses and Q -values

In order to use the formulas (9.4) and (9.9), we need to be able to compute the Q -value of the β -decay for each possible electron capture, and therefore we need the nuclear masses. In this work we used nuclear masses from several sources :

- when available, experimental mass measurements [173], [174] are used
- if the experimental measurement of a mass is not available, we use the prediction of the 10-parameter model of Duflo and Zucker [175]
- if none of those data are available, we use a liquid drop model parametrization [176]

9.2 Core-collapse simulations

In order to perform a core-collapse simulation, one needs to solve equations of general relativistic hydrodynamics, which consist of Einstein field equations (9.11) coupled with the conservation equations of baryon and lepton numbers (9.12 and 9.13), and the conservation equation of stress-energy (9.14), as already discussed in the chapter 4 with eq. (4.8) and (4.9) :

$$R_{ab} - \frac{1}{2}g_{ab}R = \frac{8\pi G}{c^4}T_{ab} \quad (9.11)$$

$$\nabla_a N_B^a = 0 \quad (9.12)$$

$$\nabla_a N_L^a = 0 \quad (9.13)$$

$$\nabla_a T^{ab} = 0 \quad (9.14)$$

where R_{ab} is the Ricci tensor, R is the scalar curvature, g_{ab} is the metric, T_{ab} is the stress-energy tensor and J_B^a and J_L^a are respectively the baryon and lepton currents.

This system of equations is closed by an equation of state for hot and dense matter and a neutrino transport scheme.

In order to perform those simulations we used the CoCoNuT code [156], completed by hot equations of state from the CompOSE database [51] and the fast multigroup transport (FMT) scheme for neutrinos [120] and section 4.5.

9.2.1 The CoCoNuT code

In order to solve equations of general relativistic hydrodynamics in a fast and accurate way, the CoCoNuT code combines the use of spectral methods to solve Einstein field equations (9.11) and a high resolution shock-capturing method to solve the hydrodynamic sector [177].

The metric solver

The metric is written in the 3+1 formalism (see e.g. [178]), we have

$$ds^2 = -\alpha^2 c^2 dt^2 + \gamma_{ij}(dx^i + \beta^i dt)(dx^j + \beta^j dt) \quad (9.15)$$

where α is the *lapse*, β^i is the *shift vector* and γ_{ij} is the *3-metric*.

The metric (4.10) discussed in the chapter 4 was a particular case of this general decomposition, $\gamma_{rr} = \psi^2$, $\gamma_{\theta\theta} = r^2$ and $\gamma_{\varphi\varphi} = r^2 \sin^2 \theta$, $\beta^i = 0$ and $\gamma_{ij} = 0$ for off-diagonal terms.

In CoCoNuT, we use the IWM (for Isenberg-Matthews-Wilson) approximation, sometimes also called conformally flat condition (CFC), in which $\gamma_{ij} = \Psi^4 \hat{\gamma}_{ij}$ where $\hat{\gamma}_{ij}$ is the flat 3-metric and Ψ is a scalar field called the conformal factor. This approximation has the particularity of suppressing gravitational waves from the solutions.

It should also be stressed that the IWM approximation is exact in spherical symmetry, as it corresponds to the isotropic gauge (different from the Schwarzschild gauge used in eq. (4.10)) :

$$ds^2 = -\alpha^2(r)c^2 dt^2 + \Psi^4(r) \left(dr^2 + r^2 d\theta^2 + r^2 \sin^2(\theta) d\varphi^2 \right) \quad (9.16)$$

The IWM equations are solved by using the **Lorene** spectral solver [179], an open source library allowing to solve elliptic problems via the use of spectral methods (see e.g. [180] for a pedagogical approach on spectral methods and their application to general relativity).

The hydrodynamic solver

Equations of hydrodynamics are written in a conservative form, which allows to exploit their hyperbolicity and make use of a finite volume scheme, enforcing conservation laws with high precision (see e.g. [181] for the general relativistic case).

Since the core-collapse mechanism relies on the propagation of a shock, we need to use a specific numerical method to correctly model the problem. In CoCoNuT we make use of a *high resolution shock capture* (HRSC) scheme (see e.g. [182] for a review on numerical hydrodynamics methods in general relativity).

9.2.2 Equation of state

In a core-collapse supernova simulation, we need to use a *general purpose equation of state* for dense matter (see sec. 3.1.3), which will have to span an extreme range of temperatures, baryon densities and electron fractions. Typically in a core-collapse we need

- a baryon density n_B going from 10^{-11} fm^{-3} to 1 fm^{-3} to model the low densities of outer layers as well as the nuclear matter core
- a temperature T going from 0.1 MeV to 100 MeV to model the matter heated by the shock
- an electron fraction Y_e going from 0.01 to 0.6 to model heavily deleptonized region as well as the proton rich neutrino driven wind

In this work we used equations of state from the **CompOSE** database [51].

Most of results of this chapter were obtained by using the HS(DD2) equation of state, which relies on the statistical model of Hempel and Schaffner-Bielich [133] coupled with *relativistic mean field* (RMF) interactions using the DD2 parametrization of the nuclear interaction [158]. This equation of state is also provided with a method to compute the detailed composition in nuclei with masses from the *finite range droplet model* (FRDM) [183].

To get an idea of equation of state-dependent effects, we also used a second equation of state, denoted as RG(SLy4). It is a *nuclear statistical equilibrium* model by Raduta and Gulminelli [134], which employs the SLy4 Skyrme effective interaction [160].

9.2.3 Neutrino transport

The neutrino transport is done with the Fast Multigroup Transport (see sec. 4.5). In this study we did not include inelastic scattering nor detailed pair production, instead we used the original code from [120], with the formulas (9.4) or (9.9) for electron capture processes.

During the infall neutrinos are mostly free-streaming, and become trapped just a few milliseconds before bounce, therefore such a crude description should be enough to describe the process.

The neutrino emissivity has been computed with either the single nucleus approximation or a detailed statistical nuclear equilibrium for the composition of the medium in nuclei.

9.2.4 Initial data : the progenitor

The progenitor models used in this work come from the detailed stellar evolution models performed in [152], which have been publicly released to be used as a starting point for core-collapse simulations.

One should keep in mind that such models contain lots of uncertainties, in particular due to the mass loss by stellar wind which is complicated to model and can be significant for the most massive stars with high metallicity.

9.3 Results

This section presents the results of the study conducted in [184] regarding the influence of electron capture rates during the infall. Note that a similar sensitivity study to EC rate has been conducted in [185], but with a uniform scaling factor for all EC rates, whereas in this study we used the physically motivated EC rates prescriptions presented in section 9.1.

If not explicitly stated otherwise, all results presented in this section have been obtained in spherical symmetry, with the **s15** progenitor of [152] ($15 M_{\odot}$ with solar metallicity), and the HS(DD2) equation of state (see sec. 9.2.2). It should be stressed that the progenitors are classified with their Zero Age Main Sequence (ZAMS) mass, i.e. the mass they have at the begin of stellar evolution, which can be very different from their mass at collapse because of mass loss processes (such as stellar winds).

9.3.1 Evolution of the electron fraction

Electron captures on nuclei during infall are responsible for about 40 % of the deleptonization of the central object that will become the neutron star. Therefore a modification of electron capture rates can have a significant impact on the number of electrons present in the core at bounce time.

The figure 9.2 represents the influence of capture rates on the electron fraction in the central cell of the grid. The label Bruenn represents the 1985 approximation (see eq. (9.4) or [129]), LMP the Langanke *et al.* fit formula [170] adapted for multigroup transport (eq. (9.9)), whereas ISO the improvement proposed in [172]. The electron fraction is freezed a few milliseconds before the core bounce because the medium becomes dense enough to trap neutrinos and stop the deleptonization.

This evolution can be understood by looking at the evolution of the total electron capture rate in the same central cell, represented in figure 9.3 (as a function of baryon density, which increases with time).

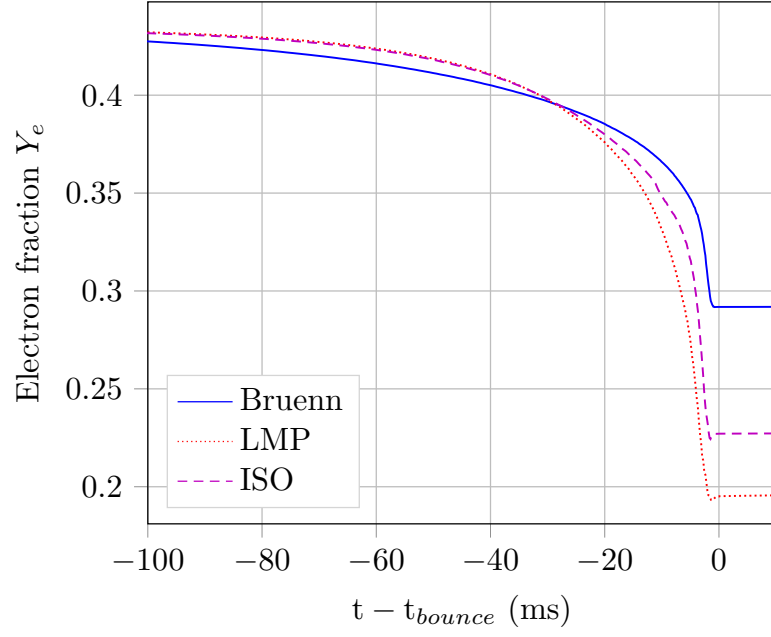


Figure 9.2: Evolution of the electron fraction as a function of time after bounce for the 3 models presented in section 9.1 [184]

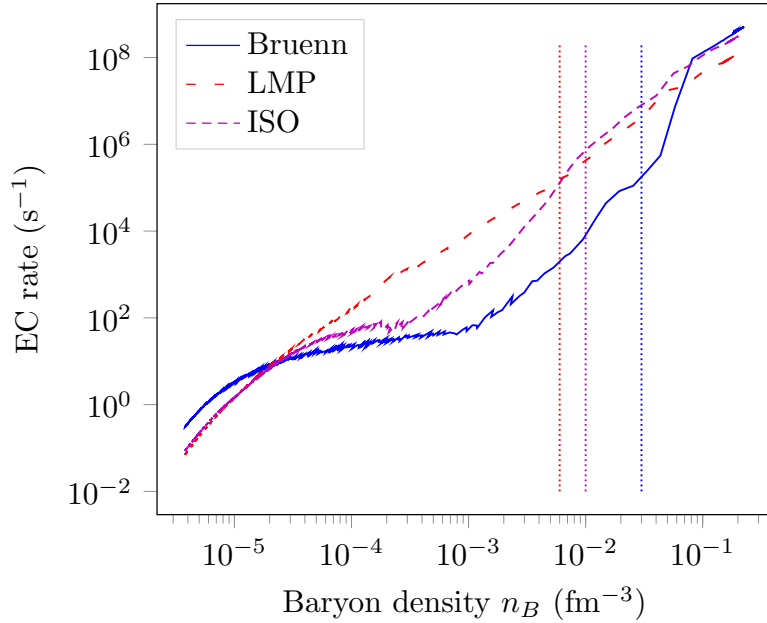


Figure 9.3: EC rate evolution (labelled by baryon density) in the central grid cell during infall using the three models presented in section 9.1. The vertical dashed lines show the density above which β -equilibrium sets in [184]

Up to a baryon density $n_B = 2 \times 10^{-5} \text{ fm}^{-3}$, electron capture rates given by the Bruenn formula (9.4) are higher than the LMP and ISO ones. Above this density this behavior gets inverted, because many neutron-rich nuclei for which the Bruenn EC rates vanishes get populated. Those figures show that such nuclei play a key role in electron captures just before the bounce and that taking them into account changes the electron fraction at bounce by about 40 %.

Regarding the electron fraction profiles in the star, figure 9.4 shows such profiles at bounce time. We see that the differences mostly appear in the central region of the collapsing core, for $r \lesssim 50 \text{ km}$. As this is the zone where neutron rich nuclei become the most abundant near the

end of the collapse, this behavior is understandable.

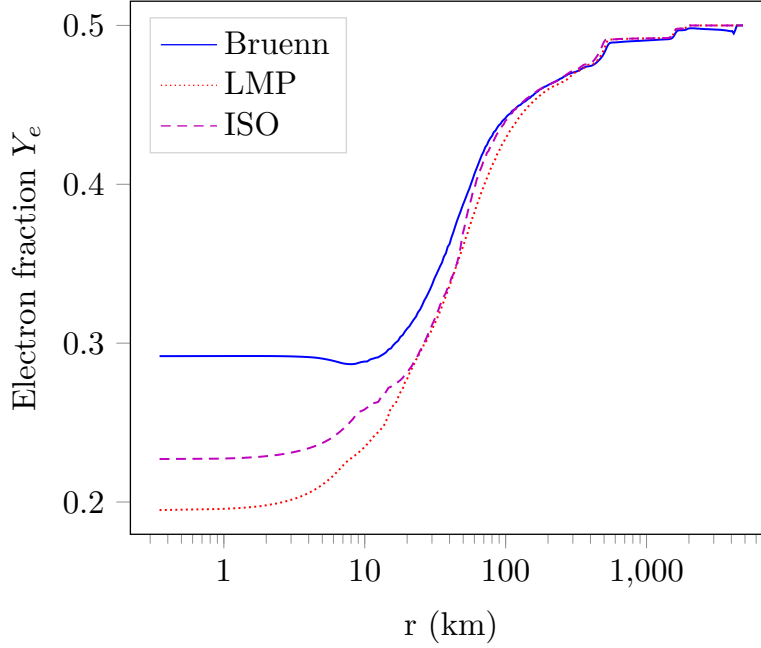


Figure 9.4: Radial profiles of the electron fraction at bounce employing the three different EC rate prescriptions in the section 9.1 [184]

9.3.2 Propagation of the shock and deleptonization burst

As the collapse of the core is essentially a free-fall, the various prescriptions for the EC rate have only a minor influence on the duration of the collapse (we see about 4 % of differences in the bounce time). But the difference of electron fraction at bounce has a major influence on the post-bounce dynamics.

Profiles of radial velocity at bounce and at two instants after bounce are shown in figure 9.5. It is clear that in the Bruenn case the shock has much more kinetic energy, it propagates faster and further than in the two other cases.

These differences can be interpreted in terms of the inner core mass. Indeed the mass of the inner core at bounce strongly depends upon the electron fraction in the inner core : it is roughly proportional to $\langle Y_e^2 \rangle$ [76]. And indeed in our models we find the inner core masses to be $0.31 M_\odot$, $0.4 M_\odot$ and $0.45 M_\odot$ for respectively the models using LMP, ISO and Bruenn rates, which is the same ordering as the core electron fraction shown figure 9.4.

A more massive inner core results in more binding energy being turned into shock kinetic energy, hence the results of figure 9.5.

Finally, the figure 9.6 illustrates the time evolution of electron neutrino luminosity a few ms before and after bounce.

Two peaks are observed, the first one corresponds to the increase of EC rates on nuclei a few ms before bounce, just before neutrino trapping occurs. When the neutrino trapping density is reached the luminosity goes down, and a secondary peak - the so called *deleptonization burst* - occurs when the shock reaches the neutrinosphere, as explained in the section 2.1.2.

Regarding the peak amplitudes, a significant dependence on the EC rate model is to be noticed. According to [185], the dependence of the peak amplitude on the EC rate relies on two effects, a low EC rate (here the case of Bruenn rates) causes the neutrinosphere to move to inner radii

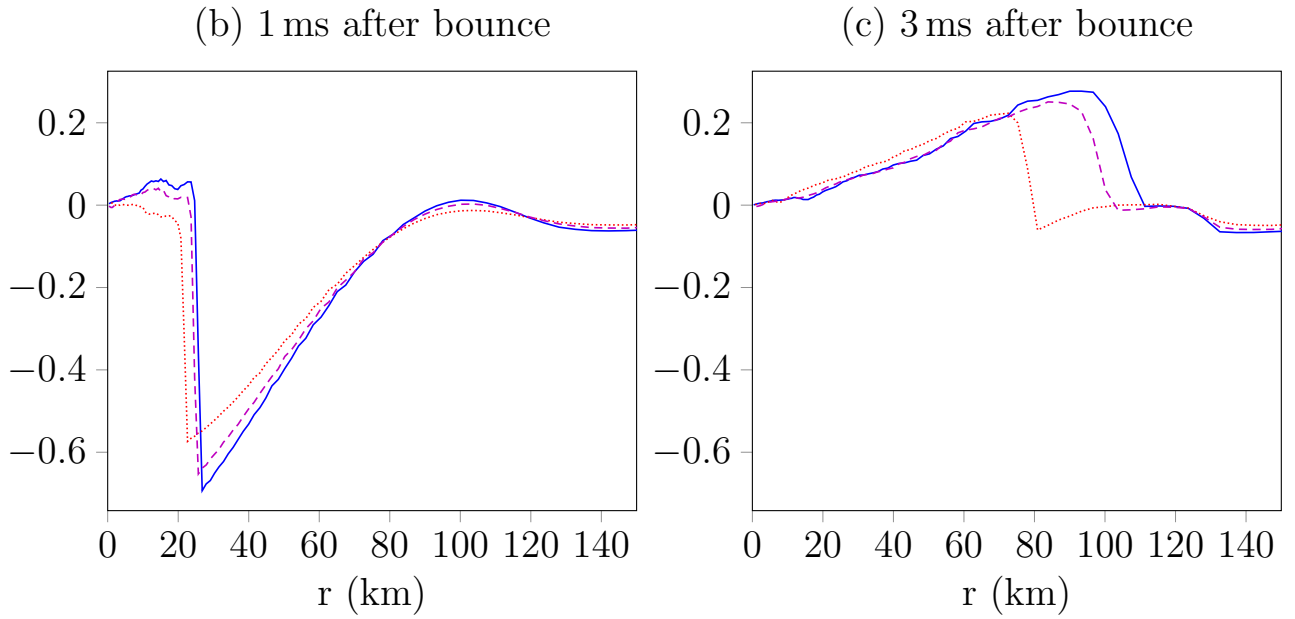


Figure 9.5: Comparison of shock propagation at different instants during the early post-bounce phase with the three different EC rate prescriptions [184]

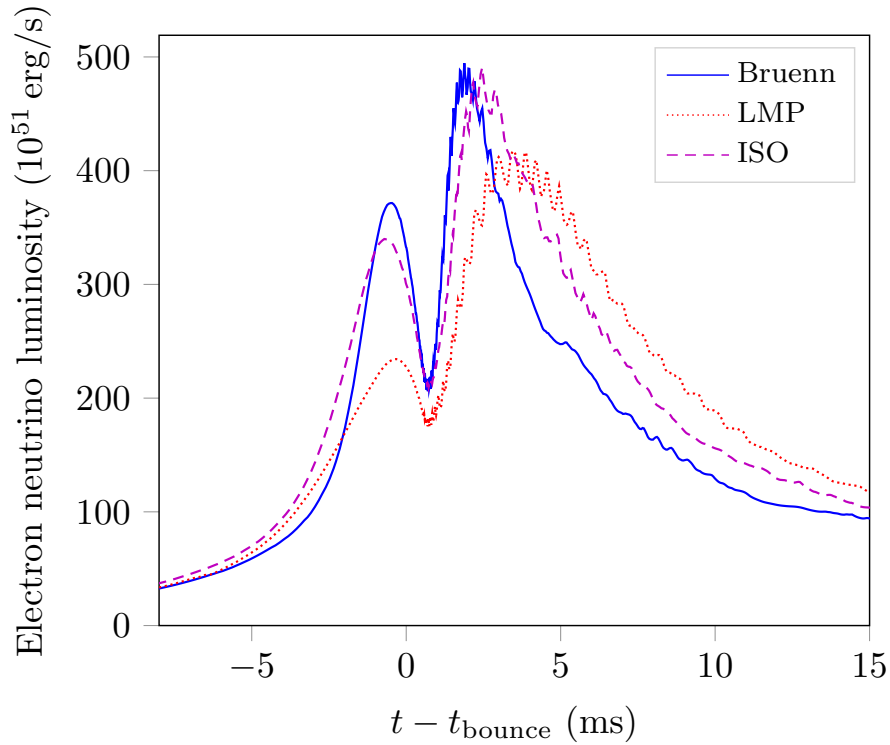


Figure 9.6: Time evolution of electron neutrino luminosity around bounce, for the three different EC rate prescriptions [184]

because of lower opacities, and also causes the shock to be stronger because of the more massive inner core. Because of those two effects, the shock reaches the neutrinosphere faster, which makes the deleptonization burst higher and sharper. In the LMP case it is the opposite : the high EC rates move the neutrinosphere far away and make the shock weaker, which gives a weaker and broader deleptonization burst.

It is worthwhile to note that the total energy carried away by electron neutrinos is roughly

independent of the EC rate model : we find 4.58×10^{51} erg in the Bruenn case, 4.90×10^{51} erg with LMP and 4.99×10^{51} erg with ISO.

9.3.3 Influence of other parameters on the infall

We have also studied the influence of other parameters on the infall evolution to estimate the relative importance of EC rate models. We have compared a nuclear statistical equilibrium (NSE) approach with the single nucleus approximation (SNA). We have also studied the influence of the equation of state and of the progenitor model.

SNA vs NSE

To estimate the influence of the SNA approach, we simulate the infall with the ISO model for electron capture rates. In SNA calculations we extract the average nucleus from the entire available NSE distribution, thermodynamic quantities are thus unchanged between SNA and NSE and we can more easily isolate neutrino reaction effects.

In the SNA case, the Q -value needed for both LMP and ISO models is computed using the nucleus obtained by rounding off the average (A, Z) to the closest integers.

The figure 9.7 presents the difference between both simulations.

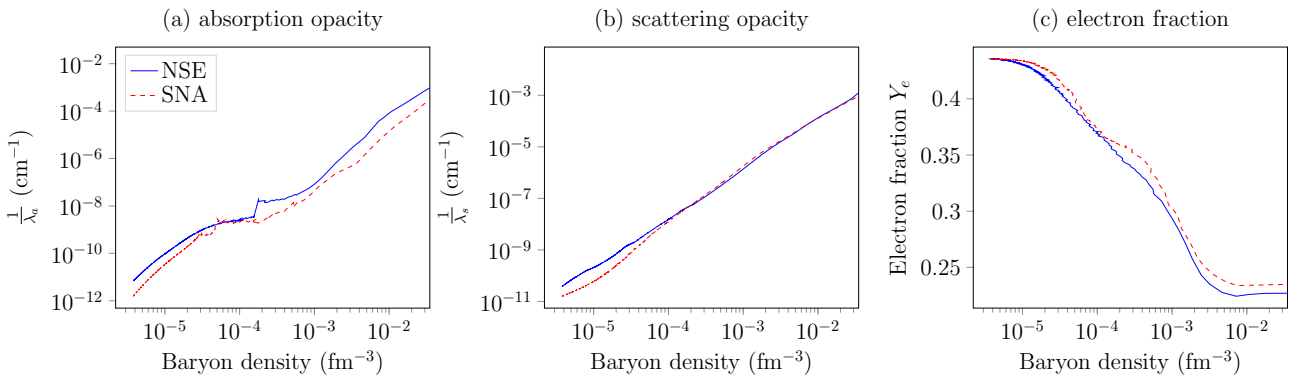


Figure 9.7: Neutrino inverse mean free path as function of baryon density in the central numerical cell with reactions computed either on a single mean nucleus (SNA) or on a statistical ensemble of nuclei (NSE) : contribution of electron capture effects only (left panel) and scattering effects only (central panel). Electron fraction time evolution for both models (right panel). [184]

As expected, most important differences appear in the density range above $n_B \gtrsim 10^{-3} \text{ fm}^{-3}$, where the nuclear distribution is large and potentially multimodal (see sec. 5.2.1). But these changes in the absorption opacity have only a minor influence on the evolution of the electron fraction (see right panel of fig. 9.7).

The previous studies comparing SNA and NSE were observing more differences between the two prescriptions, but were employing in general simplified neutrino treatments with the Bruenn rates (see e.g. [186]). As the LMP and ISO fit prescriptions are smoother over the nuclear chart, such results had to be expected.

We should stress however that all rates presented in this work average over nuclear structure effects, and that we should expect more differences between SNA and NSE if we used detailed individual microscopic rates all over the nuclear chart. But such rates are presently not available.

EoS dependence

To estimate the effect of equation of state models on the results, we have compared simulations using both extended NSE models from the HS(DD2) (Hempel *et al.* [133]) and the RG(SLy4) (Raduta and Gulminelli [134]) equations of state.

We observe very little differences between both simulations, there is almost no difference between the central value of Y_e at bounce and between the subsequent shock propagations. The only noticeable discrepancy between the two models is the prediction of the temperatures profiles, which is always larger in the HS(DD2) case.

The EoS dependence of CCSN simulation has already been addressed by several works (see e.g. [185] and [186]), and the conclusion is that there is a limited but certain effect. The very little differences observed in our case are probably due to the fact that we focused mostly on the infall, during which the density is still relatively low. And at these low densities all equations of state make similar predictions.

Progenitor dependence

The influence of the progenitor model has also been studied by performing simulations with the ISO electron capture rates using various initial profiles from [152].

In this sensitivity study we used progenitors of $15 M_\odot$, $25 M_\odot$ and $40 M_\odot$ ZAMS mass, both with solar metallicity and with $10^{-4} \times$ solar metallicity. We observe that the electron fraction and the subsequent shock propagation depend more upon the total mass on the grid than upon the details of the progenitors profiles. We thus confirm the result from Sullivan *et al.* [185], who showed that the detailed progenitor model has less influence than the electron capture rate prescription on the electron fraction at bounce.

9.3.4 Determination of the most relevant nuclei

In the previous sections we have shown that the model for electron capture rates is one of the ingredients which has the most important influence during infall. Because of this fact, this section is focused on the determination of most influential nuclei for deleptonization during infall, as theoretical and experimental work should be focused on those.

The figure 9.8 presents the time integrated deleptonization rate over the nuclear chart (for the LMP rates). Those simulations required the use of a very flexible input for the EoS and the matter composition, and therefore they have been performed with the ACCEPT code (see [189], [190] and [191]) using a perturbative method to compute the NSE distribution [192]

The nuclei represented in this figure account for about 89 % of the total time integrated electron capture rate, and can therefore be considered as the relevant set of nuclei for EC processes during the infall. Most of those nuclei are close to the $N = 50$ magic number (shell closure), in agreement with the results of [185].

The figure 9.8 also shows that detailed microscopic computations are not available for most of the relevant nuclei. Therefore any core-collapse simulation has to use a parametrization of EC rates for those nuclei, and detailed computations for those nuclei would be very welcome to make simulations with more accurate and reliable microphysics.

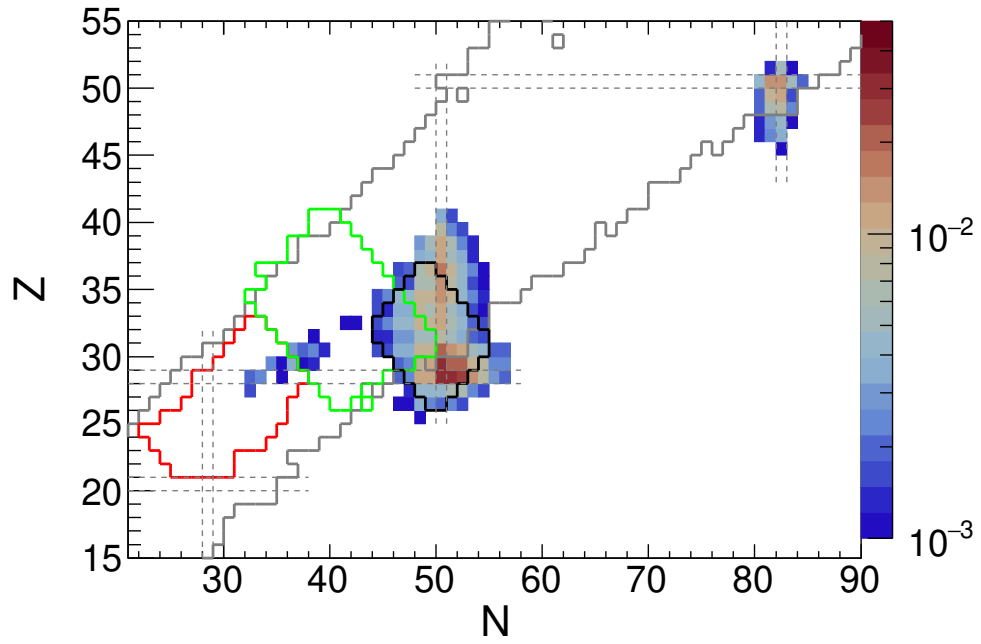


Figure 9.8: Time integrated relative deleptonization rate (color scale) associated to the different nuclear species identified by their proton Z and neutron N number [184]. The black contour indicates the most relevant nuclei for EC identified by [185] and [187]. The red and green contours indicate the nuclei for which microscopic rates are available from [169] and [188] respectively. Nuclei with experimentally known masses are situated between the grey lines.

Chapter 10

Improved charged-current reaction rates on nucleons

This chapter is focused on the various approximations used to compute the charged current reaction rates on nucleons, and the influence they have on core-collapse simulations.

$$\begin{array}{ll} p + e^- \rightleftharpoons n + \nu_e & p \rightleftharpoons n + e^+ + \nu_e \\ n + e^+ \rightleftharpoons p + \bar{\nu}_e & n \rightleftharpoons p + e^- + \bar{\nu}_e \end{array}$$

10.1 Approximations and models for charged current rates

In section 5.1.1, the general framework needed to compute reaction rates of the above processes has been presented. In particular, we saw that we need an expression for the imaginary part of the polarisation functions $\text{Im}(\Pi_V(q))$ and $\text{Im}(\Pi_A(q))$, which contain the structure of the interaction and are sensitive to the various approximations. This section details the various existing approximations and gives formulas for the polarisation functions.

Considering the equations for charged current processes presented section 5.1.1, there are two factors upon which we can act to simplify the computations :

- we can act on the phase-space integration, by neglecting the transfer of momentum to the nucleon. This is the so-called *elastic* approximation, opposed to a full-kinematic treatment
- we can act on the matrix element modeling the interaction, by choosing how to take into account the interactions between nucleons. In the simplest approximation we consider that nucleons are non-interacting with each other, and in more accurate models we take into account interactions, either at the mean field level or by adding RPA correlations

10.1.1 The Elastic approximation with non-interacting particles

As explained above, in the elastic approximation we neglect the transfer of momentum to the nucleons.

In [129], the rates are computed within this approximation by considering that the nucleons do not interact with each other. The rate of the process is then the same as in vacuum, with the

addition of Pauli blocking factors, to take into account that the final quantum states of particles may be already occupied.

With these hypotheses we obtain

$$\text{Im}(\Pi_V(q)) = \text{Im}(\Pi_A(q)) = -\pi(n_p - n_n) \delta(q_0 + \mu_n - \mu_p + m_p c^2 - m_n c^2) \quad (10.1)$$

where n_n and n_p are respectively the density of neutrons and protons, and μ_n and μ_p are the chemical potentials of neutrons and protons

The integral over the electron momentum of eq. (5.1) can then be done analytically and for the process $p + e^- \rightleftharpoons n + \nu_e$ we obtain the following emissivity and inverse mean free path :

$$j(\epsilon) = \frac{G_F^2}{\pi} |V_{ud}|^2 (1 + 3g_A^2) (n_p - n_n) (\epsilon + Q)^2 \sqrt{1 - \frac{m_e^2 c^4}{|\epsilon + Q|}} \times [1 + f_{BE}(Q + \mu_p - \mu_n)] [f_{FD}(\epsilon + Q - \mu_e)] \quad (10.2)$$

$$\frac{1}{\lambda(\epsilon)} = \frac{G_F^2}{\pi} |V_{ud}|^2 (1 + 3g_A^2) (n_p - n_n) (\epsilon + Q)^2 \sqrt{1 - \frac{m_e^2 c^4}{|\epsilon + Q|}} \times [f_{BE}(Q + \mu_p - \mu_n)] [1 - f_{FD}(\epsilon + Q - \mu_e)] \quad (10.3)$$

where $Q = m_n c^2 - m_p c^2$ is the Q -value of the neutron decay.

The corresponding rates for the three other processes are obtained in a similar manner.

It is worth mentioning that within the elastic approximation the proton decay process $p \rightleftharpoons n + e^+ + \nu_e$ is forbidden. Indeed by neglecting the momentum transfer the energy transferred to the nucleons is only the mass difference and we reach the same conclusions as in vacuum, despite the fact that proton decay can always occur if $\mu_p > \mu_n$.

10.1.2 The Elastic approximation with Mean Field corrections

Because of the nuclear interactions, a nucleon in the medium is in interaction with all other nucleons in its interaction range. In the mean field approximation (MF) we model the effect of all other nucleons by an effective interaction potential. By doing so we also neglect 2-particle correlations in the distributions functions, i.e. the state of the system is entirely characterised by the 1-particle distribution functions at equilibrium.

In this approximation the nucleons still interact with each other, via a mean field potential. Therefore the nucleons acquire an effective mass m_N^* and their energies are shifted by the mean field potential U_N . It is also convenient to define an effective chemical potential $\mu_N^* = \mu_N - U_N$ (see [126]).

The changes to the above formula are straightforward to implement : one simply has to replace the masses by the effective masses and the chemical potentials by the effective ones in the formula (10.1) for the polarisation functions :

$$\text{Im}(\Pi_V(q)) = \text{Im}(\Pi_A(q)) = -\pi(n_p - n_n) \delta(q_0 + \mu_n^* - \mu_p^* + m_p^* c^2 - m_n^* c^2) \quad (10.4)$$

As an example, the emissivity and mean free path for the process $p + e^- \rightleftharpoons n + \nu_e$ are then

given by :

$$j(\epsilon) = \frac{G_F^2}{\pi} |V_{ud}|^2 (1 + 3g_A^2) (n_p - n_n) (\epsilon + Q^*)^2 \sqrt{1 - \frac{m_e^2 c^4}{|\epsilon + Q^*|}} \times [1 + f_{BE}(Q^* + \mu_p - \mu_n)] [f_{FD}(\epsilon + Q^* - \mu_e)] \quad (10.5)$$

$$\frac{1}{\lambda(\epsilon)} = \frac{G_F^2}{\pi} |V_{ud}|^2 (1 + 3g_A^2) (n_p - n_n) (\epsilon + Q^*)^2 \sqrt{1 - \frac{m_e^2 c^4}{|\epsilon + Q^*|}} \times [f_{BE}(Q^* + \mu_p - \mu_n)] [1 - f_{FD}(\epsilon + Q^* - \mu_e)] \quad (10.6)$$

where the effective Q -value of the neutron decay is

$$Q^* = m_n^* c^2 - m_p^* c^2 + U_n - U_p \quad (10.7)$$

10.1.3 Full kinematics within the Mean Field theory (MF)

The next step is to relax the Elastic approximation and consider full-kinematics. The leptons now transfer some momentum to the nucleons. Note that in this work we have considered non-relativistic nucleons, in contrast to the work of [193], which considered full relativistic kinematics.

Within the mean field approximation, the imaginary part of the polarisation tensors are

$$\text{Im}(\Pi_V(q)) = \text{Im}(\Pi_A(q)) = \text{Im}(L(q)) \quad (10.8)$$

where $L(q)$ is the Lindhard function

$$L(q) = \lim_{\eta \rightarrow 0} \int \frac{d^3 k}{(2\pi\hbar)^3} \frac{f_{FD}(\epsilon_k^p - \mu_p^*) - f_{FD}(\epsilon_{k+q}^n - \mu_n^*)}{\epsilon_e - \epsilon_\nu + \epsilon_k^p - \epsilon_{k+q}^n + i\eta} \quad (10.9)$$

with the notation $\epsilon_k^{p/n} = \frac{\vec{k}^2}{2m_{n/p}^*} + m_{n/p}^*$

Note that the integral over the electron momentum (5.1) can no longer be carried out analytically. The section 10.2.1 will present the interpolation procedure used to effectively implement these rates in core-collapse and proto-neutron star simulations with a minimal computation time.

10.1.4 Full kinematics with the Random Phase Approximation (RPA)

To go beyond the mean field theory and include some nucleon-nucleon correlation effects in the distribution function, we use the so-called "Random Phase Approximation" (RPA). It is one of the oldest non-perturbative methods to compute ground-state correlation energies, which was first introduced to study the effect of correlations between electrons in solids [194]. Since then this approximation has also been used in molecular chemistry and in nuclear physics (see [195] for the case of asymmetric nuclear matter).

In [195], the RPA is studied in the Landau approximation, which is equivalent to replace the polarisation functions by

$$\text{Im}(\Pi_V(q)) = \text{Im} \left(\frac{L(q)}{1 - 2f_{cc}L(q)} \right) \quad (10.10)$$

$$\text{Im}(\Pi_A(q)) = \text{Im} \left(\frac{L(q)}{1 - 2g_{cc}L(q)} \right) \quad (10.11)$$

where explicit expressions for the factors f_{cc} and g_{cc} are given in [195].

But these expressions present instabilities at high densities for the axial channel with Skyrme nuclear forces [196]. In order to avoid this potential problem, in [126] we have used two other prescriptions :

- in the RPA t'_3 model, a repulsive term is added in $\text{Im}(\Pi_A(q))$ at high densities : we replace g_{cc} by $g_{cc} + t'_3 n_B^2/4$ [197]
- in the RPA $\pi\rho$ model, a microscopically motivated correction based on interactions with the π and ρ mesons is employed [198]

More details are given on those various RPA models in [126].

10.2 Resulting neutrino opacities

10.2.1 Tabulated rates and interpolation procedure

As rates with full kinematics (with either the mean field approach or the RPA) cannot be computed analytically, this begs the question of what is the most efficient method to implement them in a simulation.

The first idea to come may be to build four-dimensional tables of rates, depending upon the baryon density n_B , the temperature T , the electron fraction Y_e and the neutrino energy ϵ . But as the neutrino energy range span over several orders of magnitude (we need rates from $\epsilon \approx 0.1$ MeV to 200 MeV in order to simulate proto-neutron star cooling) the numerical size of tables needed to have a sufficient precision on the rates can become quite significant.

The solution retained in [126] was to build a polynomial fit on $\ln(\epsilon)$:

$$\ln(\kappa^*(\epsilon)) = \sum_{n=0}^N c_n(T, n_B, Y_e) \xi^n \quad (10.12)$$

where κ^* is the *opacity corrected for stimulated absorption*, as introduced by equation (4.34), whereas c_n are the tabulated coefficients of the fit and $\xi \in [-1, 1]$ is an affine mapping $\ln \epsilon = \alpha \xi + \beta$.

With this solution the tables are of acceptable size for numerical simulations and the computational cost of implementing these improved rates is minimal.

The tabulated coefficients used in [126] are available in the **CompOSE** database [51].

10.2.2 Some example of opacities

In this section we present an example of results regarding the charged current reaction rates for some thermodynamic conditions relevant in core-collapse supernova, in order to show the influence of the various approximations.

To do so, we perform a fiducial core-collapse supernova simulation, by using the core-collapse simulation code presented in section 9.2. We use the **s15** progenitor from [152] (15 M_\odot with solar metallicity) and two equations of state : HS(DD2) [133] and RG(SLy4) [134], already presented in the section 9.2.2. Our results are presented in figures 10.1 and 10.2.

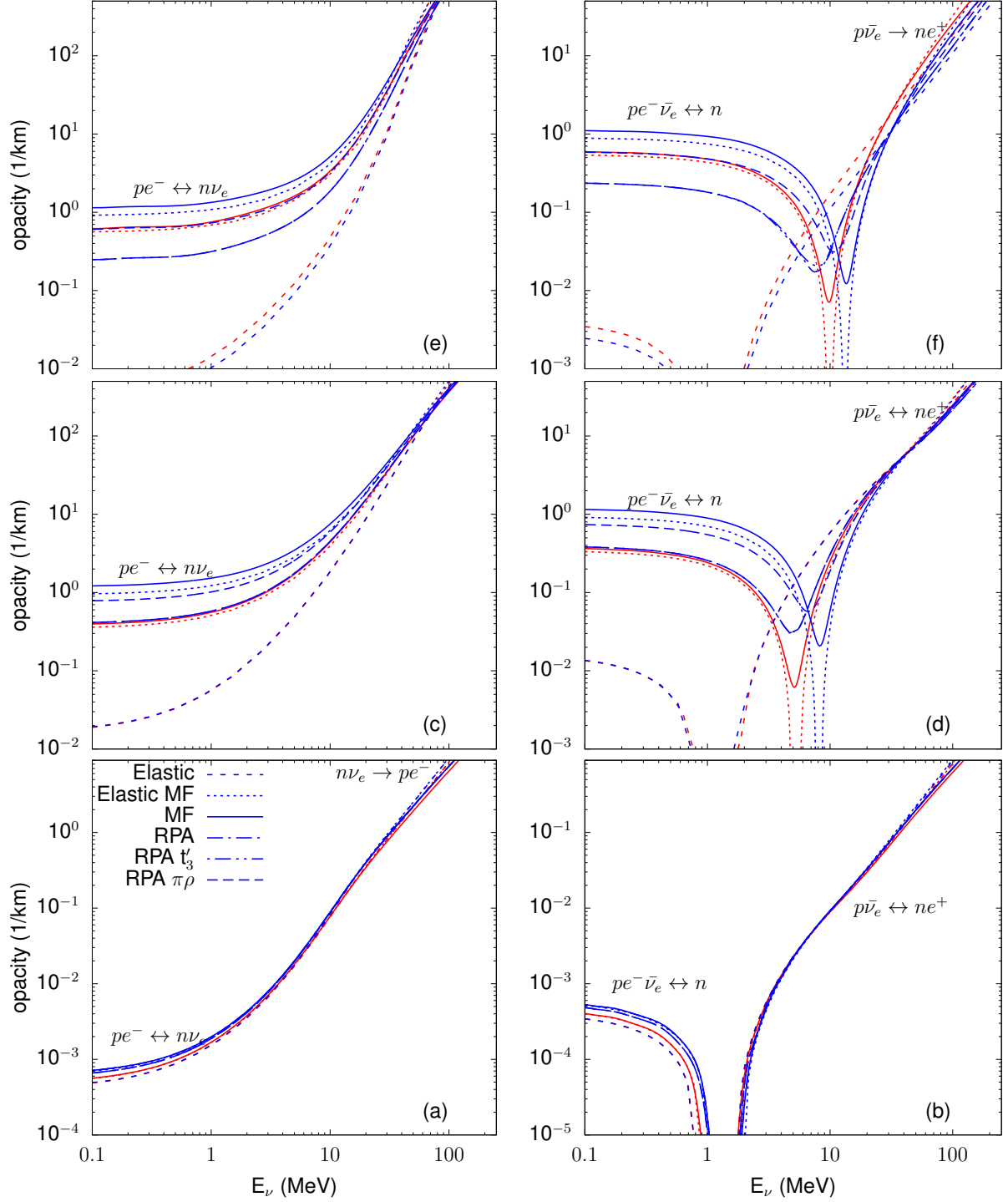


Figure 10.1: Electron neutrino (left) and anti-neutrino (right) opacities κ^* for $T = 12$ MeV, $n_B = 0.01 \text{ fm}^{-3}$ and $Y_e = 0.1$ (upper panels), $T = 19$ MeV, $n_B = 5 \times 10^{-3} \text{ fm}^{-3}$ and $Y_e = 0.1$ (middle panels), and $T = 5$ MeV, $n_B = 10^{-4} \text{ fm}^{-3}$ and $Y_e = 0.1$ (lower panels). These correspond to typical conditions close to the neutrinosphere in a CCSN from our fiducial simulation. The different line types distinguish the different approximations and results with HS(DD2) are indicated in red, whereas those with RG(SLy4) are in blue. The dominant processes contributing to the opacities in a certain energy domain are mentioned in the figure, too.

In these figures, the various line types corresponds to the various approximations presented earlier in this chapter :

- the label *Elastic* corresponds to the Elastic approximation with non-interacting nucleons
- the label *Elastic MF* corresponds to the Elastic approximation with Mean Field corrections
- the label *MF* corresponds to the rates computed with full-kinematics in the Mean Field theory
- the label *RPA* corresponds to the rates computed with full-kinematics with RPA correlations in the Landau approximation [195]
- the label *RPA t'_3* corresponds to the rates computed with full-kinematics with RPA correlations implemented with the additional repulsive term [197]
- the label *RPA $\pi\rho$* corresponds to the rates computed with full-kinematics with RPA correlations implemented with the microscopically motivated $\pi\rho$ model [198]

Note that because of their high computational cost, RPA rates have been computed only for the equation of state RG(SLy4).

We clearly see that at low enough densities (see fig. 10.1, panels (a) and (b), for $n_B = 10^{-4} \text{ fm}^{-3}$) the differences between the various approximations are very small. This result was to be expected, for two reasons :

- correlation effects only occur at very high densities, where the average distance between nucleons is small. Therefore RPA corrections are expected to have a negligible influence at low densities
- regarding momentum transfer, the situation is quite similar to the case of scattering off nucleons, already discussed in the section 5.1.2 : at low densities and temperatures only small momentum transfer are involved, which justifies the elastic approximation

The situation is different at high densities. For $n_B = 5 \times 10^{-3} \text{ fm}^{-3}$ (see fig. 10.1, panels (c) and (d)), we see that the elastic approximation is still valid, as the small differences between the *Elastic MF* and *MF* models tend to show. But the Mean Field corrections are quite significant, with at least two noticeable effects :

- the reaction threshold present for antineutrinos reactions is shifted by $Q^* - Q$
- reactions rates of low energy neutrinos are much higher

RPA correlation have a similar but opposite effect : they tend to decrease the shift of the threshold and the reaction rate of low energy neutrinos.

Finally, we see that all models make the same predictions for high energy neutrinos, as all approximations are equivalent in this case.

Another interesting comparison to make is between the effects of the choice of equation state on the rates and the effect of the approximation used to compute the charged currents (CC). We see that if at $n_B = 5 \times 10^{-3} \text{ fm}^{-3}$ both parameters (the choice of EoS and the choice of the CC prescription) have similar effects on the rates, at higher densities the effect of the CC prescription tends to have bigger effects than the choice of the equation of state (see fig. 10.1, panels (e) and (f)).

Finally, at even higher densities we see that the full kinematics become important and that the elastic approximation is no longer sufficient, which means that the momentum transfer to the nucleons becomes important (see fig. 10.2, panels (c) and (d)). This observation is similar to

the trend observed in the computations of [193], where the authors used mean field theory and full relativistic kinematics.

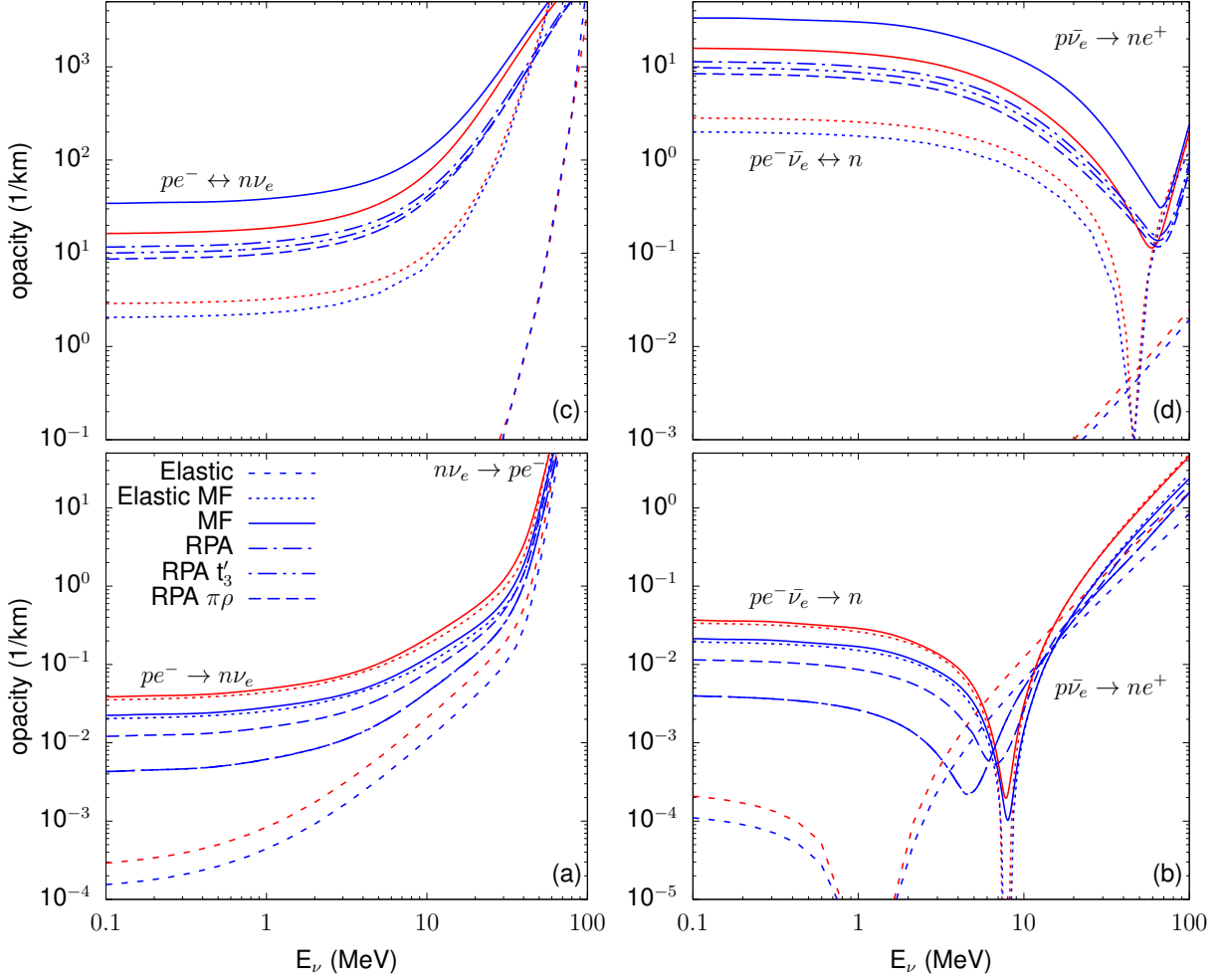


Figure 10.2: Electron neutrino (left) and anti-neutrino (right) opacities κ^* for $T = 8$ MeV, $n_B = 0.11 \text{ fm}^{-3}$ and $Y_e = 0.05$ (upper panels), and $T = 5$ MeV, $n_B = 0.01 \text{ fm}^{-3}$ and $Y_e = 0.15$ (lower panels). The different line types distinguish the different approximations and results with HS(DD2) are indicated in red, whereas those with RG(SLy4) are in blue. The dominant processes contributing to the opacities in a certain energy domain are mentioned in the figure [126]

To summarise our conclusions, we see that if the approximation made in the computation of charged currents has very little influence on neutrinos with an energy higher than a few tens of MeV, its influence on neutrinos of lower energy can be quite significant. This observation might be of importance for core-collapse, proto-neutron star and binary merger simulations.

10.3 Influence on a core-collapse

In this section the results of core-collapse simulations using the various approximations for charged current processes will be discussed.

We have again used the core-collapse simulation code presented in section 9.2 with the HS(DD2) [133] and RG(SLy4) [134] equations of state. The results presented here have been obtained with the s15 progenitor from [152] ($15 M_\odot$ with solar metallicity), but we obtained similar

conclusions with the progenitors **u18** ($18 M_{\odot}$ with $10^{-4} \times$ solar metallicity) and **u40** ($40 M_{\odot}$ with $10^{-4} \times$ solar metallicity).

10.3.1 Pre-bounce deleptonization

As already discussed in chapter 9, the infall phase is dominated by electron captures on neutron-rich nuclei, therefore we expect the charged current prescription for free nucleons to have only a small influence during this phase.

The figure 10.3 presents the electron fraction profiles at bounce. These profiles are presented as a function of the enclosed baryon number and not as a function of radius, this choice allows to account for possible time shifts at bounce.

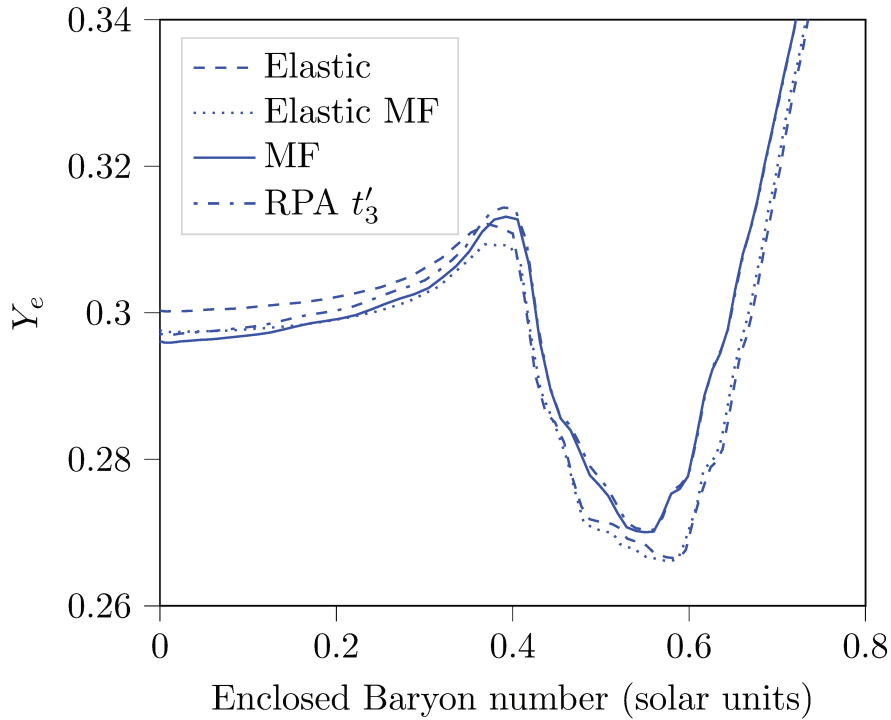


Figure 10.3: Profiles of the electron fraction at bounce as a function of the enclosed baryon mass, employing different approximation schemes to compute charged-current neutrino-nucleon interaction rates [126]

Indeed we see that the differences between the models remain small.

10.3.2 Post-bounce evolution

As discussed earlier in this chapter, we expect noticeable differences of behaviour for the case of low energy neutrinos (i.e. for $\epsilon_{\nu} \leq 10$ MeV).

The figure 10.4 presents the evolution of early post-bounce luminosity (as defined by eq. (4.29)) for four prescriptions of charged current reaction rates.

We see that the luminosities are very similar despite the differences introduced by the various prescriptions. This is because at this stage the neutrino emission is dominated by medium energy neutrinos of about 10 – 20 MeV, for which the differences introduced in the charged current rates remain small (see fig. 10.1 and 10.2).

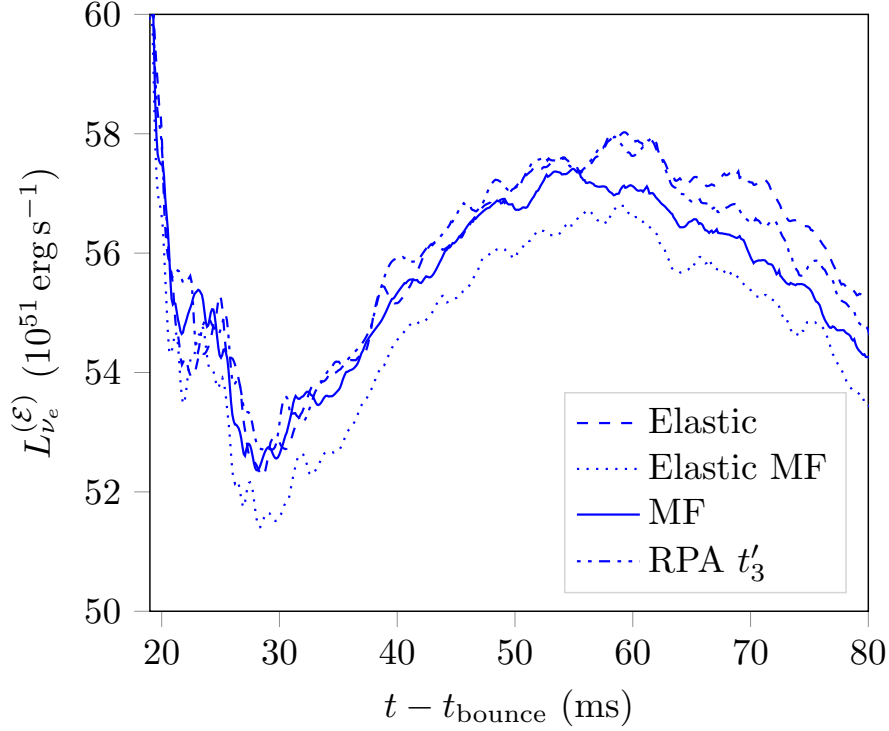


Figure 10.4: Total neutrino luminosities as a function of time after bounce. [126]

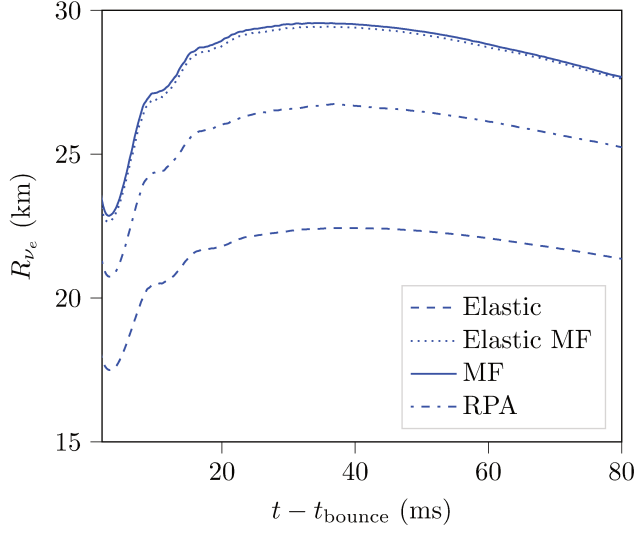
Let us now have a look at the transport properties of low energy neutrinos (below 10 MeV). The figure 10.5 shows the early post-bounce evolution of neutrinosphere radii, for electrons (anti-)neutrinos of 2 MeV and 14 MeV.

The neutrinosphere radii are computed with the definition given by eq. (2.26).

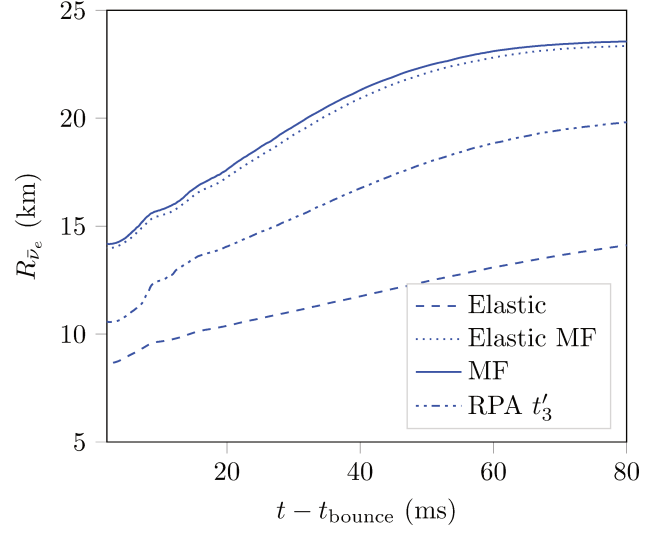
In this figure we recover the fact the trapping of neutrinos strongly depends on their energy : low energy neutrinos escape much more easily than high energy ones, and decouple from matter at small radii.

Now regarding the influence of the various prescriptions for charged current processes, we see by the small difference between the *Elastic MF* and the *MF* cases that the elastic approximation has a very small effect. But the prescription for the interaction between nucleons (non-interacting, mean field or with RPA correlations) has a significant effect. And despite the fact that these low energy neutrinos have only a marginal contribution to the luminosity, the modification of the transport properties in the central area may have an influence on the subsequent proto-neutron star evolution.

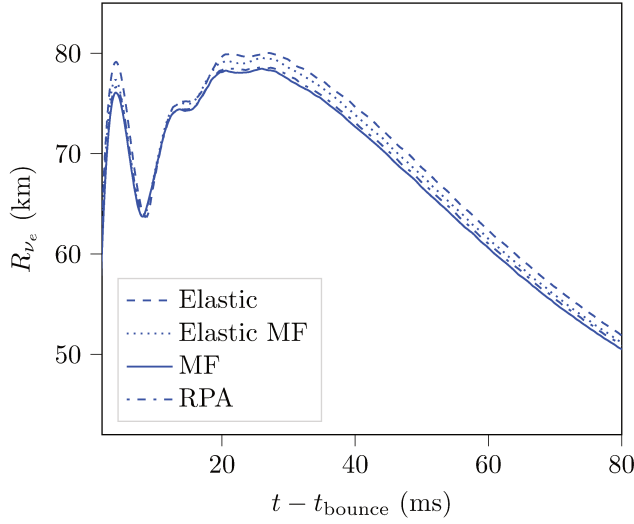
To conclude this chapter, the study presented here showed the feasibility of employing detailed state-of-the-art reaction rates for charged currents in core-collapse supernova simulations. If the simulations presented here are not pushed far enough to obtain significant differences, some important effects can be expected on longer timescales, in particular when the star cools down and that neutrinos below 10 MeV become dominant in the emission.



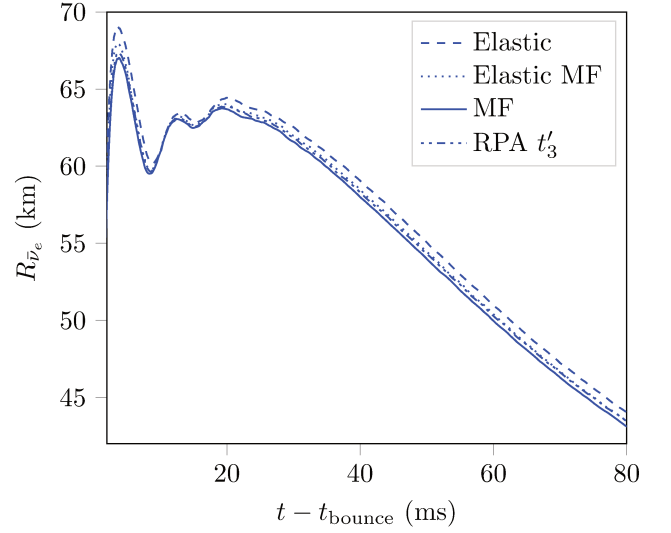
(a) Electron neutrino ν_e , energy $\epsilon_\nu = 2$ MeV



(b) Electron antineutrino $\bar{\nu}_e$, energy $\epsilon_\nu = 2$ MeV



(c) Electron neutrino ν_e , energy $\epsilon_\nu = 14$ MeV



(d) Electron antineutrino $\bar{\nu}_e$, energy $\epsilon_\nu = 14$ MeV

Figure 10.5: Neutrinosphere radii of ν_e and $\bar{\nu}_e$, as a function of time after bounce, for two different neutrino energies. [126]

Chapter 11

PNS evolution with improved reaction rates on nucleons

This chapter is the continuation of the work started in chapter 10, which was focusing on the influence of improved prescriptions for the computation of charged current rates in CCSN simulations. Here we look at the longer term evolution by using these improved prescriptions in proto-neutron star cooling simulations [150].

We will consider the following charged current processes :



11.1 Charged current rates and PNS cooling

If PNS simulations start in conditions close to those encountered in CCSN simulations, the PNS will gradually move away from these conditions as it cools down. Therefore the needs in charged current rates are slightly different in both simulations.

11.1.1 Failure of the elastic approximation

The elastic approximation presented in section 10.1.1 is commonly used in CCSN simulations, as it comes with an analytic formula for the rates and yields good results at low densities and/or high neutrino energies. But because this approximation neglects the transfer of momentum to the nucleons, the energy exchanged between the nucleons is a fixed quantity which depends only on their masses and interaction potentials. This strongly restricts the emissivity spectrum.

As a consequence there is a clear discrepancy between the predictions of this approximation at low temperatures and the formulas commonly used in neutron star cooling, which rely on the Fermi surface approximation. In particular we do not recover the dURCA threshold condition (5.10). Another issue is that some processes such as the proton decay $p \rightarrow n + e^+ + \nu_e$ are completely forbidden within the elastic approximation.

Therefore, if the elastic approximation might provide good results at the beginning of the simulation, it will inevitably fail when the PNS reaches neutrino transparency. This is why in this study we did not consider the elastic approximation but only rates computed with full kinematics, in the mean field approximation (see sec. 10.1.3) or the random phase approximation (see sec. 10.1.4).

11.1.2 Modified URCA processes

As discussed in section 5.1.1, at low temperatures the charged current processes discussed above are kinematically forbidden unless the proton fraction exceeds roughly 11 %. They can also become strongly suppressed when the final state Pauli blocking requires large energy and momentum transfer (see e.g. [4]), in which case the so-called modified URCA (mURCA) processes can become dominant. The mURCA can even have significant effects on the rates at relatively high temperatures : in [4], the authors notice important effects at $T = 8 \text{ MeV}$ and $n_B = 0.02 \text{ fm}^{-3}$.

As a reminder, they involve a spectator nucleon N which allows to lift the kinematical restriction evoked above :

$$\begin{aligned} p + e^- + N &\rightleftharpoons n + \nu_e + N & p + N &\rightleftharpoons n + e^+ + \nu_e + N \\ n + e^+ + N &\rightleftharpoons p + \bar{\nu}_e + N & n + N &\rightleftharpoons p + e^- + \bar{\nu}_e + N \end{aligned}$$

In proto-neutron star cooling, the kinematic restrictions are never really an issue, but as the temperature drops the Pauli blocking effect on the final state can strongly suppress the direct processes, and therefore modified URCA processes should play an important role when this condition is met [4].

As explained in section 5.1.1, there have not been many works focused on mURCA processes in the context of hot matter. In [4], the authors adapted the phenomenological approach developed in [199] to the case of neutral current processes, which relies on the idea that the presence of the spectator nucleon leads to collisional broadening. This effect is incorporated as a finite lifetime τ of the quasi-particle in the nuclear response. Since the vector contribution $\text{Im}(\Pi_V(q))$ vanishes in the elastic limit, it is generally assumed that the axial contribution $\text{Im}(\Pi_A(q))$ dominates, such that the collisional broadening effect is incorporated only in the axial part. In practice it enters the Lindhard function (10.9) used to determine the axial polarisation function $\text{Im}(\Pi_A(q)) = \text{Im}(L_{\text{mURCA}}(q))$ as

$$L_{\text{mURCA}}(q) = \int \frac{d^3k}{(2\pi\hbar)^3} \frac{f_{FD}(\epsilon_k^p - \mu_p^*) - f_{FD}(\epsilon_{k+q}^n - \mu_n^*)}{\epsilon_e - \epsilon_\nu + \epsilon_k^p - \epsilon_{k+q}^n + i\hbar/\tau} \left(1 - \frac{i\hbar}{\tau} \frac{1}{\epsilon_{k+q}^n - \epsilon_k^p} \right) \quad (11.1)$$

The equation (10.9) is recovered in the $\tau \rightarrow \infty$ limit. The values for the quasi-particle lifetime τ are taken from [200].

It should be stressed that this is a phenomenological model for the mURCA process, which should not be considered as quantitatively reliable. The contribution of modified URCA to the vector channel is neglected and the values of τ obtained in [200] are valid only in some specific thermodynamic conditions.

Nevertheless, this simple model should cover the main effects of collisional broadening on charged currents processes, which are the elimination of reactions thresholds (such as the thresholds presents in the antineutrino opacities, see fig. 10.1 and 10.2) and the global enhancement of reaction rates (by allowing more kinematic freedom). These effects will be illustrated in the next section.

Therefore this prescription should be sufficient in our case as the main goal of this work is to present the possible effects of mURCA and motivate further studies on the subject.

11.1.3 Example of charged-current rates relevant in PNS cooling conditions

We present here an example of charged-current opacities in conditions relevant in PNS cooling, in order to show the influence of the various prescriptions.

The figure 11.1 represent the opacities as functions of the energy of the electron (anti-)neutrino, in conditions close to neutrino transparency. They have been computed with the RG(SLy4) equation of state [134]. Various line types corresponds to the various prescriptions for charged-currents :

- the label *MF* indicates the rates computed with full-kinematics in the Mean Field approximation, discussed in section 10.1.3
- the label *MF+MURCA* indicates the MF rates for dURCA with the collisional broadening term caused by the spectator nucleon
- the label *RPA t'_3* indicates the rates computed with full-kinematics with RPA correlations implemented with the additional repulsive term [197], discussed in section 10.1.4

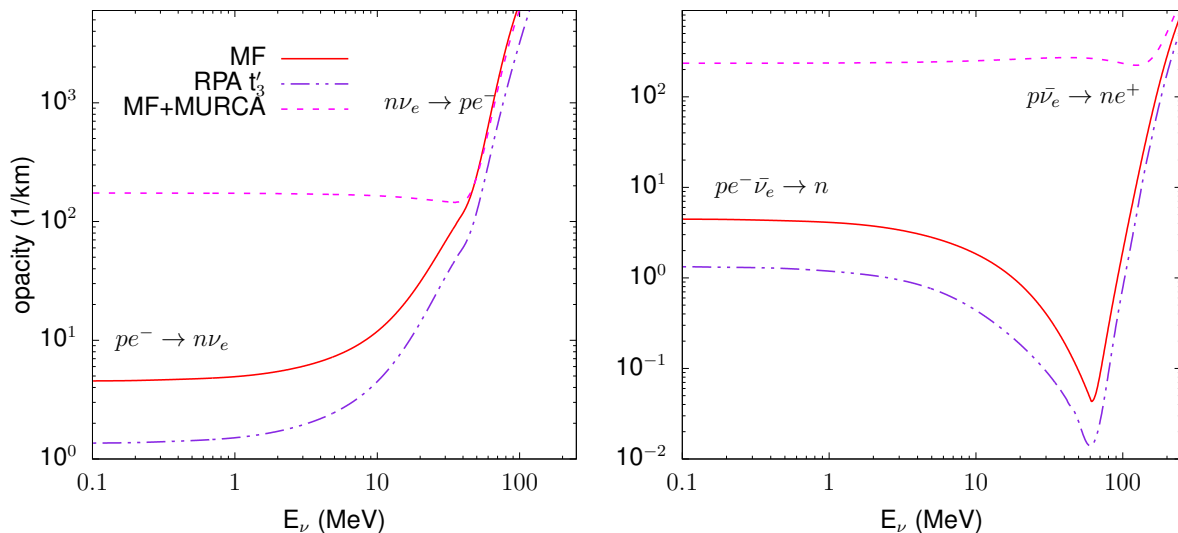


Figure 11.1: Electron neutrino (left) and antineutrino (right) opacities κ^* for $T = 5$ MeV, $n_B = 10^{-1} \text{ fm}^{-3}$ and $Y_e = 0.1$. These correspond to typical conditions in the PNS close to neutrino transparency. The dominant processes contributing to the opacities in a certain energy domain are mentioned in the figure, too.

The effect of RPA correlations is the same as discussed in section 10.2.2, they tend to decrease the reaction rate of "low" energy neutrinos (which at this low temperature are dominant in the PNS).

Now regarding the effect of collisional broadening, we see that it clearly compensates the strongly suppressed rates at low energies. We see that in these conditions the mean free path of neutrinos $\lambda = 1/\kappa^*$ is of roughly 0.1 km without collisional broadening and of roughly 0.005 km with this effect. Therefore taking into account modified URCA effects could slightly delay the transition to neutrino transparency.

This result should nevertheless be taken with caution. As explained in the previous section, the values for the quasi-particle lifetime τ are not valid in all conditions, and some additional work on the subject is required to truly quantify the effects of collisional broadening.

11.2 Results of simulations

In this section the results of proto-neutron star cooling simulations using the various approximations for charged current processes will be discussed.

The initial data have been computed as in section 6.2, with the CoCoNuT code, starting from the s15 progenitor from [152] (15 M_{\odot} with solar metallicity) and using the RG(SLy4) equation of state [134]. The prescription for charged current interactions used to compute these initial data are consistent with the prescription used in the PNS cooling simulation (i.e. we built an initial model for each prescription).

The PNS cooling simulation is then also performed with the RG(SLy4) equation of state.

11.2.1 Effect on the PNS evolution

We see very little effects from those various prescriptions on the early proto-neutron star evolution during the convective phase. But some differences start to appear when the convection stops and the luminosity starts to drop. Indeed the differences between the rates are more pronounced at relatively low neutrino energies, and therefore they are expected to have an influence once the neutron star is cold enough. This is shown in the figure 11.2, which represents the evolution of electron neutrino luminosities as a function of time. The electron anti-neutrinos luminosity is not represented but the observations are very similar to the case of electron neutrinos.

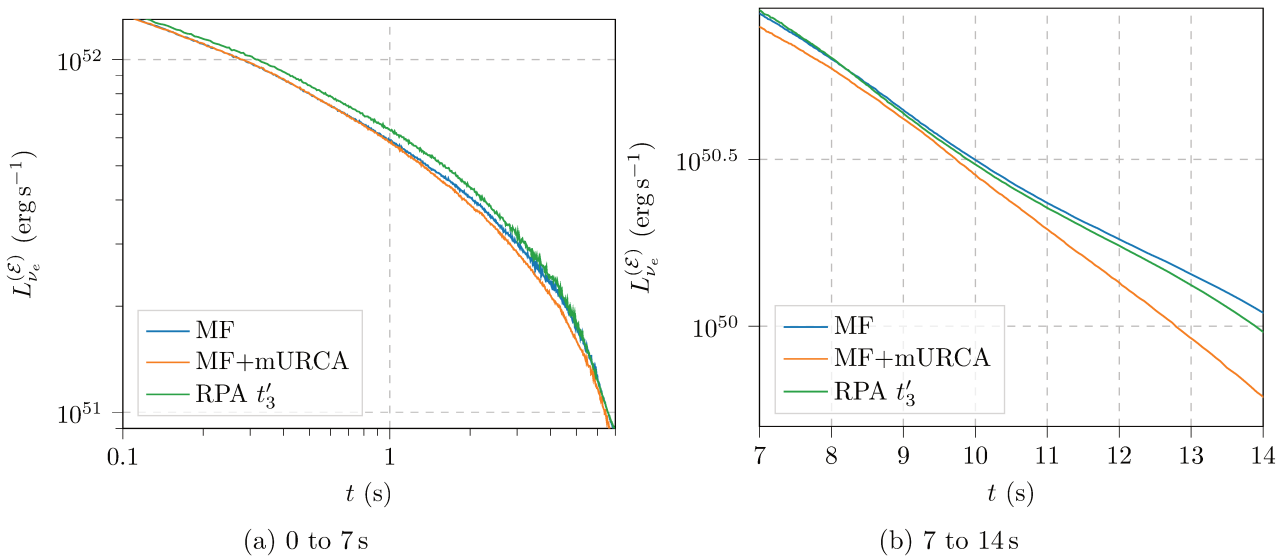


Figure 11.2: Electron neutrino energy luminosity as a function of time, for the 3 prescriptions for charged currents.

The neutrino luminosities in simulations including mURCA are always lower than in those which do not. This can easily be understood, because the opacities are globally enhanced by collisional broadening, the diffusion of heat and leptons inside the proto-neutron star is less efficient and the neutrinosphere is positioned at a lower temperature. This difference becomes more and more significant after about 10 s of evolution, when the temperature starts to drop and the differences between the prescriptions become more significant.

Simulations which include RPA effects have a higher luminosity during the first phase of the evolution. This can be understood because the decrease of opacities due to nuclear correlations improves the diffusion of heat in the PNS (the diffusion coefficient is inversely proportional to the opacity, see section 4.4.1). At later time this tendency is inverted, because the model

including RPA is colder. This behaviour is similar to the observations made in fig. 5 of [166], but some important differences can be observed. For example in [166] differences between RPA and MF starts to appear only after convection has stopped. This difference might have several origins, such as the differences in the initial model, the neutrino treatment or the equation of state, and should be investigated further before any generic conclusion on the effect of RPA can be drawn.

Now regarding the effects on lepton transport, the figure 11.3 represents the deleptonization rate $L_{\nu_e}^{(n)} - L_{\bar{\nu}_e}^{(n)}$ as a function of time.

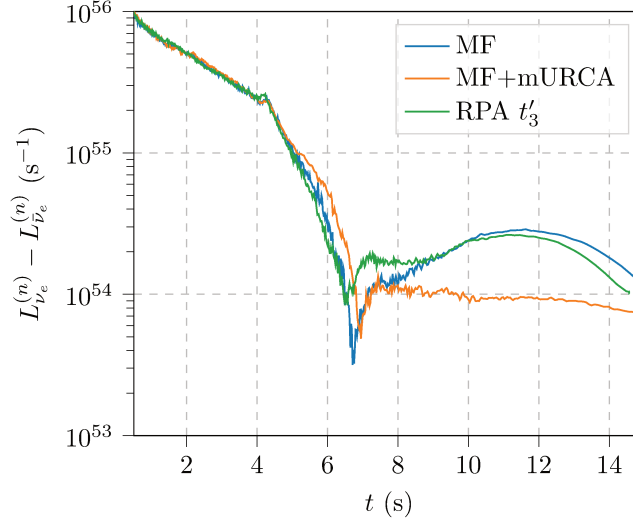


Figure 11.3: Deleptonization rate as a function of time, for the 3 prescriptions for charged currents.

Again we see that most differences appear at late time, after the convective motions stop at about 4-5s. The deleptonization rate obtained with mURCA is lower than the two other prescriptions. As discussed with the fig. 11.1, this is probably due to the fact that opacities including collisional broadening are much higher at relatively low temperatures.

11.2.2 Influence on the emitted neutrino spectrum

Now let us have a look at the emitted neutrino spectrum. The figure 11.4 represents the mean energy of emitted neutrinos (as measured by a distant observer).

The observations are similar to those discussed earlier, the differences introduced by the addition of mURCA processes are more significant than the addition of nuclear correlations with RPA. But we remind the reader that we used a phenomenological model for the mURCA and that its contribution might have been overestimated.

The addition of mURCA seems to systematically lower the mean energy of both electron neutrinos and antineutrinos, whereas the RPA seems to enhance mostly the mean energy of electron neutrinos.

Regarding the effect that these changes have on the neutrino driven wind, the figure 11.5 represents the evolution of the electron fraction in the NDW.

We see that the enhancement of the average energy of electron neutrinos induced by the RPA at early times (see fig. 11.4) has some noticeable repercussions on the electron fraction in the neutrino driven wind, which is about 4 % higher at early times.

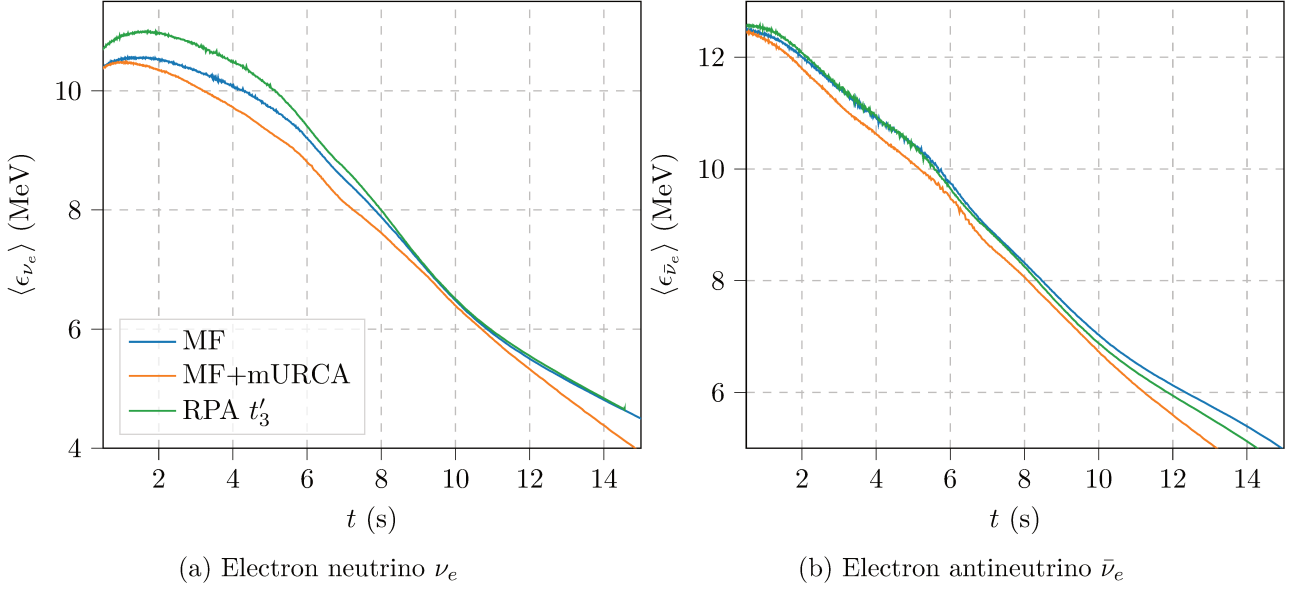


Figure 11.4: Mean energy of emitted neutrinos as a function of time, for the 3 prescriptions for charged currents.

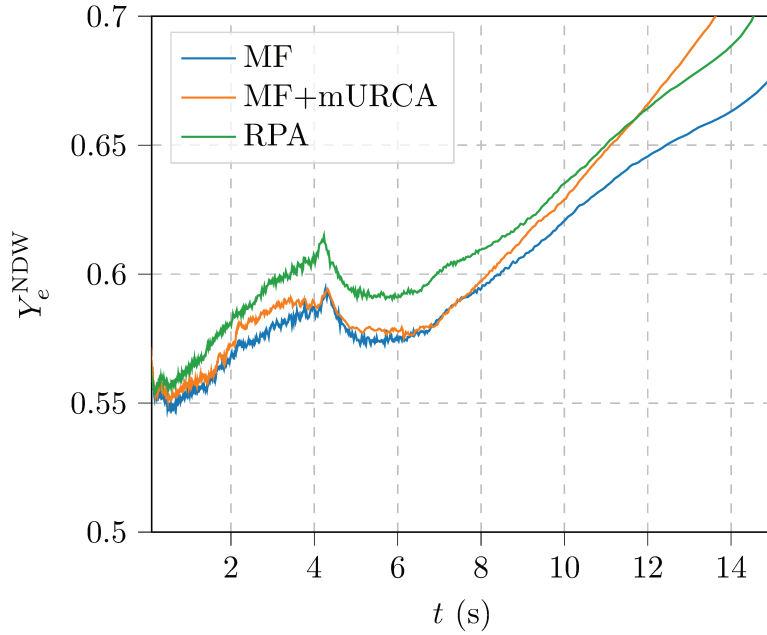


Figure 11.5: Electron fraction in the neutrino driven wind, computed with eq. (2.5), for the 3 prescriptions for charged currents.

The prediction of simulations including mURCA starts to be different after about 8 s, but the predictions of the electron fraction in the neutrino driven wind with eq. (2.5) include only the effects of free nucleons, and should therefore be considered with caution over such a long timescale.

11.2.3 Influence of the equation of state

Because of the high computational cost of RPA calculations we were not able to perform RPA simulations with different equations of state. Therefore our results are limited to the RG(SLy4) EoS.

We can nevertheless compare the influence of the choice of an equation of state and the influence of the prescription for charged currents. The figure 11.6 represents the total neutrino luminosity as a function of time for three different simulations, all of them using the mean field prescription but various equations of state.

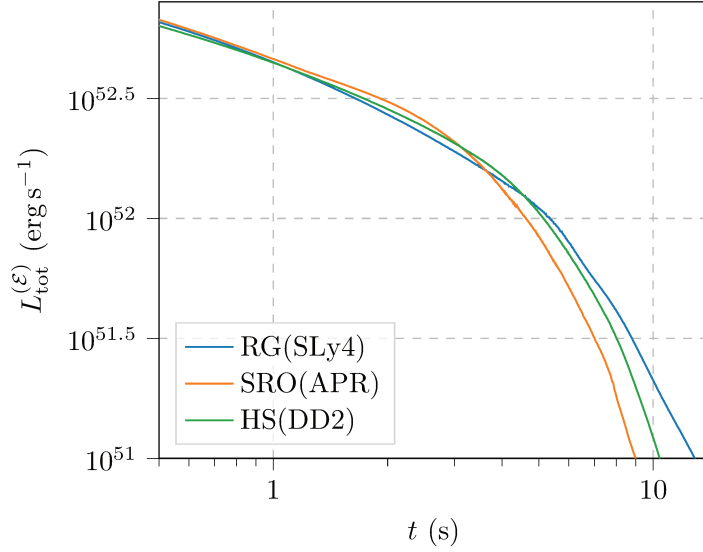


Figure 11.6: Total (sum of 6 flavors) neutrino energy luminosity as a function of time, for the mean field (MF) prescription for charged currents and with different equations of state (see the text for the signification of labels).

We used the following equations of state :

- HS(DD2), using the statistical model of [133] and the DD2 parametrization of the nuclear interaction [158]
- RG(SLy4), using the NSE model from [134] and the SLy4 Skyrme effective interaction [160]
- SRO(APR), computed in [161], is based on the SRO model [162], and uses the APR Skyrme-like effective interaction [163]

We see that the effect of the equation of state on the neutrino luminosity is comparable to the effects of the choice the prescription for charged currents. We recall here that initial data have been computed separately for each equation of state, therefore each PNS simulation starts with a different total baryonic mass, which can explain the differences observed in the luminosities.

11.2.4 Conclusion and limitations

In the continuation of our previous work on the influence of charged-currents in core-collapse simulations ([126]) we studied the influence of nuclear correlations and collisional broadening due to modified URCA processes in the cooling of proto-neutron stars. We recall that commonly used approximations in CCSN (the elastic approximation) and in NS cooling simulations (the Fermi surface approximation) are not applicable and that PNS cooling simulation should rely on charged currents rates computed with full kinematics whenever possible.

From our simulations we conclude that the addition of mURCA has a certain, though limited effect on the neutrino emission, by reducing both the mean energy and the luminosity of emitted electrons (anti-)neutrinos. The inclusion of nuclear RPA correlations mostly has an effect at the

beginning of the simulation, by enhancing the mean energy of emitted electron neutrinos, which indirectly increases the electron fraction in the neutrino driven wind.

Of course there are several limitations to this study. We performed our analysis of the effects of RPA and mURCA with only one equation of state and one progenitor, thus the validity of our conclusions is limited. The numerical method used is also not without defaults : our neutrino transport scheme is approximate and does not behave as well as some recent methods (as e.g. variable Eddington transport methods [93]) in the semi-transparent region, though it is still more elaborated than equilibrium flux limited diffusion methods and have a similar numerical cost. There is also a discontinuity in the evolution of our model in the transition between the CCSN evolution code with full-hydrodynamics and our quasi-static PNS cooling, in addition to the fact that we completely neglected the accretion process, therefore the first few hundreds of milliseconds in the evolution of our models should not be considered as reproducing accurately the conditions in core-collapse supernova. In particular we sometimes see a "re-leptonization" because our initial model is not in radiative equilibrium. But this initial phase of adaptation does not have not of a significant influence on the global evolution and does not last longer than a few hundreds of milliseconds.

We nevertheless demonstrated the feasibility of proto-neutron star studies including mixing length theory and state-of-the-art microphysics for the computation of neutrino interactions with a new low-cost numerical algorithm. This kind of method allows to study a wide parameter space in a reasonable time and will certainly prove useful as uncertainties in proto-neutron stars evolution are still numerous.

Conclusion and perspectives

Since the supernova 1987A, neutrino detectors have been considerably improved, and associated to the emergent field of gravitational wave astronomy we should be able to learn a lot from the next galactic supernova. To interpret these data we will need accurate models of the core-collapse and proto-neutron star multi-messenger emissions, and this thesis aims to add a stone to this edifice.

We focused mostly on the role of neutrinos in these phenomena, along with the emitted neutrino spectrum and luminosity, which are of interest for neutrino detectors. For this we built models using several approximations, among which we find the assumption of spherical symmetry and a simplified neutrino transport. These models should nevertheless reproduce the main effects on the studied parameters and motivate further studies on several interesting points.

Simulations of core-collapse were conducted with the **CoCoNuT** code, in which we have added the Fast Multigroup Transport for neutrinos [120]. In our results, we show that the prescription used to compute electron capture rates has a significant effect on the infall phase, and that using the Q -value dependant fits [170][172] on results of microscopic calculations yields results quantitatively different from the analytic formula obtained with the approximation of independent particles. The deleptonization before the bounce is enhanced, which yields a weaker shock. The most relevant nuclei have been identified, which should motivate further studies with microscopic computations of electron capture rates [184].

Then, a new code was developed to model the evolution of proto-neutron stars [150]. This code relies on the quasi-static approximation and is using the Fast Multigroup Transport for neutrinos. We applied this code to study the early time evolution of a proto-neutron star and obtain the corresponding evolution of its mass and radius [157]. In this context, recent studies suggest that measuring the gravitational wave emission from a proto-neutron star allows to determine its mass and radius [154]. Our study, however, concluded that it will be difficult to extract cold NS properties from PNS mass and radius because of the unknown internal structure of the PNS, in particular its entropy distribution.

We also implemented convective effects with the Mixing Length Theory (MLT) [164] and showed that models including MLT are qualitatively close to full 3D models [5], but very different from non-convective ones [150]. As MLT can be implemented in a very efficient way, we encourage further 1D studies on proto-neutron stars to systematically use it. MLT has nevertheless some shortcomings, among which the fact that it does not take into account convective overshoot. We have considered the toy model of [94] and some anelastic convection models combined with the two columns formalism of [165] as a possible improvement for our algorithm.

Finally, we studied the influence of various prescriptions for the computation of rates for charged-current processes during both core-collapse [126] and proto-neutron star evolution [150]. Among the studied effects there are the elastic approximation opposed to a full kinematic treatment, and the inclusion of nucleonic interactions via mean field effects, RPA correlations and collisional

broadening. We see very little effects on the early evolution, but the various models start to diverge after the onset of neutrino transparency, which leads us to suspect that the early evolution of the nascent neutron star might be very different depending on the prescription for charged currents. This fact might be of importance in models of crust formation [100] and deserves some attention in further studies.

Appendices

Appendix A

Analytic fit for nucleon-nucleon bremsstrahlung

In this appendix we give the explicit fit formula $s(\omega/T)$ needed for the computation of the *spin autocorrelation function* (see eq. (5.17)).

We define the dimensionless parameters $x = \frac{\omega}{T}$ and $y = \frac{m_\pi^2}{m_N T}$ where m_π is the pion mass.

Non degenerate limit

In the non-degenerate limit $\eta_* = 0$ (where η_* is defined as in eq. (5.20)), the function s is given by

$$s_{\text{ND}}(x, y) = \frac{2\sqrt{\pi}(x+2-e^{-y/12})^{3/2}[x^2+2xy+(5/3)y^2+1]}{\sqrt{\pi}+(\pi^{1/8}+x+y)^4} \quad (\text{A.1})$$

Degenerate limit

In the degenerate limit $\eta_* \gg 1$ we have

$$s_{\text{D}}(x, y, \eta_*) = 3 \left(\frac{\pi}{2} \right) \eta_*^{-5/2} \frac{(x^2 + 4\pi^2)x}{4\pi^2(1 - e^{-x})} f \left(\sqrt{\frac{y}{2\eta_*}} \right) \quad (\text{A.2})$$

where $f(u) = 1 - \frac{5u}{6} \arctan\left(\frac{2}{u}\right) + \frac{u^2}{3(u^2+4)} + \frac{u^2}{6\sqrt{2u^2+4}} \arctan\left(\frac{2\sqrt{2u^2+4}}{u^2}\right)$

Interpolation between the two limits

In the general case we use the following interpolation formula :

$$s(x, y, \eta_*) = \left[(s_{\text{ND}})^{-p(y)} + (s_{\text{D}})^{-p(y)} \right]^{-1/p(y)} \times F(x, y, \eta_*) [1 + C(x, y, \eta_*)G(x, y, \eta_*)] \quad (\text{A.3})$$

where the exponent $p(y)$ is defined as

$$p(y) = 0.67 + 0.18y^{0.4} \quad (\text{A.4})$$

and the functions F , C and G are given by

$$F(x, y, \eta_*) = 1 + \frac{1}{[3 + (x - 1.2)^2 + x^{-4}] (1 + \eta_*^2)(1 + y^4)} \quad (\text{A.5})$$

$$G(x, y, \eta_*) = 1 - 0.0044x^{1.1} \frac{y}{0.8 + 0.06y^{1.05}} \frac{\eta_*^{0.5}}{\eta_* + 0.2} \quad (\text{A.6})$$

$$C(x, y, \eta_*) = \frac{1.1x^{1.1}h(\eta_*)}{2.3 + h(\eta_*)x^{0.93} + 0.0001x^{1.2}} \frac{30}{30 + 0.005x^{2.8}} \quad \text{with } h(\eta_*) = \frac{0.1\eta_*}{2.39 + 0.1\eta_*^{1.1}} \quad (\text{A.7})$$

Appendix B

Analytic fit for the ion screening effect

In this appendix we provide the fit formula for the angular average $\langle S(\epsilon_\nu) \rangle_{\text{ion}}$ (5.27) of the dynamic structure function, from the work of [138].

We start by defining the average distance between ions a_{ion} , given by

$$a_{\text{ion}}(A, Z) = \left(\frac{4\pi n(A, Z)}{3} \right)^{-1/3} \quad (\text{B.1})$$

where $n(A, Z)$ is the density of nuclei ${}^A_Z\text{X}$.

This fit formula depend upon two dimensionless constants :

- the adimensioned neutrino energy $\bar{\epsilon}_\nu$, given by

$$\bar{\epsilon} = \frac{\epsilon_\nu a}{\hbar c} \quad (\text{B.2})$$

- the ratio of the Coulomb potential to the thermal energy Γ , given by

$$\Gamma = \frac{Z^2 \alpha}{aT} \quad (\text{B.3})$$

where $\alpha = 0.007\,297$ is the fine structure constant

The fit function is then

$$\langle S(\epsilon_\nu) \rangle_{\text{ion}} = \begin{cases} \left[1 + \exp \left(- \sum_{i=0}^6 \beta_i(\Gamma) \bar{\epsilon}^i \right) \right]^{-1} & \text{for } \bar{\epsilon} < 3 + 4/\sqrt{\Gamma} \\ 1 & \text{for } \bar{\epsilon} > 3 + 4/\sqrt{\Gamma} \end{cases} \quad (\text{B.4})$$

The three first function $\beta_i(\Gamma)$ (for $i = 0, 1, 2$) are given by

$$\beta_0(\Gamma) = \ln \left[\frac{0.3}{0.3 + 3\Gamma} \right] \quad (\text{B.5})$$

$$\beta_1(\Gamma) = 0 \quad (\text{B.6})$$

$$\beta_2(\Gamma) = 6.667 \quad (\text{B.7})$$

Finally, the other functions $\beta_i(\Gamma)$ are given as power series of $\sqrt{\Gamma}$ with tabulated coefficients :

$$\beta_i(\Gamma) = \beta_{i,1} + \beta_{i,2}\Gamma^{1/2} + \beta_{i,3}\Gamma + \beta_{i,4}\Gamma^{3/2} \quad (\text{B.8})$$

the coefficients $\beta_{i,j}$ are given in the table B.1.

Coeff.	$j = 1$	$j = 2$	$j = 3$	$j = 4$
$\beta_{3,j}$	$-7.362\,056$	$0.537\,136\,5$	$-0.107\,884\,5$	$4.189\,612 \times 10^{-3}$
$\beta_{4,j}$	$3.448\,958\,1$	$-0.402\,516\,56$	$9.087\,787\,8 \times 10^{-2}$	$-3.435\,358\,1 \times 10^{-3}$
$\beta_{5,j}$	$-0.741\,286\,45$	$0.110\,198\,55$	$-2.535\,936\,1 \times 10^{-2}$	$9.048\,774\,4 \times 10^{-4}$
$\beta_{6,j}$	$5.957\,328\,5 \times 10^{-2}$	$-1.018\,655\,2 \times 10^{-2}$	$2.279\,136\,9 \times 10^{-3}$	$-7.461\,459\,7 \times 10^{-5}$

Table B.1: Tabulated coefficients for the equation (B.8)

Appendix C

Kernel for neutrino-charged lepton scattering

In this appendix we provide expressions for the functions H_0^I and H_0^{II} used in the equation (5.29).

Thoses functions can be found in [140]. They are given with the modifications provided below eq. (C50) in [129].

We recall that ϵ represent the energy of the incoming neutrino, ϵ' the energy of the outcoming neutrino and E the energy of the charged lepton before the scattering.

The expressions depend upon the relative ordering of ϵ' and E .

Case $\epsilon' \geq E$

$$H_0^I(\epsilon, \epsilon', E) = \frac{4}{15}E^5 + \frac{4}{3}E^4\epsilon + \frac{8}{3}E^3\epsilon^2 + \Theta(\epsilon' - \epsilon)\Gamma_0(\epsilon, \epsilon') \quad (\text{C.1})$$

$$H_0^{II}(\epsilon, \epsilon', E) = \frac{4}{15}E^5 - \frac{4}{3}E^4\epsilon' + \frac{8}{3}E^3(\epsilon')^2 + \Theta(\epsilon' - \epsilon)\Gamma_0(-\epsilon', -\epsilon) \quad (\text{C.2})$$

where Θ is the usual Heaviside step function and Γ_0 is given by

$$\Gamma_0(x, y) = \frac{8}{3}E^2(x^3 - y^3) + 4E(x - y)^2 \left(\frac{x^2}{3} + \frac{2xy}{3} + y^2 \right) + 4(x - y)^3 \left(\frac{x^2}{15} + \frac{xy}{5} + \frac{2y^2}{5} \right) \quad (\text{C.3})$$

Case $\epsilon' \leq E$

$$H_0^I(\epsilon, \epsilon', E) = a_0(\epsilon, \epsilon') + b_0(\epsilon, \epsilon')E + c_0(\epsilon, \epsilon')E^2 \quad (\text{C.4})$$

$$H_0^{II}(\epsilon, \epsilon', E) = a_0(\epsilon', \epsilon) - b_0(\epsilon', \epsilon)E + c_0(\epsilon', \epsilon)E^2 \quad (\text{C.5})$$

where the functions a_0 , b_0 and c_0 are given by

$$a_0(x, y) = \begin{cases} \frac{8}{3}x^2y^3 - 4xy^4 + \frac{8}{5}y^5 & \text{if } x \geq y \\ \frac{4}{15}x^5 & \text{if } x \leq y \end{cases} \quad (\text{C.6})$$

$$b_0(x, y) = \begin{cases} \frac{16}{3}xy^3 - 4y^4 & \text{if } x \geq y \\ \frac{4}{3}x^4 & \text{if } x \leq y \end{cases} \quad (\text{C.7})$$

$$c_0(x, y) = \begin{cases} \frac{8}{3}y^3 & \text{if } x \geq y \\ \frac{8}{3}x^3 & \text{if } x \leq y \end{cases} \quad (\text{C.8})$$

Appendix D

Kernel for electron-positron pair process

In this appendix we provide expressions for the functions J_0^I and J_0^{II} used in the equation (5.31), which can be found in [129].

We consider the process

$$e^- + e^+ \rightleftharpoons \nu + \bar{\nu}$$

and we recall that ϵ represent the energy of the outgoing neutrino e^- , ϵ' the energy of the outgoing antineutrino $\bar{\nu}$ and E the energy of the electron e^- .

We also have the relation $J_l^I(\epsilon', \epsilon) = J_l^{II}(\epsilon, \epsilon')$, stemming from particle exchange symmetry.

The expressions depend upon the relative ordering of ϵ , ϵ' and E .

Case $\epsilon \geq E$ and $\epsilon' \geq E$

$$J_0^I(\epsilon, \epsilon', E) = \frac{1}{\epsilon^2(\epsilon')^2} \Theta(\epsilon + \epsilon' - E) \left[\frac{4}{15} E^5 - \frac{4}{3} E^4 \epsilon' + \frac{8}{3} E^3 (\epsilon')^2 \right] \quad (\text{D.1})$$

Case $\epsilon \leq E$ and $\epsilon' \leq E$

$$J_0^I(\epsilon, \epsilon', E) = \frac{1}{\epsilon^2(\epsilon')^2} \Theta(\epsilon + \epsilon' - E) \left[-\frac{4}{15} E^5 + \frac{4}{3} E^4 \epsilon' - \frac{8}{3} E^3 (\epsilon')^2 + \frac{8}{3} E(\epsilon + \epsilon')^2 ((\epsilon')^2 - 2\epsilon\epsilon' + 3\epsilon^2) + \frac{4}{15} (\epsilon + \epsilon')^3 ((\epsilon')^2 - 3\epsilon\epsilon' + 6\epsilon^2) \right] \quad (\text{D.2})$$

Case $\epsilon \leq E$ and $\epsilon' \geq E$

$$J_0^I(\epsilon, \epsilon', E) = \frac{\epsilon}{(\epsilon')^2} \Theta(\epsilon + \epsilon' - E) \left[\frac{8}{3} (\epsilon')^2 + 4\epsilon\epsilon' + \frac{8}{5} \epsilon^2 - \frac{16}{3} E\epsilon^2 + 4E \frac{\epsilon^3}{\epsilon'} + \frac{8}{3} E^2 \frac{\epsilon^2}{\epsilon'} \right] \quad (\text{D.3})$$

Case $\epsilon \geq E$ and $\epsilon' \leq E$

$$J_0^I(\epsilon, \epsilon', E) = \frac{1}{\epsilon\epsilon'} \Theta(\epsilon + \epsilon' - E) \left[\frac{4}{15} \frac{(\epsilon')^4}{\epsilon} - \frac{4}{3} \frac{(\epsilon')^3}{\epsilon} E + \frac{8}{3} \frac{(\epsilon')^2}{\epsilon} E^2 \right] \quad (\text{D.4})$$

Appendix E

Precomputation of functions for charged leptons processes

In this appendix we explain how to precompute the functions A^I and A^{II} (from eq. (5.29)), as well as the functions B^I and B^{II} (from eq. (5.31)), into three-dimensional numerical tables.

We introduce the notations $x = \frac{\epsilon}{T}$, $x' = \frac{\epsilon'}{T}$ and $\eta_e = \frac{\mu_e}{T}$.

The key point for the procedure is to remark that the functions $H_l^k(\epsilon, \epsilon', E)$ are polynomials homogeneous to an energy to the power of 5 (see appendix C). Therefore we can write

$$H_l^k(\epsilon, \epsilon', E) = T^5 H_l^k(x, x', y) \quad \text{where } y = \frac{E}{T} \quad (\text{E.1})$$

The eq. (5.29) can be recasted as

$$\begin{aligned} A_l^k(\epsilon, \epsilon') &= T^2 a_l^k(x, x', \eta_e) \\ \text{where } a_l^k(x, x', \eta_e) &= \frac{4G_F}{(hc)^3} \frac{1}{x^2(x')^2} \int_{\max(0, x'-x)}^{\infty} dy \frac{1}{1 + e^{y \pm \eta_e}} \\ &\quad \times \left(1 - \frac{1}{1 + e^{y+x-x' \pm \eta_e}} \right) H_l^k(x, x', y) \end{aligned} \quad (\text{E.2})$$

And we can precompute the coefficients $a_l^k(x, x', \pm \eta_e)$ and create 3D numerical tables usable in simulations.

For the case of the pair process, we use the same idea, from appendix D we have

$$J_0^I(\epsilon, \epsilon', E) = T J_0^I(x, x', y) \quad (\text{E.3})$$

and we can rewrite eq. (5.31) as

$$\begin{aligned} B_l(\epsilon, \epsilon')^k &= T^2 b_l^k(x, x', \eta_e) \\ \text{where } b_l^k(x, x', \eta_e) &= \frac{4G_F}{(hc)^3} \int_0^{x+x'} dy \frac{1}{1 + e^{y-\eta_e}} \\ &\quad \times \frac{1}{1 + e^{x+x'-y+\eta_e}} J^l(x, x', y) \end{aligned} \quad (\text{E.4})$$

and then precompute the coefficients $b_l^I(x, x', \eta_e)$ in 3D numerical tables.

Appendix F

Nuclear shell model and neutron blocking

The nuclear shell model is a model of the structure of the energy levels of an atomic nucleus which can be occupied by protons and neutrons.

It was built by analogy with the atomic shell model, as an attempt to explain the peculiar stability of some atomic nucleus which own some specific numbers of either protons and neutrons.

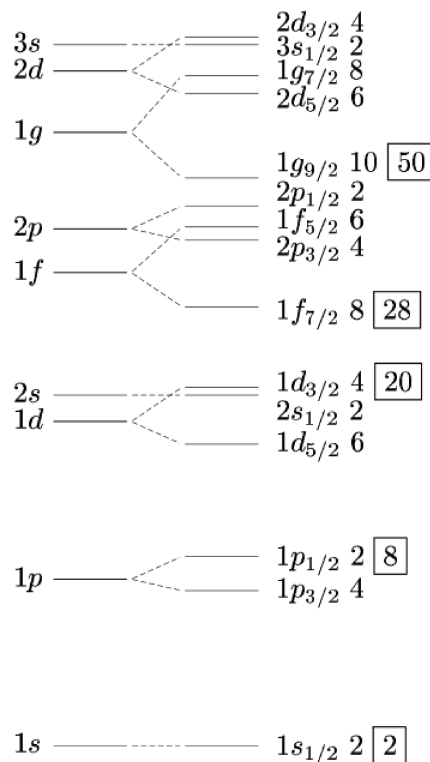


Figure F.1: Nuclear shell model. The energy levels have the degeneracy lifted by the spin-orbit interaction. The spectroscopic notation is used to designate the levels. The number of particles (protons or neutrons) which can occupy a level is indicated on the right. The magic numbers are framed.

These numbers (2,8,20,28,50,...) are called "magic numbers". The corresponding "magic nuclei" have a higher binding energy than their neighbour on the nuclear chart.

However these numbers are different from those who correspond to atomic shell closures (2,10,18,36,54,...). This is due to the spin-orbit interaction, which has a significant effect on nucleons and lift the degeneracy of energy levels, as shown on the figure F.1.

The Bruenn formula (9.4) describes a resonant Gamow-Teller transition between two-levels : $1f_{7/2} \rightarrow 1f_{5/2}$, and consider that this process is blocked for a number of neutrons $N \geq 40$ or a number of protons $Z \leq 20$.

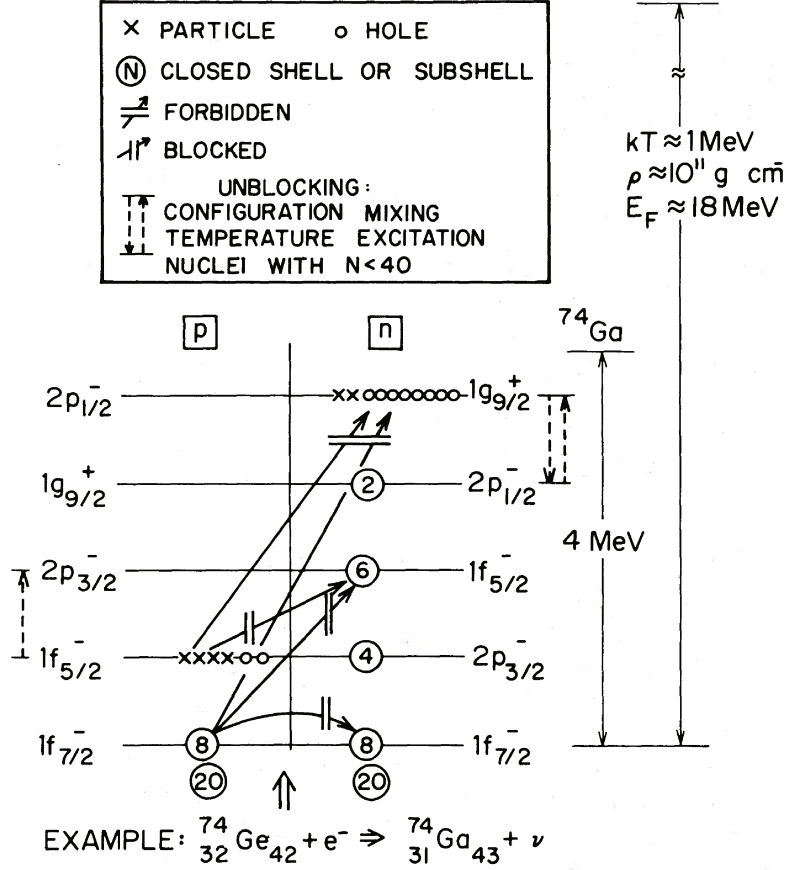


Figure F.2: Neutron shell blocking effect during core-collapse, example of ${}^{74}\text{Ge}$, figure extracted from [167]. The levels occupied by protons are represented on the left and those occupied by neutrons are on the right. All transitions toward levels lower than $2p_{1/2}^-$ are forbidden by Pauli's principle. Transitions toward $1g_{9/2}^+$ are forbidden by selection rules because of the change in parity.

This phenomena of *shell blocking* can be interpreted in the following manner : for $N \geq 40$, the neutron levels $1f_{5/2}$ and $2p_{1/2}$ are full and the associated transitions are blocked by Pauli's principle.

The only available level is $1g_{9/2}$ because the next levels are much higher in energy (this is the $N = 50$ shell closure). And this particular transition is forbidden by selection rules. Therefore the electron capture cannot happen on such a nucleus.

Appendix G

Numerical implementation of the PNS evolution code

In this appendix we describe the implementation of the above equations into the evolution algorithm that we used to model proto-neutron star evolution.

G.0.1 Grid and discrete set of equations

Lagrangian grid

For an easier implementation of the evolution equations, we use a Lagrangian grid. We introduce the enclosed baryon number coordinate :

$$a(r) = 4\pi \int_0^r n_B \psi r^2 dr \quad (\text{G.1})$$

During our simulations, the enclosed baryon number grid $\{a_i\}_{0 \leq i \leq m}$ is fixed, and therefore the Lagrangian derivative is given by a time derivative at constant a : $\frac{D}{D\tau} = \left(\frac{\partial}{\partial t} \right)_a$.

$N_B = a(R) = a_m$ is then the total baryon number in the star.

One of the difficulties of this method is the choice of the grid, as a uniform grid tends to produce a very sparse grid in the central area (at low r) and in the outer areas (at low n_B), indeed we have

$$\frac{dr}{da} = \frac{1}{4\pi n_B \psi r^2} \quad (\text{G.2})$$

and such a sparse grid in r introduces numerical errors in our neutrino transport solver.

We found that in order to produce a grid that yields good results in a wide range of situations, it is convenient to split the grid into two separate parts :

- a central area which contains m_c points and a baryon number $(N_B)_c$, for which grid points are given by

$$a_i = (N_B)_c \left(\frac{i}{m_c} \right)^3 \quad \text{for } 0 \leq i \leq m_c \quad (\text{G.3})$$

This choice corrects for the fact that $a \propto r^3$ in the central area with quasi-constant density

- an outer area which contains $m - m_c$ points for which the baryon number in a cell is given as a geometric series :

$$a_i - a_{i-1} = q^{i-m_c} \times (N_B)_c \quad \text{for } m_c + 1 \leq i \leq m \quad (\text{G.4})$$

As $q \leq 1$ this choice tends to produce a very fine grid in the outer layers and corrects for the sparsity of the radial grid at low densities

We obtain the correct total baryon number if

$$N_B = \frac{1 - q^{m-m_c+1}}{1 - q} (N_B)_c \quad (\text{G.5})$$

we found that a choice of parameters that gives good results is given by $m_c = m/40$ and $q^{m-m_c+1} = 0.1$.

Finite volume scheme

Now, since the evolution relies on the conservation equations of lepton number and entropy, we implemented the radial grid discretization with a finite volume scheme, as this kind of methods is conservative.

We start by defining the baryon number contained in a cell as

$$\mathcal{A}_i = a_i - a_{i-1} \quad (\text{G.6})$$

and the volume of a cell as

$$\mathcal{V}_i = \frac{4}{3}\pi (r_i^3 - r_{i-1}^3) \quad (\text{G.7})$$

thus the finite volume discretization of eq. (G.1) is

$$\mathcal{A}_i = (n_B)_i \psi_i \mathcal{V}_i \quad (\text{G.8})$$

In practice we use the above equation to compute the volume of all cells $\{\mathcal{V}_i\}_{1 \leq i \leq m}$, and we deduce the radial grid $\{r_i\}_{0 \leq i \leq m}$.

Finally, we introduce the expression of the surface of a cell, which will be needed to compute numerical fluxes :

$$\mathcal{S}_i = 4\pi r_i^2 \quad (\text{G.9})$$

Discretization of PNS evolution equations

Because of the significant computational cost of an implicit neutrino transport scheme we choosed to solve the time evolution equations of the proto-neutron with an explicit scheme. It should be stressed that because of this choice the value of the timestep δt is limited in order to have relatively small variations of the electron fraction and the entropy per baryon. We found that limiting such variations to 0.5 % per time step allows to obtain good results and is a good compromise compared with an implicit scheme.

Within a finite volume scheme, conservation laws are implemented under their integral form. For the electron conservation law (6.11) we obtain

$$\delta_t \{[\mathcal{A}Y_e]_i\} = [(\Gamma_{\bar{\nu}_e} - \Gamma_{\nu_e}) \alpha \psi \mathcal{V}]_i \quad (\text{G.10})$$

where $\delta_t \{X\}$ represent the discrete time derivative of X for an explicit Euler scheme :

$$\delta_t \{X\} = \frac{1}{\delta t} (X(t + \delta t) - X(t)) \quad (\text{G.11})$$

And for the entropy conservation law (6.14) we obtain

$$\delta_t \{[\mathcal{A}s]_i\} = \left[\left(-\frac{(Q_{\nu_e} + Q_{\bar{\nu}_e} + 4Q_{\nu_x})}{Tn_B} + \frac{\mu_e (\Gamma_{\nu_e} - \Gamma_{\bar{\nu}_e})}{T} \right) \alpha \psi \mathcal{V} \right]_i \quad (\text{G.12})$$

Resolution of structure equations

The value of the metric potentials ψ and α on cell interfaces are noted ψ_{if} and α_{if} . They are defined as $\psi_i = ([\psi_{\text{if}}]_i + [\psi_{\text{if}}]_{i-1})/2$ and $\alpha_i = ([\alpha_{\text{if}}]_i + [\alpha_{\text{if}}]_{i-1})/2$.

The TOV equations (6.4), (6.5) and (6.6) are then discretized as follows :

$$\psi_{\text{if}} = \left(1 - \frac{2Gm_i}{r_i c^2} \right)^{-1/2} \quad (\text{G.13})$$

$$m_i = m_{i-1} + \frac{1}{c^2} \left[\mathcal{A} \frac{\mathcal{E}}{n_B \psi} \right]_i \quad (\text{G.14})$$

$$g_i = G \left[\psi_{\text{if}}^2 \left(\frac{m}{r^2} + 4\pi r^2 \frac{p}{c^2} \right) \right]_i \quad (\text{G.15})$$

Then, to be compatible with future implementations of the Euler hydrodynamic equation, the hydrostatic equilibrium equation (6.8) has been discretized as follows :

$$(P_{i+1} - P_i) \mathcal{S}_i = -\frac{1}{c^2} [(\mathcal{E} + P)g\mathcal{V}]_i \quad (\text{G.16})$$

The boundary conditions are $m_0 = 0$ and $P_N = P_{\text{surf}}$, where P_{surf} is a fixed value of the pressure. The value of P_{surf} is chosen to be the best compromise that satisfies the following constraints :

- P_{surf} should be low enough to model the structure of the PNS accurately, the ideal value being $P_{\text{surf}} = 0$. The solution in the mantle becomes less and less accurate with high values of P_{surf} .
- The timestep is inversely proportional to the surface density, indeed in eq. (6.11) and (6.14) the source terms depend on $1/n_B$. Therefore the surface pressure should be high enough to limit the timestep to reasonable values.

We found that a value $P_{\text{surf}} = 10^{-6} \text{ MeV fm}^{-3}$ is a good compromise, and we used this value in our simulations.

Finally, we need to compute the lapse α needed in transport equations, which is given by

$$[\ln \alpha]_i = [\ln \alpha]_{i+1} - \frac{g_i}{c^2} (\bar{r}_{i+1} - \bar{r}_i) \quad (\text{G.17})$$

with the averaged radius given by

$$\bar{r}_i^3 = \frac{1}{2} (r_i^3 + r_{i-1}^3) \quad (\text{G.18})$$

G.0.2 Treatment of neutrino transport

Energy grid and moments of neutrino distributions

The energy grid $\{\epsilon_i\}_{1 \leq i \leq n}$ is built such that

$$\epsilon_i = \exp \left(\frac{1}{2} (\ln(\epsilon_{max}) + \ln(\epsilon_{min})) + \frac{x_i}{2} (\ln(\epsilon_{max}) - \ln(\epsilon_{min})) \right) \quad (\text{G.19})$$

where $-1 \leq x_i \leq 1$. The grid $\{x_i\}_{1 \leq i \leq n}$ is a Gauss-Legendre grid (see appendix H). We note w_i the weights associated to the nodes x_i .

This choice allows to express the moment integrals of the distributions as

$$\int f(\epsilon) \epsilon^k d\epsilon \approx \frac{\ln(\epsilon_{max}) - \ln(\epsilon_{min})}{2} \sum_{i=1}^n f_i \epsilon_i^{k+1} w_i \quad (\text{G.20})$$

where $f_i \sim f(\epsilon_i)$

In all the simulations presented in this document we used 20 points in the energy grid.

Neutrino transport scheme

Regarding the neutrino transport, we start by solving the two-ray problem with (4.84) and (4.85) in order to obtain the flux factor h_ν with eq. (4.88). This problem is solved as in [120], by using a Ricatti transformation. Then we integrate the steady-state neutrino flux equation (4.83). This equation is extremely stiff, which means that an integration with an explicit method can easily fail if the spatial step is too high, as the derivative of H_ν strongly depends on the function H_ν itself. Therefore we integrate this equation with an implicit scheme.

For $h_\nu < 0$ we obtain

$$\left[\frac{H_\nu \mathcal{S}}{\alpha^2} \right]_{i+1} - \left[\frac{H_\nu \mathcal{S}}{\alpha^2} \right]_i = \left[j \frac{\psi \mathcal{V}}{\alpha^2} \right]_{i+1} - \left[\chi \frac{\psi \mathcal{V}}{\alpha^2} \right]_{i+1} \left[\frac{H_\nu}{h_\nu} \right]_i \quad (\text{G.21})$$

thus we perform an inward integration ($(H_\nu)_i$ is computed by using the value of $(H_\nu)_{i+1}$)

$$[H_\nu]_i = \left(\left[\frac{H_\nu \mathcal{S}}{\alpha^2} \right]_{i+1} - \left[j \frac{\psi \mathcal{V}}{\alpha^2} \right]_{i+1} \right) / \left(\left[\frac{\mathcal{S}}{\alpha^2} \right]_i - \left[\chi \frac{\psi \mathcal{V}}{\alpha^2} \right]_{i+1} \left[\frac{1}{h_\nu} \right]_i \right) \quad (\text{G.22})$$

And for $h_\nu > 0$ we obtain

$$\left[\frac{H_\nu \mathcal{S}}{\alpha^2} \right]_i - \left[\frac{H_\nu \mathcal{S}}{\alpha^2} \right]_{i-1} = \left[j \frac{\psi \mathcal{V}}{\alpha^2} \right]_i - \left[\chi \frac{\psi \mathcal{V}}{\alpha^2} \right]_i \left[\frac{H_\nu}{h_\nu} \right]_i \quad (\text{G.23})$$

thus we perform an outward integration ($(H_\nu)_i$ is computed by using the value of $(H_\nu)_{i-1}$)

$$[H_\nu]_i = \left(\left[\frac{H_\nu \mathcal{S}}{\alpha^2} \right]_{i-1} + \left[j \frac{\psi \mathcal{V}}{\alpha^2} \right]_{i+1} \right) / \left(\left[\frac{\mathcal{S}}{\alpha^2} \right]_i + \left[\chi \frac{\psi \mathcal{V}}{\alpha^2} \right]_i \left[\frac{1}{h_\nu} \right]_i \right)$$

Note that for $h_\nu > 0.5$ we use the two-moments equation (4.91) to compute h_ν instead of using the two stream solution. As this equation is not stiff we can integrate it with an explicit scheme. We use a Runge-Kutta of fourth order.

Hydrodynamic source terms

In order to have neutrino luminosities consistent with the deleptonization and cooling rate, we implement the source terms as the finite-volume divergences of outgoing neutrinos fluxes, as given by eq. (4.80) and (4.81) :

$$[\Gamma_\nu \alpha \psi \mathcal{V}]_i = [\alpha \mathcal{S} F_\nu^{(n)}]_i - [\alpha \mathcal{S} F_\nu^{(n)}]_{i-1} \quad (\text{G.24})$$

$$[Q_\nu \alpha^2 \psi \mathcal{V}]_i = [\alpha^2 \mathcal{S} F_\nu^{(\mathcal{E})}]_i - [\alpha^2 \mathcal{S} F_\nu^{(\mathcal{E})}]_{i-1} \quad (\text{G.25})$$

For the case of the electron conservation law, we can see that this method allows the number luminosity to be equal to the deleptonization rate up to machine precision, indeed with eq. (G.10) we obtain

$$\sum_i \delta_t \{[\mathcal{A} Y_e]_i\} = [\alpha \mathcal{S} (F_{\nu_e}^{(n)} - F_{\bar{\nu}_e}^{(n)})]_n \quad (\text{G.26})$$

This fact has been verified for our algorithm as a test of the implementation of the finite volume scheme.

Appendix H

Gauss-Legendre quadrature method

A Gauss-Legendre quadrature method is an approximation to compute the integral of a function $f(x)$ defined on the interval $[-1, 1]$.

The quadrature rule can be written as

$$\int_{-1}^1 f(x) dx \approx \sum_{i=1}^n w_i f(x_i) \quad (\text{H.1})$$

where x_i are the roots of the n^{th} Legendre polynomial $P_n(x)$, and w_i are the quadrature weights, given by

$$w_i = \frac{2}{(1 - x_i^2) [P'_n(x_i)]^2} \quad (\text{H.2})$$

This method has the advantage of being extremely accurate, and is exact if $f(x)$ is a polynomial of degree $2n - 1$.

But it has the disadvantage of requiring the value of the function at some specific points, and is therefore not adapted to all situations.

It is possible to map the points x_i to other coordinates $y_i = g(x_i)$ (as done in eq. (G.19)), and in this case we have

$$\int_{g(-1)}^{g(1)} f(y_i) dy \approx \sum_{i=1}^n w_i f(y_i) g'(x_i) \quad (\text{H.3})$$

Appendix I

Implicit solver for the MLT scheme

This appendix presents the implicit scheme used to compute the effects of MLT without restriction of timestep (see section 8.2.3).

The MLT diffusion equation for the quantity $x = Y_e, s$ can be written as

$$\frac{1}{\alpha} \frac{Dx}{Dt} = \frac{1}{r^2 \alpha \psi} \frac{\partial}{\partial r} \left(\alpha r^2 D^{\text{MLT}} n_B \frac{\partial x}{\partial r} \right) \quad (\text{I.1})$$

it is discretized as follows :

$$\frac{1}{\delta t} \left([\mathcal{A}x]_1^t - [\mathcal{A}x]_1^{t-\delta t} \right) = \left[\frac{d_1}{\mathcal{A}_1} [\mathcal{A}x]_1 - \frac{d_1}{\mathcal{A}_2} [\mathcal{A}x]_2 \right]^t \quad (\text{I.2})$$

$$\frac{1}{\delta t} \left([\mathcal{A}x]_i^t - [\mathcal{A}x]_i^{t-\delta t} \right) = \left[\frac{d_i + d_{i-1}}{\mathcal{A}_i} [\mathcal{A}x]_i - \frac{d_{i-1}}{\mathcal{A}_{i-1}} [\mathcal{A}x]_{i-1} - \frac{d_i}{\mathcal{A}_{i+1}} [\mathcal{A}x]_{i+1} \right]^t \quad (\text{I.3})$$

$$\frac{1}{\delta t} \left([\mathcal{A}x]_m^t - [\mathcal{A}x]_m^{t-\delta t} \right) = \left[\frac{d_{m-1}}{\mathcal{A}_m} [\mathcal{A}x]_m - \frac{d_{m-1}}{\mathcal{A}_{m-1}} [\mathcal{A}x]_{m-1} \right]^t \quad (\text{I.4})$$

$$\text{where } d = \frac{n_B \mathcal{S} D^{\text{MLT}} \alpha}{\delta r}$$

We can check that this discretization is conservative for $[\mathcal{A}x]$:

$$\sum_{i=1}^m \frac{1}{\delta t} \left([\mathcal{A}x]_i^t - [\mathcal{A}x]_i^{t-\delta t} \right) = 0 \quad (\text{I.5})$$

(I.2-I.4) is a linear system of equations on the vector $[\mathcal{A}x]_{1 \leq i \leq m}^t$:

$$\frac{1}{\delta t} \left([\mathcal{A}x]_i^t - [\mathcal{A}x]_i^{t-\delta t} \right) = M_{ij} [\mathcal{A}x]_j^t \quad (\text{I.6})$$

we write this system as

$$[\text{Id} - \delta t M]_{ij} [\mathcal{A}x]_j^t = [\mathcal{A}x]_i^{t-\delta t} \quad (\text{I.7})$$

The matrix $\text{Id} - \delta t M$ is a sparse matrix, and the equation (I.7) can be solved almost without additional computational cost with a sparse LU solver.

References

- [1] H. Th. Janka, K. Langanke, A. Marek, G. Martínez-Pinedo, and B. Müller. “Theory of core-collapse supernovae”. In: *Phys. Rep.* 442.1-6 (Apr. 2007), pp. 38–74. DOI: [10.1016/j.physrep.2007.02.002](https://doi.org/10.1016/j.physrep.2007.02.002). arXiv: [astro-ph/0612072](https://arxiv.org/abs/astro-ph/0612072) [astro-ph].
- [2] Hans-Thomas Janka. “Explosion Mechanisms of Core-Collapse Supernovae”. In: *Annual Review of Nuclear and Particle Science* 62.1 (Nov. 2012), pp. 407–451. DOI: [10.1146/annurev-nucl-102711-094901](https://doi.org/10.1146/annurev-nucl-102711-094901). arXiv: [1206.2503](https://arxiv.org/abs/1206.2503) [astro-ph.SR].
- [3] Madappa Prakash, James M. Lattimer, Jose A. Pons, Andrew W. Steiner, and Sanjay Reddy. “Evolution of a Neutron Star from Its Birth to Old Age”. In: *Physics of Neutron Star Interiors*. Ed. by D. Blaschke, N. K. Glendenning, and A. Sedrakian. Vol. 578. 2001, p. 364.
- [4] L. F. Roberts, Sanjay Reddy, and Gang Shen. “Medium modification of the charged-current neutrino opacity and its implications”. In: *Phys. Rev. C* 86.6, 065803 (Dec. 2012), p. 065803. DOI: [10.1103/PhysRevC.86.065803](https://doi.org/10.1103/PhysRevC.86.065803). arXiv: [1205.4066](https://arxiv.org/abs/1205.4066) [astro-ph.HE].
- [5] Hiroki Nagakura, Adam Burrows, David Radice, and David Vartanyan. “A systematic study of proto-neutron star convection in three-dimensional core-collapse supernova simulations”. In: *MNRAS* 492.4 (Mar. 2020), pp. 5764–5779. DOI: [10.1093/mnras/staa261](https://doi.org/10.1093/mnras/staa261). arXiv: [1912.07615](https://arxiv.org/abs/1912.07615) [astro-ph.HE].
- [6] W. Baade and F. Zwicky. “Cosmic Rays from Super-novae”. In: *Proceedings of the National Academy of Science* 20.5 (May 1934), pp. 259–263. DOI: [10.1073/pnas.20.5.259](https://doi.org/10.1073/pnas.20.5.259).
- [7] J. Chadwick. “Possible Existence of a Neutron”. In: *Nature* 129.3252 (Feb. 1932), p. 312. DOI: [10.1038/129312a0](https://doi.org/10.1038/129312a0).
- [8] J. R. Oppenheimer and G. M. Volkoff. “On Massive Neutron Cores”. In: *Physical Review* 55.4 (Feb. 1939), pp. 374–381. DOI: [10.1103/PhysRev.55.374](https://doi.org/10.1103/PhysRev.55.374).
- [9] Richard C. Tolman. “Static Solutions of Einstein’s Field Equations for Spheres of Fluid”. In: *Physical Review* 55.4 (Feb. 1939), pp. 364–373. DOI: [10.1103/PhysRev.55.364](https://doi.org/10.1103/PhysRev.55.364).
- [10] A. G. W. Cameron. “Neutron Stars”. In: *ARA&A* 8 (Jan. 1970), p. 179. DOI: [10.1146/annurev.aa.08.090170.001143](https://doi.org/10.1146/annurev.aa.08.090170.001143).
- [11] A. B. Migdal. “Superfluidity and the moments of inertia of nuclei”. In: *Nuclear Physics* 13.5 (Nov. 1959), pp. 655–674. DOI: [10.1016/0029-5582\(59\)90264-0](https://doi.org/10.1016/0029-5582(59)90264-0).
- [12] A. Hewish, S. J. Bell, J. D. H. Pilkington, P. F. Scott, and R. A. Collins. “Observation of a Rapidly Pulsating Radio Source”. In: *Nature* 217.5130 (Feb. 1968), pp. 709–713. DOI: [10.1038/217709a0](https://doi.org/10.1038/217709a0).
- [13] R. A. Hulse and H. J. Taylor. “Discovery of a Pulsar in a Close Binary System.” In: *BAAS*. Vol. 6. Sept. 1974, p. 453.
- [14] Y. Totsuka, K. Hirata, T. Kajita, M. Koshihara, M. Nakahata, Y. Oyama, N. Sato, A. Suzuki, M. Takita, Y. Totsuka, T. Kifune, T. Suda, K. Takahashi, T. Tanimori, K. Miyano, M. Yamada, E. W. Beier, S. B. Kim, A. K. Mann, F. M. Newcomer, R. van Bert, and W. Zhang. “Observation of a neutrino burst from the supernova SN1987a”. In: *Nucl. Phys. A* 478 (Feb. 1988), pp. 189–195. DOI: [10.1016/0375-9474\(88\)90844-5](https://doi.org/10.1016/0375-9474(88)90844-5).

- [15] R. P. Mignani. “Optical Observations of Isolated Neutron Stars”. In: *Neutron Stars and Pulsars: Thirty Years after the Discovery*. Ed. by N. Shibasaki. Jan. 1998, p. 335. arXiv: [astro-ph/9810036](#) [[astro-ph](#)].
- [16] LIGO Scientific Collaboration and Virgo Collaboration. “GW170817: Observation of Gravitational Waves from a Binary Neutron Star Inspiral”. In: *Phys. Rev. Lett.* 119.16, 161101 (Oct. 2017), p. 161101. DOI: [10.1103/PhysRevLett.119.161101](#). arXiv: [1710.05832](#) [[gr-qc](#)].
- [17] E. Troja, L. Piro, H. van Eerten, R. T. Wollaeger, M. Im, O. D. Fox, N. R. Butler, S. B. Cenko, T. Sakamoto, C. L. Fryer, R. Ricci, A. Lien, R. E. Ryan, O. Korobkin, S. K. Lee, J. M. Burgess, W. H. Lee, A. M. Watson, C. Choi, S. Covino, P. D’Avanzo, C. J. Fontes, J. Becerra González, H. G. Khandrika, J. Kim, S. L. Kim, C. U. Lee, H. M. Lee, A. Kuttyrev, G. Lim, R. Sánchez-Ramírez, S. Veilleux, M. H. Wieringa, and Y. Yoon. “The X-ray counterpart to the gravitational-wave event GW170817”. In: *Nature* 551.7678 (Nov. 2017), pp. 71–74. DOI: [10.1038/nature24290](#). arXiv: [1710.05433](#) [[astro-ph.HE](#)].
- [18] Aniello Grado and Grawita Collaboration. “The optical electromagnetic counterpart of the gravitational wave event GW170817”. In: *Nuclear and Particle Physics Proceedings* 306-308 (Sept. 2019), pp. 42–49. DOI: [10.1016/j.nuclphysbps.2019.07.006](#).
- [19] Anatoly Spitkovsky. “Time-dependent Force-free Pulsar Magnetospheres: Axisymmetric and Oblique Rotators”. In: *ApJ* 648.1 (Sept. 2006), pp. L51–L54. DOI: [10.1086/507518](#). arXiv: [astro-ph/0603147](#) [[astro-ph](#)].
- [20] Slavko Bogdanov, Frederick K. Lamb, Simin Mahmoodifar, M. Coleman Miller, Sharon M. Morsink, Thomas E. Riley, Tod E. Strohmayer, Albert K. Tung, Anna L. Watts, Alexander J. Dittmann, Deepto Chakrabarty, Sebastien Guillot, Zaven Arzumian, and Keith C. Gendreau. “Constraining the Neutron Star Mass-Radius Relation and Dense Matter Equation of State with NICER. II. Emission from Hot Spots on a Rapidly Rotating Neutron Star”. In: *ApJ* 887.1, L26 (Dec. 2019), p. L26. DOI: [10.3847/2041-8213/ab5968](#). arXiv: [1912.05707](#) [[astro-ph.HE](#)].
- [21] F. Coti Zelati, N. Rea, J. A. Pons, S. Campana, and P. Esposito. “Systematic study of magnetar outbursts”. In: *Journal of Physics Conference Series*. Vol. 932. Journal of Physics Conference Series. Dec. 2017, 012022, p. 012022. DOI: [10.1088/1742-6596/932/1/012022](#).
- [22] Ingrid H. Stairs. “Testing General Relativity with Pulsar Timing”. In: *Living Reviews in Relativity* 6.1, 5 (Sept. 2003), p. 5. DOI: [10.12942/lrr-2003-5](#). arXiv: [astro-ph/0307536](#) [[astro-ph](#)].
- [23] G. Hobbs, A. Archibald, Z. Arzumian, D. Backer, M. Bailes, N. D. R. Bhat, M. Burgay, S. Burke-Spolaor, D. Champion, I. Cognard, W. Coles, J. Cordes, P. Demorest, G. Desvignes, R. D. Ferdman, L. Finn, P. Freire, M. Gonzalez, J. Hessels, A. Hotan, G. Janssen, F. Jenet, A. Jessner, C. Jordan, V. Kaspi, M. Kramer, V. Kondratiev, J. Lazio, K. Lazaridis, K. J. Lee, Y. Levin, A. Lommen, D. Lorimer, R. Lynch, A. Lyne, R. Manchester, M. McLaughlin, D. Nice, S. Osłowski, M. Pilia, A. Possenti, M. Purver, S. Ransom, J. Reynolds, S. Sanidas, J. Sarkissian, A. Sesana, R. Shannon, X. Siemens, I. Stairs, B. Stappers, D. Stinebring, G. Theureau, R. van Haasteren, W. van Straten, J. P. W. Verbiest, D. R. B. Yardley, and X. P. You. “The International Pulsar Timing Array project: using pulsars as a gravitational wave detector”. In: *Classical and Quantum Gravity* 27.8, 084013 (Apr. 2010), p. 084013. DOI: [10.1088/0264-9381/27/8/084013](#). arXiv: [0911.5206](#) [[astro-ph.SR](#)].
- [24] Feryal Özel and Paulo Freire. “Masses, Radii, and the Equation of State of Neutron Stars”. In: *ARA&A* 54 (Sept. 2016), pp. 401–440. DOI: [10.1146/annurev-astro-081915-023322](#). arXiv: [1603.02698](#) [[astro-ph.HE](#)].

- [25] Emmanuel Fonseca, H. Thankful Cromartie, Timothy T. Pennucci, Paul S. Ray, Aida Yu. Kirichenko, Scott M. Ransom, Paul B. Demorest, Ingrid H. Stairs, Zaven Arzoumanian, Lucas Guillemot, Aditya Parthasarathy, Matthew Kerr, Ismael Cognard, Paul T. Baker, Harsha Blumer, Paul R. Brook, Megan DeCesar, Timothy Dolch, F. Adam Dong, Elizabeth C. Ferrara, William Fiore, Nathaniel Garver-Daniels, Deborah C. Good, Ross Jennings, Megan L. Jones, Victoria M. Kaspi, Michael T. Lam, Duncan R. Lorimer, Jing Luo, Alexander McEwen, James W. McKee, Maura A. McLaughlin, Natasha McMann, Bradley W. Meyers, Arun Naidu, Cherry Ng, David J. Nice, Nihan Pol, Henri A. Radovan, Brent Shapiro-Albert, Chia Min Tan, Shriharsh P. Tendulkar, Joseph K. Swiggum, Haley M. Wahl, and Weiwei Zhu. “Refined Mass and Geometric Measurements of the High-Mass PSR J0740+6620”. In: *arXiv e-prints*, arXiv:2104.00880 (Apr. 2021), arXiv:2104.00880. arXiv: [2104.00880 \[astro-ph.HE\]](#).
- [26] Feryal Özel, Dimitrios Psaltis, Ramesh Narayan, and Antonio Santos Villarreal. “On the Mass Distribution and Birth Masses of Neutron Stars”. In: *ApJ* 757.1, 55 (Sept. 2012), p. 55. DOI: [10.1088/0004-637X/757/1/55](#). arXiv: [1201.1006 \[astro-ph.HE\]](#).
- [27] Paulo C. C. Freire, Scott M. Ransom, Steve Bégin, Ingrid H. Stairs, Jason W. T. Hessels, Lucille H. Frey, and Fernando Camilo. “Eight New Millisecond Pulsars in NGC 6440 and NGC 6441”. In: *ApJ* 675.1 (Mar. 2008), pp. 670–682. DOI: [10.1086/526338](#). arXiv: [0711.0925 \[astro-ph\]](#).
- [28] Zaven Arzoumanian, Adam Brazier, Sarah Burke-Spolaor, Sydney Chamberlin, Shami Chatterjee, Brian Christy, James M. Cordes, Neil J. Cornish, Fronefield Crawford, H. Thankful Cromartie, Kathryn Crowter, Megan E. DeCesar, Paul B. Demorest, Timothy Dolch, Justin A. Ellis, Robert D. Ferdman, Elizabeth C. Ferrara, Emmanuel Fonseca, Nathan Garver-Daniels, Peter A. Gentile, Daniel Halmrast, E. A. Huerta, Fredrick A. Jenet, Cody Jessup, Glenn Jones, Megan L. Jones, David L. Kaplan, Michael T. Lam, T. Joseph W. Lazio, Lina Levin, Andrea Lommen, Duncan R. Lorimer, Jing Luo, Ryan S. Lynch, Dustin Madison, Allison M. Matthews, Maura A. McLaughlin, Sean T. McWilliams, Chiara Mingarelli, Cherry Ng, David J. Nice, Timothy T. Pennucci, Scott M. Ransom, Paul S. Ray, Xavier Siemens, Joseph Simon, Renée Spiewak, Ingrid H. Stairs, Daniel R. Stinebring, Kevin Stovall, Joseph K. Swiggum, Stephen R. Taylor, Michele Vallisneri, Rutger van Haasteren, Sarah J. Vigeland, Weiwei Zhu, and NANOGrav Collaboration. “The NANOGrav 11-year Data Set: High-precision Timing of 45 Millisecond Pulsars”. In: *ApJS* 235.2, 37 (Apr. 2018), p. 37. DOI: [10.3847/1538-4365/aab5b0](#). arXiv: [1801.01837 \[astro-ph.HE\]](#).
- [29] P. B. Demorest, T. Pennucci, S. M. Ransom, M. S. E. Roberts, and J. W. T. Hessels. “A two-solar-mass neutron star measured using Shapiro delay”. In: *Nature* 467.7319 (Oct. 2010), pp. 1081–1083. DOI: [10.1038/nature09466](#). arXiv: [1010.5788 \[astro-ph.HE\]](#).
- [30] John Antoniadis, Paulo C. C. Freire, Norbert Wex, Thomas M. Tauris, Ryan S. Lynch, Marten H. van Kerkwijk, Michael Kramer, Cees Bassa, Vik S. Dhillon, Thomas Driebe, Jason W. T. Hessels, Victoria M. Kaspi, Vladislav I. Kondratiev, Norbert Langer, Thomas R. Marsh, Maura A. McLaughlin, Timothy T. Pennucci, Scott M. Ransom, Ingrid H. Stairs, Joeri van Leeuwen, Joris P. W. Verbiest, and David G. Whelan. “A Massive Pulsar in a Compact Relativistic Binary”. In: *Science* 340.6131 (Apr. 2013), p. 448. DOI: [10.1126/science.1233232](#). arXiv: [1304.6875 \[astro-ph.HE\]](#).
- [31] J. G. Martinez, K. Stovall, P. C. C. Freire, J. S. Deneva, F. A. Jenet, M. A. McLaughlin, M. Bagchi, S. D. Bates, and A. Ridolfi. “Pulsar J0453+1559: A Double Neutron Star System with a Large Mass Asymmetry”. In: *ApJ* 812.2, 143 (Oct. 2015), p. 143. DOI: [10.1088/0004-637X/812/2/143](#). arXiv: [1509.08805 \[astro-ph.HE\]](#).

- [32] Alexander Y. Potekhin, Andrea De Luca, and José A. Pons. “Neutron Stars—Thermal Emitters”. In: *Space Sci. Rev.* 191.1-4 (Oct. 2015), pp. 171–206. DOI: [10.1007/s11214-014-0102-2](https://doi.org/10.1007/s11214-014-0102-2). arXiv: [1409.7666](https://arxiv.org/abs/1409.7666) [[astro-ph.HE](#)].
- [33] Craig O. Heinke and Wynn C. G. Ho. “Direct Observation of the Cooling of the Cassiopeia A Neutron Star”. In: *ApJ* 719.2 (Aug. 2010), pp. L167–L171. DOI: [10.1088/2041-8205/719/2/L167](https://doi.org/10.1088/2041-8205/719/2/L167). arXiv: [1007.4719](https://arxiv.org/abs/1007.4719) [[astro-ph.HE](#)].
- [34] B. Posselt and G. G. Pavlov. “Upper Limits on the Rapid Cooling of the Central Compact Object in Cas A”. In: *ApJ* 864.2, 135 (Sept. 2018), p. 135. DOI: [10.3847/1538-4357/aad7fc](https://doi.org/10.3847/1538-4357/aad7fc). arXiv: [1808.00531](https://arxiv.org/abs/1808.00531) [[astro-ph.HE](#)].
- [35] Agnieszka Majczyna, Jerzy Madej, Mirosław Należyty, Agata Różańska, and Bartosz Bełdycki. “Precision of Mass and Radius Determination for Neutron Stars from the ATHENA Mission”. In: *ApJ* 888.2, 123 (Jan. 2020), p. 123. DOI: [10.3847/1538-4357/ab5dc9](https://doi.org/10.3847/1538-4357/ab5dc9).
- [36] Slavko Bogdanov, Sebastien Guillot, Paul S. Ray, Michael T. Wolff, Deepto Chakrabarty, Wynn C. G. Ho, Matthew Kerr, Frederick K. Lamb, Andrea Lommen, Renee M. Ludlam, Reilly Milburn, Sergio Montano, M. Coleman Miller, Michi Bauböck, Feryal Özel, Dimitrios Psaltis, Ronald A. Remillard, Thomas E. Riley, James F. Steiner, Tod E. Strohmayer, Anna L. Watts, Kent S. Wood, Jesse Zeldes, Teruaki Enoto, Takashi Okajima, James W. Kellogg, Charles Baker, Craig B. Markwardt, Zaven Arzoumanian, and Keith C. Gendreau. “Constraining the Neutron Star Mass-Radius Relation and Dense Matter Equation of State with NICER. I. The Millisecond Pulsar X-Ray Data Set”. In: *ApJ* 887.1, L25 (Dec. 2019), p. L25. DOI: [10.3847/2041-8213/ab53eb](https://doi.org/10.3847/2041-8213/ab53eb). arXiv: [1912.05706](https://arxiv.org/abs/1912.05706) [[astro-ph.HE](#)].
- [37] LIGO Scientific Collaboration and Virgo Collaboration. “GW170817: Measurements of Neutron Star Radii and Equation of State”. In: *Phys. Rev. Lett.* 121.16, 161101 (Oct. 2018), p. 161101. DOI: [10.1103/PhysRevLett.121.161101](https://doi.org/10.1103/PhysRevLett.121.161101). arXiv: [1805.11581](https://arxiv.org/abs/1805.11581) [[gr-qc](#)].
- [38] A. Yu Potekhin. “Atmospheres and radiating surfaces of neutron stars”. In: *Physics Uspekhi* 57.8, 735–770 (Aug. 2014), pp. 735–770. DOI: [10.3367/UFNe.0184.201408a.0793](https://doi.org/10.3367/UFNe.0184.201408a.0793). arXiv: [1403.0074](https://arxiv.org/abs/1403.0074) [[astro-ph.SR](#)].
- [39] Anna L. Watts, Nils Andersson, Deepto Chakrabarty, Marco Feroci, Kai Hebeler, Gianluca Israel, Frederick K. Lamb, M. Coleman Miller, Sharon Morsink, Feryal Özel, Alessandro Patruno, Juri Poutanen, Dimitrios Psaltis, Achim Schwenk, Andrew W. Steiner, Luigi Stella, Laura Tolos, and Michiel van der Klis. “Colloquium: Measuring the neutron star equation of state using x-ray timing”. In: *Reviews of Modern Physics* 88.2, 021001 (Apr. 2016), p. 021001. DOI: [10.1103/RevModPhys.88.021001](https://doi.org/10.1103/RevModPhys.88.021001). arXiv: [1602.01081](https://arxiv.org/abs/1602.01081) [[astro-ph.HE](#)].
- [40] Thomas E. Riley, Anna L. Watts, Paul S. Ray, Slavko Bogdanov, Sebastien Guillot, Sharon M. Morsink, Anna V. Bilous, Zaven Arzoumanian, Devarshi Choudhury, Julia S. Deneva, Keith C. Gendreau, Alice K. Harding, Wynn C. G. Ho, James M. Lattimer, Michael Loewenstein, Renee M. Ludlam, Craig B. Markwardt, Takashi Okajima, Chanda Prescod-Weinstein, Ronald A. Remillard, Michael T. Wolff, Emmanuel Fonseca, H. Thankful Cromartie, Matthew Kerr, Timothy T. Pennucci, Aditya Parthasarathy, Scott Ransom, Ingrid Stairs, Lucas Guillemot, and Ismael Cognard. “A NICER View of the Massive Pulsar PSR J0740+6620 Informed by Radio Timing and XMM-Newton Spectroscopy”. In: *arXiv e-prints*, arXiv:2105.06980 (May 2021), arXiv:2105.06980. arXiv: [2105.06980](https://arxiv.org/abs/2105.06980) [[astro-ph.HE](#)].
- [41] M. C. Miller, F. K. Lamb, A. J. Dittmann, S. Bogdanov, Z. Arzoumanian, K. C. Gendreau, S. Guillot, W. C. G. Ho, J. M. Lattimer, M. Loewenstein, S. M. Morsink, P. S. Ray, M. T. Wolff, C. L. Baker, T. Cazeau, S. Manthripragada, C. B. Markwardt, T. Okajima, S.

- Pollard, I. Cognard, H. T. Cromartie, E. Fonseca, L. Guillemot, M. Kerr, A. Parthasarathy, T. T. Pennucci, S. Ransom, and I. Stairs. “The Radius of PSR J0740+6620 from NICER and XMM-Newton Data”. In: *arXiv e-prints*, arXiv:2105.06979 (May 2021), arXiv:2105.06979. arXiv: [2105.06979 \[astro-ph.HE\]](#).
- [42] Daniel A. Godzieba, Rossella Gamba, David Radice, and Sebastiano Bernuzzi. “Updated universal relations for tidal deformabilities of neutron stars from phenomenological equations of state”. In: *Phys. Rev. D* 103.6, 063036 (Mar. 2021), p. 063036. DOI: [10.1103/PhysRevD.103.063036](#). arXiv: [2012.12151 \[astro-ph.HE\]](#).
- [43] LIGO Scientific Collaboration and Virgo Collaboration. “GW190425: Observation of a Compact Binary Coalescence with Total Mass $\sim 3.4 M_{\odot}$ ”. In: *ApJ* 892.1, L3 (Mar. 2020), p. L3. DOI: [10.3847/2041-8213/ab75f5](#). arXiv: [2001.01761 \[astro-ph.HE\]](#).
- [44] Tim Dietrich, Michael W. Coughlin, Peter T. H. Pang, Mattia Bulla, Jack Heinzl, Lina Issa, Ingo Tews, and Sarah Antier. “Multimessenger constraints on the neutron-star equation of state and the Hubble constant”. In: *Science* 370.6523 (Dec. 2020), pp. 1450–1453. DOI: [10.1126/science.abb4317](#). arXiv: [2002.11355 \[astro-ph.HE\]](#).
- [45] G. Raaijmakers, S. K. Greif, T. E. Riley, T. Hinderer, K. Hebeler, A. Schwenk, A. L. Watts, S. Nissanke, S. Guillot, J. M. Lattimer, and R. M. Ludlam. “Constraining the Dense Matter Equation of State with Joint Analysis of NICER and LIGO/Virgo Measurements”. In: *ApJ* 893.1, L21 (Apr. 2020), p. L21. DOI: [10.3847/2041-8213/ab822f](#). arXiv: [1912.11031 \[astro-ph.HE\]](#).
- [46] Mark G. Alford and Steven P. Harris. “Damping of density oscillations in neutrino-transparent nuclear matter”. In: *Phys. Rev. C* 100.3, 035803 (Sept. 2019), p. 035803. DOI: [10.1103/PhysRevC.100.035803](#). arXiv: [1907.03795 \[nucl-th\]](#).
- [47] P. Haensel and J. L. Zdunik. “Non-equilibrium processes in the crust of an accreting neutron star”. In: *A&A* 227.2 (Jan. 1990), pp. 431–436.
- [48] M. Oertel, M. Hempel, T. Klähn, and S. Typel. “Equations of state for supernovae and compact stars”. In: *Reviews of Modern Physics* 89.1, 015007 (Jan. 2017), p. 015007. DOI: [10.1103/RevModPhys.89.015007](#). arXiv: [1610.03361 \[astro-ph.HE\]](#).
- [49] S. K. Greif, K. Hebeler, J. M. Lattimer, C. J. Pethick, and A. Schwenk. “Equation of state constraints from nuclear physics, neutron star masses, and future moment of inertia measurements”. In: *arXiv e-prints*, arXiv:2005.14164 (May 2020), arXiv:2005.14164. arXiv: [2005.14164 \[astro-ph.HE\]](#).
- [50] *NICER mission overview*. URL: https://heasarc.gsfc.nasa.gov/docs/nicer/nicer_about.html (visited on 11/19/2020).
- [51] Stefan Typer, Micaela Oertel, Thomas Klähn, and Chikako Ishizuka. *CompStar Online Supernovae Equation of State*. <https://compose.obspm.fr/>.
- [52] Yudai Suwa, Takashi Yoshida, Masaru Shibata, Hideyuki Umeda, and Koh Takahashi. “On the minimum mass of neutron stars”. In: *MNRAS* 481.3 (Dec. 2018), pp. 3305–3312. DOI: [10.1093/mnras/sty2460](#). arXiv: [1808.02328 \[astro-ph.HE\]](#).
- [53] Adam Burrows. “Colloquium: Perspectives on core-collapse supernova theory”. In: *Reviews of Modern Physics* 85.1 (Jan. 2013), pp. 245–261. DOI: [10.1103/RevModPhys.85.245](#). arXiv: [1210.4921 \[astro-ph.SR\]](#).
- [54] Matthias Liebendörfer, O. E. Bronson Messer, Anthony Mezzacappa, Stephen W. Bruenn, Christian Y. Cardall, and F. K. Thielemann. “A Finite Difference Representation of Neutrino Radiation Hydrodynamics in Spherically Symmetric General Relativistic Space-time”. In: *ApJS* 150.1 (Jan. 2004), pp. 263–316. DOI: [10.1086/380191](#). arXiv: [astro-ph/0207036 \[astro-ph\]](#).
- [55] T. Foglizzo, P. Galletti, L. Scheck, and H. Th. Janka. “Instability of a Stalled Accretion Shock: Evidence for the Advective-Acoustic Cycle”. In: *ApJ* 654.2 (Jan. 2007), pp. 1006–1021. DOI: [10.1086/509612](#). arXiv: [astro-ph/0606640 \[astro-ph\]](#).

- [56] Eric J. Lentz, Stephen W. Bruenn, W. Raphael Hix, Anthony Mezzacappa, O. E. Bronson Messer, Eirik Endeve, John M. Blondin, J. Austin Harris, Pedro Marronetti, and Konstantin N. Yakunin. “Three-dimensional Core-collapse Supernova Simulated Using a 15 Ms Progenitor”. In: *ApJ* 807.2, L31 (July 2015), p. L31. DOI: [10.1088/2041-8205/807/2/L31](https://doi.org/10.1088/2041-8205/807/2/L31). arXiv: [1505.05110](https://arxiv.org/abs/1505.05110) [[astro-ph.SR](#)].
- [57] David Vartanyan, Adam Burrows, David Radice, M. Aaron Skinner, and Joshua Dolence. “A successful 3D core-collapse supernova explosion model”. In: *MNRAS* 482.1 (Jan. 2019), pp. 351–369. DOI: [10.1093/mnras/sty2585](https://doi.org/10.1093/mnras/sty2585). arXiv: [1809.05106](https://arxiv.org/abs/1809.05106) [[astro-ph.HE](#)].
- [58] Jade Powell and Bernhard Müller. “Three-dimensional core-collapse supernova simulations of massive and rotating progenitors”. In: *MNRAS* 494.4 (June 2020), pp. 4665–4675. DOI: [10.1093/mnras/staa1048](https://doi.org/10.1093/mnras/staa1048). arXiv: [2002.10115](https://arxiv.org/abs/2002.10115) [[astro-ph.HE](#)].
- [59] A. Wongwathanarat, E. Müller, and H. Th. Janka. “Three-dimensional simulations of core-collapse supernovae: from shock revival to shock breakout”. In: *A&A* 577, A48 (May 2015), A48. DOI: [10.1051/0004-6361/201425025](https://doi.org/10.1051/0004-6361/201425025). arXiv: [1409.5431](https://arxiv.org/abs/1409.5431) [[astro-ph.HE](#)].
- [60] M. Obergaulinger and M. Á. Aloy. “Magnetorotational core collapse of possible GRB progenitors. III. Three-dimensional models”. In: *MNRAS* (Feb. 2021). DOI: [10.1093/mnras/stab295](https://doi.org/10.1093/mnras/stab295). arXiv: [2008.07205](https://arxiv.org/abs/2008.07205) [[astro-ph.HE](#)].
- [61] Wakana Iwakami, Hirotada Okawa, Hiroki Nagakura, Akira Harada, Shun Furusawa, Kosuke Sumiyoshi, Hideo Matsufuru, and Shoichi Yamada. “Simulations of the Early Postbounce Phase of Core-collapse Supernovae in Three-dimensional Space with Full Boltzmann Neutrino Transport”. In: *ApJ* 903.2, 82 (Nov. 2020), p. 82. DOI: [10.3847/1538-4357/abb8cf](https://doi.org/10.3847/1538-4357/abb8cf). arXiv: [2004.02091](https://arxiv.org/abs/2004.02091) [[astro-ph.HE](#)].
- [62] Kazuhiro Hayama, Takami Kuroda, Kei Kotake, and Tomoya Takiwaki. “Coherent network analysis of gravitational waves from three-dimensional core-collapse supernova models”. In: *Phys. Rev. D* 92.12, 122001 (Dec. 2015), p. 122001. DOI: [10.1103/PhysRevD.92.122001](https://doi.org/10.1103/PhysRevD.92.122001). arXiv: [1501.00966](https://arxiv.org/abs/1501.00966) [[astro-ph.HE](#)].
- [63] Conrad Chan, Bernhard Müller, Alexander Heger, Rüdiger Pakmor, and Volker Springel. “Black Hole Formation and Fallback during the Supernova Explosion of a 40 solar mass Star”. In: *ApJ* 852.1, L19 (Jan. 2018), p. L19. DOI: [10.3847/2041-8213/aaa28c](https://doi.org/10.3847/2041-8213/aaa28c). arXiv: [1710.00838](https://arxiv.org/abs/1710.00838) [[astro-ph.SR](#)].
- [64] A. Arcones and F. K. Thielemann. “Neutrino-driven wind simulations and nucleosynthesis of heavy elements”. In: *Journal of Physics G Nuclear Physics* 40.1, 013201 (Jan. 2013), p. 013201. DOI: [10.1088/0954-3899/40/1/013201](https://doi.org/10.1088/0954-3899/40/1/013201). arXiv: [1207.2527](https://arxiv.org/abs/1207.2527) [[astro-ph.SR](#)].
- [65] T. Rauscher and C. Fröhlich. “Proton-rich nucleosynthesis and nuclear physics”. In: *Origin of Matter and Evolution of Galaxies 2011*. Ed. by Shigeru Kubono, Takehito Hayakawa, Toshitaka Kajino, Hiroari Miyatake, Tohru Motobayashi, and Ken’ichi Nomoto. Vol. 1484. American Institute of Physics Conference Series. Nov. 2012, pp. 73–78. DOI: [10.1063/1.4763376](https://doi.org/10.1063/1.4763376). arXiv: [1304.0929](https://arxiv.org/abs/1304.0929) [[astro-ph.SR](#)].
- [66] Y. Z. Qian and S. E. Woosley. “Nucleosynthesis in Neutrino-driven Winds. I. The Physical Conditions”. In: *ApJ* 471 (Nov. 1996), p. 331. DOI: [10.1086/177973](https://doi.org/10.1086/177973). arXiv: [astro-ph/9611094](https://arxiv.org/abs/astro-ph/9611094) [[astro-ph](#)].
- [67] Bradley S. Meyer, Gail C. McLaughlin, and George M. Fuller. “Neutrino capture and r-process nucleosynthesis”. In: *Phys. Rev. C* 58.6 (Dec. 1998), pp. 3696–3710. DOI: [10.1103/PhysRevC.58.3696](https://doi.org/10.1103/PhysRevC.58.3696). arXiv: [astro-ph/9809242](https://arxiv.org/abs/astro-ph/9809242) [[astro-ph](#)].
- [68] Gail C. McLaughlin, George M. Fuller, and James R. Wilson. “The Influence of Nuclear Composition on the Electron Fraction in the Post-Core Bounce Supernova Environment”. In: *ApJ* 472 (Dec. 1996), p. 440. DOI: [10.1086/178077](https://doi.org/10.1086/178077). arXiv: [astro-ph/9701114](https://arxiv.org/abs/astro-ph/9701114) [[astro-ph](#)].
- [69] Todd A. Thompson, Adam Burrows, and Jorge E. Horvath. “ μ and τ neutrino thermalization and production in supernovae: Processes and time scales”. In: *Phys. Rev. C*

- 62.3, 035802 (Sept. 2000), p. 035802. DOI: [10.1103/PhysRevC.62.035802](https://doi.org/10.1103/PhysRevC.62.035802). arXiv: [astro-ph/0003054](https://arxiv.org/abs/astro-ph/0003054) [astro-ph].
- [70] Steen Hannestad and Georg Raffelt. “Supernova Neutrino Opacity from Nucleon-Nucleon Bremsstrahlung and Related Processes”. In: *ApJ* 507.1 (Nov. 1998), pp. 339–352. DOI: [10.1086/306303](https://doi.org/10.1086/306303). arXiv: [astro-ph/9711132](https://arxiv.org/abs/astro-ph/9711132) [astro-ph].
 - [71] Paul J. Schinder, David N. Schramm, Paul J. Wiita, Steven H. Margolis, and David L. Tubbs. “Neutrino Emission by the Pair, Plasma, and Photo Processes in the Weinberg-Salam Model”. In: *ApJ* 313 (Feb. 1987), p. 531. DOI: [10.1086/164993](https://doi.org/10.1086/164993).
 - [72] C. J. Horowitz. “Weak magnetism for antineutrinos in supernovae”. In: *Phys. Rev. D* 65.4, 043001 (Feb. 2002), p. 043001. DOI: [10.1103/PhysRevD.65.043001](https://doi.org/10.1103/PhysRevD.65.043001). arXiv: [astro-ph/0109209](https://arxiv.org/abs/astro-ph/0109209) [astro-ph].
 - [73] R. Bollig, H. T. Janka, A. Lohs, G. Martínez-Pinedo, C. J. Horowitz, and T. Melson. “Muon Creation in Supernova Matter Facilitates Neutrino-Driven Explosions”. In: *Phys. Rev. Lett.* 119.24, 242702 (Dec. 2017), p. 242702. DOI: [10.1103/PhysRevLett.119.242702](https://doi.org/10.1103/PhysRevLett.119.242702). arXiv: [1706.04630](https://arxiv.org/abs/1706.04630) [astro-ph.HE].
 - [74] Daniel Z. Freedman. “Coherent effects of a weak neutral current”. In: *Phys. Rev. D* 9.5 (Mar. 1974), pp. 1389–1392. DOI: [10.1103/PhysRevD.9.1389](https://doi.org/10.1103/PhysRevD.9.1389).
 - [75] A. Burrows and T. J. Mazurek. “Postshock neutrino transport and electron capture in stellar collapse”. In: *ApJ* 259 (Aug. 1982), pp. 330–340. DOI: [10.1086/160169](https://doi.org/10.1086/160169).
 - [76] J. M. Lattimer, A. Burrows, and A. Yahil. “Type II supernova energetics”. In: *ApJ* 288 (Jan. 1985), pp. 644–652. DOI: [10.1086/162830](https://doi.org/10.1086/162830).
 - [77] Ulrich R. M. E. Geppert. “Thermal Evolution of Neutron Stars”. In: *Handbook of Supernovae*. Ed. by Athem W. Alsabti and Paul Murdin. 2017, p. 1353. DOI: [10.1007/978-3-319-21846-5_69](https://doi.org/10.1007/978-3-319-21846-5_69).
 - [78] Adam Burrows and Burce A. Fryxell. “A Convective Trigger for Supernova Explosions”. In: *ApJ* 418 (Nov. 1993), p. L33. DOI: [10.1086/187109](https://doi.org/10.1086/187109).
 - [79] Marc Herant, Willy Benz, W. Raphael Hix, Chris L. Fryer, and Stirling A. Colgate. “Inside the Supernova: A Powerful Convective Engine”. In: *ApJ* 435 (Nov. 1994), p. 339. DOI: [10.1086/174817](https://doi.org/10.1086/174817). arXiv: [astro-ph/9404024](https://arxiv.org/abs/astro-ph/9404024) [astro-ph].
 - [80] Wolfgang Keil, H. Thomas Janka, and Ewald Mueller. “Ledoux Convection in Protoneutron Stars—A Clue to Supernova Nucleosynthesis?” In: *ApJ* 473 (Dec. 1996), p. L111. DOI: [10.1086/310404](https://doi.org/10.1086/310404). arXiv: [astro-ph/9610203](https://arxiv.org/abs/astro-ph/9610203) [astro-ph].
 - [81] L. F. Roberts, G. Shen, V. Cirigliano, J. A. Pons, S. Reddy, and S. E. Woosley. “Protoneutron Star Cooling with Convection: The Effect of the Symmetry Energy”. In: *Phys. Rev. Lett.* 108.6, 061103 (Feb. 2012), p. 061103. DOI: [10.1103/PhysRevLett.108.061103](https://doi.org/10.1103/PhysRevLett.108.061103). arXiv: [1112.0335](https://arxiv.org/abs/1112.0335) [astro-ph.HE].
 - [82] Sherwood Richers, Christian D. Ott, Ernazar Abdikamalov, Evan O’Connor, and Chris Sullivan. “Equation of state effects on gravitational waves from rotating core collapse”. In: *Phys. Rev. D* 95.6, 063019 (Mar. 2017), p. 063019. DOI: [10.1103/PhysRevD.95.063019](https://doi.org/10.1103/PhysRevD.95.063019). arXiv: [1701.02752](https://arxiv.org/abs/1701.02752) [astro-ph.HE].
 - [83] Alejandro Torres-Forné, Pablo Cerdá-Durán, Andrea Passamonti, and José A. Font. “Towards asteroseismology of core-collapse supernovae with gravitational-wave observations - I. Cowling approximation”. In: *MNRAS* 474.4 (Mar. 2018), pp. 5272–5286. DOI: [10.1093/mnras/stx3067](https://doi.org/10.1093/mnras/stx3067). arXiv: [1708.01920](https://arxiv.org/abs/1708.01920) [astro-ph.SR].
 - [84] H. Andresen, B. Müller, E. Müller, and H. Th. Janka. “Gravitational wave signals from 3D neutrino hydrodynamics simulations of core-collapse supernovae”. In: *MNRAS* 468.2 (June 2017), pp. 2032–2051. DOI: [10.1093/mnras/stx618](https://doi.org/10.1093/mnras/stx618). arXiv: [1607.05199](https://arxiv.org/abs/1607.05199) [astro-ph.HE].

- [85] Evan P. O Connor and Sean M. Couch. “Exploring Fundamentally Three-dimensional Phenomena in High-fidelity Simulations of Core-collapse Supernovae”. In: *ApJ* 865.2, 81 (Oct. 2018), p. 81. DOI: [10.3847/1538-4357/aadcf7](https://doi.org/10.3847/1538-4357/aadcf7). arXiv: [1807.07579](https://arxiv.org/abs/1807.07579) [[astro-ph.HE](#)].
- [86] David Radice, Viktoriya Morozova, Adam Burrows, David Vartanyan, and Hiroki Nagakura. “Characterizing the Gravitational Wave Signal from Core-collapse Supernovae”. In: *ApJ* 876.1, L9 (May 2019), p. L9. DOI: [10.3847/2041-8213/ab191a](https://doi.org/10.3847/2041-8213/ab191a). arXiv: [1812.07703](https://arxiv.org/abs/1812.07703) [[astro-ph.HE](#)].
- [87] Jade Powell and Bernhard Müller. “Gravitational wave emission from 3D explosion models of core-collapse supernovae with low and normal explosion energies”. In: *MNRAS* 487.1 (July 2019), pp. 1178–1190. DOI: [10.1093/mnras/stz1304](https://doi.org/10.1093/mnras/stz1304). arXiv: [1812.05738](https://arxiv.org/abs/1812.05738) [[astro-ph.HE](#)].
- [88] Anthony Mezzacappa, Pedro Marronetti, Ryan E. Landfield, Eric J. Lentz, Konstantin N. Yakunin, Stephen W. Bruenn, W. Raphael Hix, O. E. Bronson Messer, Eirik Endeve, John M. Blondin, and J. Austin Harris. “Gravitational-wave signal of a core-collapse supernova explosion of a 15 Ms star”. In: *Phys. Rev. D* 102.2, 023027 (July 2020), p. 023027. DOI: [10.1103/PhysRevD.102.023027](https://doi.org/10.1103/PhysRevD.102.023027). arXiv: [2007.15099](https://arxiv.org/abs/2007.15099) [[astro-ph.HE](#)].
- [89] A. Burrows and J. M. Lattimer. “The Birth of Neutron Stars”. In: *ApJ* 307 (Aug. 1986), p. 178. DOI: [10.1086/164405](https://doi.org/10.1086/164405).
- [90] W. Keil and H. T. Janka. “Hadronic phase transitions at supranuclear densities and the delayed collapse of newly formed neutron stars.” In: *A&A* 296 (Apr. 1995), p. 145.
- [91] K. Sumiyoshi, H. Suzuki, and H. Toki. “Influence of the symmetry energy on the birth of neutron stars and supernova neutrinos.” In: *A&A* 303 (Nov. 1995), p. 475. arXiv: [astro-ph/9506024](https://arxiv.org/abs/astro-ph/9506024) [[astro-ph](#)].
- [92] J. A. Pons, S. Reddy, M. Prakash, J. M. Lattimer, and J. A. Miralles. “Evolution of Proto-Neutron Stars”. In: *ApJ* 513.2 (Mar. 1999), pp. 780–804. DOI: [10.1086/306889](https://doi.org/10.1086/306889). arXiv: [astro-ph/9807040](https://arxiv.org/abs/astro-ph/9807040) [[astro-ph](#)].
- [93] L. F. Roberts. “A New Code for Proto-neutron Star Evolution”. In: *ApJ* 755.2, 126 (Aug. 2012), p. 126. DOI: [10.1088/0004-637X/755/2/126](https://doi.org/10.1088/0004-637X/755/2/126). arXiv: [1205.3228](https://arxiv.org/abs/1205.3228) [[astro-ph.HE](#)].
- [94] Rémi Kazeroni, Brendan K. Krueger, Jérôme Guilet, Thierry Foglizzo, and Daniel Pomarède. “The non-linear onset of neutrino-driven convection in two- and three-dimensional core-collapse supernovae”. In: *MNRAS* 480.1 (Oct. 2018), pp. 261–280. DOI: [10.1093/mnras/sty1742](https://doi.org/10.1093/mnras/sty1742). arXiv: [1802.08125](https://arxiv.org/abs/1802.08125) [[astro-ph.SR](#)].
- [95] Raphaël Raynaud, Pablo Cerdá-Durán, and Jérôme Guilet. “Gravitational wave signature of proto-neutron star convection: I. MHD numerical simulations”. In: *arXiv e-prints*, arXiv:2103.12445 (Mar. 2021), arXiv:2103.12445. arXiv: [2103.12445](https://arxiv.org/abs/2103.12445) [[astro-ph.SR](#)].
- [96] Tobias Fischer, Gang Guo, Alan A. Dzhiyev, Gabriel Martínez-Pinedo, Meng-Ru Wu, Andreas Lohs, and Yong-Zhong Qian. “Neutrino signal from proto-neutron star evolution: Effects of opacities from charged-current-neutrino interactions and inverse neutron decay”. In: *Phys. Rev. C* 101.2, 025804 (Feb. 2020), p. 025804. DOI: [10.1103/PhysRevC.101.025804](https://doi.org/10.1103/PhysRevC.101.025804). arXiv: [1804.10890](https://arxiv.org/abs/1804.10890) [[astro-ph.HE](#)].
- [97] Eric J. Lentz, Stephen W. Bruenn, W. Raphael Hix, Anthony Mezzacappa, O. E. Bronson Messer, Eirik Endeve, John M. Blondin, J. Austin Harris, Pedro Marronetti, and Konstantin N. Yakunin. “Three-dimensional Core-collapse Supernova Simulated Using a 15 Ms Progenitor”. In: *ApJ* 807.2, L31 (July 2015), p. L31. DOI: [10.1088/2041-8205/807/2/L31](https://doi.org/10.1088/2041-8205/807/2/L31). arXiv: [1505.05110](https://arxiv.org/abs/1505.05110) [[astro-ph.SR](#)].
- [98] Adam Burrows, David Radice, and David Vartanyan. “Three-dimensional supernova explosion simulations of 9-, 10-, 11-, 12-, and 13-Ms stars”. In: *MNRAS* 485.3 (May 2019), pp. 3153–3168. DOI: [10.1093/mnras/stz543](https://doi.org/10.1093/mnras/stz543). arXiv: [1902.00547](https://arxiv.org/abs/1902.00547) [[astro-ph.SR](#)].
- [99] Yudai Suwa. “From supernovae to neutron stars”. In: *PASJ* 66.2, L1 (Apr. 2014), p. L1. DOI: [10.1093/pasj/pst030](https://doi.org/10.1093/pasj/pst030). arXiv: [1311.7249](https://arxiv.org/abs/1311.7249) [[astro-ph.HE](#)].

- [100] A. F. Fantina, S. De Ridder, N. Chamel, and F. Gulminelli. “Crystallization of the outer crust of a non-accreting neutron star”. In: *A&A* 633, A149 (Jan. 2020), A149. DOI: [10.1051/0004-6361/201936359](https://doi.org/10.1051/0004-6361/201936359). arXiv: [1912.02849](https://arxiv.org/abs/1912.02849) [[astro-ph.HE](#)].
- [101] D. G. Yakovlev and C. J. Pethick. “Neutron Star Cooling”. In: *ARA&A* 42.1 (Sept. 2004), pp. 169–210. DOI: [10.1146/annurev.astro.42.053102.134013](https://doi.org/10.1146/annurev.astro.42.053102.134013). arXiv: [astro-ph/0402143](https://arxiv.org/abs/astro-ph/0402143) [[astro-ph](#)].
- [102] Giovanni Cameli, Leonardo Gualtieri, José A. Pons, and Valeria Ferrari. “Spin evolution of a proto-neutron star”. In: *Phys. Rev. D* 94.2, 024008 (July 2016), p. 024008. DOI: [10.1103/PhysRevD.94.024008](https://doi.org/10.1103/PhysRevD.94.024008). arXiv: [1601.02945](https://arxiv.org/abs/1601.02945) [[astro-ph.HE](#)].
- [103] Raymond Davis. “Solar Neutrinos. II. Experimental”. In: *Phys. Rev. Lett.* 12.11 (Mar. 1964), pp. 303–305. DOI: [10.1103/PhysRevLett.12.303](https://doi.org/10.1103/PhysRevLett.12.303).
- [104] K. Hirata, T. Kajita, M. Koshiba, M. Nakahata, Y. Oyama, N. Sato, A. Suzuki, M. Takita, Y. Totsuka, T. Kifune, T. Suda, K. Takahashi, T. Tanimori, K. Miyano, M. Yamada, E. W. Beier, L. R. Feldscher, S. B. Kim, A. K. Mann, F. M. Newcomer, R. van, W. Zhang, and B. G. Cortez. “Observation of a neutrino burst from the supernova SN1987A”. In: *Phys. Rev. Lett.* 58.14 (Apr. 1987), pp. 1490–1493. DOI: [10.1103/PhysRevLett.58.1490](https://doi.org/10.1103/PhysRevLett.58.1490).
- [105] R. M. Bionta, G. Blewitt, C. B. Bratton, D. Casper, A. Ciocio, R. Claus, B. Cortez, M. Crouch, S. T. Dye, S. Errede, G. W. Foster, W. Gajewski, K. S. Ganezer, M. Goldhaber, T. J. Haines, T. W. Jones, D. Kielczewska, W. R. Kropp, J. G. Learned, J. M. Losecco, J. Matthews, R. Miller, M. S. Mudan, H. S. Park, L. R. Price, F. Reines, J. Schultz, S. Seidel, E. Shumard, D. Sinclair, H. W. Sobel, J. L. Stone, L. R. Sulak, R. Svoboda, G. Thornton, J. C. van der Velde, and C. Wuest. “Observation of a neutrino burst in coincidence with supernova 1987A in the Large Magellanic Cloud”. In: *Phys. Rev. Lett.* 58.14 (Apr. 1987), pp. 1494–1496. DOI: [10.1103/PhysRevLett.58.1494](https://doi.org/10.1103/PhysRevLett.58.1494).
- [106] E. N. Alekseev, L. N. Alekseeva, V. I. Volchenko, and I. V. Krivosheina. “Possible detection of a neutrino signal on 23 February 1987 at the Baksan underground scintillation telescope of the Institute of Nuclear Research”. In: *Soviet Journal of Experimental and Theoretical Physics Letters* 45 (May 1987), p. 589.
- [107] James M. Lattimer and A. Yahil. “Analysis of the Neutrino Events from Supernova 1987A”. In: *ApJ* 340 (May 1989), p. 426. DOI: [10.1086/167404](https://doi.org/10.1086/167404).
- [108] Kate Scholberg. “Supernova Neutrino Detection”. In: *Annual Review of Nuclear and Particle Science* 62 (Nov. 2012), pp. 81–103. DOI: [10.1146/annurev-nucl-102711-095006](https://doi.org/10.1146/annurev-nucl-102711-095006). arXiv: [1205.6003](https://arxiv.org/abs/1205.6003) [[astro-ph.IM](#)].
- [109] M. Ikeda et al. “Search for Supernova Neutrino Bursts at Super-Kamiokande”. In: *ApJ* 669.1 (Nov. 2007), pp. 519–524. DOI: [10.1086/521547](https://doi.org/10.1086/521547). arXiv: [0706.2283](https://arxiv.org/abs/0706.2283) [[astro-ph](#)].
- [110] N. Yu. Agafonova, M. Aglietta, P. Antonioli, G. Bari, A. Bonardi, V. V. Boyarkin, G. Bruno, W. Fulgione, P. Galeotti, M. Garbini, P. L. Ghia, P. Giusti, F. Gomez, E. Kemp, V. V. Kuznetsov, V. A. Kuznetsov, A. S. Malguin, H. Menghetti, A. Pesci, R. Persiani, I. A. Pless, A. Porta, V. G. Riasny, O. G. Ryazhskaya, O. Saavedra, G. Sartorelli, M. Selvi, C. Vigorito, L. Votano, V. F. Yakushev, G. T. Zatsepin, and A. Zichichi. “On-line recognition of supernova neutrino bursts in the LVD”. In: *Astroparticle Physics* 28.6 (Jan. 2008), pp. 516–522. DOI: [10.1016/j.astropartphys.2007.09.005](https://doi.org/10.1016/j.astropartphys.2007.09.005). arXiv: [0710.0259](https://arxiv.org/abs/0710.0259) [[astro-ph](#)].
- [111] C. Cuesta. “Core-Collapse Supernove Burst Neutrinos in DUNE”. In: *arXiv e-prints*, arXiv:2011.06969 (Nov. 2020), arXiv:2011.06969. arXiv: [2011.06969](https://arxiv.org/abs/2011.06969) [[physics.ins-det](#)].
- [112] C. A. Duba, F. Duncan, J. Farine, A. Habig, A. Hime, R. G. H. Robertson, K. Scholberg, T. Shantz, C. J. Virtue, J. F. Wilkerson, and S. Yen. “HALO the helium and lead observatory for supernova neutrinos”. In: *Journal of Physics Conference Series*. Vol. 136. Journal of Physics Conference Series. Nov. 2008, 042077, p. 042077. DOI: [10.1088/1742-6596/136/4/042077](https://doi.org/10.1088/1742-6596/136/4/042077).

- [113] Pietro Antonioli, Richard Tresch Fienberg, Rabrice Fleurot, Yoshiyuki Fukuda, Walter Fulgione, Alec Habig, Jaret Heise, Arthur B. McDonald, Corrinne Mills, Toshio Namba, Leif J. Robinson, Kate Scholberg, Michael Schwendener, Roger W. Sinnott, Blake Stacey, Yoichiro Suzuki, Réda Tafirout, Carlo Vigorito, Brett Viren, Clarence Virtue, and Antonino Zichichi. “SNEWS: the SuperNova Early Warning System”. In: *New Journal of Physics* 6 (July 2004), p. 114. DOI: [10.1088/1367-2630/6/1/114](https://doi.org/10.1088/1367-2630/6/1/114). arXiv: [astro-ph/0406214](https://arxiv.org/abs/astro-ph/0406214) [[astro-ph](#)].
- [114] F. Debbasch and W. A. van Leeuwen. “General relativistic Boltzmann equation, I: Covariant treatment”. In: *Physica A Statistical Mechanics and its Applications* 388.7 (Apr. 2009), pp. 1079–1104. DOI: [10.1016/j.physa.2008.12.023](https://doi.org/10.1016/j.physa.2008.12.023).
- [115] M. Aker et al. “Improved Upper Limit on the Neutrino Mass from a Direct Kinematic Method by KATRIN”. In: *Phys. Rev. Lett.* 123.22, 221802 (Nov. 2019), p. 221802. DOI: [10.1103/PhysRevLett.123.221802](https://doi.org/10.1103/PhysRevLett.123.221802). arXiv: [1909.06048](https://arxiv.org/abs/1909.06048) [[hep-ex](#)].
- [116] Gilberto M. Kremer. “The Boltzmann equation in special and general relativity”. In: *28th International Symposium on Rarefied Gas Dynamics 2012*. Ed. by Michel Mareschal and Andrés Santos. Vol. 1501. American Institute of Physics Conference Series. Nov. 2012, pp. 160–167. DOI: [10.1063/1.4769495](https://doi.org/10.1063/1.4769495). arXiv: [1207.3977](https://arxiv.org/abs/1207.3977) [[cond-mat.stat-mech](#)].
- [117] F. Debbasch and W. A. van Leeuwen. “General relativistic Boltzmann equation, II: Manifestly covariant treatment”. In: *Physica A Statistical Mechanics and its Applications* 388.9 (May 2009), pp. 1818–1834. DOI: [10.1016/j.physa.2009.01.009](https://doi.org/10.1016/j.physa.2009.01.009).
- [118] Gregory V. Vereshchagin and Alexey G. Aksenov. *Relativistic Kinetic Theory*. 2017.
- [119] J. Chernohorsky. “Symmetries in Neutrino-Electron Scattering”. In: *ApJ* 433 (Sept. 1994), p. 247. DOI: [10.1086/174639](https://doi.org/10.1086/174639).
- [120] B. Müller and H. Th. Janka. “Non-radial instabilities and progenitor asphericities in core-collapse supernovae”. In: *MNRAS* 448.3 (Apr. 2015), pp. 2141–2174. DOI: [10.1093/mnras/stv101](https://doi.org/10.1093/mnras/stv101). arXiv: [1409.4783](https://arxiv.org/abs/1409.4783) [[astro-ph.SR](#)].
- [121] E. M. Murchikova, E. Abdikamalov, and T. Urbatsch. “Analytic closures for M1 neutrino transport”. In: *MNRAS* 469.2 (Aug. 2017), pp. 1725–1737. DOI: [10.1093/mnras/stx986](https://doi.org/10.1093/mnras/stx986). arXiv: [1701.07027](https://arxiv.org/abs/1701.07027) [[astro-ph.HE](#)].
- [122] C. D. Levermore and G. C. Pomraning. “A flux-limited diffusion theory”. In: *ApJ* 248 (Aug. 1981), pp. 321–334. DOI: [10.1086/159157](https://doi.org/10.1086/159157).
- [123] R. L. Bowers and J. R. Wilson. “A numerical model for stellar core collapse calculations.” In: *ApJS* 50 (Nov. 1982), pp. 115–159. DOI: [10.1086/190822](https://doi.org/10.1086/190822).
- [124] Takami Kuroda, Kei Kotake, and Tomoya Takiwaki. “Fully General Relativistic Simulations of Core-collapse Supernovae with an Approximate Neutrino Transport”. In: *ApJ* 755.1, 11 (Aug. 2012), p. 11. DOI: [10.1088/0004-637X/755/1/11](https://doi.org/10.1088/0004-637X/755/1/11). arXiv: [1202.2487](https://arxiv.org/abs/1202.2487) [[astro-ph.HE](#)].
- [125] Bernhard Müller, Hans-Thomas Janka, and Harald Dimmelmeier. “A New Multi-dimensional General Relativistic Neutrino Hydrodynamic Code for Core-collapse Supernovae. I. Method and Code Tests in Spherical Symmetry”. In: *ApJS* 189.1 (July 2010), pp. 104–133. DOI: [10.1088/0067-0049/189/1/104](https://doi.org/10.1088/0067-0049/189/1/104). arXiv: [1001.4841](https://arxiv.org/abs/1001.4841) [[astro-ph.SR](#)].
- [126] Micaela Oertel, Aurélien Pascal, Marco Mancini, and Jérôme Novak. “Improved neutrino-nucleon interactions in dense and hot matter for numerical simulations”. In: *Phys. Rev. C* 102.3, 035802 (Sept. 2020), p. 035802. DOI: [10.1103/PhysRevC.102.035802](https://doi.org/10.1103/PhysRevC.102.035802). arXiv: [2003.02152](https://arxiv.org/abs/2003.02152) [[astro-ph.HE](#)].
- [127] James M. Lattimer, C. J. Pethick, Madappa Prakash, and Pawel Haensel. “Direct URCA process in neutron stars”. In: *Phys. Rev. Lett.* 66.21 (May 1991), pp. 2701–2704. DOI: [10.1103/PhysRevLett.66.2701](https://doi.org/10.1103/PhysRevLett.66.2701).
- [128] B. L. Friman and O. V. Maxwell. “Neutrino emissivities of neutron stars.” In: *ApJ* 232 (Sept. 1979), pp. 541–557. DOI: [10.1086/157313](https://doi.org/10.1086/157313).

- [129] S. W. Bruenn. “Stellar core collapse - Numerical model and infall epoch”. In: *ApJS* 58 (Aug. 1985), pp. 771–841. DOI: [10.1086/191056](https://doi.org/10.1086/191056).
- [130] Georg Raffelt and Thomas Strobel. “Reduction of weak interaction rates in neutron stars by nucleon spin fluctuations: Degenerate case”. In: *Phys. Rev. D* 55.2 (Jan. 1997), pp. 523–527. DOI: [10.1103/PhysRevD.55.523](https://doi.org/10.1103/PhysRevD.55.523). arXiv: [astro-ph/9610193](https://arxiv.org/abs/astro-ph/9610193) [[astro-ph](#)].
- [131] Georg Raffelt and David Seckel. “Self-consistent approach to neutral-current processes in supernova cores”. In: *Phys. Rev. D* 52.4 (Aug. 1995), pp. 1780–1799. DOI: [10.1103/PhysRevD.52.1780](https://doi.org/10.1103/PhysRevD.52.1780). arXiv: [astro-ph/9312019](https://arxiv.org/abs/astro-ph/9312019) [[astro-ph](#)].
- [132] A. Bartl, R. Bollig, H. T. Janka, and A. Schwenk. “Impact of nucleon-nucleon bremsstrahlung rates beyond one-pion exchange”. In: *Phys. Rev. D* 94.8, 083009 (Oct. 2016), p. 083009. DOI: [10.1103/PhysRevD.94.083009](https://doi.org/10.1103/PhysRevD.94.083009). arXiv: [1608.05037](https://arxiv.org/abs/1608.05037) [[nucl-th](#)].
- [133] Matthias Hempel and Jürgen Schaffner-Bielich. “A statistical model for a complete supernova equation of state”. In: *Nucl. Phys. A* 837.3-4 (June 2010), pp. 210–254. DOI: [10.1016/j.nuclphysa.2010.02.010](https://doi.org/10.1016/j.nuclphysa.2010.02.010). arXiv: [0911.4073](https://arxiv.org/abs/0911.4073) [[nucl-th](#)].
- [134] F. Gulminelli and Ad. R. Raduta. “Unified treatment of subsaturation stellar matter at zero and finite temperature”. In: *Phys. Rev. C* 92.5, 055803 (Nov. 2015), p. 055803. DOI: [10.1103/PhysRevC.92.055803](https://doi.org/10.1103/PhysRevC.92.055803). arXiv: [1504.04493](https://arxiv.org/abs/1504.04493) [[nucl-th](#)].
- [135] Ad. R. Raduta, F. Gulminelli, and M. Oertel. “Modification of magicity toward the dripline and its impact on electron- capture rates for stellar core collapse”. In: *Phys. Rev. C* 93, 025803 (Feb. 2016), p. 025803. DOI: [10.1103/PhysRevC.93.025803](https://doi.org/10.1103/PhysRevC.93.025803).
- [136] W. R. Hix, O. E. Messer, A. Mezzacappa, M. Liebendörfer, J. Sampaio, K. Langanke, D. J. Dean, and G. Martínez-Pinedo. “Consequences of Nuclear Electron Capture in Core Collapse Supernovae”. In: *Phys. Rev. Lett.* 91.20, 201102 (Nov. 2003), p. 201102. DOI: [10.1103/PhysRevLett.91.201102](https://doi.org/10.1103/PhysRevLett.91.201102). arXiv: [astro-ph/0310883](https://arxiv.org/abs/astro-ph/0310883) [[astro-ph](#)].
- [137] S. W. Bruenn and A. Mezzacappa. “Ion screening effects and stellar collapse”. In: *Phys. Rev. D* 56.12 (Dec. 1997), pp. 7529–7547. DOI: [10.1103/PhysRevD.56.7529](https://doi.org/10.1103/PhysRevD.56.7529).
- [138] C. J. Horowitz. “Neutrino trapping in a supernova and the screening of weak neutral currents”. In: *Phys. Rev. D* 55.8 (Apr. 1997), pp. 4577–4581. DOI: [10.1103/PhysRevD.55.4577](https://doi.org/10.1103/PhysRevD.55.4577). arXiv: [astro-ph/9603138](https://arxiv.org/abs/astro-ph/9603138) [[astro-ph](#)].
- [139] Markus Rampp. “Radiation hydrodynamics with neutrinos: stellar core collapse and the explosion mechanism of type ii supernovae”. PhD thesis. Technische Universität München, 2000.
- [140] W. R. Yueh and J. R. Buchler. “Neutrino transport in supernova models: S/N method.” In: *ApJ* 217 (Oct. 1977), pp. 565–577. DOI: [10.1086/155605](https://doi.org/10.1086/155605).
- [141] Eric Braaten and Daniel Segel. “Neutrino energy loss from the plasma process at all temperatures and densities”. In: *Phys. Rev. D* 48.4 (Aug. 1993), pp. 1478–1491. DOI: [10.1103/PhysRevD.48.1478](https://doi.org/10.1103/PhysRevD.48.1478). arXiv: [hep-ph/9302213](https://arxiv.org/abs/hep-ph/9302213) [[hep-ph](#)].
- [142] Saša Ratković, Sharada Iyer Dutta, and Madappa Prakash. “Differential neutrino rates and emissivities from the plasma process in astrophysical systems”. In: *Phys. Rev. D* 67.12, 123002 (June 2003), p. 123002. DOI: [10.1103/PhysRevD.67.123002](https://doi.org/10.1103/PhysRevD.67.123002). arXiv: [astro-ph/0303501](https://arxiv.org/abs/astro-ph/0303501) [[astro-ph](#)].
- [143] Robert Buras, Hans-Thomas Janka, Mathias Th. Keil, Georg G. Raffelt, and Markus Rampp. “Electron Neutrino Pair Annihilation: A New Source for Muon and Tau Neutrinos in Supernovae”. In: *ApJ* 587.1 (Apr. 2003), pp. 320–326. DOI: [10.1086/368015](https://doi.org/10.1086/368015). arXiv: [astro-ph/0205006](https://arxiv.org/abs/astro-ph/0205006) [[astro-ph](#)].
- [144] B. Pontecorvo. “Mesonium and Antimesonium”. In: *Soviet Journal of Experimental and Theoretical Physics* 6 (Jan. 1958), p. 429.
- [145] E. Kearns, T. Kajita, and Y. Totsuka. “Detecting massive neutrinos.” In: *Scientific American* 281.2 (Aug. 1999), pp. 48–55.

- [146] L. Wolfenstein. “Neutrino oscillations in matter”. In: Phys. Rev. D 17.9 (May 1978), pp. 2369–2374. DOI: [10.1103/PhysRevD.17.2369](https://doi.org/10.1103/PhysRevD.17.2369).
- [147] S. P. Mikheyev and A. Yu. Smirnov. “Resonance enhancement of oscillations in matter and solar neutrino spectroscopy”. In: *Yadernaya Fizika* 42 (Jan. 1985), pp. 1441–1448.
- [148] Sajad Abbar, Huaiyu Duan, Kohsuke Sumiyoshi, Tomoya Takiwaki, and Maria Cristina Volpe. “On the occurrence of fast neutrino flavor conversions in multidimensional supernova models”. In: Phys. Rev. D 100.4, 043004 (Aug. 2019), p. 043004. DOI: [10.1103/PhysRevD.100.043004](https://doi.org/10.1103/PhysRevD.100.043004). arXiv: [1812.06883](https://arxiv.org/abs/1812.06883) [[astro-ph.HE](#)].
- [149] P. Strack and A. Burrows. “Generalized Boltzmann formalism for oscillating neutrinos”. In: Phys. Rev. D 71.9, 093004 (May 2005), p. 093004. DOI: [10.1103/PhysRevD.71.093004](https://doi.org/10.1103/PhysRevD.71.093004). arXiv: [hep-ph/0504035](https://arxiv.org/abs/hep-ph/0504035) [[hep-ph](#)].
- [150] Aurélien Pascal, Micaela Oertel, Marco Mancini, and Jérôme Novak. “Proto-neutron stars cooling with improved neutrino-nucleons interactions”. In: (in prep.).
- [151] Ch. C. Moustakidis, T. Gaitanos, Ch. Margaritis, and G. A. Lalazissis. “Bounds on the speed of sound in dense matter, and neutron star structure”. In: Phys. Rev. C 95.4, 045801 (Apr. 2017), p. 045801. DOI: [10.1103/PhysRevC.95.045801](https://doi.org/10.1103/PhysRevC.95.045801). arXiv: [1608.00344](https://arxiv.org/abs/1608.00344) [[nucl-th](#)].
- [152] S. E. Woosley, A. Heger, and T. A. Weaver. “The evolution and explosion of massive stars”. In: *Reviews of Modern Physics* 74.4 (Nov. 2002), pp. 1015–1071. DOI: [10.1103/RevModPhys.74.1015](https://doi.org/10.1103/RevModPhys.74.1015).
- [153] T. Fischer, S. C. Whitehouse, A. Mezzacappa, F. K. Thielemann, and M. Liebendörfer. “Protoneutron star evolution and the neutrino-driven wind in general relativistic neutrino radiation hydrodynamics simulations”. In: A&A 517, A80 (July 2010), A80. DOI: [10.1051/0004-6361/200913106](https://doi.org/10.1051/0004-6361/200913106). arXiv: [0908.1871](https://arxiv.org/abs/0908.1871) [[astro-ph.HE](#)].
- [154] Alejandro Torres-Forné, Pablo Cerdá-Durán, Martin Obergaulinger, Bernhard Müller, and José A. Font. “Universal Relations for Gravitational-Wave Asteroseismology of Protoneutron Stars”. In: Phys. Rev. Lett. 123.5, 051102 (Aug. 2019), p. 051102. DOI: [10.1103/PhysRevLett.123.051102](https://doi.org/10.1103/PhysRevLett.123.051102). arXiv: [1902.10048](https://arxiv.org/abs/1902.10048) [[gr-qc](#)].
- [155] O. Just, M. Obergaulinger, and H. T. Janka. “A new multidimensional, energy-dependent two-moment transport code for neutrino-hydrodynamics”. In: MNRAS 453.4 (Nov. 2015), pp. 3386–3413. DOI: [10.1093/mnras/stv1892](https://doi.org/10.1093/mnras/stv1892). arXiv: [1501.02999](https://arxiv.org/abs/1501.02999) [[astro-ph.HE](#)].
- [156] Harald Dimmelmeier, Jérôme Novak, and Pablo Cerdá-Durán. *CoCoNuT: General relativistic hydrodynamics code with dynamical space-time evolution*. Feb. 2012. ascl: [1202.012](https://ascl.net/1202.012).
- [157] Edwan Preau, Aurélien Pascal, Jérôme Novak, and Micaela Oertel. “What can be learned from a proto-neutron star’s mass and radius?” In: *arXiv e-prints*, arXiv:2102.05923 (Feb. 2021), arXiv:2102.05923. arXiv: [2102.05923](https://arxiv.org/abs/2102.05923) [[astro-ph.HE](#)].
- [158] S. Typel, G. Röpke, T. Klähn, D. Blaschke, and H. H. Wolter. “Composition and thermodynamics of nuclear matter with light clusters”. In: Phys. Rev. C 81.1, 015803 (Jan. 2010), p. 015803. DOI: [10.1103/PhysRevC.81.015803](https://doi.org/10.1103/PhysRevC.81.015803). arXiv: [0908.2344](https://arxiv.org/abs/0908.2344) [[nucl-th](#)].
- [159] A. W. Steiner, M. Hempel, and T. Fischer. “Core-collapse Supernova Equations of State Based on Neutron Star Observations”. In: ApJ 774.1, 17 (Sept. 2013), p. 17. DOI: [10.1088/0004-637X/774/1/17](https://doi.org/10.1088/0004-637X/774/1/17). arXiv: [1207.2184](https://arxiv.org/abs/1207.2184) [[astro-ph.SR](#)].
- [160] E. Chabanat, P. Bonche, P. Haensel, J. Meyer, and R. Schaeffer. “A Skyrme parametrization from subnuclear to neutron star densities”. In: Nucl. Phys. A 627 (Feb. 1997), pp. 710–746. DOI: [10.1016/S0375-9474\(97\)00596-4](https://doi.org/10.1016/S0375-9474(97)00596-4).
- [161] A. S. Schneider, C. Constantinou, B. Muccioli, and M. Prakash. “Akmal-Pandharipande-Ravenhall equation of state for simulations of supernovae, neutron stars, and binary mergers”. In: Phys. Rev. C 100.2, 025803 (Aug. 2019), p. 025803. DOI: [10.1103/PhysRevC.100.025803](https://doi.org/10.1103/PhysRevC.100.025803). arXiv: [1901.09652](https://arxiv.org/abs/1901.09652) [[nucl-th](#)].

- [162] A. S. Schneider, L. F. Roberts, and C. D. Ott. “Open-source nuclear equation of state framework based on the liquid-drop model with Skyrme interaction”. In: *Phys. Rev. C* 96.6, 065802 (Dec. 2017), p. 065802. DOI: [10.1103/PhysRevC.96.065802](https://doi.org/10.1103/PhysRevC.96.065802).
- [163] A. Akmal, V. R. Pandharipande, and D. G. Ravenhall. “Equation of state of nucleon matter and neutron star structure”. In: *Phys. Rev. C* 58.3 (Sept. 1998), pp. 1804–1828. DOI: [10.1103/PhysRevC.58.1804](https://doi.org/10.1103/PhysRevC.58.1804). arXiv: [nuc1-th/9804027](https://arxiv.org/abs/nuc1-th/9804027) [[nuc1-th](#)].
- [164] A. Mirizzi, I. Tamborra, H. Th. Janka, N. Saviano, K. Scholberg, R. Bollig, L. Hüdepohl, and S. Chakraborty. “Supernova neutrinos: production, oscillations and detection”. In: *Nuovo Cimento Rivista Serie* 39.1-2 (Feb. 2016), pp. 1–112. DOI: [10.1393/ncr/i2016-10120-8](https://doi.org/10.1393/ncr/i2016-10120-8). arXiv: [1508.00785](https://arxiv.org/abs/1508.00785) [[astro-ph.HE](#)].
- [165] A. Stökl. “A two-column formalism for time-dependent modelling of stellar convection. I. Description of the method”. In: *A&A* 490.3 (Nov. 2008), pp. 1181–1195. DOI: [10.1051/0004-6361:200810144](https://doi.org/10.1051/0004-6361:200810144). arXiv: [0809.0862](https://arxiv.org/abs/0809.0862) [[astro-ph](#)].
- [166] Luke F. Roberts and Sanjay Reddy. “Neutrino Signatures from Young Neutron Stars”. In: *Handbook of Supernovae*. Ed. by Athem W. Alsabti and Paul Murdin. 2017, p. 1605. DOI: [10.1007/978-3-319-21846-5_5](https://doi.org/10.1007/978-3-319-21846-5_5).
- [167] G. M. Fuller. “Neutron shell blocking of electron capture during gravitational collapse”. In: *ApJ* 252 (Jan. 1982), pp. 741–764. DOI: [10.1086/159598](https://doi.org/10.1086/159598).
- [168] K. Langanke and G. Martínez-Pinedo. “Shell-model calculations of stellar weak interaction rates: II. Weak rates for nuclei in the mass range $A=45-65$ in supernovae environments”. In: *Nucl. Phys. A* 673.1-4 (June 2000), pp. 481–508. DOI: [10.1016/S0375-9474\(00\)00131-7](https://doi.org/10.1016/S0375-9474(00)00131-7). arXiv: [nuc1-th/0001018](https://arxiv.org/abs/nuc1-th/0001018) [[nuc1-th](#)].
- [169] Karlheinz Langanke and G. Martínez-Pinedo. “Rate tables for the weak processes of pf-shell nuclei in stellar environments”. In: *Atomic Data and Nuclear Data Tables* 79.1 (2001), pp. 1–46.
- [170] K. Langanke, G. Martínez-Pinedo, J. M. Sampaio, D. J. Dean, W. R. Hix, O. E. Messer, A. Mezzacappa, M. Liebendörfer, H. Th. Janka, and M. Rampp. “Electron Capture Rates on Nuclei and Implications for Stellar Core Collapse”. In: *Phys. Rev. Lett.* 90.24, 241102 (June 2003), p. 241102. DOI: [10.1103/PhysRevLett.90.241102](https://doi.org/10.1103/PhysRevLett.90.241102). arXiv: [astro-ph/0302459](https://arxiv.org/abs/astro-ph/0302459) [[astro-ph](#)].
- [171] G. M. Fuller, W. A. Fowler, and M. J. Newman. “Stellar weak interaction rates for intermediate-mass nuclei. IV - Interpolation procedures for rapidly varying lepton capture rates using effective log (ft)-values”. In: *ApJ* 293 (June 1985), pp. 1–16. DOI: [10.1086/163208](https://doi.org/10.1086/163208).
- [172] Ad. R. Raduta, F. Gulminelli, and M. Oertel. “Stellar electron capture rates on neutron-rich nuclei and their impact on stellar core collapse”. In: *Phys. Rev. C* 95.2, 025805 (Feb. 2017), p. 025805. DOI: [10.1103/PhysRevC.95.025805](https://doi.org/10.1103/PhysRevC.95.025805). arXiv: [1611.01744](https://arxiv.org/abs/1611.01744) [[nuc1-th](#)].
- [173] G. Audi, Kondev F. G., Wang M., B. Pfeiffer, Sun X., J. Blachot, and M. MacCormick. “The Nubase2012 evaluation of nuclear properties”. In: *Chinese Physics C* 36.12 (Dec. 2012), p. 001. DOI: [10.1088/1674-1137/36/12/001](https://doi.org/10.1088/1674-1137/36/12/001).
- [174] Wang M., G. Audi, Wapstra A. H., Kondev F. G., M. MacCormick, X. Xu, and B. Pfeiffer. “The Ame2012 atomic mass evaluation”. In: *Chinese Physics C* 36.12 (Dec. 2012), p. 003. DOI: [10.1088/1674-1137/36/12/003](https://doi.org/10.1088/1674-1137/36/12/003).
- [175] J. Duflo and A. P. Zuker. “Microscopic mass formulas”. In: *Phys. Rev. C* 52.1 (July 1995), R23–R27. DOI: [10.1103/PhysRevC.52.R23](https://doi.org/10.1103/PhysRevC.52.R23). arXiv: [nuc1-th/9505011](https://arxiv.org/abs/nuc1-th/9505011) [[nuc1-th](#)].
- [176] Paweł Danielewicz and Jenny Lee. “Symmetry energy I: Semi-infinite matter”. In: *Nucl. Phys. A* 818.1 (Feb. 2009), pp. 36–96. DOI: [10.1016/j.nuclphysa.2008.11.007](https://doi.org/10.1016/j.nuclphysa.2008.11.007). arXiv: [0807.3743](https://arxiv.org/abs/0807.3743) [[nuc1-th](#)].
- [177] Harald Dimmelmeier, Jérôme Novak, José A. Font, José M. Ibáñez, and Ewald Müller. “Combining spectral and shock-capturing methods: A new numerical approach for 3D

- relativistic core collapse simulations”. In: *Phys. Rev. D* 71.6, 064023 (Mar. 2005), p. 064023. DOI: [10.1103/PhysRevD.71.064023](https://doi.org/10.1103/PhysRevD.71.064023). arXiv: [astro-ph/0407174](https://arxiv.org/abs/astro-ph/0407174) [[astro-ph](#)].
- [178] Ericourgoulhon. “3+1 Formalism and Bases of Numerical Relativity”. In: *arXiv e-prints*, gr-qc/0703035 (Mar. 2007), gr-qc/0703035. arXiv: [gr-qc/0703035](https://arxiv.org/abs/gr-qc/0703035) [[gr-qc](#)].
- [179] Ericourgoulhon, Philippe Grandclément, Jean-Alain Marck, Jérôme Novak, and Keisuke Taniguchi. *LORENE: Spectral methods differential equations solver*. Aug. 2016. ascl: [1608.018](https://ascl.net/1608.018).
- [180] Philippe Grandclément and Jérôme Novak. “Spectral Methods for Numerical Relativity”. In: *Living Reviews in Relativity* 12.1, 1 (Jan. 2009), p. 1. DOI: [10.12942/lrr-2009-1](https://doi.org/10.12942/lrr-2009-1). arXiv: [0706.2286](https://arxiv.org/abs/0706.2286) [[gr-qc](#)].
- [181] Francesc Banyuls, José A. Font, José M. Ibáñez, José M. Martí, and Juan A. Miralles. “Numerical $\{3 + 1\}$ General Relativistic Hydrodynamics: A Local Characteristic Approach”. In: *ApJ* 476.1 (Feb. 1997), pp. 221–231. DOI: [10.1086/303604](https://doi.org/10.1086/303604).
- [182] José A. Font. “Numerical Hydrodynamics and Magnetohydrodynamics in General Relativity”. In: *Living Reviews in Relativity* 11.1, 7 (Sept. 2008), p. 7. DOI: [10.12942/lrr-2008-7](https://doi.org/10.12942/lrr-2008-7).
- [183] P. Möller, J. R. Nix, W. D. Myers, and W. J. Swiatecki. “Nuclear Ground-State Masses and Deformations”. In: *Atomic Data and Nuclear Data Tables* 59 (Jan. 1995), p. 185. DOI: [10.1006/adnd.1995.1002](https://doi.org/10.1006/adnd.1995.1002). arXiv: [nuc1-th/9308022](https://arxiv.org/abs/nuc1-th/9308022) [[nuc1-th](#)].
- [184] Aurélien Pascal, Simon Giraud, Anthea F. Fantina, Francesca Gulminelli, Jérôme Novak, Micaela Oertel, and Adriana R. Raduta. “Impact of electron capture rates for nuclei far from stability on core-collapse supernovae”. In: *Phys. Rev. C* 101.1, 015803 (Jan. 2020), p. 015803. DOI: [10.1103/PhysRevC.101.015803](https://doi.org/10.1103/PhysRevC.101.015803). arXiv: [1906.05114](https://arxiv.org/abs/1906.05114) [[astro-ph.HE](#)].
- [185] Chris Sullivan, Evan O’Connor, Remco G. T. Zegers, Thomas Grubb, and Sam M. Austin. “The Sensitivity of Core-collapse Supernovae to Nuclear Electron Capture”. In: *ApJ* 816.1, 44 (Jan. 2016), p. 44. DOI: [10.3847/0004-637X/816/1/44](https://doi.org/10.3847/0004-637X/816/1/44). arXiv: [1508.07348](https://arxiv.org/abs/1508.07348) [[astro-ph.HE](#)].
- [186] M. Hempel, T. Fischer, J. Schaffner-Bielich, and M. Liebendörfer. “New Equations of State in Simulations of Core-collapse Supernovae”. In: *ApJ* 748.1, 70 (Mar. 2012), p. 70. DOI: [10.1088/0004-637X/748/1/70](https://doi.org/10.1088/0004-637X/748/1/70). arXiv: [1108.0848](https://arxiv.org/abs/1108.0848) [[astro-ph.HE](#)].
- [187] Rachel Titus, Chris Sullivan, Remco GT Zegers, B Alex Brown, and Bingshui Gao. “Impact of electron-captures on nuclei near $N = 50$ on core-collapse supernovae”. In: *Journal of Physics G: Nuclear and Particle Physics* 45.1 (2017), p. 014004.
- [188] Jason Pruet and George M. Fuller. “Estimates of Stellar Weak Interaction Rates for Nuclei in the Mass Range $A=65-80$ ”. In: *ApJS* 149.1 (Nov. 2003), pp. 189–203. DOI: [10.1086/376753](https://doi.org/10.1086/376753). arXiv: [astro-ph/0211262](https://arxiv.org/abs/astro-ph/0211262) [[astro-ph](#)].
- [189] Jose V. Romero, Jose M. A. Ibanez, Jose M. A. Marti, and Juan A. Miralles. “A New Spherically Symmetric General Relativistic Hydrodynamical Code”. In: *ApJ* 462 (May 1996), p. 839. DOI: [10.1086/177198](https://doi.org/10.1086/177198). arXiv: [astro-ph/9509121](https://arxiv.org/abs/astro-ph/9509121) [[astro-ph](#)].
- [190] J. A. Miralles, J. A. Morales, and D. Sáez. *Some topics on general relativity and gravitational radiation. Proceedings*. 1997, p. 289.
- [191] Anthea Francesca Fantina. “Supernovae theory: study of electro-weak processes during gravitational collapse of massive stars”. PhD thesis. Universite de Paris XI, 2010.
- [192] G. Grams, S. Giraud, A. F. Fantina, and F. Gulminelli. “Distribution of nuclei in equilibrium stellar matter from the free-energy density in a Wigner-Seitz cell”. In: *Phys. Rev. C* 97.3, 035807 (Mar. 2018), p. 035807. DOI: [10.1103/PhysRevC.97.035807](https://doi.org/10.1103/PhysRevC.97.035807).
- [193] Luke F. Roberts and Sanjay Reddy. “Charged current neutrino interactions in hot and dense matter”. In: *Phys. Rev. C* 95.4, 045807 (Apr. 2017), p. 045807. DOI: [10.1103/PhysRevC.95.045807](https://doi.org/10.1103/PhysRevC.95.045807). arXiv: [1612.02764](https://arxiv.org/abs/1612.02764) [[astro-ph.HE](#)].

- [194] David Bohm and David Pines. “A Collective Description of Electron Interactions. I. Magnetic Interactions”. In: *Physical Review* 82.5 (June 1951), pp. 625–634. DOI: [10.1103/PhysRev.82.625](#).
- [195] E. S. Hernández, J. Navarro, and A. Polls. “Response of asymmetric nuclear matter to isospin-flip probes”. In: *Nucl. Phys. A* 658.4 (Dec. 1999), pp. 327–342. DOI: [10.1016/S0375-9474\(99\)00363-2](#).
- [196] A. Pastore, D. Davesne, and J. Navarro. “Linear response of homogeneous nuclear matter with energy density functionals”. In: *Phys. Rep.* 563 (Mar. 2015), pp. 1–67. DOI: [10.1016/j.physrep.2014.11.002](#). arXiv: [1412.2339 \[nucl-th\]](#).
- [197] J. Margueron and H. Sagawa. “Extended Skyrme interaction: I. Spin fluctuations in dense matter”. In: *Journal of Physics G Nuclear Physics* 36.12, 125102 (Dec. 2009), p. 125102. DOI: [10.1088/0954-3899/36/12/125102](#). arXiv: [0905.1931 \[nucl-th\]](#).
- [198] Sanjay Reddy, Madappa Prakash, James M. Lattimer, and Jose A. Pons. “Effects of strong and electromagnetic correlations on neutrino interactions in dense matter”. In: *Phys. Rev. C* 59.5 (May 1999), pp. 2888–2918. DOI: [10.1103/PhysRevC.59.2888](#). arXiv: [astro-ph/9811294 \[astro-ph\]](#).
- [199] G. I. Lykasov, C. J. Pethick, and A. Schwenk. “Unified approach to structure factors and neutrino processes in nucleon matter”. In: *Phys. Rev. C* 78.4, 045803 (Oct. 2008), p. 045803. DOI: [10.1103/PhysRevC.78.045803](#). arXiv: [0808.0330 \[nucl-th\]](#).
- [200] S. Bacca, K. Hally, M. Liebendörfer, A. Perego, C. J. Pethick, and A. Schwenk. “Neutrino Processes in Partially Degenerate Neutron Matter”. In: *ApJ* 758.1, 34 (Oct. 2012), p. 34. DOI: [10.1088/0004-637X/758/1/34](#). arXiv: [1112.5185 \[astro-ph.HE\]](#).

RÉSUMÉ

Si les principaux aspects du mécanisme des supernovas à effondrement de cœur sont aujourd'hui compris, des détails importants sur la microphysique restent sujets à beaucoup d'incertitudes. En particulier, les neutrinos jouent un rôle clé dans le mécanisme mais les taux d'interactions des neutrinos sont difficiles à déterminer avec précision dans la matière dense soumise à l'interaction forte. Dans cette thèse nous présentons un nouveau code d'évolution des proto-étoiles à neutrons, et l'utilisons avec le code de simulation de supernova à effondrement de cœur CoCoNuT pour étudier l'influence des incertitudes sur les taux de réaction des neutrinos. Les effets convectifs, qui jouent un rôle majeur dans l'évolution des proto-étoiles à neutrons, ont été pris en compte avec la théorie de la longueur de mélange.

MOTS CLÉS

Phénomènes astrophysiques de haute énergie, Objets compacts, Étoiles à neutrons, Supernovas à effondrement de cœur, Transport de neutrinos, Convection

ABSTRACT

If the main features of the core-collapse supernova mechanism are now understood, some important details about the microphysics are still subject to a lot of uncertainties. In particular, neutrinos are playing a key role in the core-collapse mechanism but interaction rates of neutrinos are difficult to determine precisely due to the strongly interacting dense matter. In this thesis we present a new code for proto-neutron star evolution, and we use it together with the CoCoNuT core-collapse code to study the influence of the uncertainties on neutrino reaction rates. Convective effects, which play a crucial role in proto-neutron stars evolution, have been taken into account with the mixing length theory.

KEYWORDS

High energy astrophysical phenomena, Compact objects, Neutron stars, Core-collapse supernova, Neutrino transport, Convection